

**Metal Nitride Cluster as a Template to
Tune the Electronic and Magnetic Properties of
Rare-Earth Metal Containing Endohedral Fullerenes**

DISSERTATION

zur Erlangung des akademischen Grades doctor rerum naturalium

(Dr. rer. nat.)

Vorgelegt dem Rat der Chemisch-Geowissenschaftlichen Fakultät der

Friedrich-Schiller-Universität Jena

Von

M.Sc. Yang Zhang

geboren am 7. März 1983 in Beijing, China

Reviewers:

Prof. Dr. Rainer Beckert, Friedrich-Schiller-Universität Jena

Prof. Dr. Lothar Dunsch, Leibniz Institute for Solid State and Materials Research Dresden

Defense date: October 16th, 2013

ZUSAMMENFASSUNG

Seltenerdmetalle enthaltende endohedrale Fullerene haben große Beachtung gefunden auf Grund ihrer Eigenschaft Metallatome, Atome oder ganze Cluster innerhalb eines Kohlenstoffkäfigs einzuschließen. Durch Anregung der im Kohlenstoffkäfig eingeschlossenen Atome oder Cluster können die physikalischen und chemischen Eigenschaften dieser Fullerene zielgerichtet verändert und eingestellt werden. Das Verständnis der magnetischen und elektrochemischen Eigenschaften von endohedralen Fullerenen spielt eine wichtige Rolle in der Grundlagenforschung und bietet ein hohes Potential für Anwendungen in der Materialentwicklung. In dieser Arbeit wird die Herstellung von Seltenerdmetallstrukturen beinhaltenden Fullerenen und die Charakterisierung deren grundlegenden Eigenschaften beschrieben. Gleichzeitig werden Wege zur zielgerichteten Veränderung ihrer elektronischen und magnetischen Eigenschaften aufgezeigt.

Im Lichtbogenverfahren nach Krätschmer-Huffman konnten verschiedene Lanthanit basierende gemischte Metall-Nitrid-Clusterfullerene (MMNCF) hergestellt werden. Diese Seltenerdmetalle enthaltende endohedrale Fullerene wurden in einem mehrstufigen Flüssigkeitstrennverfahren (HPLC) getrennt. Anschließend wurden diese Strukturen mittels spektroskopischer Verfahren wie UV-vis-NIR, FTIR, Raman, LDI-TOF Massenspektroskopie, NMR, Elektrochemie und in situ Spektroelektrochemie charakterisiert.

Die Holmium basierenden gemischt Metall-Nitrid-Clusterfullerene $\text{Ho}_x\text{M}_{3-x}\text{N}@C_{80}$ ($M = \text{Sc}, \text{Lu}, \text{Y}; x=1, 2$) wurden in einer "reactive gas atmosphere" oder "selective organic solid" Verfahren hergestellt. Die getrennten und gereinigten Proben wurden mit LDI-TOF Massenspektroskopie, UV-vis-NIR, FTIR, Raman-Spektroskopie und NMR-Spektroskopie charakterisiert. Die ^{13}C -NMR-Spektroskopie Untersuchungen zeigen ein außergewöhnliches NMR-Verhalten was von der Änderung des zweiten Metalls innerhalb des Metall-Nitrid-Clusters $\text{Ho}_x\text{M}_{3-x}\text{N}$ von Sc zu Lu und weiter zu Y herrührt.

Die Strukturen $\text{LnSc}_2\text{N}@C_{80}$ ($\text{Ln} = \text{Ce}, \text{Pr}, \text{Nd}, \text{Tb}, \text{Dy}, \text{Ho}, \text{Lu}$) MMNCF wurden sowohl mit ^{13}C als auch ^{45}Sc -NMR-Spektroskopie untersucht. Entsprechend der Bleaney-Theorie konnte nach der Reilly-Methode die Unterscheidung von δ^{PC} und δ^{con} von δ^{para} durch eine primäre ^{13}C und ^{45}Sc -Analyse des $\text{LnSc}_2\text{N}@C_{80}$ (I) gezeigt werden. Die sehr gute lineare Anpassung ($R^2 = 0.99$) wurde bei der Betrachtung eines eingeschlossenen Clusters LnSc_2N

(Ln= Ce, Pr, Nd, Tb, Dy, Ho, Lu) innerhalb eines $C_{80:I_h}$ Käfigs erreicht. Dies zeigt die fantastische Natur der magnetischen Anisotropie von Lanthanitenmetallen.

Die $Ce_xY_{3-x}N@C_{2n}$ ($x= 1, 2$; $2n= 80-88$) MMNCF Strukturen wurden mit dem Verfahren "selective organic solid" hergestellt. Die daraus isolierten Proben wurden mit LDI-TOF Massenspektroskopie, UV-vis-NIR-Spektroskopie, NMR-Spektroskopie und elektrochemischen Methoden untersucht. Das elektrochemische Oxidationsverhalten von $CeM_2N@C_{80}$ ($M= Sc, Lu$ und Y) wurde vom eingeschlossenen Cluster (CeM_2N ; $M= Sc, Lu$ und Y) beeinflusst. Diese Annahme wird durch die ^{13}C und ^{45}Sc NMR Untersuchungen von $[CeM_2N@C_{80}]^+$ und DFT Berechnungen gestützt.

Soweit wir wissen ist dies die erstmalige Entdeckung und der Nachweis

(a) von paramagnetischen Zuständen von Seltenerdmetallen innerhalb endohedraler Fullereene durch ein zweites diamagnetisches Metall mit unterschiedlichem Ionenradius zielgerichtet beeinflusst werden können.

(b) dass das elektrochemische Verhalten von Ce basierenden endohedralen Fullerenen durch den eingeschlossenen Cluster CeM_2N ($M= Sc, Lu$ und Y) eingestellt werden kann.

ABSTRACT

Rare-earth metal containing endohedral fullerenes have attracted much attention due to the feasibility of encaging metal atom, atoms or cluster inside of carbon cages. By switching the metal atom or cluster entrapped inside of the carbon cage the physical and chemical properties of the fullerene compounds can be tuned. The understanding of magnetic and electrochemical properties of endohedral fullerenes plays an essential role in fundamental scientific researches and potential applications in materials science. In this thesis, synthesizing novel rare-earth metal containing endohedral fullerene structures, studying the properties of these isolated endohedral fullerenes and the strategies of tuning the electronic and magnetic properties of endohedral fullerenes were introduced.

The DC-arc discharging synthesis of different lanthanide metal-based (Ho, Ce and Pr) mixed metal nitride clusterfullerenes was achieved. Those rare-earth metal containing endohedral fullerenes were isolated by multi-step HPLC. The isolated samples were characterized by spectroscopic techniques included UV-vis-NIR, FTIR, Raman, LDI-TOF mass spectrometry, NMR and electrochemistry.

The Ho-based mixed metal nitride clusterfullerenes $\text{Ho}_x\text{M}_{3-x}\text{N}@C_{80}$ ($M = \text{Sc, Lu, Y; } x = 1, 2$) were synthesized by “reactive gas atmosphere” method or “selective organic solid” route. The isolated samples were characterized by LDI-TOF mass spectrometry, UV-vis-NIR, FTIR, Raman and NMR spectroscopy. The ^{13}C NMR spectroscopic studies demonstrated exceptional NMR behaviors that resulted from switching the second metal inside of the mixed metal nitride cluster $\text{Ho}_x\text{M}_{3-x}\text{N}$ from Sc to Lu and further to Y.

The $\text{LnSc}_2\text{N}@C_{80}$ ($\text{Ln} = \text{Ce, Pr, Nd, Tb, Dy, Ho, Lu}$) MMNCFs were characterized by ^{13}C and ^{45}Sc NMR study respectively. According to Bleaney’s theory and Reilley method, the separation of δ^{PC} and δ^{con} from δ^{para} was achieved by the primary ^{13}C and ^{45}Sc NMR analysis of $\text{LnSc}_2\text{N}@C_{80}$ (I). The good linear fitting ($R^2 = 0.99$) was obtained by considering the encapsulating LnSc_2N cluster ($\text{Ln} = \text{Ce, Pr, Nd, Tb, Dy, Ho, Lu}$) inside $C_{80}:I_h$ cage which indicated the fantastic nature of magnetic anisotropy of lanthanide metals.

The $\text{Ce}_x\text{Y}_{3-x}\text{N}@C_{2n}$ ($x = 1, 2; 2n = 80-88$) MMNCFs were synthesized by “selective organic solid” route. The isolated samples were characterized by LDI-TOF mass spectrometry, UV-vis-NIR, NMR spectroscopy and electrochemistry. The electrochemical oxidation behaviors of $\text{CeM}_2\text{N}@C_{80}$ ($M = \text{Sc, Lu and Y}$) were interpreted as the strain-driven endohedral redox

couple $\text{Ce}^{\text{IV}}/\text{Ce}^{\text{III}}$ in $\text{CeM}_2\text{N@C}_{80}$ which supported by ^{13}C and/or ^{45}Sc NMR study of $[\text{CeM}_2\text{N@C}_{80}]^+$ and DFT calculations.

As far as we know, this work is the first discovery of (a) the (para)magnetic properties of rare-earth metal containing endohedral fullerenes can be tuned by the second diamagnetic metal with different metal ionic radius and (b) electrochemical properties of Ce-based endohedral fullerenes can be tuned by the strain-driven between the encaged cluster and carbon cage.

TABLE OF CONTENTS

ZUSAMMENFASSUNG	I
ABSTRACT	III
TABLE OF CONTENTS.....	V
LIST OF FIGURES	VII
Chapter 1 Introduction.....	1
1.1 Synthesis and isolation of endohedral fullerenes	1
1.2 Properties of metal nitride clusterfullerenes.....	3
1.2.1 Spectroscopic properties	3
1.2.2 Electrochemical and spectroelectrochemical properties	6
1.2.3 Magnetic properties.....	11
1.3 Motivation	16
Chapter 2 Synthesis and Isolation of Mixed Metal Nitride Clusterfullerenes.....	19
2.1 Introduction	19
2.2 Synthesis and isolation of $\text{Ho}_x\text{M}_{3-x}\text{N}@C_{80}$	21
2.2.1 Synthesis and isolation of $\text{Ho}_x\text{Sc}_{3-x}\text{N}@C_{80}$ (x= 1, 2)	21
2.2.2 Synthesis and isolation of $\text{Ho}_x\text{Y}_{3-x}\text{N}@C_{80}$ (x=1, 2).....	26
2.2.3 Synthesis and Isolation of $\text{Ho}_x\text{Lu}_{3-x}\text{N}@C_{80}$ (x=1, 2).....	30
2.3 Synthesis and isolation of Ce-based MMNCFs	35
2.3.1 Synthesis and isolation of $\text{CeY}_2\text{N}@C_{80}$ (I).....	35
2.3.2 Synthesis and isolation of $\text{Ce}_x\text{Y}_{3-x}\text{N}@C_{2n}$ (2n= 84-88)	37
2.3.3 Synthesis and isolation of $\text{CeSc}_2\text{N}@C_{80}$ (II).....	41
2.4 Synthesis and Isolation of Pr-based MMNCFs	44
2.5 Conclusion.....	48
Chapter 3 Spectroscopic Characterization of Mixed Metal Nitride Clusterfullerenes ...	49
3.1 UV-Vis-NIR spectroscopy of MMNCFs	49
3.2 Vibrational spectroscopy of MMNCFs	56
3.2.1 FTIR Vibrational Spectroscopic study of MMNCFs	56
3.2.2 Raman Spectroscopic study of MMNCFs.....	63
3.3 NMR spectroscopy of Ln-based MMNCFs	68
3.4 Conclusion.....	71
Chapter 4 Magnetic Properties of Mixed Metal Nitride Clusterfullerenes	72
4.1 ^{13}C NMR spectroscopic study of $\text{CeM}_2\text{N}@C_{80}$	72

4.2 ^{45}Sc NMR spectroscopic study of MMNCFs.....	80
4.3 The analysis of NMR spectroscopy of $\text{LnSc}_2\text{N@C}_{80}$	87
4.4 Conclusion.....	91
Chapter 5 Electrochemical Study of Ce-based Mixed Metal Nitride Clusterfullerenes..	92
5.1 Electrochemical study of $\text{CeY}_2\text{N@C}_{80}$	93
5.2 Electrochemical study of $\text{Ce}_x\text{Y}_{3-x}\text{N@C}_{2n}$ ($2n= 84, 86, 88$).....	99
5.3 Conclusion.....	108
Conclusion of Thesis.....	109
Reference.....	112
Acknowledgement	125
Appendix I: Experimental details	126
1. Synthesis and Extraction	126
2. HPLC isolation.....	126
3. Spectroscopic and electrochemical characterizations	127
Curriculum Vitae	128

LIST OF FIGURES

Figure 1.1 The scheme of fullerenes generator.....	2
Figure 1.2 FTIR spectra of $\text{Sc}_3\text{N@C}_{80}$ (I), $\text{Sc}_3\text{N@C}_{78}$ and $\text{Sc}_3\text{N@C}_{68}$	5
Figure 1.3 M-N antisymmetric mode frequency in $\text{M}_3\text{N@C}_{80}$ (I; M= Gd, Tb, Dy, Ho, Er, Tm, Lu and Y) as a function of the ionic radius of the metal. The inset shows DFT-optimized structure of $\text{Gd}_3\text{N@C}_{80-I_h}$; pyramidalization of the Gd_3N cluster can be clearly seen.....	6
Figure 1.4 Cyclic voltammogram of the I_h and D_{5h} isomers of (left) $\text{Sc}_3\text{N@C}_{80}$ and (right) $\text{Lu}_3\text{N@C}_{80}$ in <i>o</i> -dichlorobenzene solution, 0.1 M TBABF ₄ , scan rate: 500 mV/s.....	8
Figure 1.5 Cyclic voltammograms of $\text{Dy}_3\text{N@C}_{80}$ (II) (solid line) and $\text{Dy}_3\text{N@C}_{80}$ (I) (dash line) in TBABF ₄ / <i>o</i> -DCB. Scan rate: 0.1 Vs ⁻¹ . The asterisk labels an unidentified reduction peak.....	9
Figure 1.6 Cyclic voltammograms of $\text{Gd}_3\text{N@C}_{2n}$ (2n= 80-88) compounds obtained in <i>o</i> -DCB + 0.05M (n-Bu) ₄ NPF ₆ (scan rate 0.1 V/s).....	10
Figure 1.7 Cyclic voltammetry of $\text{TiSc}_2\text{N@C}_{80}$ measured in <i>o</i> -DCB solution (room temperature, TBABF ₄ as supporting electrolyte) at a scan rate of 20 mV/s. Dotted vertical bars denote reversible redox potentials of $\text{Sc}_3\text{N@C}_{80}$ (I).....	11
Figure 1.8 (a) ¹³ C NMR spectrum of La@C_{82} anion, (b) its expanded views.....	12
Figure 1.9 ¹³ C NMR spectrums of (a) Ce@C_{82} anion and (b) La@C_{82} anion.....	12
Figure 1.10 The experimental data $M(H,T)$ for $\text{Ho}_3\text{N@C}_{80}$ and $\text{Tb}_3\text{N@C}_{80}$ (symbols) corrected for the diamagnetic contribution and normalized to the saturation. The solid line represents the fitted Langevin function with a magnetic moment $\mu= 21 \mu_B$ for $\text{Ho}_3\text{N@C}_{80}$ and $\mu= 17 \mu_B$ for $\text{Tb}_3\text{N@C}_{80}$	13
Figure 1.11 a) Structure of an $\text{M}_3\text{N@C}_{80}$ molecule, blue: carbon, green: nitrogen, and red: lanthanide metal atoms; b) orientation of the individual R magnetic moments m (arrows) in the M_3N cluster in $\text{M}_3\text{N@C}_{80}$ (M= Ho or Tb).....	14
Figure 1.12 97.2 MHz ⁴⁵ Sc solution NMR spectra of $\text{CeSc}_2\text{N@C}_{80}$ in 1, 2-dichlorobenzene at various temperatures and $\text{Sc}_3\text{N@C}_{80}$ (I_h) in 1, 2-dichlorobenzene.....	15
Figure 1.13 ¹³ C NMR spectra of $\text{Lu}_2\text{CeN@C}_{80}$ compared with $\text{Lu}_3\text{N@C}_{80}$ (left side) were measured at room temperature; and ¹³ C chemical shifts in the NMR spectra of $\text{Lu}_2\text{CeN@C}_{80}$ and their extrapolation to T ⁻² = 0 (right side). The room-temperature ¹³ C shifts	

for CeSc ₂ N@C ₈₀ as well as a series of some diamagnetic M ₃ N@C ₈₀ are also shown for comparison.	16
Figure 2.1 Chromatogram of a raw Ho _x Sc _{3-x} N@C _{2n} fullerenes extract synthesized by the “reactive gas atmosphere” method (linear combination of two 4.6×250 mm Buckyprep columns, flow rate 1.6 ml/min, injection volume 200 μL, toluene as mobile phase, 40 °C). The inset shows the enlarged chromatographic region of 28.0-33.0 min.	21
Figure 2.2 The HPLC isolation of fraction A by three-step recycling HPLC. (a) Removal of HoSc ₂ N@C ₈₀ (I) (10×250 mm Buckyprep column; flow rate 1.5 ml/min; injection volume 5 ml; toluene as eluent; 20 °C). (b) Removal of Sc ₃ N@C ₇₈ and HoSc ₂ N@C ₇₈ (10×250 mm Buckyclutcher column; flow rate 1.5 ml/min; injection volume 5 ml; toluene as eluent). (c) Removal of Ho ₃ N@C ₈₀ (I) (10×250 mm Buckyprep column; flow rate 1.5 ml/min; injection volume 5 ml; toluene as eluent), (d) shows the enlarged chromatographic region at 1025-1125 min.	22
Figure 2.3 The HPLC isolation of fraction B by recycling HPLC. The removal of Sc ₃ N@C ₇₈ , HoSc ₂ N@C ₇₈ and Ho ₂ ScN@C ₈₀ (I) (10×250 mm Buckyprep column; flow rate 1.5 ml/min; injection volume 5 ml; toluene as eluent; 20 °C).....	23
Figure 2.4 The HPLC isolation of fraction C by recycling HPLC.....	24
Figure 2.5 The isolation of fraction D. The removal of Ho ₂ ScN@C ₈₀ (II) and Sc ₃ N@C ₈₀ (II) (10×250 mm Buckyprep column; flow rate 1.5 ml/min; injection volume 5 ml; toluene as eluent; 20 °C).....	25
Figure 2.6 Positive Ion LDI-TOF mass spectra of the isolated Ho _x Sc _{3-x} N@C ₈₀ (I, II; x= 1, 2).....	26
Figure 2.7 Chromatogram of a raw Ho _x Y _{3-x} N@C _{2n} fullerenes extract synthesized by the “selective organic solid” method (linear combination of two 4.6×250 mm Buckyprep columns, flow rate 1.6 ml/min, injection volume 200 μL, toluene as mobile phase, 40 °C). The inset shows the enlarged chromatographic region of 29.5-34.5 min.	26
Figure 2.8 The HPLC isolation of fraction 3. (10×250 mm Buckyprep column; flow rate 1.5 ml/min; injection volume 5 ml; toluene as eluent; 20 °C).....	27
Figure 2.9 The isolation of fraction Fr 32. (10×250 mm Buckyprep column; flow rate 1.5 ml/min; injection volume 5 ml; toluene as eluent; 20 °C).....	28
Figure 2.10 The isolation of fraction Fr 33. (10×250 mm Buckyprep column; flow rate 1.5 ml/min; injection volume 5 ml; toluene as eluent; 20 °C).....	29

Figure 2.11 The isolated samples of $\text{Ho}_x\text{Y}_{3-x}\text{N}@C_{80}$ (I; $x=1, 2$) were identified by laser-desorption time-of-flight (LDI-TOF) mass spectrum analysis, which confirmed their high purity.	30
Figure 2.12 Chromatogram of a raw $\text{Ho}_x\text{Lu}_{3-x}\text{N}@C_{2n}$ fullerenes extract synthesized by the “reactive gas atmosphere” method (linear combination of two 4.6×250 mm Buckyprep columns, flow rate 1.6 ml/min, injection volume 200 μL , toluene as mobile phase, 40 °C). The inset shows the enlarged chromatographic region of 28.0 - 31.5 min.	30
Figure 2.13 The isolation of fraction Fr 1. (10×250 mm Buckyprep column; flow rate 1.5 ml/min; injection volume 5 ml; toluene as eluent; 20 °C).....	31
Figure 2.14 The isolation of fraction Fr 12. (10×250 mm Buckyprep column; flow rate 1.5 ml/min; injection volume is 5 ml; toluene as eluent; 40 °C).....	32
Figure 2.15 The isolation of fraction Fr 122. (10×250 mm Buckyprep column; flow rate 1.5 ml/min; injection volume 4 ml; toluene as eluent; 20 °C).....	33
Figure 2.16 The isolation of fraction Fr 121. (10×250 mm Buckyprep column; flow rate 1.5 ml/min; injection volume is 4 ml; toluene as eluent; 20 °C).....	34
Figure 2.17 The isolated samples of $\text{Ho}_x\text{Lu}_{3-x}\text{N}@C_{80}$ (I; $x=1, 2$) were identified by laser-desorption time-of-flight (LDI-TOF) mass spectrum analysis, which confirmed their high purity.	35
Figure 2.18 Chromatogram of $\text{Ce}_x\text{Y}_{3-x}\text{N}@C_{2n}$ ($2n= 80-88$) fullerene extract mixture synthesized by the “SOS” method (combination of two 4.6×250 mm Buckyprep columns, flow rate 1.6 ml/min, injection volume 200 μL , toluene as mobile phase, 40 °C).....	35
Figure 2.19 The isolation of $\text{CeY}_2\text{N}@C_{80}$ (I). $\text{CeY}_2\text{N}@C_{80}$ (I) was obtained by recycling HPLC after 29 cycles (10×250 mm Buckyprep column; flow rate 1.5 ml/min; injection volume is 5 ml; toluene as eluent; room temperature); the inset shows the last cycle (between 2870 and 2970 min).....	36
Figure 2.20 The LDI-TOF mass spectrum of purified $\text{CeY}_2\text{N}@C_{80}$ (I).	37
Figure 2.21 Chromatogram of $\text{Ce}_x\text{Y}_{3-x}\text{N}@C_{2n}$ fullerenes extract mixture synthesized by the “SOS” method (combination of two 4.6×250 mm Buckyprep columns, flow rate 1.6 ml/min, injection volume 200 μL , toluene as mobile phase, 40 °C).....	37
Figure 2.22 Chromatogram of the Fraction 7 of $\text{Ce}_x\text{Y}_{3-x}\text{N}@C_{86}$ fullerenes extract mixture synthesized by the “SOS” method (combination of two 4.6×250 mm Buckyprep columns, flow rate was set at 3.0 ml/min, injection volume 3 mL, toluene as mobile phase, room temperature).	38

Figure 2.23 Chromatogram of the Fraction 8 of $Ce_xY_{3-x}N@C_{84}$ fullerenes extract mixture synthesized by the “SOS” method (combination of two 4.6×250 mm Buckyprep columns, flow rate 2.0 ml/min, injection volume 3 mL, toluene as mobile phase, room temperature).	39
Figure 2.24 Chromatogram of the Fraction 9 of $Ce_xY_{3-x}N@C_{88}$ fullerenes extract mixture synthesized by the “SOS” method (combination of two 4.6×250 mm Buckyprep columns, flow rate 2.0 ml/min, injection volume 3 mL, toluene as mobile phase, room temperature).	40
Figure 2.25 Chromatogram of $Ce_xSc_{3-x}N@C_{2n}$ ($2n= 78-88$) fullerene extract mixture synthesized by the “SOS” method (combination of two 4.6×250 mm Buckyprep columns, flow rate 1.6 ml/min, injection volume 200 μ L, toluene as mobile phase, 40 $^{\circ}$ C).....	41
Figure 2.26 The isolation of $CeSc_2N@C_{80}$ (II). (a) $CeSc_2N@C_{80}$ (II) was obtained by recycling HPLC after 24 cycles (10×250 mm Buckyprep column; flow rate 1.5 ml/min; injection volume is 5 ml; toluene as eluent; room temperature); (b) The enlarged views of 9 th and 25 th cycle from (a) are shown in (b) and (c) respectively, ($t_{ret}= 910-1020$ min and $t_{ret}= 2580-2700$ min).....	42
Figure 2.27 The LDI-TOF mass spectrum of purified $CeSc_2N@C_{80}$ (II).....	43
Figure 2.28 Chromatogram of $Pr_xSc_{3-x}N@C_{2n}$ ($2n= 78-88$) fullerene extract mixture which synthesized by the “SOS” method (combination of two 4.6×250 mm Buckyprep columns, flow rate 1.6 ml/min, injection volume 200 μ L, toluene as mobile phase, 40 $^{\circ}$ C).....	44
Figure 2.29 The isolation of $PrSc_2N@C_{80}$ (I). $PrSc_2N@C_{80}$ (I) was obtained by recycling HPLC after 35 cycles (10×250 mm Buckyprep column; flow rate 1.5 ml/min; injection volume is 5 ml of Fraction 4; toluene as eluent; room temperature); The enlarged views of 9 th and 35 th cycle from (a) are shown in (b) and (c) respectively, ($t_{ret}= 860 - 965$ min and $t_{ret}= 3465 - 3670$ min).	45
Figure 2.30 The LDI-TOF mass spectrum of purified $PrSc_2N@C_{80}$ (I).	45
Figure 2.31 The isolation of $PrSc_2N@C_{80}$ (II). $PrSc_2N@C_{80}$ (II) was obtained by recycling HPLC after 37 cycles (10×250 mm Buckyprep column; flow rate 1.5 ml/min; injection volume is 5 ml of Fraction 5; toluene as eluent; room temperature); The enlarged views of 14 th and 37 th cycle from (a) are shown in (b) and (c) respectively, ($t_{ret}= 1430 - 1540$ min and $t_{ret}= 3830 - 3940$ min).....	46
Figure 2.32 The LDI-TOF mass spectrum of purified $PrSc_2N@C_{80}$ (II).	47
Figure 3.1 UV-vis-NIR spectra of (a) $Ho_xSc_{3-x}N@C_{80}$ (I; $x= 0-3$) and (b) $Ho_xSc_{3-x}N@C_{80}$ (II; $x= 0-2$) in toluene.	50

Figure 3.2 UV-vis-NIR spectra of $\text{Ho}_x\text{Y}_{3-x}\text{N}@C_{80}$ (I; $x= 0-3$) and $\text{Ho}_x\text{Lu}_{3-x}\text{N}@C_{80}$ (I; $x= 0-3$).....	51
Figure 3.3 UV-Vis-NIR spectra of $\text{CeM}_2\text{N}@C_{80}$ (I; $M= \text{Y, Lu and Sc}$).....	52
Figure 3.4 UV-Vis-NIR spectra of (up) $\text{MSc}_2\text{N}@C_{80}$ (I; $M= \text{Ce, Pr and Nd}$) and (bottom) $\text{MSc}_2\text{N}@C_{80}$ (I; $M= \text{Ce, Pr}$) which compared with $\text{Sc}_3\text{N}@C_{80}$ (I) and $\text{Sc}_3\text{N}@C_{80}$ (II) respectively.....	53
Figure 3.5 UV-Vis-NIR spectra of $\text{Ce}_x\text{Y}_{3-x}\text{N}@C_{2n}$ ($x= 0-2$; $2n= 84, 86$ and 88).	55
Figure 3.6 FTIR spectra of (a) $\text{Ho}_x\text{Sc}_{3-x}\text{N}@C_{80}$ (I; $x= 0-3$) and (b) $\text{Ho}_x\text{Sc}_{3-x}\text{N}@C_{80}$ (II; $x= 0-2$).	56
Figure 3.7 The FTIR spectra of (a) $\text{Ho}_x\text{Y}_{3-x}\text{N}@C_{80}$ and $\text{Ho}_x\text{Lu}_{3-x}\text{N}@C_{80}$ (I; $x= 0-3$).	57
Figure 3.8 FTIR spectra of (a) $\text{Ln}_2\text{ScN}@C_{80}$ (I; $\text{Ln}= \text{Nd, Gd, Tb, Dy, Ho, Er and Lu}$) and $\text{Sc}_3\text{N}@C_{80}$ (I); (b) the dependence of $\nu_{\text{Sc-N}}$ and $\nu_{\text{Ln-N}}$ of $\text{Ln}_2\text{ScN}@C_{80}$ on the ionic radius (r) of the engaged Lanthanide metal.....	60
Figure 3.9 FTIR spectra of (a) $\text{LnSc}_2\text{N}@C_{80}$ (I; $\text{Ln}= \text{Ce, Pr, Nd, Gd, Tb, Dy, Ho, Er and Lu}$) and $\text{Sc}_3\text{N}@C_{80}$ (I); (b) the dependence of $\nu_{\text{Sc-N}}$ and $\nu_{\text{Ln-N}}$ of $\text{LnSc}_2\text{N}@C_{80}$ on the ionic radius (r) of the engaged Lanthanide metal.	61
Figure 3.10 FTIR spectra of $\text{MSc}_2\text{N}@C_{80}$ (a) and $\text{M}_2\text{ScN}@C_{80}$ (b) (II; $M= \text{Gd, Dy, Ho and Lu}$; $x= 1, 2$) compared with $\text{Sc}_3\text{N}@C_{80}$ (II).	62
Figure 3.11 Raman spectra of (a) $\text{Ho}_x\text{Sc}_{3-x}\text{N}@C_{80}$ (I; $x= 0-2$) and (b) $\text{Ho}_x\text{Sc}_{3-x}\text{N}@C_{80}$ (II; $x= 0-2$) measured at 120 K and with the laser wavelength of 647 nm.	64
Figure 3.12 The low-energy Raman spectra of $\text{Ho}_x\text{Sc}_{3-x}\text{N}@C_{80}$ (I, II; $x= 0-2$) measured at 120 K and with the laser wavelength of 647 nm.....	66
Figure 3.13 The low-energy Raman spectra of (a) $\text{Ho}_x\text{Lu}_{3-x}\text{N}@C_{80}$ (I; $x= 1-3$) and (b) $\text{Ho}_x\text{Y}_{3-x}\text{N}@C_{80}$ (I; $x= 1-3$) were obtained at 120 K and with the laser wavelength of 647 nm.	67
Figure 3.14 ^{13}C NMR spectra of $\text{CeY}_2\text{N}@C_{80}$ (I), $\text{PrSc}_2\text{N}@C_{80}$ (I), $\text{Y}_3\text{N}@C_{80}$ (I) and $\text{Sc}_3\text{N}@C_{80}$ (I) respectively at 298 K.....	68
Figure 3.15 ^{13}C NMR spectra of (a) $\text{HoM}_2\text{N}@C_{80}$ and (b) $\text{Ho}_2\text{MN}@C_{80}$ (I; $M= \text{Y, Lu and Sc}$) $\text{CS}_2/\text{d}_6\text{-acetone}$ at the room temperature. Black dots denote $\text{Lu}_3\text{N}@C_{80}$ (I) in (a). Asterisks denote the signals of the solvent.....	69
Figure 3.16 ^{45}Sc NMR spectra of $\text{HoSc}_2\text{N}@C_{80}$ (I, II), $\text{PrSc}_2\text{N}@C_{80}$ (I) measured in the solution of $\text{CS}_2/\text{d}_6\text{-acetone}$ at 298 K which compared with $\text{LuSc}_2\text{N}@C_{80}$ (I).	70
Figure 4.1 The 125 MHz ^{13}C NMR spectra of $\text{CeM}_2\text{N}@C_{80}$ and $\text{LuM}_2\text{N}@C_{80}$ (I; $M= \text{Sc, Lu and Y}$) in $\text{CS}_2/\text{d}_6\text{-acetone}$ at 298 K.	72

Figure 4.2 The variable-temperature ^{13}C NMR spectra of $\text{CeY}_2\text{N@C}_{80}$ (I) in the temperature range of 268-308 K.	74
Figure 4.3 The variable-temperature ^{13}C NMR spectra of $\text{CeSc}_2\text{N@C}_{80}$ (I) in the temperature range of 268-308 K.	75
Figure 4.4 The line-fitting plots for ^{13}C NMR chemical shift δ vs. T^{-2} are shown for $\text{CeY}_2\text{N@C}_{80}$ (I) (red), $\text{CeLu}_2\text{N@C}_{80}$ (I) (black) and $\text{CeSc}_2\text{N@C}_{80}$ (I) (blue).	75
Figure 4.5 The variable-temperature ^{13}C NMR spectra of $\text{PrSc}_2\text{N@C}_{80}$ (I) in the temperature range of 268-308 K.	76
Figure 4.6 The variable-temperature ^{13}C NMR spectra of $\text{NdSc}_2\text{N@C}_{80}$ (I) in the temperature range of 268-308 K.	76
Figure 4.7 The line-fitting plots for ^{13}C chemical shift δ vs. T^{-2} are shown for $\text{CeSc}_2\text{N@C}_{80}$ (I) (black), $\text{PrSc}_2\text{N@C}_{80}$ (I) (blue) and $\text{NdSc}_2\text{N@C}_{80}$ (I) (brown).	77
Figure 4.8 ^{13}C NMR spectra of $\text{Ho}_x\text{Sc}_{3-x}\text{N@C}_{80}$ (I; $x= 0-2$) CS_2/d_6 -acetone at the room temperature. An asterisk denotes the signal of the solvent.	78
Figure 4.9 ^{13}C NMR spectra of $\text{HoM}_2\text{N@C}_{80}$ and $\text{Ho}_2\text{MN@C}_{80}$ (I; $M= \text{Sc, Lu and Y}$) CS_2/d_6 -acetone at the room temperature. Black dots denote $\text{Lu}_3\text{N@C}_{80}$ (I) in a). Asterisks denote the signal of the solvent.	79
Figure 4.10 The variable-temperature ^{45}Sc NMR spectra of $\text{PrSc}_2\text{N@C}_{80}$ (I) in the temperature range of 268-308 K.	81
Figure 4.11 The line-fitting plots for ^{45}Sc NMR chemical shift δ vs. T^{-2} are shown for $\text{PrSc}_2\text{N@C}_{80}$ (I).	81
Figure 4.12 The variable-temperature ^{45}Sc NMR spectra of $\text{NdSc}_2\text{N@C}_{80}$ (I) in the temperature range of 268-308 K.	82
Figure 4.13 The line-fitting plots for ^{45}Sc NMR chemical shift δ vs. T^{-2} are shown for $\text{NdSc}_2\text{N@C}_{80}$ (I).	82
Figure 4.14 ^{45}Sc NMR spectra of (a) $\text{HoSc}_2\text{N@C}_{80}$ (I) and (b) $\text{HoSc}_2\text{N@C}_{80}$ (II) measured at the different temperature.	83
Figure 4.15 The line-fitting plots for chemical shift δ vs. T^{-2} are shown for a) $\text{HoSc}_2\text{N@C}_{80}$ (I) and $\text{HoSc}_2\text{N@C}_{80}$ (II).	85
Figure 4.15 The scheme of lanthanide-induced paramagnetic shifts in $\text{LnSc}_2\text{N@C}_{80}$	87
Figure 4.16 ^{13}C NMR spectra of $\text{LnSc}_2\text{N@C}_{80}$ (I; $\text{Ln}= \text{Ce, Pr, Nd, Tb, Dy, Ho and Lu}$) CS_2/d_6 -acetone at 288 K.	88
Figure 4.17 Plots of $\Delta\delta / \langle S_z \rangle_{\text{Ln}}$ vs. $C_{\text{Ln}} / \langle S_z \rangle_{\text{Ln}}$ for ^{13}C NMR chemical shifts of $\text{LnSc}_2\text{N@C}_{80}$ (I; $\text{Ln}= \text{Ce, Pr, Nd, Tb, Dy, Ho and Lu}$).	88

Figure 4.18 ^{45}Sc NMR spectra of $\text{LnSc}_2\text{N@C}_{80}$ (I; M= Ce, Pr, Nd, Tb, Ho and Lu) CS_2/d_6 -acetone at 288 K.....	90
Figure 5.1 Cyclic voltammograms of $\text{CeM}_2\text{N@C}_{80}$ (M= Sc, Lu and Y) and $\text{PrSc}_2\text{N@C}_{80}$ measured at room temperature in o-DCB solution with TBABF_4 as supporting electrolyte, scan rate 100 mV/s.	94
Figure 5.2 (a) ^{13}C NMR spectra of paramagnetic $\text{Ce}^{\text{III}}\text{M}_2\text{N@C}_{80}$ (M= Sc, Lu, Y) and their oxidized diamagnetic counterparts $[\text{Ce}^{\text{IV}}\text{Y}_2\text{N@C}_{80}]^+$ measured in o- d_4 -DCB at 288 K; (b) ^{45}Sc NMR spectra of $\text{CeSc}_2\text{N@C}_{80}$ and $[\text{CeSc}_2\text{N@C}_{80}]^+$	95
Figure 5.3 DFT-optimized structures of (a) $\text{Ce}^{\text{III}}\text{Y}_2\text{N@C}_{80}$ and (b) $[\text{Ce}^{\text{IV}}\text{Y}_2\text{N@C}_{80}]^+$	97
Figure 5.4 DFT-optimized bond lengths (\AA) of the $\text{Ce}^{\text{III}}\text{M}_2\text{N}$ and $\text{Ce}^{\text{IV}}\text{M}_2\text{N}$ clusters (M= Y, Lu and Sc) in $\text{CeM}_2\text{N@C}_{80}$ and $[\text{CeM}_2\text{N@C}_{80}]^+$, respectively.	98
Figure 5.5 Cyclic voltammogram of $\text{Y}_3\text{N@C}_{88}$, $\text{CeY}_2\text{N@C}_{88}$ and $\text{Ce}_2\text{YN@C}_{88}$ (vs. $\text{Fc}(\text{Cp})_2^{+/0}$) measured in o-DCB solution with 0.1 M TBABF_4 as supporting electrolyte, scan rate is 100 mV /s.	100
Figure 5.6 Cyclic voltammogram of $\text{Y}_3\text{N@C}_{86}$, $\text{CeY}_2\text{N@C}_{86}$ and the mixture of $\text{Ce}_2\text{YN@C}_{86}$ and $\text{Y}_3\text{N@C}_{86}$ measured in o-DCB solution with 0.1 M TBABF_4 as supporting electrolyte, scan rate is 100 mV /s.	102
Figure 5.7 Cyclic voltammogram of $\text{Y}_3\text{N@C}_{84}$ and $\text{CeY}_2\text{N@C}_{84}$ measured in o-DCB solution with 0.1 M TBABF_4 as supporting electrolyte, scan rate is 100 mV /s.	103
Figure 5.8 CV scan rate study of the first reduction wave of $\text{CeY}_2\text{N@C}_{84}$. Scan rates of 0.10, 0.25, 0.50, 1.00 V/s.	104
Figure 5.9 DFT-optimized structures of (a) $\text{CeY}_2\text{N@C}_{88}$ -a and (b) $\text{CeY}_2\text{N@C}_{88}$ -b.	106
Figure 5.10 DFT-optimized structures of (a) $\text{Ce}_2\text{YN@C}_{88}$ -a, (b) $\text{Ce}_2\text{YN@C}_{88}$ -b and (c) $\text{Ce}_2\text{YN@C}_{88}$ -c.	106
Figure 5.11 DFT-optimized structures of (a) $\text{CeY}_2\text{N@C}_{86}$ and (b) $\text{Ce}_2\text{YN@C}_{86}$	107
Figure 5.12 DFT-optimized structures of (a) $\text{CeY}_2\text{N@C}_{84}$ -a and (b) $\text{CeY}_2\text{N@C}_{84}$ -b.	107

Chapter 1 Introduction

Since the discovery of fullerene (C_{60}) in 1985, it has hogged the limelight as the potential materials.¹ As the fourth allotrope of carbon, C_{60} was detected in a laser-vaporized cluster beam mass spectrum by Kroto et al. It has always been regarded as promising material in applications for nanoelectronics, superconductors, optical switching and field-effect transistor.² Due to the intrinsic nature of fullerene molecules, the empty space inside the carbon cages could be utilized to host atom, atoms, clusters and even molecules. Soon after the discovery of C_{60} , the encapsulation of lanthanum metal ion into fullerene cages was achieved. In the process of laser vaporization of the mixture of $LaCl_3$ and graphite, LaC_{60} was detected as the first endohedral metallofullerene which indicated a wide prospect of all lanthanide metals.³ In the following years, plenty of metals had been trapped into the fullerene cages which included not only lanthanide metals but Group I-III metals as well which further classified as mono-,⁴ di-⁵ and tri-⁶ metallofullerenes according to the number of metal ions. Clusterfullerenes are a new class of fullerene family which includes metal carbide clusters,⁷ metal nitride clusters,⁸ metal oxide clusters⁹ and metal sulfide clusters¹⁰ with respect to non-metal element. Metal carbide clusterfullerenes were found as the minor structures during the production of metallofullerenes. The low yield of metal carbide clusterfullerenes hindered the deep studies on their properties. In 1999, metal nitride clusterfullerenes (NCFs) $Sc_3N@C_{2n}$ were discovered by Dorn et al by introducing a small amount of nitrogen gas into the Krätschmer-Huffman generator during the process of DC-arc discharging. The dominant structures demonstrated a higher yield than that of all other endohedral fullerenes. This novel method for producing $M_3N@C_{2n}$ structures was named “trimetallic nitride template” (TNT) process. Since then, great efforts have been made for enhancing the yield and producing new structures. Dunsch et al proposed a new strategy to modify arc-burning process with the idea of the reactive-gas atmosphere which powerfully extended the family endohedral fullerenes.¹¹

1.1 Synthesis and isolation of endohedral fullerenes

Looking through the history of fullerenes, two classical methods were employed to synthesize fullerene structures. High temperature laser vaporization method was firstly conducted to prepare empty fullerenes and endohedral fullerenes. The attainment of macroscopic amounts $La@C_{82}$ was successfully fulfilled and then stimulated further studies

on endohedral fullerene structures and indicated the potential applications of endohedral fullerenes in many fields. DC-arc discharging method has been regarded as the fantastic contribution to the development of fullerenes studies. Currently, the modified Krätschmer-Huffman DC-arc discharging method is popularly applied in fullerene production. Briefly speaking, two hollow graphite rods packed with the mixture of metal oxides (or metals) and graphite powders are fixed in the generator as anode and cathode. During the process of DC-arc discharging, the anode and cathode are switched to efficiently evaporate both rods and prevent excess disorder of carbon depositing on the cathode. Normally, it is necessary to remove the air inside the graphite rods by a short time preheating at high temperature which could depress the yield of empty fullerenes and enhance the yield of NCFs simultaneously. The configuration of the reactor is demonstrated in Figure 1.1.

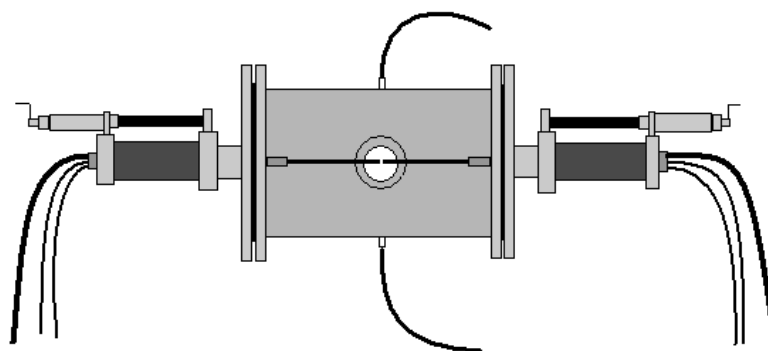


Figure 1.1 The scheme of fullerenes generator.

The flourish of endohedral fullerenes family is usually accompanied by the innovation of synthesis condition. The introducing of nitrogen source plays an essential role in synthesizing metal nitride clusterfullerenes. As mentioned before, $\text{Sc}_3\text{N@C}_{80}$ was the first NCF which using the “Trimetallic Nitride Template” (TNT) method by adding small amount of nitrogen. But the problem that the total amount of NCFs is quite low in the soot extract (less than 5%) could not be solved until the Dunsch and co-workers switched the nitrogen source from nitrogen (N_2) to solid state of nitrogen-containing compound. Calcium cyanamide has prominent influence on the status of NCFs in the family of endohedral fullerenes. On the one hand, the yield of $\text{Sc}_3\text{N@C}_{80}$ was significantly enhanced (from 3% to 42%) and NCFs were the dominant product for the first time. On the other hand, the relative yield of empty fullerenes and metallofullerenes were considerably suppressed which facilitated the process of purification in the next step. Dunsch and co-workers kept exploring novel approaches for improving the yield of NCFs. Ammonia (NH_3) was chosen as reactive gas made remarkable

improvement. The total yield of NCFs could reach 80% of fullerenes in the soot. This route for preparing NCFs was named “reactive gas atmosphere” method. Recently, Dunsch and co-workers proposed another strategy, “selective organic solid” (SOS) route, guanidine thiocyanate ($\text{CH}_3\text{N}_3\text{HSCN}$) was employed as the solid-state nitrogen source which further improved the total yield of NCFs and formed a new kind cluster fullerenes, named as metal sulfide clusterfullerenes.

High performance liquid chromatography (HPLC) is widely used for isolating of mixtures of EMFs.¹²⁻²⁸ Because the polarity, electric charge, the size of the molecule is different from each other, the mixture of EMFs can be separated when they move across the column.

1.2 Properties of metal nitride clusterfullerenes

Since the discovery of $\text{Sc}_3\text{N@C}_{80}$, it has been always regarded as the prototype of homogenous metal nitride clusterfullerenes (NCFs) in the form of $\text{M}_3\text{N@C}_{80}$. As revealed from the electronic studies of $\text{Sc}_3\text{N@C}_{80}$, Sc_3N is stabilized by the icosahedral $\text{C}_{80}I_h$ cage through transferring six electrons from nitride cluster to the carbon cage which proved by the ^{13}C NMR and electrochemical analysis. Therefore, substantial efforts have been devoted to extend the family of metal NCFs with several strategies. Switching the encapsulated metal atoms inside the nitride cluster is one of the practical ways to synthesize new metal nitride clusterfullerenes. Up to now, plenty of group III metals have been successfully engaged into the C_{80} cage in the form of $\text{M}_3\text{N@C}_{80}$ where M includes Scandium, Yttrium, Praseodymium, Neodymium, Gadolinium, Terbium, Dysprosium, Holmium, Erbium, Thulium and Lutetium.^{29,30} Substituting one or two metals in the cluster made the new class of NCFs named as mixed metal nitride clusterfullerenes (MMNCFs). MMNCFs provide broad possibilities to study the spectroscopic, electronic and magnetic properties of metal NCFs.³¹

1.2.1 Spectroscopic properties

The absorption spectrum of nitride cluster fullerenes in the visible and near-IR range are predominantly due to the π - π^* excitations of the carbon cage, which is directly dependent on the structure and the charge state of the carbon cage.³² Based on the theoretical calculations and experimental data, the highest occupied molecular orbital (HOMO) of endohedral fullerenes is anticipated to be localized on the carbon cage while the lowest unoccupied molecular orbital (LUMO) is primarily on the engaged clusters.³³ Their absorption features mainly depend on the cage symmetry and the engaged clusters have minor influence on the absorption features of NCFs. Therefore, the absorption spectra of $\text{M}_3\text{N@C}_{80}$ (M= Y, Pr, Nd,

Gd, Tb, Dy, Ho, Er, Tm and Lu) are almost identical which indicates that the electronic state in the case of same cage isomer is the same.³⁴

It is well known that the time resolution of vibrational spectra is much higher than that of NMR. Vibrational spectroscopy could be employed to figure out: a) the interaction between carbon cage and encapsulated species; b) the interaction inside encapsulated species and c) the configurations of encapsulated species and carbon cage. When the ¹³C NMR and X-ray single crystal studies are not available due to the lower symmetry of the carbon cage or limited amount of the materials, vibrational spectra could provide supplemental information about the structure of endohedral fullerenes. Combining the experimental IR and Raman spectra with theoretical calculations, the interpretation of vibrational spectra could be achieved for specific vibrations such as metal-nitrogen or carbon-carbon bonding. Reliable prediction of vibrational modes in IR and Raman spectra could be done in the case of switching the clusters inside the same cage or changing cage size but preserving the same cluster.³⁵

As a class of endohedral fullerenes, metal nitride clusterfullerenes comprise more than 60 atoms which afford a bunch of information about molecule configuration and electronic structure. The striking difference in number of atoms inside the carbon cage and on the carbon cages indicates that the vibrations of endohedral fullerenes largely come from vibrations of their carbon cages. The tangential C₈₀ cage modes (800-1600 cm⁻¹ and 400-600 cm⁻¹) are almost identical for all of homogeneous metal NCFs because they own the same cage symmetry. Since inheriting features from the corresponding empty fullerenes, the vibrational spectroscopic studies of endohedral fullerenes are actually sensitive to the isomeric structures of carbon cage. However, the noticeable distinction between the mass number of carbon atom and metal atoms, the modes related to engaged species could be observed at low frequencies.

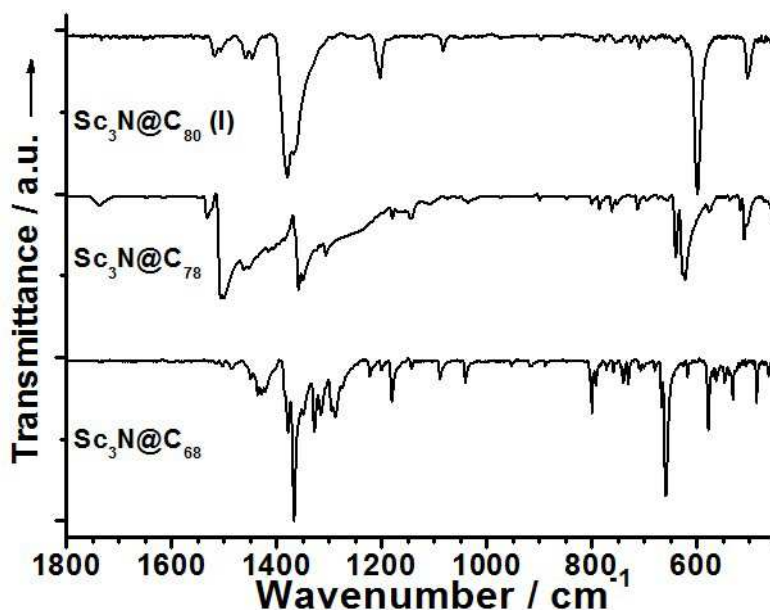


Figure 1.2 FTIR spectra of $\text{Sc}_3\text{N}@C_{80}$ (I), $\text{Sc}_3\text{N}@C_{78}$ and $\text{Sc}_3\text{N}@C_{68}$.

The antisymmetric metal-nitrogen stretching vibrational modes are assigned to the most intense low-energy IR lines in the $600\text{--}800\text{ cm}^{-1}$ range which are sensitively dependent on the composition of the encaged metal M. Furthermore, in Raman spectra the cage modes are dominating above 220 cm^{-1} while the metal-based modes are seen at lower frequencies. A remarkable example is that the studies of experimental IR spectra of $\text{Sc}_3\text{N}@C_{2n}$ ($2n = 68, 78$ and $80; I_h$) which compared with theoretical studies,³⁶ see Figure 1.2. The cage modes are unique for each structure and the experimental data and theoretical calculations agree well. The metal-nitrogen stretching vibrational modes $\nu_{\text{Sc-N}}$ increases from 599 cm^{-1} in $\text{Sc}_3\text{N}@C_{80}$ (I) to 623 cm^{-1} in $\text{Sc}_3\text{N}@C_{78}$ and 660 cm^{-1} in $\text{Sc}_3\text{N}@C_{68}$. The recent reports on the analysis of vibrational spectra of the metal NCFs combined with DFT calculations indicated that inherent strain of the Sc_3N cluster are strongly influenced by the different size of carbon cage.³⁰ Unveiling from DFT-computed IR spectra, the interpretation of IR spectra could not be obtained by the superposition of the individual $(\text{Sc}_3\text{N})^{6+}$ cation and C_{2n}^{6-} anion spectra.^{37,38} The covalent contribution to the cluster-cage interactions should be considered as well.³⁹ Y could be chosen as model for lanthanide metal with those ionic radius identical or smaller than Dy^{3+} which facilitates modeling of the vibrational spectra of lanthanide-containing NCFs. DFT calculations are still available for the analysis of lanthanide-containing NCFs under the consideration of similar ionic radius and different mass of Y and Dy atoms. The correlation could be found between the ionic radius of the metal and anti-symmetric metal-nitrogen frequency in a series of $\text{M}_3\text{N}@C_{80}$ (I). Specially, for lanthanide-containing NCFs which ionic radius smaller than Dy^{3+} , the frequency remains almost constant (around 710 cm^{-1}), see

Figure 1.3. From X-ray single crystal characterization, the geometry of metal nitride cluster transform from planar (i.e. Dy_3N or Y_3N) to pyramidal structure (i.e. Tb_3N or Gd_3N) result in the decrease of vibrational frequency originate from the changing the effective force constant. The increase of the radii of the lanthanide metal strengthen the inherent strain of $\text{M}_3\text{N}@C_{80}$ (I_h) and result in that the inner space of C_{80} (I_h) cage is insufficient for M_3N clusters due to the large lanthanides. But, this kind of inherent strain of all non-Sc $\text{M}_3\text{N}@C_{80}$ caused by the limited space inside the carbon cage become appreciably released when the metal atoms is replaced by one or two Sc atoms with smaller ionic radius.^{34,37} The details will be presented in the chapter 3.

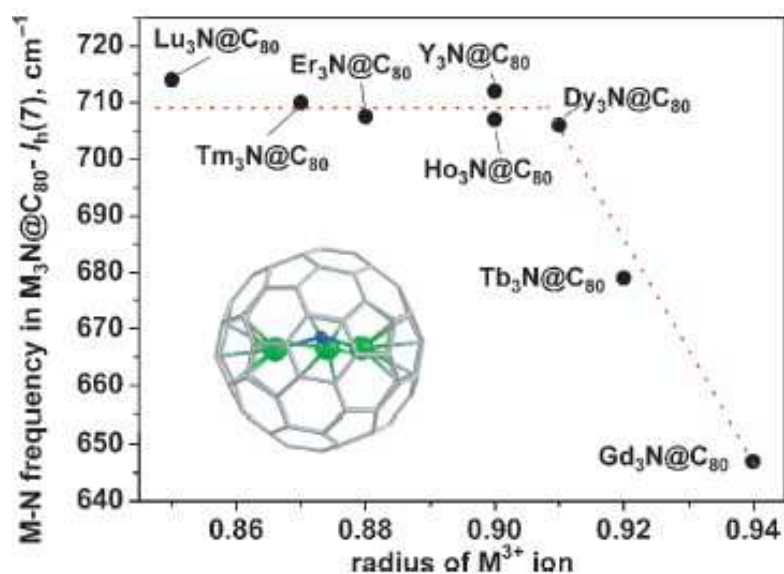


Figure 1.3 M-N antisymmetric mode frequency in $\text{M}_3\text{N}@C_{80}$ (I_h ; $\text{M} = \text{Gd}, \text{Tb}, \text{Dy}, \text{Ho}, \text{Er}, \text{Tm}, \text{Lu}$ and Y) as a function of the ionic radius of the metal. The inset shows DFT-optimized structure of $\text{Gd}_3\text{N}@C_{80}-I_h$; pyramidalization of the Gd_3N cluster can be clearly seen.

1.2.2 Electrochemical and spectroelectrochemical properties

Since the discovery of $\text{Sc}_3\text{N}@C_{80}$ as first metal nitride clusterfullerene (NCF) that has been successfully synthesized, the electronic properties of metal NCFs have attracted a lot of attention. The electronic structure of metal NCFs can be described in the form of $(\text{M}_3\text{N})^{6+}@(\text{C}_{2n})^{6-}$, namely, six electrons transfer from the inside cluster to the outside cage. Cyclic voltammetry was employed to measure the redox properties of fullerene compounds, which provide the information about the electrochemical HOMO-LUMO gap energy and of the relative energies of the molecule frontier orbital. In the most of common case, the HOMO-LUMO gaps of metal NCFs decrease progressively as the size of the carbon cage increases

from C_{80} to C_{88} , and the irreversible reductions become reversible when the carbon cage reaches the C_{88} size.⁴⁰ However, $La_3N@C_{88}$ is one of the exceptions of the family of $M_3N@C_{88}$ due to its unusual electrochemical behaviors.⁴¹ Two irreversible oxidations, a reversible first reduction and a quasi-reversible reduction of $La_3N@C_{88}$ were reported by Echegoyen and co-workers.

As supposed by Campanera and co-workers, the large HOMO-LUMO gap which observed in metal NCFs can be estimated from the corresponding empty fullerenes. Theoretical calculations had predicted that the C_{80} have been remarkably stabilized by the six electrons which transfer from the encapsulated M_3N cluster. The experimental work revealed that six electrons formally transfer to the HOMO on the carbon cage which forming an electronically closed-shell ground state. The existence of second isomer of $Sc_3N@C_{80}$ (D_{5h}) was firstly proposed by Dorn and co-workers. They performed room temperature ^{13}C NMR to the mixture of $Sc_3N@C_{80}$ (I_h) and $Sc_3N@C_{80}$ (D_{5h}). Apart from the two major lines assigned to the I_h symmetry, six additional lines in ratio of 1:2:2:1:1:1 matched the pattern of $C_{80}:D_{5h}$. Then, the isolation and spectroscopic characterization was reported by Dunsch and co-workers and the lowest absorption of UV-vis-NIR data suggested that the optical gap of $Sc_3N@C_{80}$ (I_h , 1.7 eV) is a little bit larger than $Sc_3N@C_{80}$ (D_{5h} , 1.6 eV). The electrochemical properties of the two isomers of $Sc_3N@C_{80}$ and $Lu_3N@C_{80}$ were measured by cyclic voltammetry, Dorn and co-workers revealed two reduction peaks and one oxidation peak for each compound. They observed the first reduction potentials for the D_{5h} isomers of $Sc_3N@C_{80}$ and $Lu_3N@C_{80}$ are slightly more negative than those of the I_h isomers of $Sc_3N@C_{80}$ and $Lu_3N@C_{80}$ respectively, see Figure 1.4. However, the oxidation potential of the D_{5h} isomers of $Sc_3N@C_{80}$ and $Lu_3N@C_{80}$ is lower than those of the I_h isomers, which is consistent with the result from Echegoyen's group. The electrochemical gaps for the D_{5h} isomers of $Sc_3N@C_{80}$ and $Lu_3N@C_{80}$ are significantly smaller than those of the D_{5h} isomers which agree well their optical gap.

Combining the experimental data and theoretical molecular orbital calculations, it could be concluded that the HOMO and LUMO energies of $M_3N@C_{80}$ (I and II) are largely dependent on the electronic structure of the C_{80} cage. The resemblance of the energy levels of HOMO for $M_3N@C_{80}$ manifests that the electron density distribution around the carbon cage for their compounds could be expressed as $(M_3N)^{6+}@C_{80}^{6-}$. However, it should be mentioned that a minor contribution from the metal nitride cluster due to the electropositive character of encaged metal. For instance, the LUMO energies of the $Sc_3N@C_{80}$ (I and II) are related to the

encapsulating Sc_3N cluster. The smaller electrochemical gap of $\text{M}_3\text{N}@C_{80}$ (D_{5h}) indicates its relatively higher reactivity than the corresponding I_h isomer.

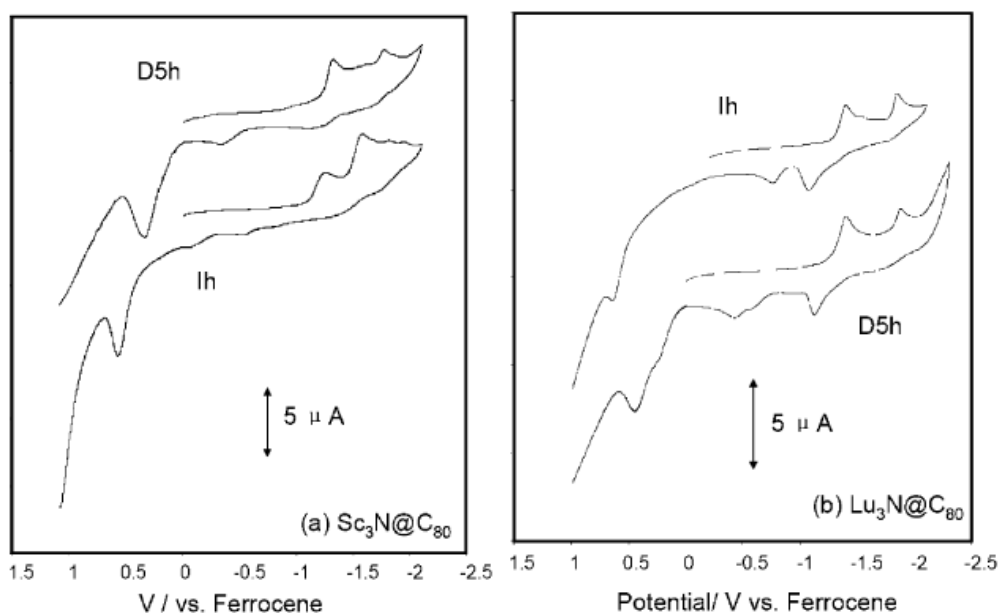
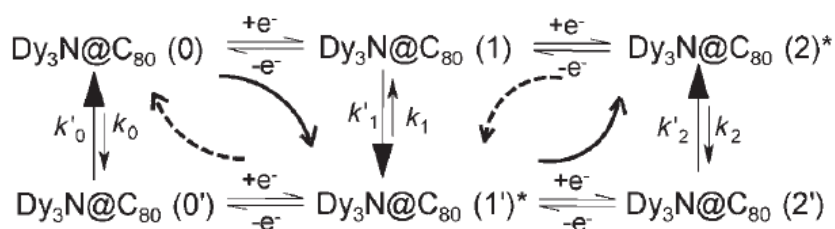


Figure 1.4 Cyclic voltammogram of the I_h and D_{5h} isomers of (left) $\text{Sc}_3\text{N}@C_{80}$ and (right) $\text{Lu}_3\text{N}@C_{80}$ in *o*-dichlorobenzene solution, 0.1 M TBABF_4 , scan rate: 500 mV/s.

The cyclic voltammograms of $\text{Dy}_3\text{N}@C_{80}$ (I, II) were reported by Dunsch and co-workers.⁴² The cyclic voltammogram of $\text{Dy}_3\text{N}@C_{80}$ (I) exhibits two electrochemically irreversible, but chemically reversible reduction steps and one reversible oxidation step. Compared with $\text{Tm}_3\text{N}@C_{80}$ (I) and $\text{Sc}_3\text{N}@C_{80}$ (I), both the redox potentials and electrochemical gap of $\text{Dy}_3\text{N}@C_{80}$ (I) exhibit a striking resemblance to those of $\text{Tm}_3\text{N}@C_{80}$ (I) rather than to $\text{Sc}_3\text{N}@C_{80}$ (I). Based on a fast-scan CV study, Dunsch and coworkers proposed a double-square reaction scheme accounting for the observed redox-reaction behavior including the charge induced reversible rearrangement of the $\text{Dy}_3\text{N}@C_{80}$ (I) monoanion, see Scheme 1.1. The first oxidation potential of $\text{Dy}_3\text{N}@C_{80}$ (D_{5h}) has a negative shift relative to that of $\text{Dy}_3\text{N}@C_{80}$ (I_h), indicating that lowering the molecular symmetry of the clusterfullerenes cage results in a pronounced increase in the electron-donating property, while the reduction potentials remain unchanged for these two isomers.



Scheme 1.1 Double-square reaction scheme of the electrochemical redox reaction of $\text{Dy}_3\text{N@C}_{80}$ (I). $\text{Dy}_3\text{N@C}_{80} (0)$, $\text{Dy}_3\text{N@C}_{80} (1)$, and $\text{Dy}_3\text{N@C}_{80} (2)$ represent the initial state of the molecule, the monoanion, and the dianion, respectively. Charge at the cage is not given. The stable species generated by the structural rearrangement are marked by asterisks. Black arrows with wider heads symbolize the preferable and fast structural rearrangements. The arc arrows show the main reaction pathways proposed (electrochemical–chemical–electrochemical–chemical (ECEC) mechanisms; forward scan=solid arrows, back scan=dashed arrows).

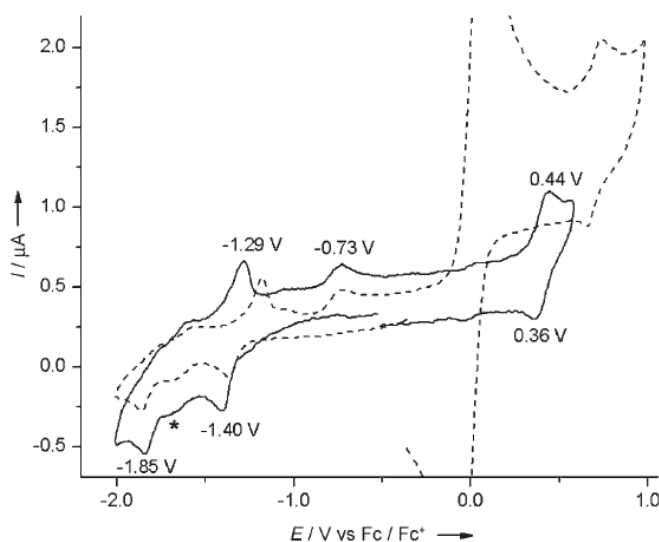


Figure 1.5 Cyclic voltammograms of $\text{Dy}_3\text{N@C}_{80}$ (II) (solid line) and $\text{Dy}_3\text{N@C}_{80}$ (I) (dash line) in $\text{TBABF}_4/\text{o-DCB}$. Scan rate: 0.1 Vs^{-1} . The asterisk labels an unidentified reduction peak.

Metal NCFs have wide distribution of cage sizes, which range from cages as small as C_{68} to those as large as C_{98} . Echegoyen and co-workers firstly reported the isolation of $\text{Gd}_3\text{N@C}_{2n}$ ($n=40, 42$ and 44).⁴³ In Figure 1.6, their electrochemical studies demonstrated that the electronic properties of metal NCFs with large cages change dramatically with the size of the cage. For instance, irreversible CV behavior is observed for $\text{Gd}_3\text{N@C}_{80}$ and $\text{Gd}_3\text{N@C}_{84}$ at the reductions step, while both reduction and oxidation steps of $\text{Gd}_3\text{N@C}_{88}$ exhibit reversible electrochemical processes. In addition, $\text{Gd}_3\text{N@C}_{88}$ exhibits the smallest electrochemical HOMO-LUMO gap among of the known NCFs structures. The homogeneous metal nitride

clusterfullerenes with C_{84} and C_{86} cages have similar HOMO-LUMO gaps, which are intermediated between those of C_{80} and C_{88} . Similar conclusions could be obtained from other lanthanide containing $M_3N@C_{2n}$ ($M= Ce, Pr$ and Nd ; $2n= 80-88$).⁴⁴

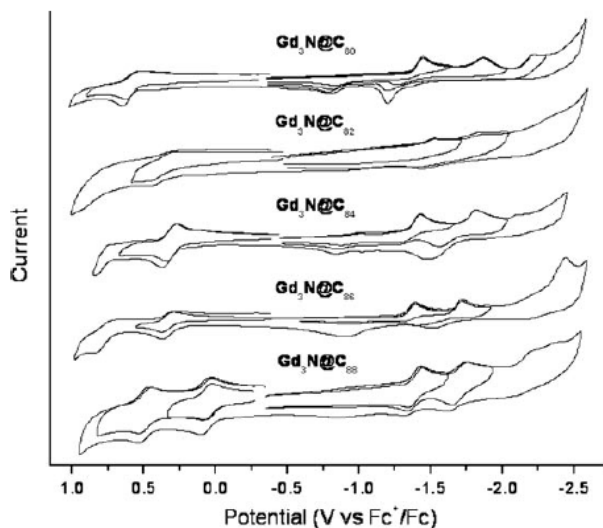


Figure 1.6 Cyclic voltammograms of $Gd_3N@C_{2n}$ ($2n= 80-88$) compounds obtained in o -DCB + 0.05M $(n\text{-Bu})_4NPF_6$ (scan rate 0.1 V/s).

Generally, the studies of a redox behavior of C_{80} -based NCFs have shown that the endohedral cluster is redox-inert, while the oxidation or reduction of NCFs occurs by changing the charge state of the carbon cage. Recently, Popov, Yang and Dunsch reported that $TiSc_2N@C_{80}$ (I) demonstrates an extraordinary redox behavior that the valence state of the Ti within $TiSc_2N$ changes from Ti^{3+} (in the neutral state) to Ti^{2+} (in the anion) and to Ti^{4+} (in the cation) in the process of first reduction and oxidation steps, while in former reported $M_3N@C_{80}$ (I) structures the cage electron is removed upon oxidation,⁴⁵ see Figure 1.7.

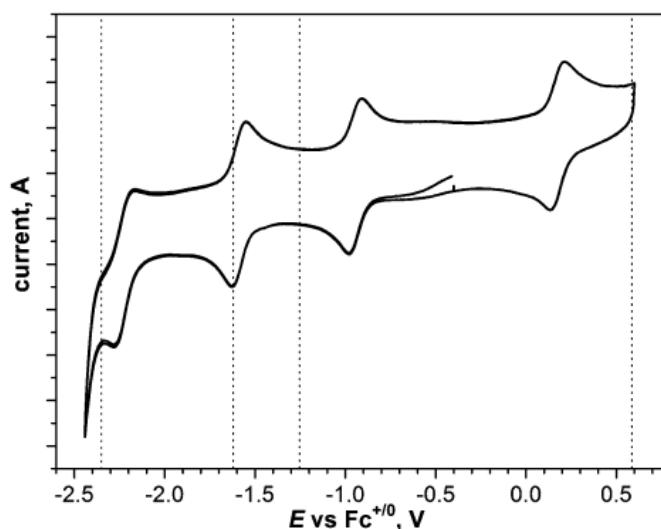


Figure 1.7 Cyclic voltammetry of $\text{TiSc}_2\text{N@C}_{80}$ measured in *o*-DCB solution (room temperature, TBABF_4 as supporting electrolyte) at a scan rate of 20 mV/s. Dotted vertical bars denote reversible redox potentials of $\text{Sc}_3\text{N@C}_{80}$ (I).

1.2.3 Magnetic properties

Endohedral fullerenes (with lanthanide atom, atoms or cluster encapsulated inside the carbon cage) have attracted broad interests due to the magnetic anisotropy of lanthanide ions. Magnetic properties of EMFs are usually studied by SQUID magnetometry and X-ray magnetic dichroism.¹⁹ The lanthanide-induced chemical shifts in NMR spectra can also give valuable information on the magnetic properties of EMFs, but the main bottlenecks in extensive studies of the magnetic properties of endohedral fullerenes NMR are their low yield in synthesis, time-consuming purification, low cage symmetry and severe broadening of the NMR spectral lines because of the shortened relaxation times.⁴⁶⁻⁴⁸ Furthermore, when carbon cage is also paramagnetic, NMR studies are usually not possible at all. For instance, the characterizations of metallofullerenes such as La@C_{82} in the pristine form were not successful because of the paramagnetic cage state. According to the oxidation state of metal atom inside, M@C_{82} are classified into two groups with divalent metals ($\text{M}^{2+}\text{@C}_{82}^{2-}$) and trivalent metals ($\text{M}^{3+}\text{@C}_{82}^{3-}$). For the former (Tm@C_{82} , Yb@C_{82} and Sm@C_{82}), NMR studies are in principle possible because the carbon cage is diamagnetic. For $\text{M}^{3+}\text{@C}_{82}^{3-}$, the ^{13}C NMR measurements of metallofullerenes in anionic forms were considered as a practical tool for structural determination. Much effort has been paid to understand the electronic and magnetic properties of metallofullerenes which have 4f electron(s) such as M@C_{82} ($\text{M} = \text{La, Tm, Ce, Pr}$ and Gd). The 125 MHz ^{13}C NMR spectrum of La@C_{82} (A) anion exhibits 17 distinct lines of near-

equal intensity and 7 lines of half the intensity which clearly indicates that La@C₈₂ (A) has C_{2v} symmetry which have been predicted by theoretical calculations and then confirmed by the XRD characterization (Figure 1.8).⁴⁹

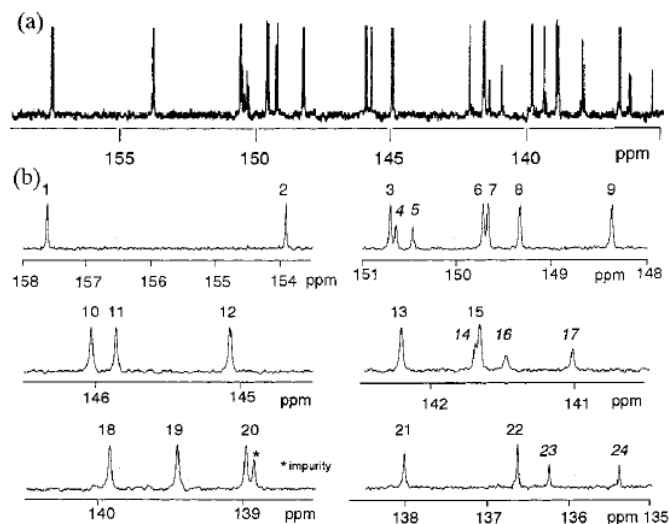


Figure 1.8 (a) ¹³C NMR spectrum of La@C₈₂ anion, (b) its expanded views.

The spin-spin interaction between the lanthanide metal (M³⁺, except for La³⁺ and Lu³⁺) and carbon cage has pronounced influence on the ¹³C NMR studies. The lanthanide-induced chemical shifts originate from the magnetic anisotropy of the ionic state of lanthanide metal. All carbon chemical shifts demonstrate temperature dependent chemical shifts which could be explained as the sum of diamagnetic contribution, Fermi contact and pseudocontact contribution. Compare to La@C₈₂ anion, the chemical shifts of Ce@C₈₂ anion was confirmed as the dominant pseudocontact mechanism and the Ce atom in Ce@C₈₂ as well as its anion is located at an off-centered position adjacent to a hexagonal ring along the C₂ axis of the C_{2v}-C₈₂ cage,⁵⁰ see Figure 1.9.

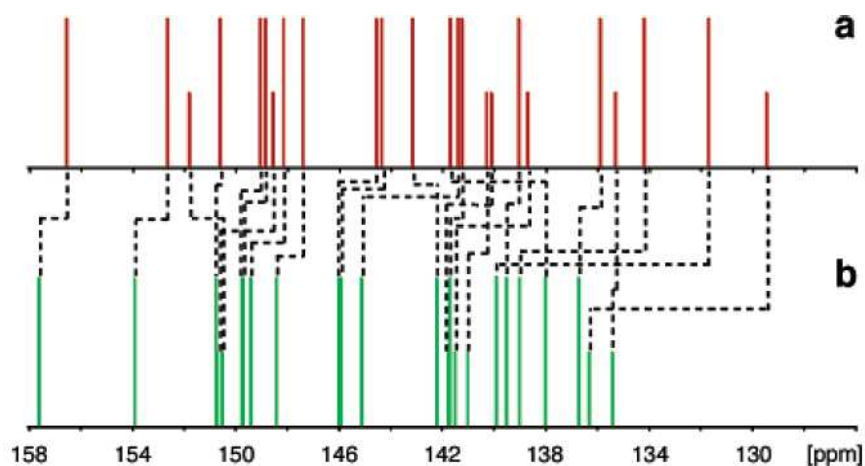


Figure 1.9 ¹³C NMR spectrums of (a) Ce@C₈₂ anion and (b) La@C₈₂ anion.

As mentioned in the beginning of this section, metal NCFs could be regarded as the suitable candidate to study magnetic properties of metal NCFs due to their relatively high yield. However, among of all lanthanide-containing metal NCFs in the form of $M_3N@C_{80}$ (except for Lu) no ^{13}C NMR study is available because the complex interaction between three lanthanide metals and carbon cage. The magnetic studies of $Ho_3N@C_{80}$ and $Tb_3N@C_{80}$ were performed by our group in 2005.⁵¹ The magnetic moment of $Ho_3N@C_{80}$ and $Tb_3N@C_{80}$ is found to be $21 \mu_B$ and $17 \mu_B$ respectively. The strong ligand field within the M_3N cluster of the nitride cluster fullerenes $Ho_3N@C_{80}$ accounts for the unusual net magnetic moment of the compounds. As a result of these interactions the individual magnetic moments m of the Ho metal ions are not parallel or antiparallel to each other, but parallel to the M-N bond (see Figure 1.10 and 11).

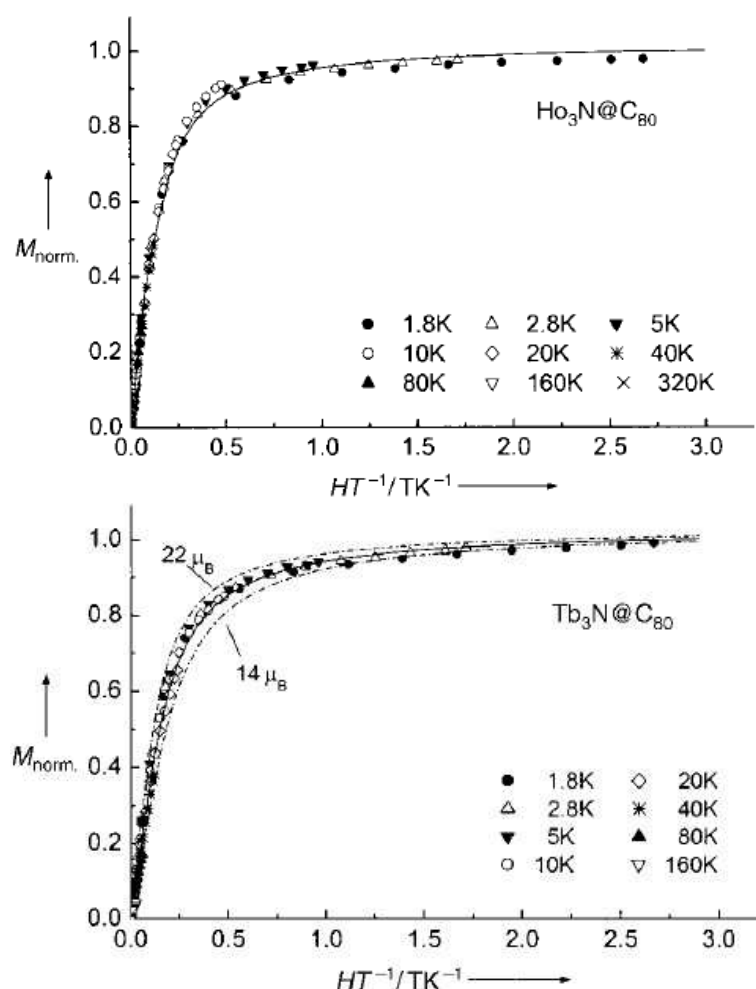


Figure 1.10 The experimental data $M(H,T)$ for $Ho_3N@C_{80}$ and $Tb_3N@C_{80}$ (symbols) corrected for the diamagnetic contribution and normalized to the saturation. The solid line represents the fitted Langevin function with a magnetic moment $\mu = 21 \mu_B$ for $Ho_3N@C_{80}$ and $\mu = 17 \mu_B$ for $Tb_3N@C_{80}$.

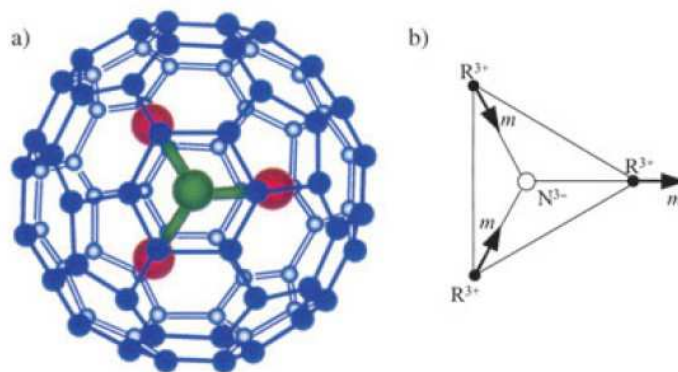


Figure 1.11 a) Structure of an $M_3N@C_{80}$ molecule, blue: carbon, green: nitrogen, and red: lanthanide metal atoms; b) orientation of the individual R magnetic moments m (arrows) in the M_3N cluster in $M_3N@C_{80}$ ($M= Ho$ or Tb).

For MMNCFs, with two non-magnetic atoms inside the nitride cluster could be an appropriate template to understand the role of lanthanide metal on the NMR studies. In particular, Sc-based MMNCFs are known to have a relatively higher yield compared to that of the homogeneous NCFs with other lanthanides. Based on its relatively high yield and known cage symmetry, it is advantageous to study Sc-based MMNCFs in the form of $MSc_2N@C_{80}$ ($M=$ Lanthanide metal, except for Lu). To investigate role of lanthanide metal inside the MSc_2N , we have chance to switch the lanthanide metal from Ce to other ones. Up to now, the only paramagnetic ^{13}C NMR studies of Ce-containing MMNCFs were reported for $CeSc_2N@C_{80}$ and $CeLu_2N@C_{80}$ (I_h).⁵²

metallofullerene	^{13}C NMR chemical shifts (ppm)	
$Sc_3N@C_{80}(I_h)^{21}$	144.57	137.24
$Lu_3N@C_{80}(I_h)^{28}$	144.0	137.4
$CeSc_2N@C_{80}$	142.85	135.90
$Ce_2@C_{80}^{40}$	148.6	124.7

Table 1.1 Comparison of chemical shifts in ^{13}C NMR spectra of several endohedral fullerenes.

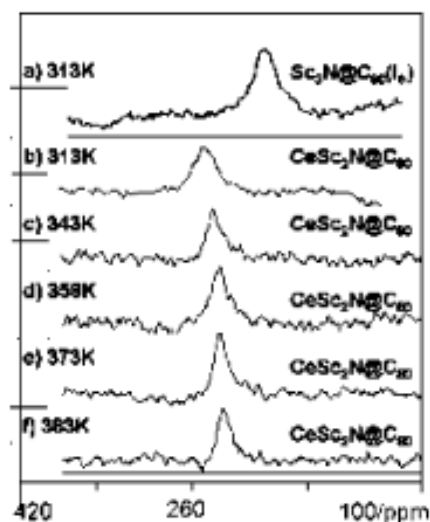


Figure 1.12 97.2 MHz ^{45}Sc solution NMR spectra of $\text{CeSc}_2\text{N}@C_{80}$ in 1, 2-dichlorobenzene at various temperatures and $\text{Sc}_3\text{N}@C_{80}$ (I_h) in 1, 2-dichlorobenzene.

Reported by Dorn and co-workers, the chemical shift difference between $\text{CeSc}_2\text{N}@C_{80}$ and $\text{Sc}_3\text{N}@C_{80}$ is a subtle upfield shift of approximately 1.5 ppm for two ^{13}C signals, see Figure 1.11. Comparable ^{13}C NMR shifts were reported for $\text{Ce}_2@C_{80}$ (I_h) which encapsulated two Ce^{3+} ions.⁵³ The ^{45}Sc NMR chemical shift of $\text{CeSc}_2\text{N}@C_{80}$ exhibits a temperature-dependent Curie upfield chemical shift and a single ^{45}Sc signal, see Figure 1.12. Similarly, the ^{13}C NMR spectrum of $\text{Lu}_2\text{CeN}@C_{80}$ in CS_2 at room temperature exhibits only two lines at 136.48 and 142.65 ppm with an intensity ratio of 1 : 3,⁵⁴ respectively (see Figure 1.13). It should be noted that the chemical upfield-shifts and broadening of the ^{13}C signals originates from the single f electron spin remaining on the Ce^{3+} ($4f^15d^0$). Those results also indicated that at room temperature: a) rotation of the Lu_2CeN (or CeSc_2N) cluster is fast enough to provide the effective icosahedral symmetry of the cage; b) the internal motion provides the same average electronic environment for the two Sc atoms in the CeSc_2N cluster. To get a better insight into the effect of Ce^{3+} variable-temperature (VT) NMR studies were performed in the range of 268-308 K (see Figure 1.13). Confirmed by the analysis of VT ^{45}Sc and ^{13}C NMR, the pseudocontact term has a dominant contribution to the paramagnetic chemical shift of scandium atoms in $\text{CeSc}_2\text{N}@C_{80}$ and of carbon atoms and $\text{Lu}_2\text{CeN}@C_{80}$ respectively.

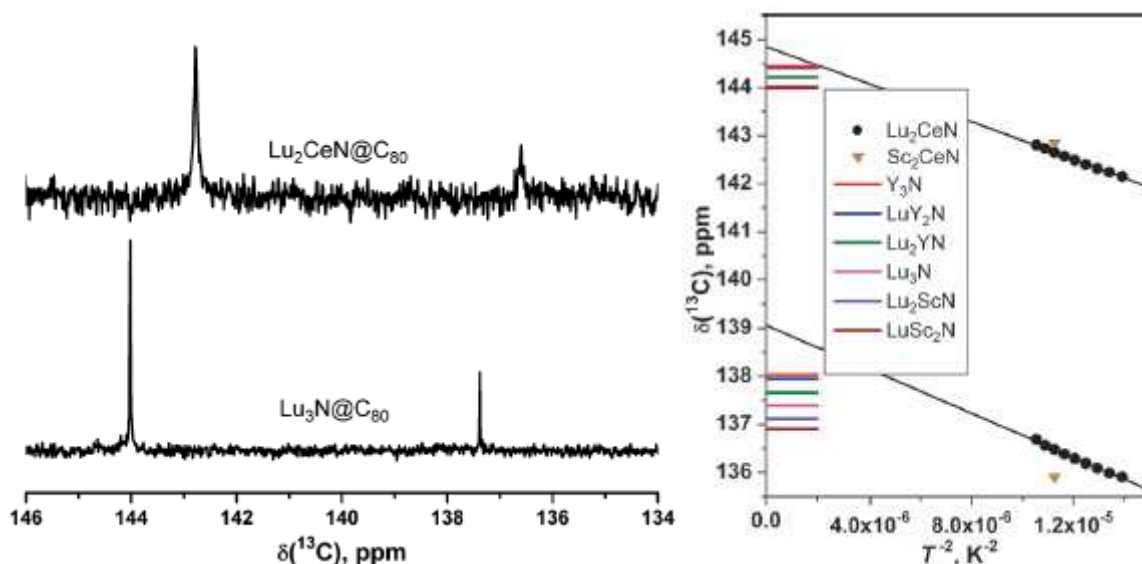


Figure 1.13 ^{13}C NMR spectra of $\text{Lu}_2\text{CeN}@C_{80}$ compared with $\text{Lu}_3\text{N}@C_{80}$ (left side) were measured at room temperature; and ^{13}C chemical shifts in the NMR spectra of $\text{Lu}_2\text{CeN}@C_{80}$ and their extrapolation to $T^{-2} = 0$ (right side). The room-temperature ^{13}C shifts for $\text{CeSc}_2\text{N}@C_{80}$ as well as a series of some diamagnetic $\text{M}_3\text{N}@C_{80}$ are also shown for comparison.

1.3 Motivation

Mixed metal nitride clusterfullerenes (MMNCFs) represent a new class of fullerenes which attracted much attention due to their electronic features as a consequence of charge transfer and interactions between the encaged cluster and the carbon cage. Based on the former studies, choosing the different kinds and numbers of rare-earth metal can significantly influence the electronic and magnetic properties of MMNCFs. In particular, the latter can be tuned by the composition of mixed metal nitride cluster (e.g. metal ionic state and metal-nitrogen bond length) and the magnetic moment from the encaged metal atoms. Although many contributions have been made in the field of EMF research, there are still open questions in understanding the situation in EMFs to be explored. It is unknown that tuning the physical and chemical properties of MMNCFs by switching the second metal M in the mixed metal

nitride cluster template $\text{Ln}_x\text{M}_{3-x}\text{N}$. Since the inner strain between the encaged cluster and cage can be tuned by changing the component of mixed metal nitride cluster, it could be realized by extending the size of carbon cage (from C_{80} to C_{88}) as well. Therefore, the relationship between inner strains resulting from encapsulated cluster and carbon cage and properties of MMNCFs should be clarified and studied in detail. Furthermore, the search for new structures with new properties is of high importance.

The reasons that we choose those lanthanide metals in my PhD work can be explained as: (a) The C_{80} cage is quite suitable for the formation of MMNCFs and the yield of C_{80} -based MMNCFs is quite high; (b) The Ho has more unpaired 4f electrons than Ce and Pr. It would be valuable to study the paramagnetic property of $\text{Ho}_x\text{M}_{3-x}\text{N}$ MMNCFs with different second metal even they are diamagnetic; (c) According to former studies, the Ce-based endohedral fullerenes can be considered as the good candidate for the electrochemical studies.

Electrochemical properties

1. The electrochemical studies on endohedral clusterfullerene $\text{CeY}_2\text{N}@C_{80}$ (I) are highly important due to the extremely large encaged cluster inside the $\text{C}_{80}:I_h$ cage. The redox behavior of $\text{CeY}_2\text{N}@C_{80}$ (I) in the anodic range makes it outstanding compared to the $\text{CeLu}_2\text{N}@C_{80}$ (I) and $\text{CeSc}_2\text{N}@C_{80}$ (I). Our group recently reported that the removal of the Ce 4f electron bypassed the carbon cage leads to the formation of Ce^{IV} . It is quite important to confirm whether the inner strain between CeM_2N cluster and carbon cage can release during the oxidation process. The geometry of CeY_2N could be expected to be switching from the pyramidal to planar structure. Comparing the inner strain between CeM_2N cluster and carbon cage, the oxidation potential of the $\text{CeY}_2\text{N}@C_{80}$ (I) should be somehow lower than the case of $\text{CeLu}_2\text{N}@C_{80}$ (I) and $\text{CeSc}_2\text{N}@C_{80}$ (I) due to the decrease of cluster size. The ^{13}C NMR study of $\text{Ce}^{\text{III}}\text{M}_2\text{N}@C_{80}$ and $[\text{Ce}^{\text{IV}}\text{M}_2\text{N}@C_{80}]^+$ combined with theoretical study could provide further valuable information.
2. The cage size dependence of the electrochemical properties of MMNCFs (cage size larger than C_{80}) has to overcome the barrier of relatively low yield and time-consuming purification. However, it is promising to find out whether the pyramidal CeY_2N unit could gradually become planar form by extending the cage size from C_{80} to C_{88} . Based on the former studies ($\text{M}_3\text{N}@C_{2n}$, $\text{M} = \text{Ce}, \text{Pr}$ and Nd ; $2n = 80-88$), the redox behavior of the series compounds of $\text{Ce}_x\text{Y}_{3-x}\text{N}@C_{2n}$ ($2n = 80, 84, 86$ and 88 ; $x = 0-3$) help us understand

the contribution from the single 4f electron on the Ce atom during the planarization of CeY₂N unit.

3. The study of paramagnetic PrSc₂N@C₈₀ (I) is the first attempting to understand the even number 4f-electrons influence on the chemical shift of carbon signal and electrochemical property. Compared with CeSc₂N@C₈₀ (I) and CeLu₂N@C₈₀ (I), one more 4f electron could change the spin density on the nitride cluster, and the oxidation potential will shift accordingly. The variable temperature ¹³C and ⁴⁵Sc NMR study armed with vibrational spectroscopic study could provide some additional information.

NMR Magnetic studies

The NMR investigation of Ho-based endohedral fullerenes has been hindered in a long time. In principle, the 4f¹⁰ electrons locate on the Ho atom could result in remarkably broad NMR peaks and strong paramagnetic chemical shifts in the NMR spectra. To gain insight into the nature of influence of different encaged Ho atoms with 10 4f-electrons, it is still imperative to do ¹³C NMR studies on MMNCFs which would be the key to opening up additional opportunities for the studies on Ho³⁺-induced paramagnetic properties. Ho_xM_{3-x}N@I_h-C₈₀ (M= Sc, Lu, Y; x=1, 2) were chosen as the radius of their trivalent ions are sufficiently different to detailed study the influence of different cluster size and geometry on the cluster-cage interaction. Meanwhile, a variable temperature ⁴⁵Sc NMR spectroscopic study of two isomers of HoSc₂N@C₈₀ could be regarded as the probe for the Ho³⁺-induced paramagnetic chemical shift.

Based on the lanthanide-involved MMNCFs in the form of LnSc₂N@I_h-C₈₀ (Ln= Ce, Pr, Nd, Tb, Dy, Ho, Lu), the single Ln atom inside C₈₀-I_h carbon cage could induce the paramagnetic ¹³C and ⁴⁵Sc NMR chemical shifts derived from their anisotropy in the susceptibility. The systematic analysis of NMR chemical shifts of LnSc₂N@I_h-C₈₀ could help us interpret the magnetic behavior of lanthanide metals. As the minor isomer of C₈₀, the investigation of ¹³C NMR C₈₀-D_{5h} could be anticipated much more complicated because the decrease of symmetry of carbon cage.

Chapter 2 Synthesis and Isolation of Mixed Metal Nitride Clusterfullerenes

2.1 Introduction

After the discovery of $\text{Sc}_3\text{N@C}_{80}$ in 1999, continuous efforts have been dedicated to attaining Scandium-, Yttrium- and Lanthanide-based homogeneous and mixed metal nitride clusterfullerenes.⁵⁵ One of the directions in which nitride clusterfullerenes (NCFs) research branched was the study of mixed metal nitride clusterfullerenes (MMNCFs) with two or three different metals in the nitride cluster. Numerous C_{80} -based MMNCFs have been successfully isolated and characterized over the last decade, including $\text{MSc}_2\text{N@C}_{80}$ (I; $\text{M} = \text{Ti},^{56} \text{Y},^{57} \text{Ce},^{52} \text{Nd},^{34} \text{Dy},^{34} \text{Tb}^{58}$ and Er^{59}), $\text{M}_2\text{ScN@C}_{80}$ (I; $\text{M} = \text{Y},^{57} \text{Nd},^{34} \text{Dy}^{34}$ and Er^{34}), ScYErN@C_{80} ,⁶⁰ $\text{Gd}_x\text{Sc}_{3-x}\text{N@C}_{80}$ (I, II; $x = 1, 2$),⁶¹ $\text{Lu}_x\text{Sc}_{3-x}\text{N@C}_{80}$ (I, II; $x = 1, 2$)³⁴ and $\text{Lu}_x\text{Y}_{3-x}\text{N@C}_{80}$ (I; $x = 1, 2$).⁶² Furthermore, the feasibility of varying the encapsulated metal atoms, stabilizing different cage sizes (i.e. $\text{Lu}_x\text{Sc}_{3-x}\text{N@C}_{68}$ ($x = 1, 2$),⁶³ $\text{DySc}_2\text{N@C}_{68}$ ⁶³ and $\text{DySc}_2\text{N@C}_{76}$ ⁶⁴) and the existence of different isomeric structures are believed to give rise to special electrochemical, optical and magnetic properties of MMNCFs. Taking into the account the paramagnetic contribution of the 4f-electrons from the encaged metals, among the existing of homogenous metal NCFs and MMNCFs, only $\text{CeSc}_2\text{N@C}_{80}$ (I)⁵² and $\text{CeLu}_2\text{N@C}_{80}$ (I)⁵⁴ have been successfully studied by ^{13}C NMR. Besides, the ^{45}Sc NMR exhibited a temperature-dependent chemical shift for $\text{CeSc}_2\text{N@C}_{80}$ (I), and the redox behaviour of $\text{CeLu}_2\text{N@C}_{80}$ (I) in the anodic range revealed that the removal of the Ce 4f-electron was fulfilled bypassing the carbon cage. To gain a further insight into the nature of influence of the different entrapped metals with more than one 4f-electron, it is still imperative to do the NMR study of MMNCFs which would be the key to open up additional opportunities for the studies of their magnetic properties and cluster-cage interactions.

In this chapter, the synthesis and isolation of Ho-based, Ce-based and Pr-based MMNCFs is presented. Ho is chosen as the major components of the mixed metal nitride cluster, namely $\text{Ho}_x\text{M}_{3-x}\text{N}$ ($\text{M} = \text{Sc}, \text{Lu}$ and Y). For $\text{Ho}_x\text{Sc}_{3-x}\text{N}$, because: a) Sc-involved MMNCFs are known to have a relatively higher yield compared to that of the homogeneous metal NCFs with other

lanthanides; b) the radii of their trivalent ions are sufficiently different to study the influence of the different cluster size and the geometry on the cluster-cage interaction; c) the knowledge about dependence of the (para)magnetic behaviour of metal NCFs comprising lanthanides with more than single 4f-electron is still scarce. Then, Lu and Y are chosen because their M^{3+} ions are diamagnetic and because their ionic radii are somewhat smaller (Lu^{3+}) and somewhat larger (Y^{3+}) than Ho. Thus, variation of the "second" metal from Sc to Lu to Y offers us a chance to study whether the Ho-based magnetic properties of MMNCFs rely on the geometry of metal nitride cluster. To the best of our knowledge, this work will be the first investigation of 1) the ^{13}C NMR spectra of $Ln_2MN@C_{80}$ (I; Ln= Lanthanide, except for Lutetium; M= Sc, Lu and Y); 2) ^{45}Sc NMR spectra for the D_{5h} isomer of $LnSc_2N@C_{80}$, which is significantly complicated by the relative low-yield (compared to the I_h isomer) and the time-consuming multi-steps isolation necessary to obtain the studied compounds in isomerically pure form; 3) the vibrational spectroscopic studies of $Ln_{3-x}Sc_xN@C_{80}$ (I; Ln= Lanthanide, except for Lutetium).

To tune the electronic properties of metal NCFs, mixed metal nitride cluster template provides a convenient platform to achieve this goal. By selectively encapsulating the redox-active metal into the nitride cluster, the oxidation behaviors of metal NCFs could be manipulated by the specific metal rather than be dominated by the charge transfer on the carbon cage. However, there is still scarce knowledge about the dependence of the redox properties on the other properties of the nitride cluster. Unfortunately, $Ce_3N@C_{80}$ is not reported yet which could be reasonably concluded that the unbearable inner strains between the pyramidal Ce_3N cluster and the C_{80} cage. Therefore, Ce-based mixed metal nitride clusters are promising to undertake this task. Combination of Ce and other metals, the inner strain could be preserved and fine-tuned by switching the second metal, for instance from Sc to Lu or Y. Furthermore, with extending the size of carbon cage from C_{80} to C_{88} , the inner strains could be released accordingly as well. Hence, there are plenty of open and interesting questions to be answered. The relationship between the geometry of endohedral cluster and the inner strains induced by the pyramidal cluster should be illustrated.

Among C_{80} -based MMNCFs, Praseodymium-containing structures have not been reported. Although Echegoyen and co-workers reported the synthesis, isolation and electrochemical study of $Pr_3N@C_{2n}$ ($2n= 80-88$), the low yield of Pr-compounds hinders the further NMR studies. The motivations of the Pr-based MMNCFs are their vibrational spectroscopic and the NMR study. The comparative study of $MSc_2N@C_{80}$ (I; M= Lanthanide metals) could reveal: a) the dependence of their electronic and vibrational properties on the encapsulated metal due

to the well-known Lanthanide contraction; b) their different paramagnetic ^{13}C and ^{45}Sc NMR behaviors could be compared considering their similar ionic radii but different 4f-electrons configurations.

2.2 Synthesis and isolation of $\text{Ho}_x\text{M}_{3-x}\text{N}@C_{80}$

2.2.2 Synthesis and isolation of $\text{Ho}_x\text{Sc}_{3-x}\text{N}@C_{80}$ ($x = 1, 2$)

The synthesis of $\text{Ho}_x\text{Sc}_{3-x}\text{N}@C_{80}$ MMNCFs was achieved by the “reactive gas atmosphere” method as previously described. By a modified Krätschmer-Huffman DC-arc discharging method with the addition of NH_3 (20 mbar) as described elsewhere. Briefly, a mixture of Ho_2O_3 and Sc_2O_3 (99.9%, MaTeck GmbH, Germany) and graphite powder was used (molar ratio $\text{Ho}/\text{Sc}/\text{C}=1:1:15$). After dc-arc discharging, the soot was pre-extracted by acetone and further Soxhlet-extracted by CS_2 for 20h. Figure 2.1 displays a typical HPLC chromatogram of the $\text{Ho}_x\text{Sc}_{3-x}\text{N}@C_{2n}$ ($x=0-3$) fullerenes extract obtained under the optimized condition. Analyzed by the integrated areas of the corresponding chromatographic peaks, the dominant products are two isomers of $\text{Ho}_x\text{Sc}_{3-x}\text{N}@C_{80}$ ($x=1, 2$), and the relative yield of $\text{Sc}_3\text{N}@C_{80}$ (I and II) is around 20%.

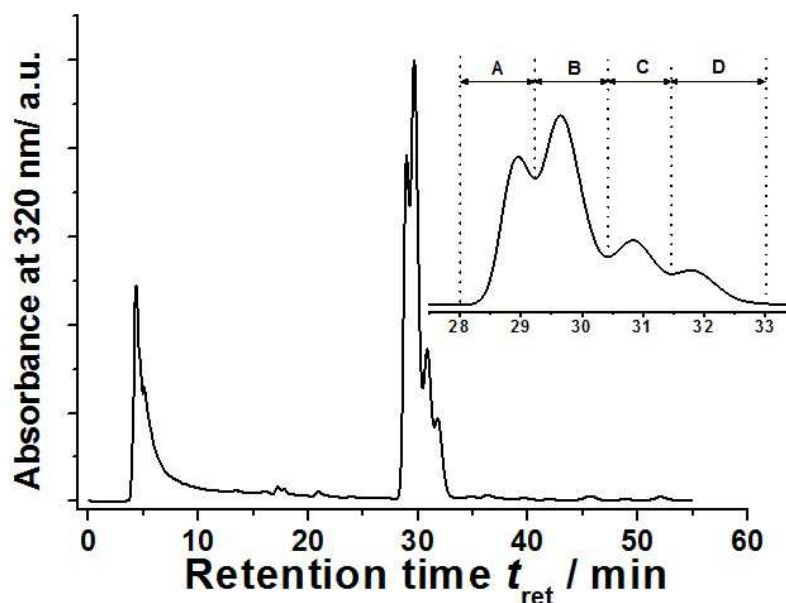


Figure 2.1 Chromatogram of a raw $\text{Ho}_x\text{Sc}_{3-x}\text{N}@C_{2n}$ fullerenes extract synthesized by the “reactive gas atmosphere” method (linear combination of two 4.6×250 mm Buckyprep columns, flow rate 1.6 ml/min, injection volume 200 μL , toluene as mobile phase, 40 $^\circ\text{C}$). The inset shows the enlarged chromatographic region of 28.0-33.0 min.

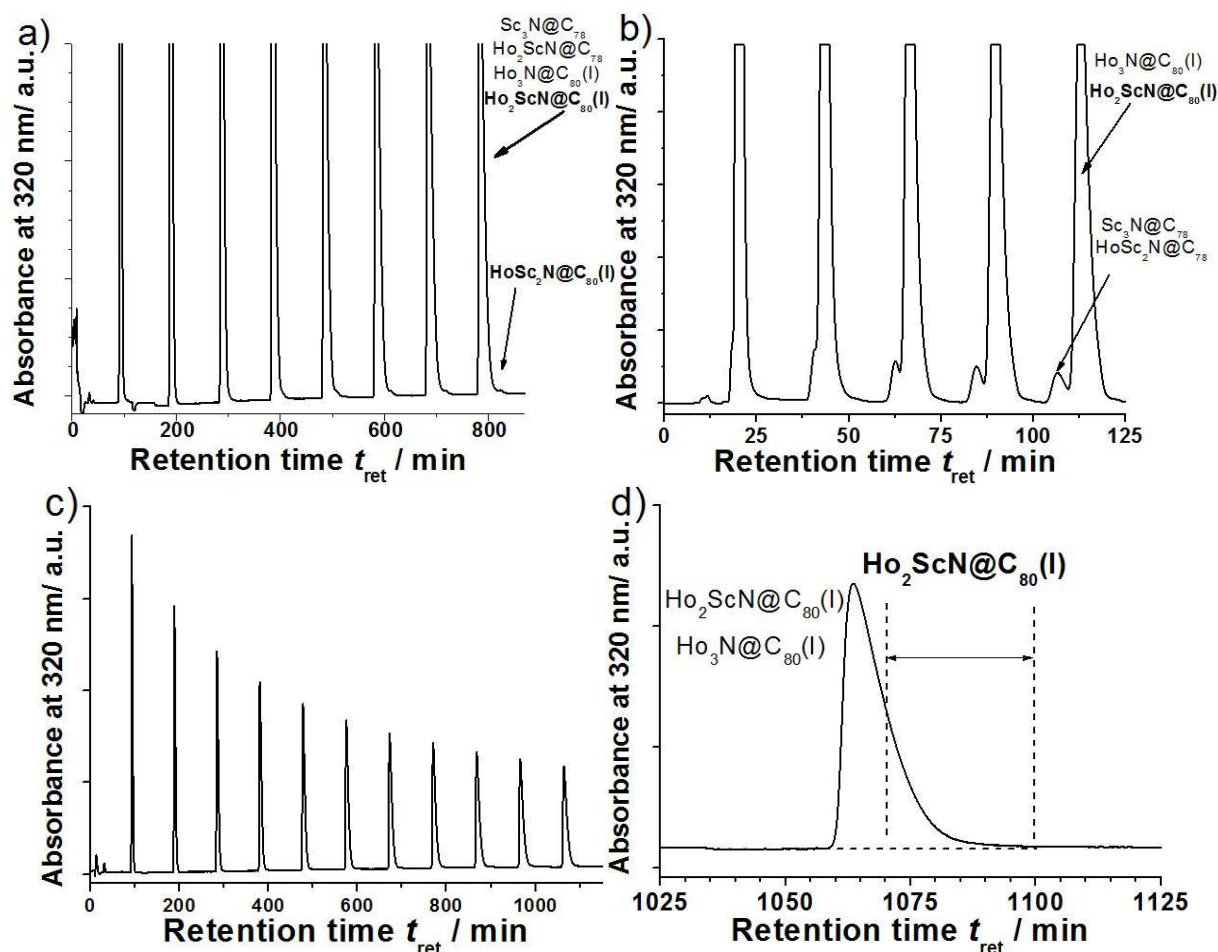


Figure 2.2 The HPLC isolation of fraction A by three-step recycling HPLC. (a) Removal of $HoSc_2N@C_{80}(I)$ (10×250 mm Buckyprep column; flow rate 1.5 ml/min; injection volume 5 ml; toluene as eluent; 20 °C). (b) Removal of $Sc_3N@C_{78}$ and $HoSc_2N@C_{78}$ (10×250 mm Buckyclutcher column; flow rate 1.5 ml/min; injection volume 5 ml; toluene as eluent). (c) Removal of $Ho_3N@C_{80}(I)$ (10×250 mm Buckyprep column; flow rate 1.5 ml/min; injection volume 5 ml; toluene as eluent), (d) shows the enlarged chromatographic region at 1025-1125 min.

Two isomers of $Ho_xSc_{3-x}N@C_{80}$ ($x = 1, 2$) were isolated by the multi-step HPLC (see Figures 2.1-2.5). At the first step, linear combination of two 4.6×250 mm Buckyprep columns was used to separate fractions A-D (Figure 2.1). Each of the fractions was then subjected to the isolation by recycling HPLC on a Buckyprep and/or Buckyclutcher column. In particular, to isolate $Ho_2ScN@C_{80}(I)$ from fraction A, first, the Buckyprep column was employed to remove the $HoSc_2N@C_{80}(I)$ (Figure 2.2 a); second, the Buckyclutcher column was employed to remove $Sc_3N@C_{78}$ and $HoSc_2N@C_{78}$ (Figure 2.2 b); third, due to the close retention times of the $Ho_3N@C_{80}(I)$ and $Ho_2ScN@C_{80}(I)$, only small amount of pure $Ho_2ScN@C_{80}(I)$ was obtained by recycling HPLC after 11 cycles (Figure 2.2 c and d).

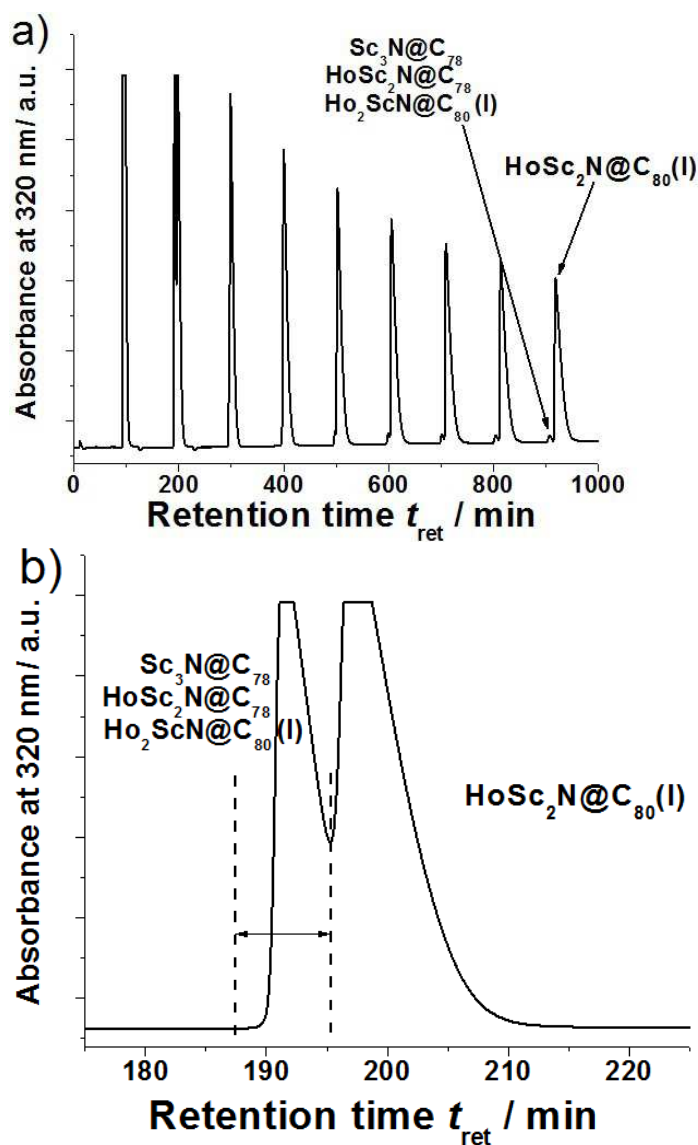


Figure 2.3 The HPLC isolation of fraction B by recycling HPLC. The removal of $Sc_3N@C_{78}$, $HoSc_2N@C_{78}$ and $Ho_2ScN@C_{80}$ (I) (10×250 mm Buckyprep column; flow rate 1.5 ml/min; injection volume 5 ml; toluene as eluent; 20 °C).

Compared to the $Ho_2ScN@C_{80}$ (I), the isolation of $HoSc_2N@C_{80}$ (I) was achieved after recycling fraction B 10 times to remove the other structures which included $Sc_3N@C_{78}$, $HoSc_2N@C_{78}$ and $Ho_2ScN@C_{80}$ (I). Due to the peak tailing in the first step (Figure 2. 1 inset), considerable amount of minor structures in the Fraction B was removed in the second cycle, see Figure 2. 3b.

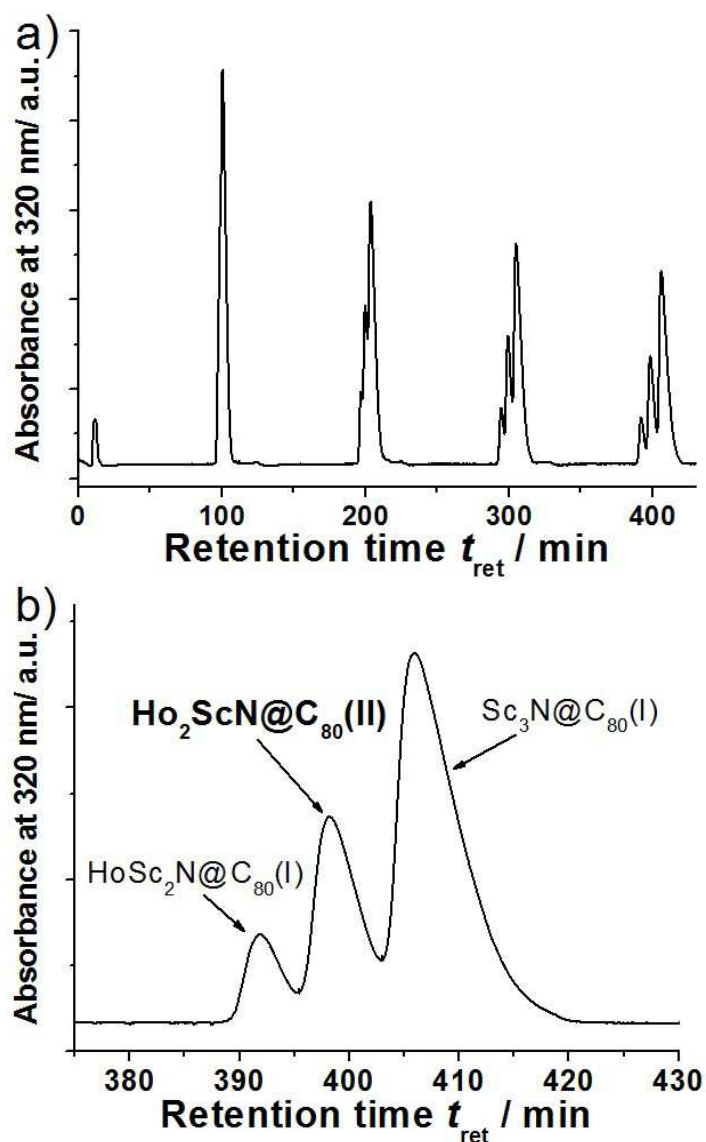


Figure 2.4 The HPLC isolation of fraction C by recycling HPLC.

The isolation of $\text{Ho}_2\text{ScN@C}_{80}(\text{II})$ from the fraction C was accomplished by collecting the fraction between $\text{HoSc}_2\text{N@C}_{80}(\text{I})$ and $\text{Sc}_3\text{N@C}_{80}(\text{I})$ after several cycles (Figure 2.4). Retention times of $\text{HoSc}_2\text{N@C}_{80}(\text{II})$ and $\text{Sc}_3\text{N@C}_{80}(\text{II})$ are quite close; moreover, the amount of these two compounds is quite low in the fraction D. So the mixture of these two compounds had to be enriched in the first step (Figure 2.5a), then after 24 cycles, limited amount of the purified $\text{HoSc}_2\text{N@C}_{80}(\text{II})$ could be obtained (Figure 2.5 b and c).

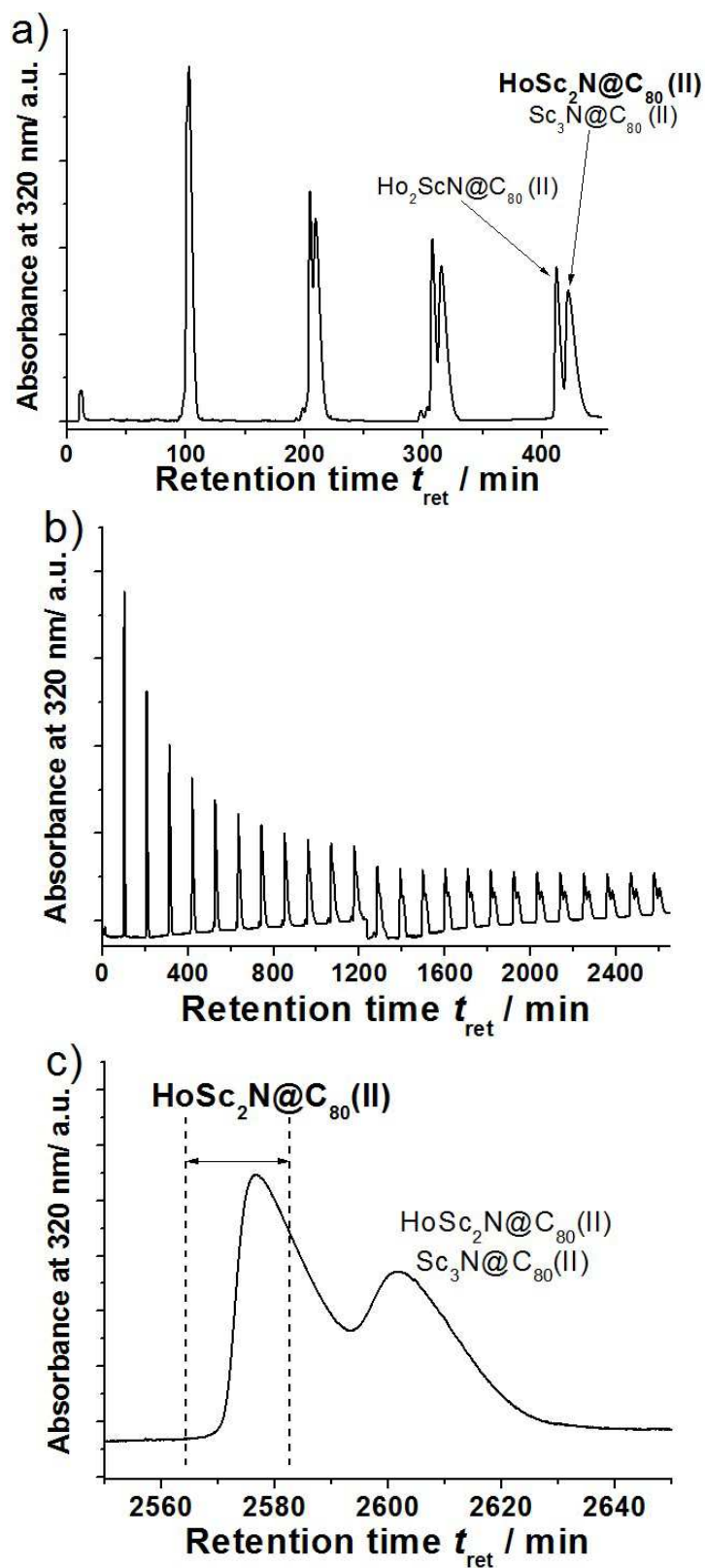


Figure 2.5 The isolation of fraction D. The removal of $\text{Ho}_2\text{ScN@C}_{80}$ (II) and $\text{Sc}_3\text{N@C}_{80}$ (II) (10×250 mm Buckyprep column; flow rate 1.5 ml/min; injection volume 5 ml; toluene as eluent; 20 °C).

The isolated samples of $\text{Ho}_x\text{Sc}_{3-x}\text{N}@C_{80}$ (I, II; $x=1, 2$) were identified by laser desorption/ionization time-of-flight (LDI-TOF) mass spectrum analysis (Figure 2. 6), which confirmed their high purity.

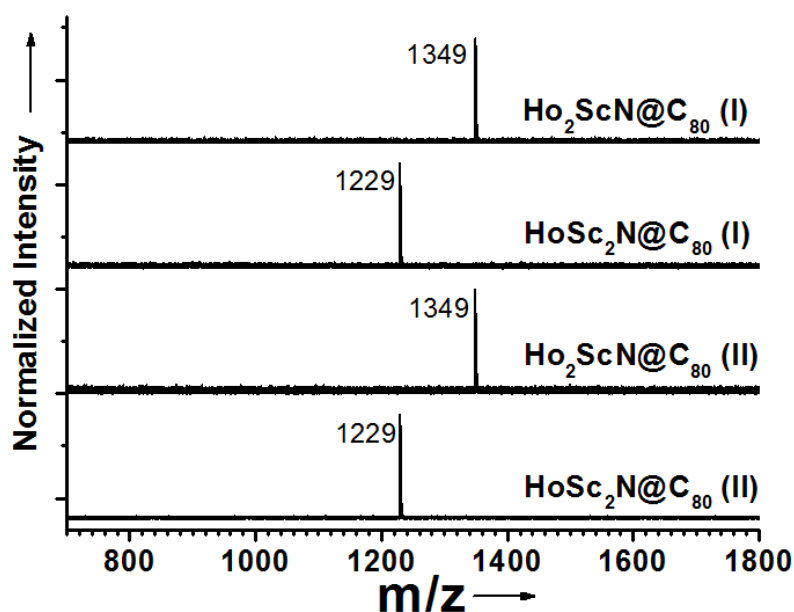


Figure 2.6 Positive Ion LDI-TOF mass spectra of the isolated $\text{Ho}_x\text{Sc}_{3-x}\text{N}@C_{80}$ (I, II; $x=1, 2$).

2.2.2 Synthesis and isolation of $\text{Ho}_x\text{Y}_{3-x}\text{N}@C_{80}$ ($x=1, 2$)

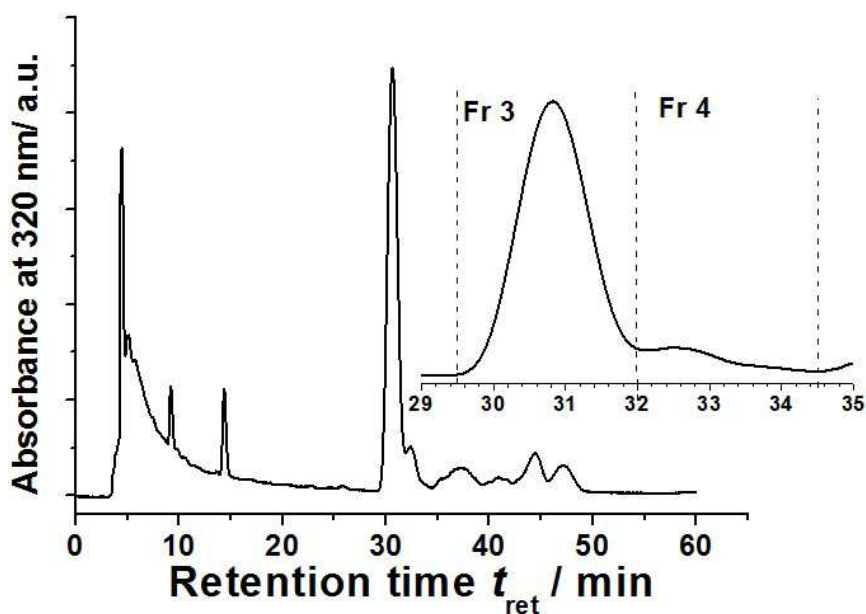


Figure 2.7 Chromatogram of a raw $\text{Ho}_x\text{Y}_{3-x}\text{N}@C_{2n}$ fullerenes extract synthesized by the “selective organic solid” method (linear combination of two 4.6×250 mm Buckyprep columns, flow rate 1.6 ml/min, injection volume 200 μL , toluene as mobile phase, 40 $^\circ\text{C}$). The inset shows the enlarged chromatographic region of 29.5-34.5 min.

The synthesis of $\text{Ho}_x\text{Y}_{3-x}\text{N@C}_{80}$ (I ; $x=1, 2$) was achieved by “selective organic solid” route as previously described in chapter 1. The process of dc-arc discharging and solution extraction was the same in the production of $\text{Ho}_x\text{Sc}_{3-x}\text{N@C}_{80}$. A mixture of Ho_2O_3 and Y_2O_3 (99.9%, MaTeck GmbH, Germany), guanidine thiocyanate (GT) and graphite powder was used (molar ratio $\text{Ho}/\text{Y}/\text{GT}/\text{C}=1:1:2.5:15$). The typical chromatogram of the extracted $\text{Ho}_x\text{Y}_{3-x}\text{N@C}_{2n}$ fullerenes is shown in Figure 2.7.

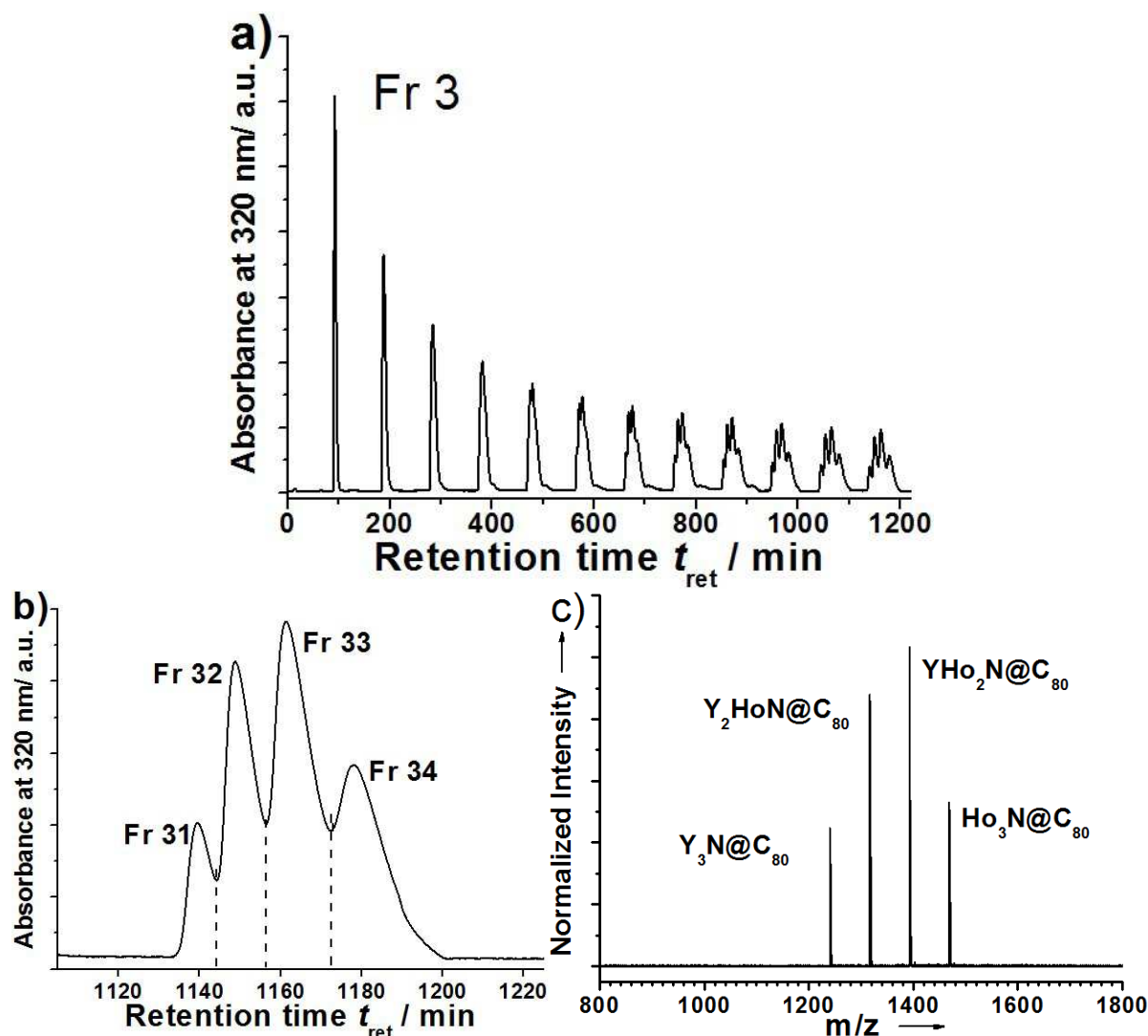


Figure 2.8 The HPLC isolation of fraction 3. (10×250 mm Buckyprep column; flow rate 1.5 ml/min; injection volume 5 ml; toluene as eluent; 20 °C).

Two isomer of $\text{Ho}_x\text{Y}_{3-x}\text{N@C}_{80}$ ($x=0-3$) were isolated by multistep HPLC (see Figure 2.8 - 2.10). Firstly, the analytical HPLC was employed to collect $\text{Ho}_x\text{Y}_{3-x}\text{N@C}_{80}$ (I) (Fraction 3) and $\text{Ho}_x\text{Y}_{3-x}\text{N@C}_{80}$ (II) (Fraction 4) respectively. Different to $\text{Ho}_x\text{Sc}_{3-x}\text{N@C}_{80}$ (I ; $x=1, 2$), the retention time of $\text{Ho}_x\text{Y}_{3-x}\text{N@C}_{80}$ (I) in Buckyprep column (4.6×250 mm) are identical. Secondly, the Fr 3 was subjected to isolation by recycling HPLC on a Buckyprep column

(10×250 mm), see Figure 2. 8a. After 12 recycling cycles, four sub-fractions could be obtained which marked as Fr 31 to Fr 34. The relative yield of $\text{Ho}_x\text{Y}_{3-x}\text{N@C}_{80}$ ($x=0-3$) could be estimated from the integrated areas of the corresponding chromatographic peaks which agrees well with mass spectrum result of fraction 3 (Figure 2. 8b and c).

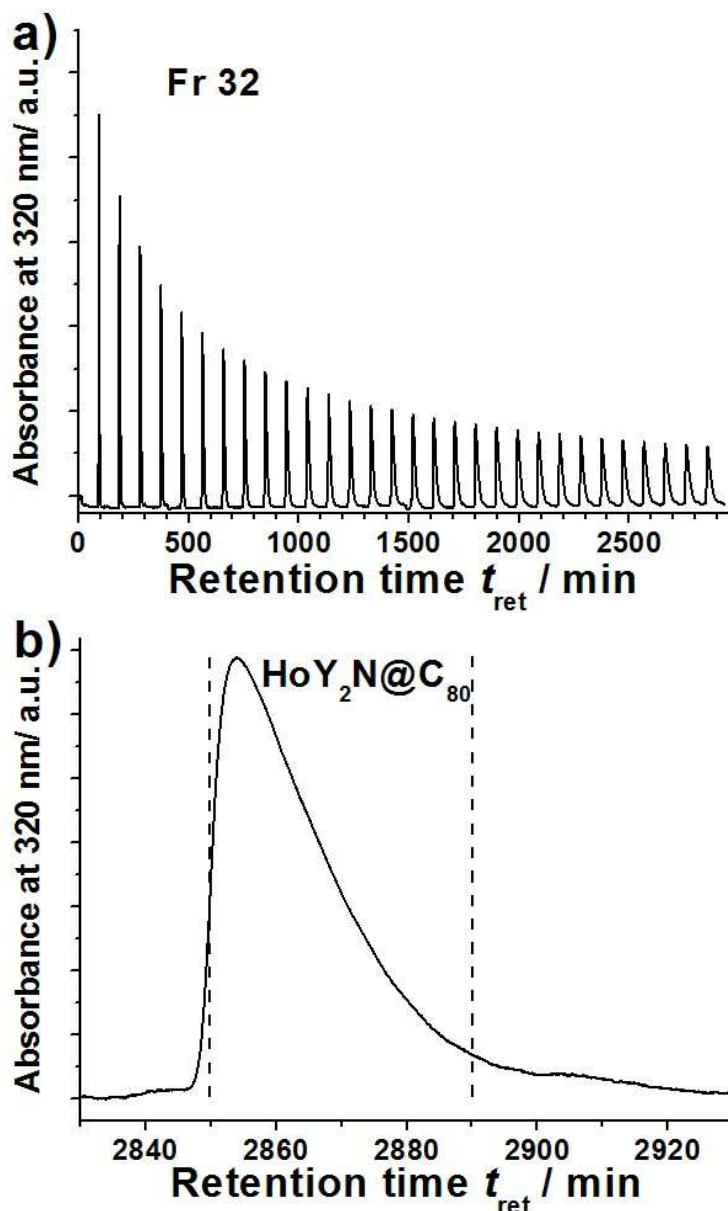


Figure 2.9 The isolation of fraction Fr 32. (10×250 mm Buckyprep column; flow rate 1.5 ml/min; injection volume 5 ml; toluene as eluent; 20 °C).

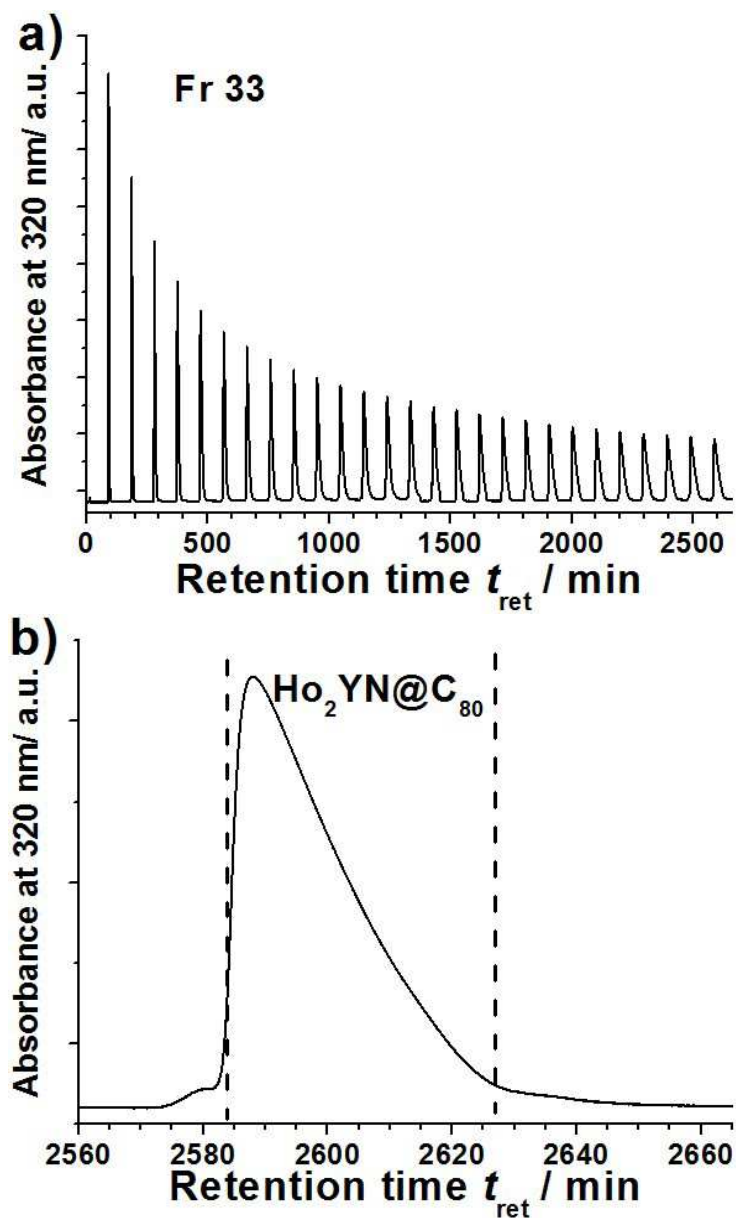


Figure 2.10 The isolation of fraction Fr 33. (10×250 mm Buckyprep column; flow rate 1.5 ml/min; injection volume 5 ml; toluene as eluent; 20 °C).

Isolation of $HoY_2N@C_{80}$ (I) was accomplished by removing the small amount of $Y_3N@C_{80}$ (I) and $Ho_2YN@C_{80}$ (I) from fraction 32 after 30 cycles. Likewise, the pure $Ho_2YN@C_{80}$ (I) could be obtained by removing the minor structures ($HoY_2N@C_{80}$ (I) and $Ho_3N@C_{80}$ (I)) in fraction 33 through 27 cycles. The purity of $Ho_xY_{3-x}N@C_{80}$ (I; $x = 1, 2$) were confirmed by LDI-TOF mass spectroscopy (Figure 2.10 and 2.11).

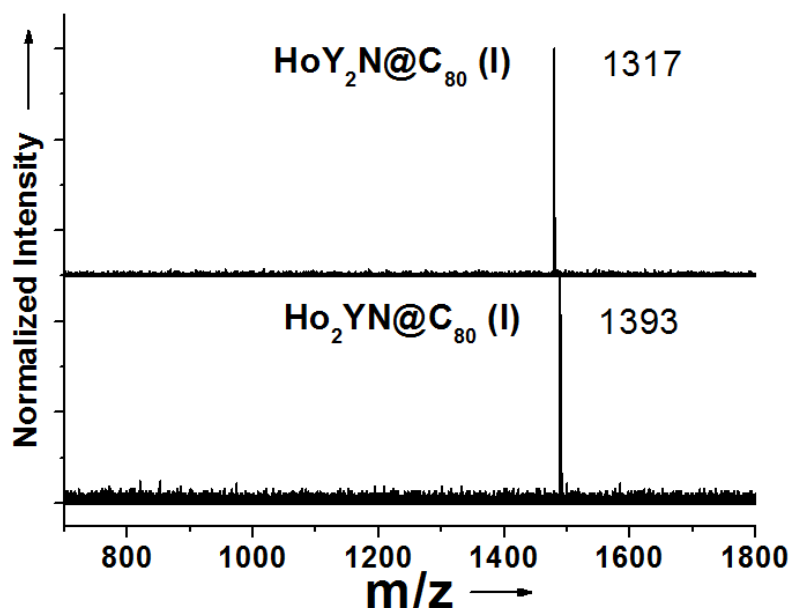


Figure 2.11 The isolated samples of $\text{Ho}_x\text{Y}_{3-x}\text{N@C}_{80}$ (I; $x=1, 2$) were identified by laser-desorption time-of-flight (LDI-TOF) mass spectrum analysis, which confirmed their high purity.

2.2.3 Synthesis and Isolation of $\text{Ho}_x\text{Lu}_{3-x}\text{N@C}_{80}$ ($x=1, 2$)

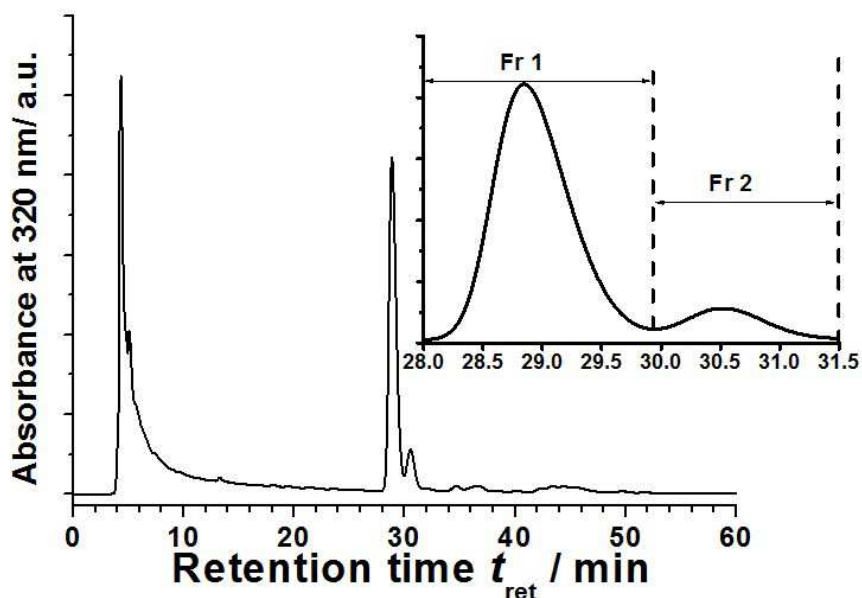


Figure 2.12 Chromatogram of a raw $\text{Ho}_x\text{Lu}_{3-x}\text{N@C}_{2n}$ fullerenes extract synthesized by the “reactive gas atmosphere” method (linear combination of two 4.6×250 mm Buckyprep columns, flow rate 1.6 ml/min, injection volume 200 μL , toluene as mobile phase, 40 °C). The inset shows the enlarged chromatographic region of 28.0 - 31.5 min.

The synthesis of $\text{Ho}_x\text{Lu}_{3-x}\text{N@C}_{80}$ ($x=1, 2$) was achieved by “selective organic solid” route as previously described in the synthesis of $\text{Ho}_x\text{Y}_{3-x}\text{N@C}_{80}$ (I; $x=1, 2$). The process of dc-arc

discharging and solution extraction was the same procedure of $\text{Ho}_x\text{Y}_{3-x}\text{N@C}_{80}$. A mixture of Ho_2O_3 and Lu_2O_3 (99.9%, MaTeck GmbH, Germany), guanidine thiocyanate (GT) and graphite powder was used (molar ratio $\text{Ho/Lu/GT/C}=1:1:2.5:15$).

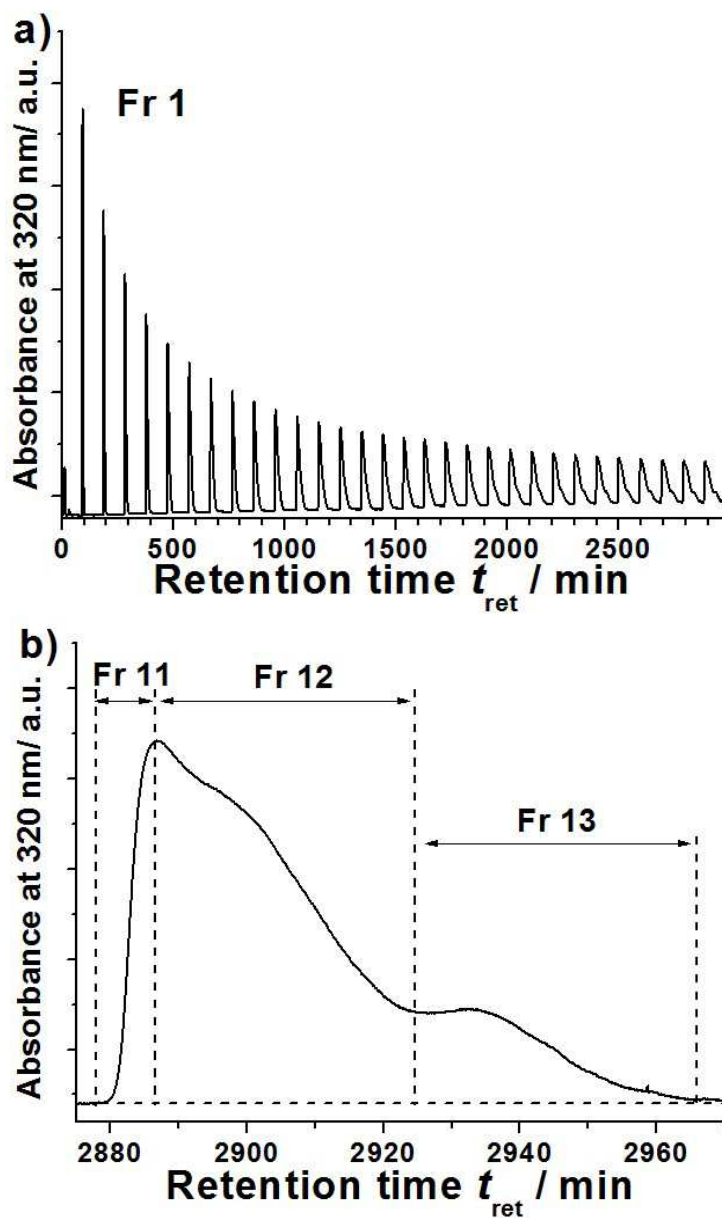


Figure 2.13 The isolation of fraction Fr 1. (10×250 mm Buckyprep column; flow rate 1.5 ml/min; injection volume 5 ml; toluene as eluent; 20 °C).

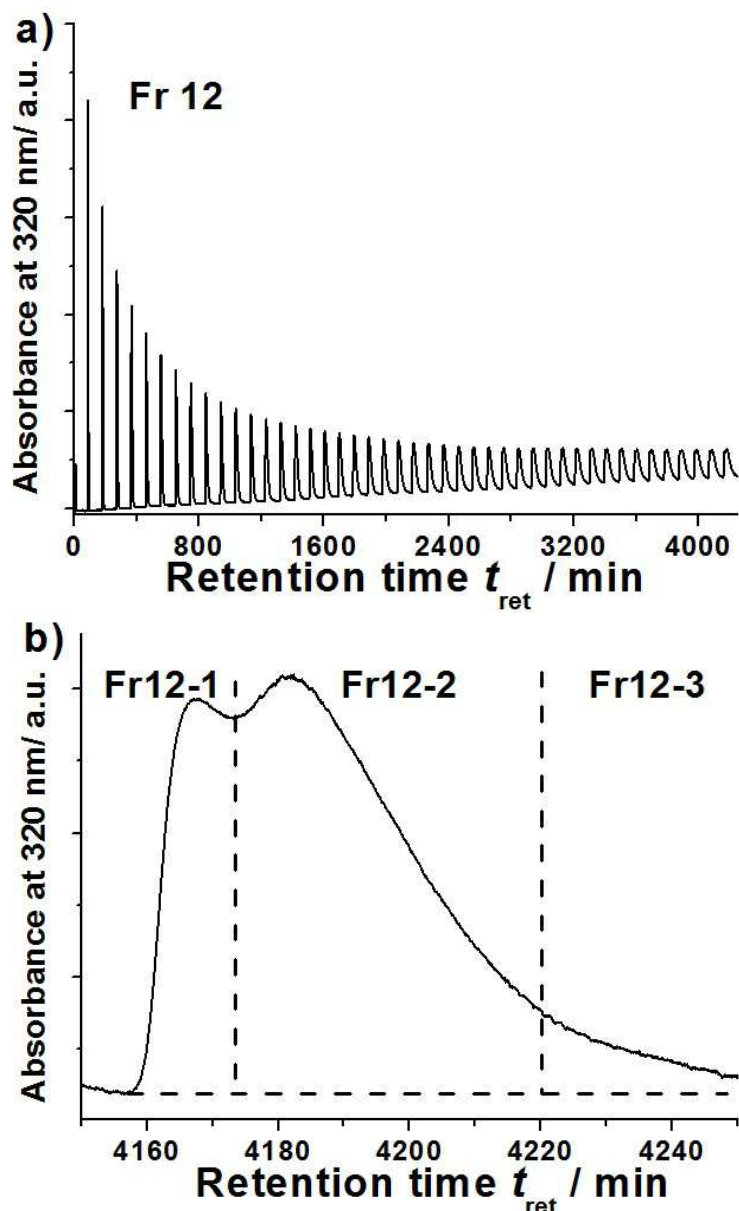


Figure 2.14 The isolation of fraction Fr 12. (10×250 mm Buckyprep column; flow rate 1.5 ml/min; injection volume is 5 ml; toluene as eluent; 20 °C).

The mixture of $\text{Ho}_x\text{Lu}_{3-x}\text{N@C}_{2n}$ was subjected to isolation by analytical HPLC in the first step (Figure 2.12). $\text{Ho}_x\text{Lu}_{3-x}\text{N@C}_{80}$ (I) and $\text{Ho}_x\text{Lu}_{3-x}\text{N@C}_{80}$ (II) were separated into Fr 1 (28.0 - 29.9 min) and Fr 2 (29.9 - 31.5 min) respectively according to the difference of their cage symmetry. In the second step, three sub-fractions could be obtained after recycling fraction 1 over 30 times which then named as Fr 11, Fr 12 and Fr 13. Checking by mass spectrum, the dominant structure in Fr 12 is $\text{Ho}_x\text{Lu}_{3-x}\text{N@C}_{80}$ (I) (Figure 2.13). In the third step, the Fr 12 was subjected to recycling HPLC again for removing minor structures ($\text{HoLu}_2\text{N@C}_{80}$ (I) and $\text{Ho}_3\text{N@C}_{80}$ (I)). As shown in Figure 2.14, Fr 122 was collected after 44 cycles. In the fourth step, after running another 44 cycles, the isolation of $\text{Ho}_2\text{LuN@C}_{80}$ (I)

was successfully achieved and its purity was confirmed by LDI-TOF mass spectroscopy (Figure 2.15).

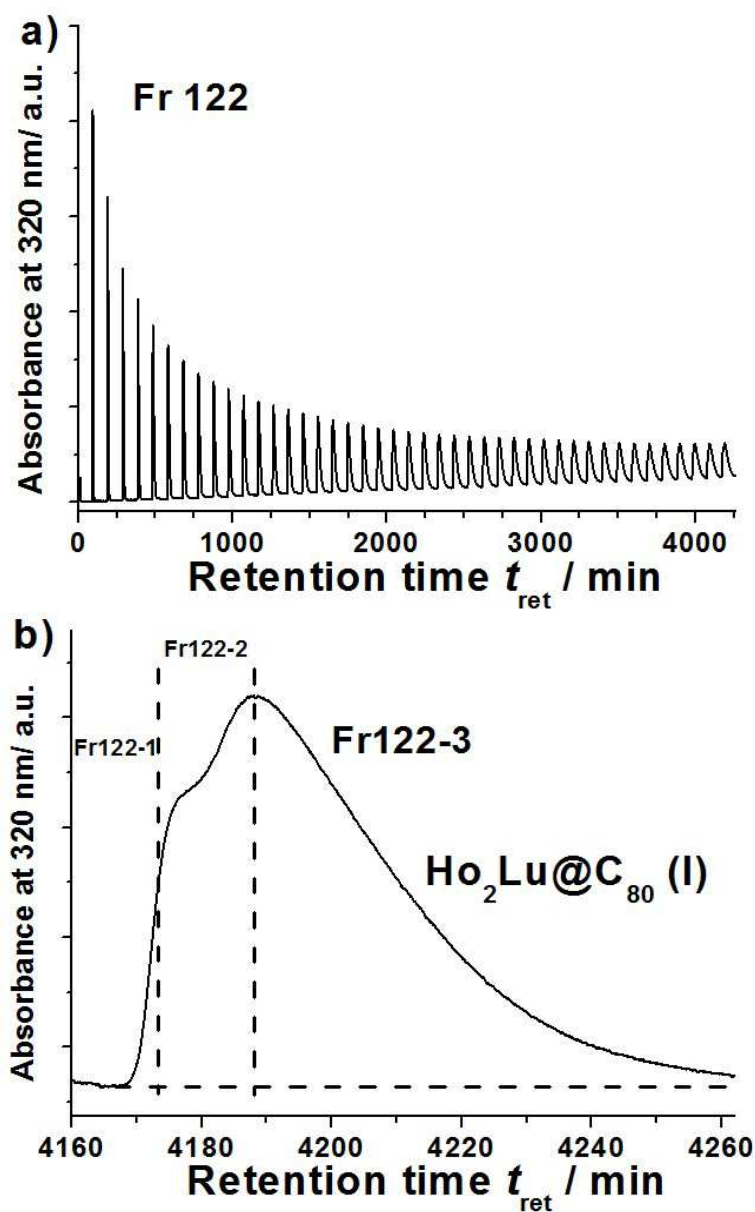


Figure 2.15 The isolation of fraction Fr 122. (10×250 mm Buckyprep column; flow rate 1.5 ml/min; injection volume 4 ml; toluene as eluent; 20 °C).

Similar to Ho₂LuN@C₈₀ (I), the isolation of HoLu₂N@C₈₀ (I) is extremely time-consuming due to the retention time of Lu₃N@C₈₀ (I) and HoLu₂N@C₈₀ (I) is almost identical. Only by running on recycling HPLC over 73 cycles, small amount of HoLu₂N@C₈₀ (I) was obtained, see Figure 2.16. The purity of HoLu₂N@C₈₀ (I) was confirmed by LDI-TOF mass spectroscopy (Figure 2.17).

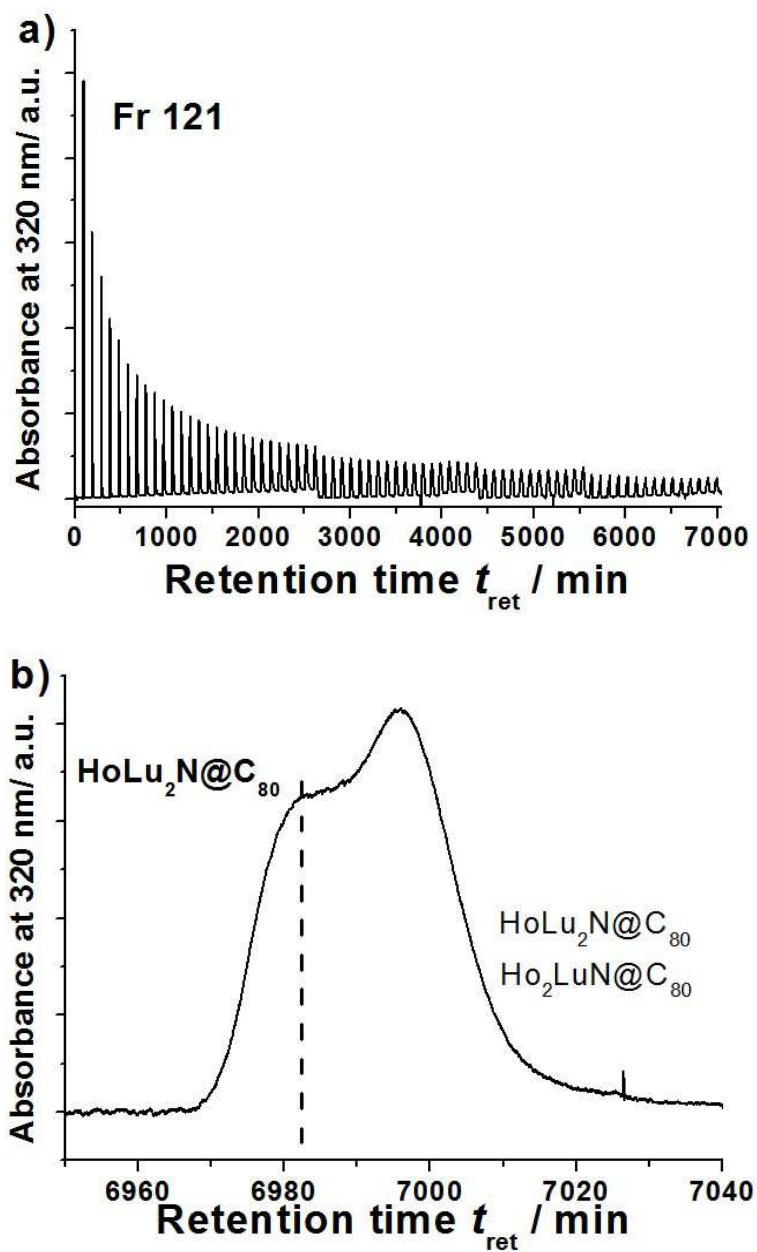


Figure 2.16 The isolation of fraction Fr 121. (10×250 mm Buckyprep column; flow rate 1.5 ml/min; injection volume is 4 ml; toluene as eluent; 20 °C).

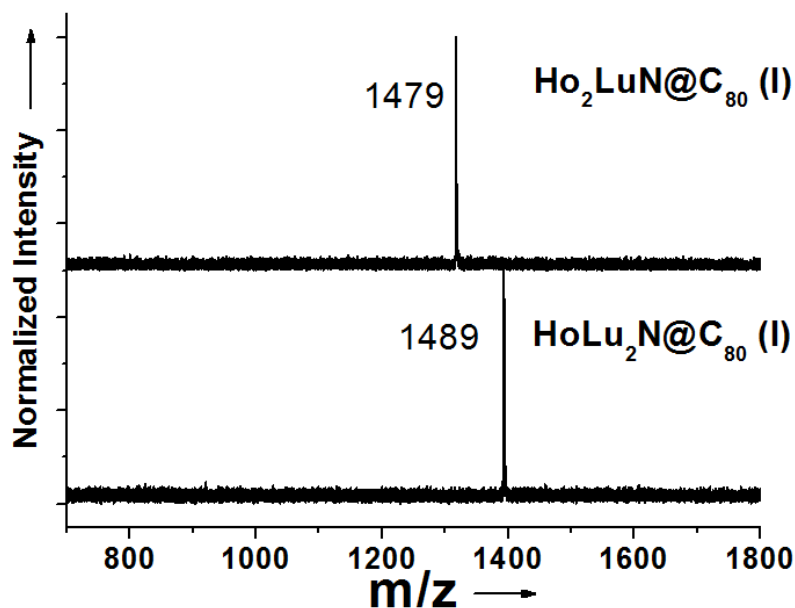


Figure 2.17 The isolated samples of $\text{Ho}_x\text{Lu}_{3-x}\text{N}@C_{80}$ (I ; $x=1, 2$) were identified by laser-desorption time-of-flight (LDI-TOF) mass spectrum analysis, which confirmed their high purity.

2.3 Synthesis and isolation of Ce-based MMNCFs

2.3.1 Synthesis and isolation of $\text{CeY}_2\text{N}@C_{80}$ (I)

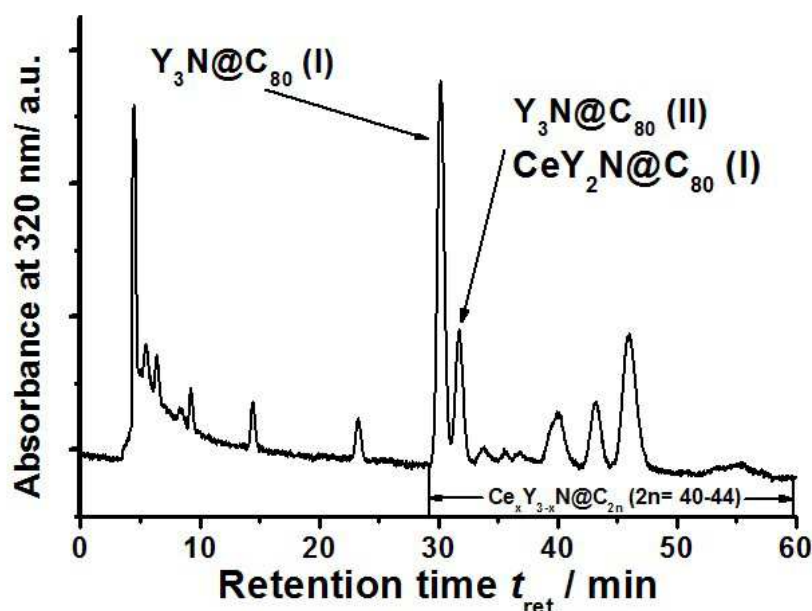


Figure 2.18 Chromatogram of $\text{Ce}_x\text{Y}_{3-x}\text{N}@C_{2n}$ ($2n=80-88$) fullerene extract mixture synthesized by the “SOS” method (combination of two 4.6×250 mm Buckyprep columns, flow rate 1.6 ml/min, injection volume 200 μL , toluene as mobile phase, 40 $^\circ\text{C}$).

$\text{CeY}_2\text{N}@C_{80}$ (I) was synthesized by the “selective organic solid” (SOS) route (using guanidine thiocyanate (GT) as the nitrogen source). After dc-arc discharging, the soot was

pre-extracted by acetone and further Soxhlet-extracted by CS_2 for 20h. The extraction solution was dried and then endohedral fullerenes-containing crude mixture was dissolved in toluene. Figure 2.1 shows a typical chromatogram of $\text{Ce}_x\text{Y}_{3-x}\text{N}@C_{2n}$ ($2n= 80-88$) fullerene extract mixture obtained under the optimized condition (molar ratio $\text{Ce}/\text{Y}/\text{GT}/\text{C}= 1:1:2.5:15$). The largest peak ($t_{\text{ret}}= 29.0-31.0$ min) in the chromatogram is assigned to $\text{Y}_3\text{N}@C_{80}$ (I) and the dominated fraction ($t_{\text{ret}}= 31.0-33.0$ min) contains $\text{Y}_3\text{N}@C_{80}$ (II) and $\text{CeY}_2\text{N}@C_{80}$ (I). The Ce-based mixed metal nitride ($\text{Ce}_x\text{Y}_{3-x}\text{N}$) could be encaged into the carbon cages larger than C_{80} as well, which included the cage size from C_{82} to C_{88} with retention time longer than 33.0 min. Their isolation and characterization will be discussed later.

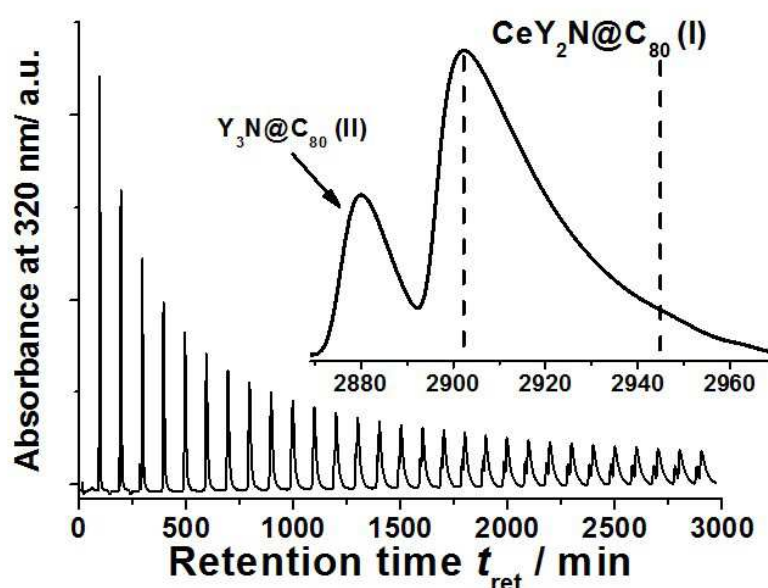


Figure 2.19 The isolation of $\text{CeY}_2\text{N}@C_{80}$ (I). $\text{CeY}_2\text{N}@C_{80}$ (I) was obtained by recycling HPLC after 29 cycles (10×250 mm Buckyprep column; flow rate 1.5 ml/min; injection volume is 5 ml; toluene as eluent; room temperature); the inset shows the last cycle (between 2870 and 2970 min).

Due to the retention time of $\text{CeY}_2\text{N}@C_{80}$ (I) and $\text{Y}_3\text{N}@C_{80}$ (II) is quite close, this fraction was subjected to isolation by recycling HPLC on a Buckyprep column. Pure $\text{CeY}_2\text{N}@C_{80}$ (I) was obtained by recycling HPLC after 29 cycles and further characterized by laser-desorption time-of-flight (LDI-TOF) mass spectroscopy which confirmed its high purity (see Figure 2.20).

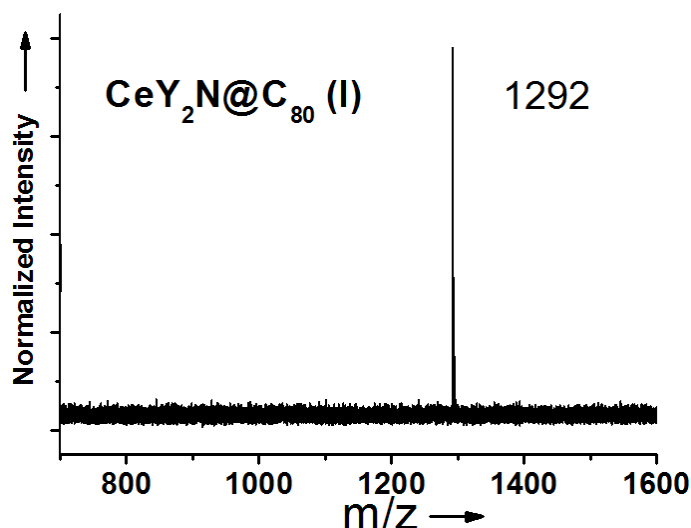


Figure 2.20 The LDI-TOF mass spectrum of purified $\text{CeY}_2\text{N@C}_{80}$ (I).

2.3.2 Synthesis and isolation of $\text{Ce}_x\text{Y}_{3-x}\text{N@C}_{2n}$ ($2n = 84-88$)

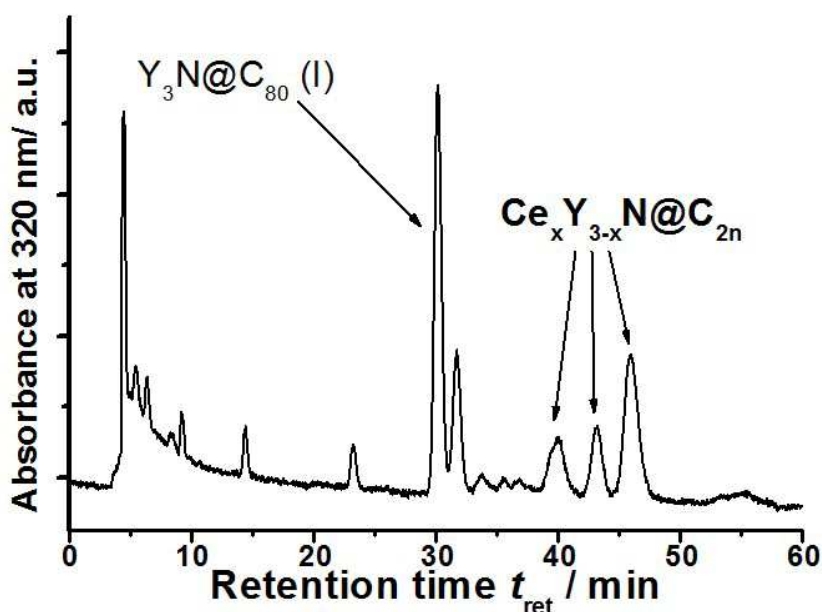


Figure 2.21 Chromatogram of $\text{Ce}_x\text{Y}_{3-x}\text{N@C}_{2n}$ fullerenes extract mixture synthesized by the “SOS” method (combination of two 4.6×250 mm Buckyprep columns, flow rate 1.6 ml/min, injection volume 200 μL , toluene as mobile phase, 40 $^\circ\text{C}$).

Ce-based large MMNCFs, namely $\text{Ce}_x\text{Y}_{3-x}\text{N@C}_{2n}$ ($2n = 84-88$), were synthesized by the “selective organic solid” (SOS) route as described previously. After dc-arc discharging, the soot was extracted by acetone and by CS_2 respectively. As mentioned, the largest peak in the chromatogram is assigned to $\text{Y}_3\text{N@C}_{80}$ (I), and the Fraction 7 ($t_{\text{ret}} = 38.5-42.0$ min) contains $\text{Ce}_x\text{Y}_{3-x}\text{N@C}_{86}$, the Fraction 8 ($t_{\text{ret}} = 42.0-44.5$ min) contains $\text{Ce}_x\text{Y}_{3-x}\text{N@C}_{84}$ and the Fraction 9 ($t_{\text{ret}} = 42.0-44.5$ min) contains $\text{Ce}_x\text{Y}_{3-x}\text{N@C}_{88}$, respectively.

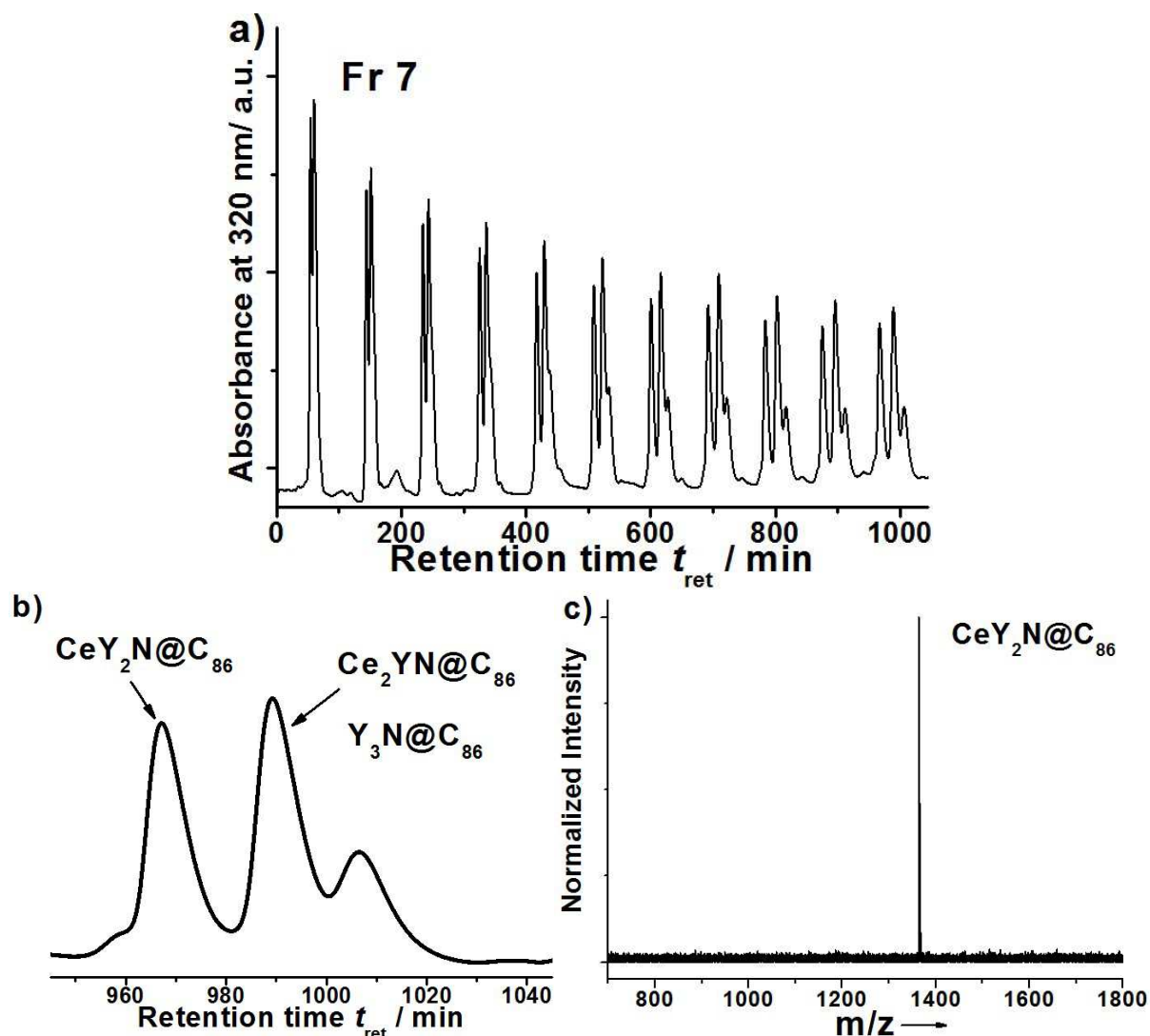


Figure 2.22 Chromatogram of the Fraction 7 of $Ce_xY_{3-x}N@C_{86}$ fullerenes extract mixture synthesized by the “SOS” method (combination of two 4.6×250 mm Buckyprep columns, flow rate was set at 3.0 ml/min, injection volume 3 mL, toluene as mobile phase, room temperature).

According to the integrated area of Fraction labeled in Figure 2.21, it could be estimated that the relative yield of $Ce_xY_{3-x}N@C_{2n}$ ($2n = 84-88$) are much lower than the $Y_3N@C_{80}$ (I). Pure $CeY_2N@C_{86}$ could be isolated by running recycling HPLC with Fr 7, see Figure 2.22 b and c. Because the retention time of $Y_3N@C_{86}$ and $Ce_2YN@C_{86}$ is quite close, this sub-fraction was collected as the mixture of these two structures.

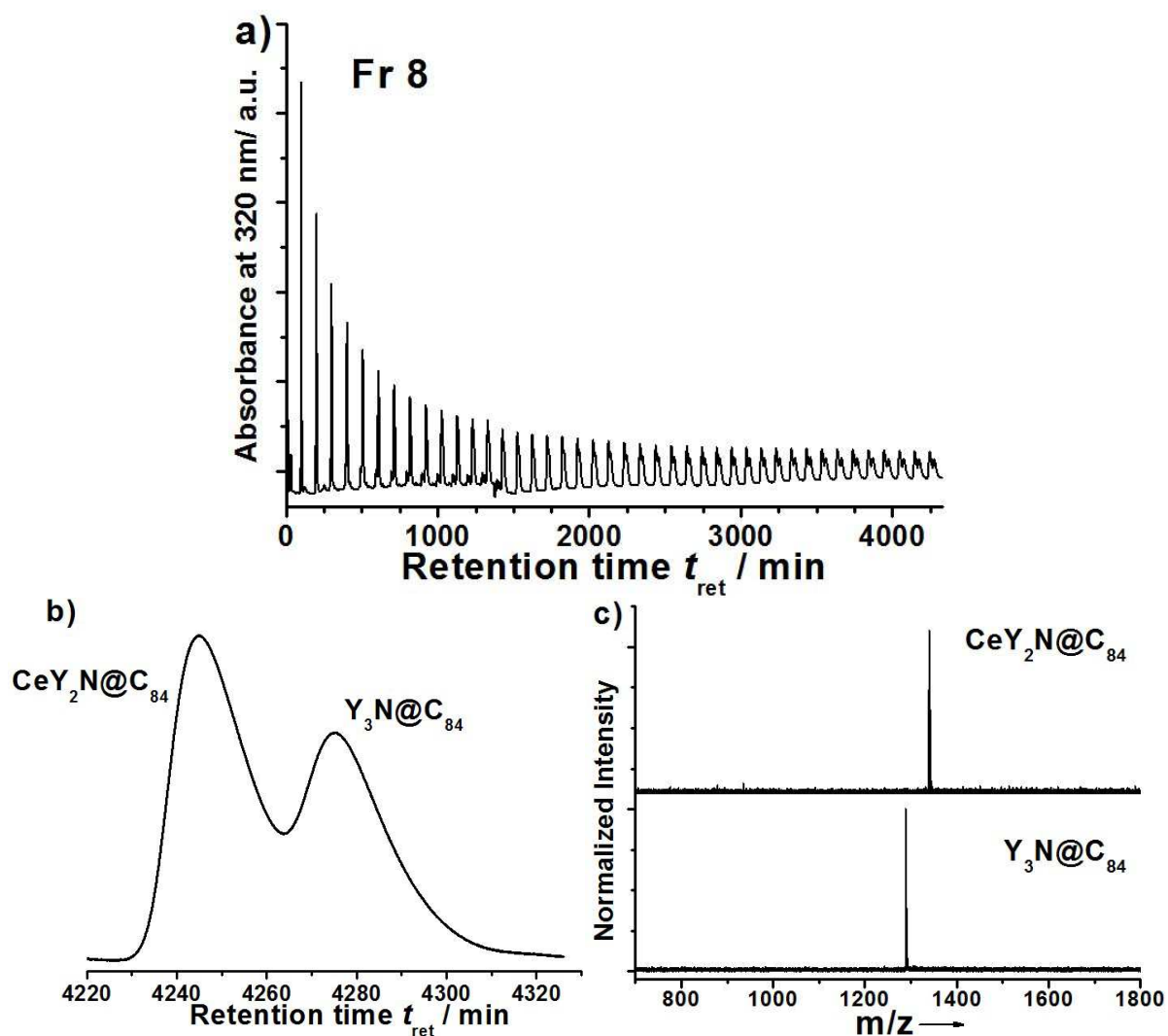


Figure 2.23 Chromatogram of the Fraction 8 of $Ce_xY_{3-x}N@C_{84}$ fullerenes extract mixture synthesized by the “SOS” method (combination of two 4.6×250 mm Buckyprep columns, flow rate 2.0 ml/min, injection volume 3 mL, toluene as mobile phase, room temperature).

$CeY_2N@C_{84}$ and $Y_3N@C_{84}$ are major structures in the Fraction 8, see Figure 2.23 a. Both of them were isolated after 42 cycles. They were characterized by LDI-TOF mass spectroscopy which confirmed their high purity.

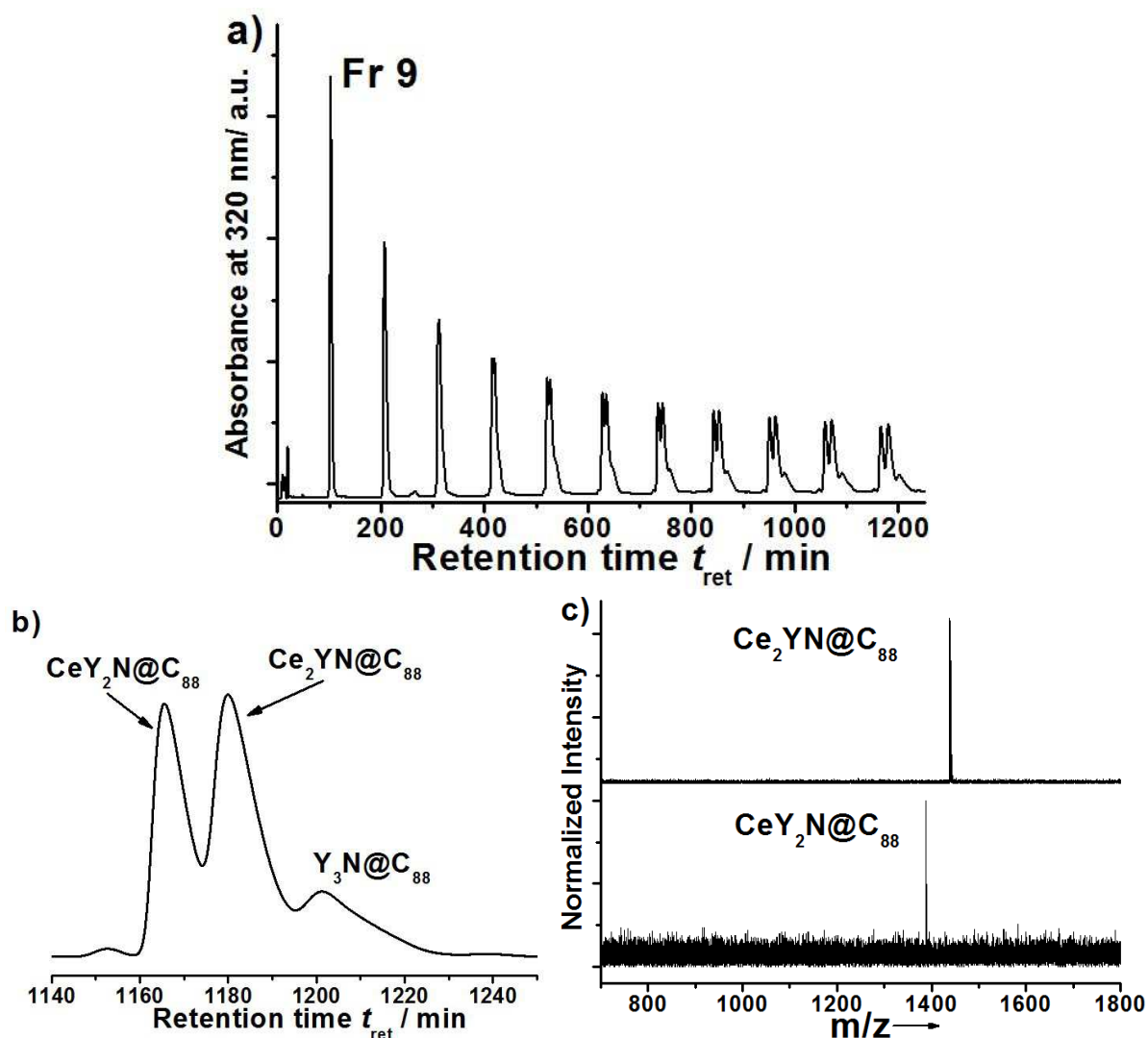


Figure 2.24 Chromatogram of the Fraction 9 of $Ce_xY_{3-x}N@C_{88}$ fullerenes extract mixture synthesized by the “SOS” method (combination of two 4.6×250 mm Buckyprep columns, flow rate 2.0 ml/min, injection volume 3 mL, toluene as mobile phase, room temperature).

In Fraction 9, $Ce_2YN@C_{88}$ and $CeY_2N@C_{88}$ were isolated after 11 cycles, see Figure 2.24. Confirmation of their high purity was performed by LDI-TOF mass spectroscopy.

2.3.3 Synthesis and isolation of CeSc₂N@C₈₀ (II)

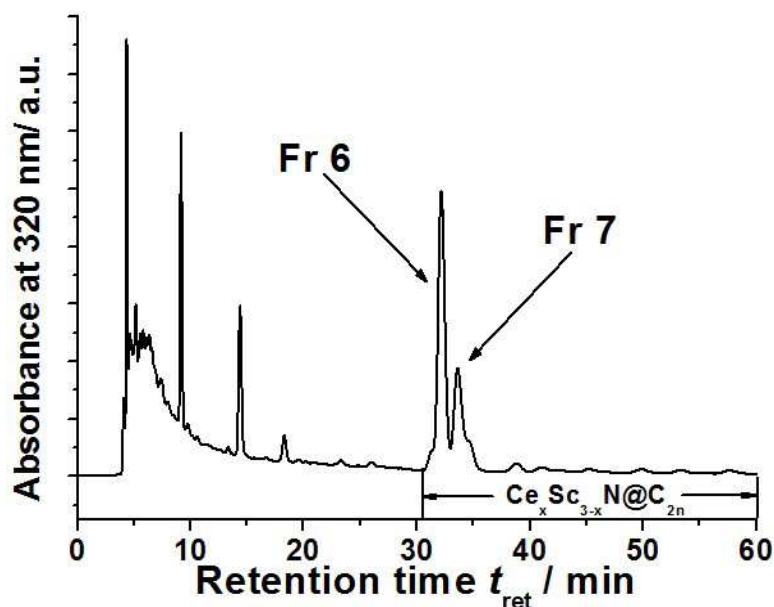


Figure 2.25 Chromatogram of Ce_xSc_{3-x}N@C_{2n} (2n= 78-88) fullerene extract mixture synthesized by the “SOS” method (combination of two 4.6×250 mm Buckyprep columns, flow rate 1.6 ml/min, injection volume 200 μL, toluene as mobile phase, 40 °C).

The synthesis of CeSc₂N@C₈₀ (I and II) was achieved by SOS route. The procedure of the soot treatment was the same to CeY₂N@C₈₀ (I). The typical HPLC chromatogram of Ce_xSc_{3-x}N@C_{2n} (2n= 78-88) fullerene extract mixture obtained under the optimized condition (molar ratio Ce/Sc/GT/C= 1:1:2.5:15) in Figure 2.25.

In Figure 2.25, the Fraction 7 (t_{ret} = 30.0-36.4 min) in the chromatogram contains CeSc₂N@C₈₀ (II) and two isomers of Sc₃N@C₈₀. The isolation of CeSc₂N@C₈₀ (II) was accomplished in two stages. In the first stage, the Sc₃N@C₈₀ (II) was removed after 10 cycles (see Figure 2.5 b). Because the retention time of CeSc₂N@C₈₀ (II) is very close Sc₃N@C₈₀ (I), small amount of CeSc₂N@C₈₀ (II) could be obtained after 25 cycles (see Figure 2.26 c). The high purity of CeSc₂N@C₈₀ (II) was confirmed by LDI-TOF mass spectroscopy which shown in Figure 2.27.

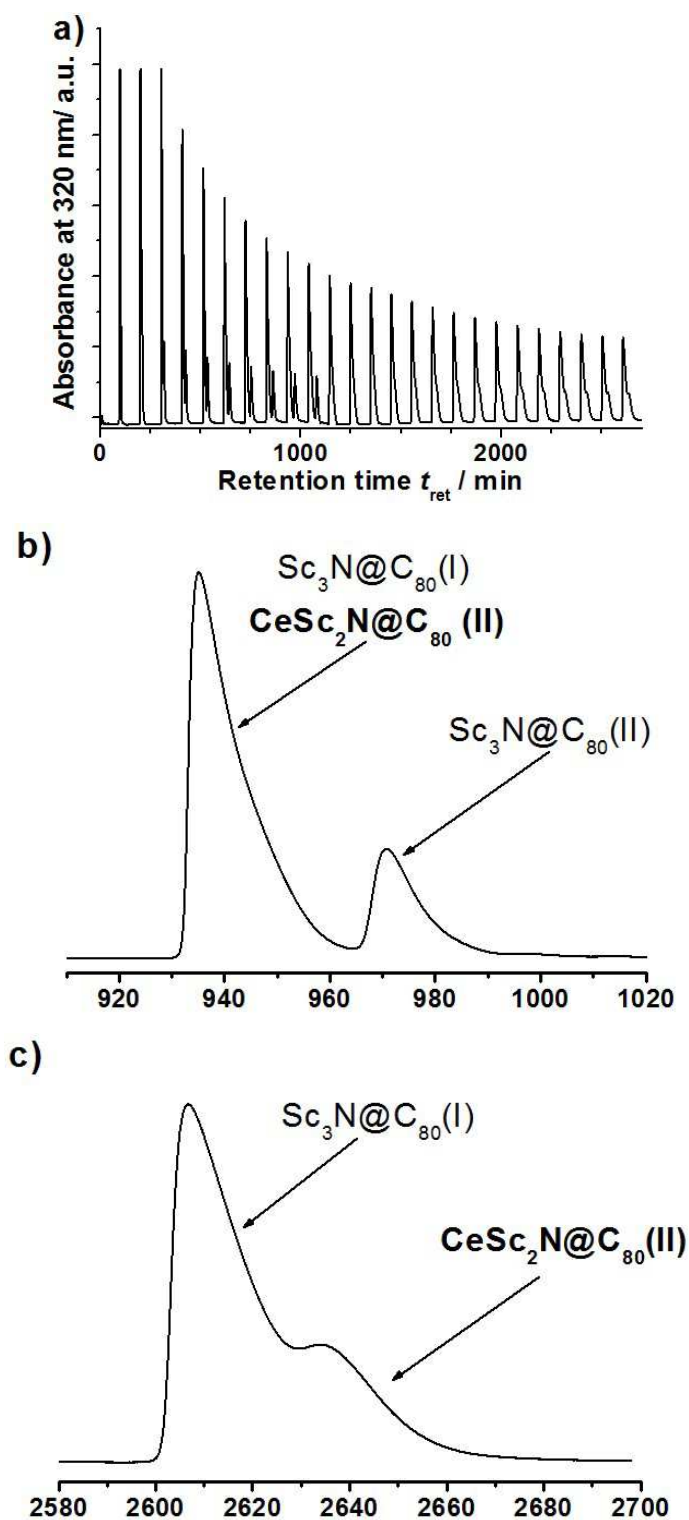


Figure 2.26 The isolation of $CeSc_2N@C_{80}(II)$. (a) $CeSc_2N@C_{80}(II)$ was obtained by recycling HPLC after 24 cycles (10×250 mm Buckyprep column; flow rate 1.5 ml/min; injection volume is 5 ml; toluene as eluent; room temperature); (b) The enlarged views of 9th and 25th cycle from (a) are shown in (b) and (c) respectively, ($t_{ret}= 910-1020$ min and $t_{ret}= 2580-2700$ min).

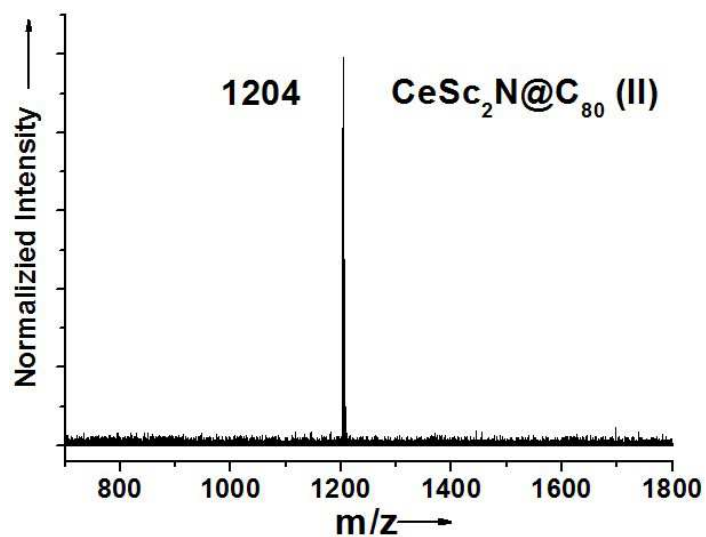


Figure 2.27 The LDI-TOF mass spectrum of purified CeSc₂N@C₈₀ (II).

2.4 Synthesis and Isolation of Pr-based MMNCFs

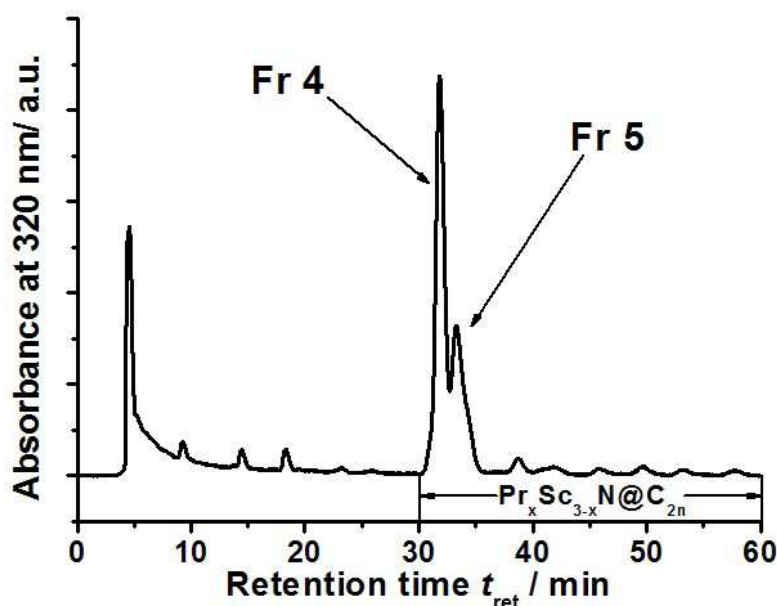


Figure 2.28 Chromatogram of $\text{Pr}_x\text{Sc}_{3-x}\text{N}@C_{2n}$ ($2n= 78-88$) fullerene extract mixture which synthesized by the “SOS” method (combination of two 4.6×250 mm Buckyprep columns, flow rate 1.6 ml/min, injection volume 200 μL , toluene as mobile phase, 40 $^\circ\text{C}$).

Two isomers of $\text{PrSc}_2\text{N}@C_{80}$ were synthesized by the “selective organic solid” (SOS) route (using guanidine thiocyanate (GT) as the nitrogen source). After dc-arc discharging, the soot was pre-extracted by acetone and further Soxhlet-extracted by CS_2 for 20h. The extraction solution was dried and then endohedral fullerenes-containing crude mixture was dissolved in toluene. The HPLC chromatogram of $\text{Pr}_x\text{Sc}_{3-x}\text{N}@C_{2n}$ ($2n= 78-88$) fullerene extract mixture obtained under the optimized condition (molar ratio $\text{Pr}/\text{Sc}/\text{GT}/\text{C}= 1:1:2.5:15$) is shown in Figure 4.1. The largest peak ($t_{\text{ret}}= 30.2-32.7$ min) in the chromatogram is correlated to C_{80} -based $\text{PrSc}_2\text{N}@C_{80}$ (I) and $\text{Pr}_2\text{ScN}@C_{80}$ (I), and C_{78} -based $\text{PrSc}_2\text{N}@C_{78}$ and $\text{Sc}_3\text{N}@C_{78}$ (Fraction 4). The second dominated fraction ($t_{\text{ret}}= 32.7-36.0$ min) mainly contains $\text{PrSc}_2\text{N}@C_{80}$ (II) and two isomers of $\text{Sc}_3\text{N}@C_{80}$ (Fraction 5). The Ce-based mixed metal nitride ($\text{Pr}_x\text{Sc}_{3-x}\text{N}$) could be encaged into the carbon cages ranging from C_{82} to C_{88} with retention time between 37.0 and 59.0 min.

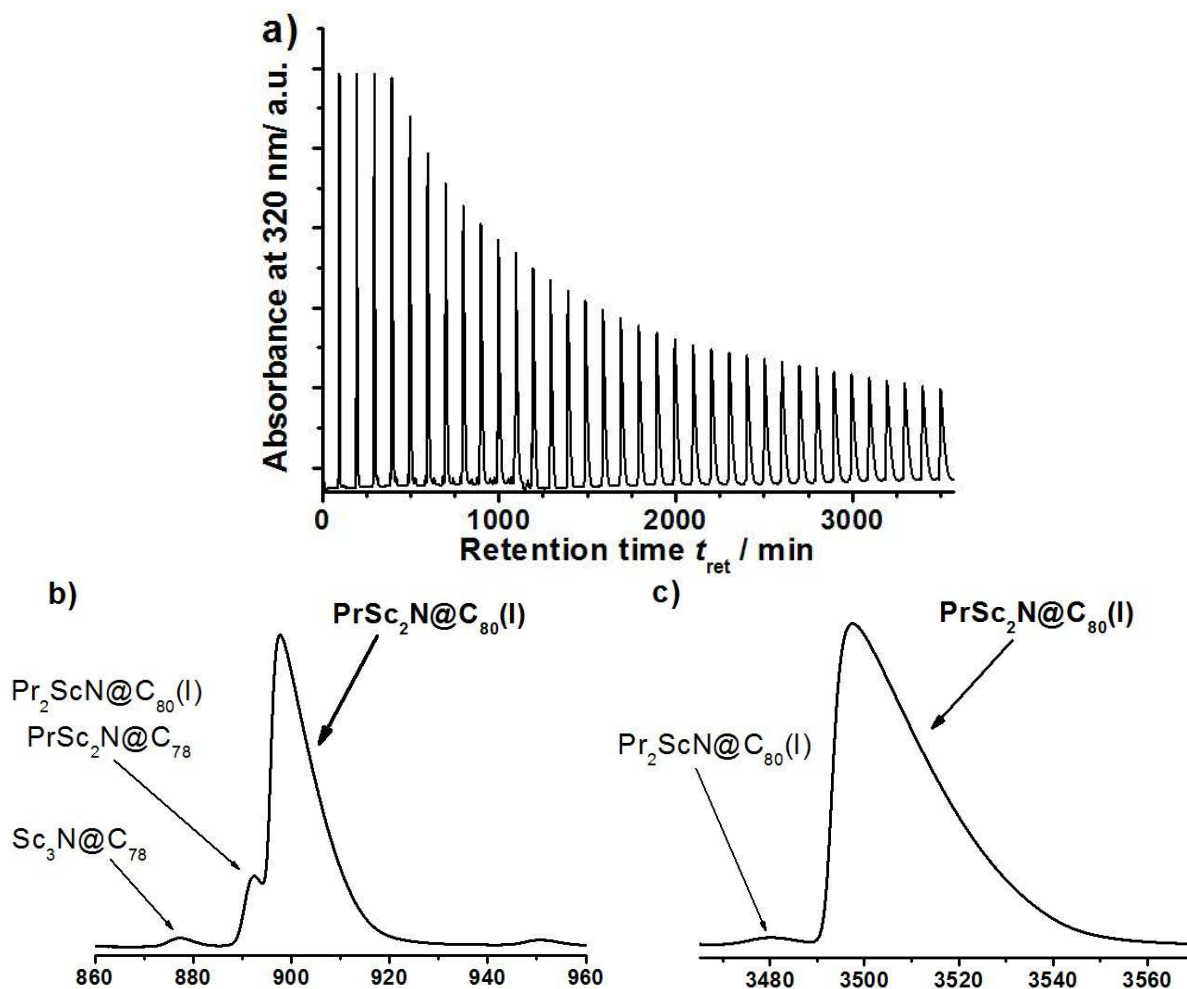


Figure 2.29 The isolation of $\text{PrSc}_2\text{N}@C_{80}$ (I). $\text{PrSc}_2\text{N}@C_{80}$ (I) was obtained by recycling HPLC after 35 cycles (10×250 mm Buckyprep column; flow rate 1.5 ml/min; injection volume is 5 ml of Fraction 4; toluene as eluent; room temperature); The enlarged views of 9th and 35th cycle from (a) are shown in (b) and (c) respectively, ($t_{\text{ret}}= 860 - 965$ min and $t_{\text{ret}}= 3465 - 3670$ min).

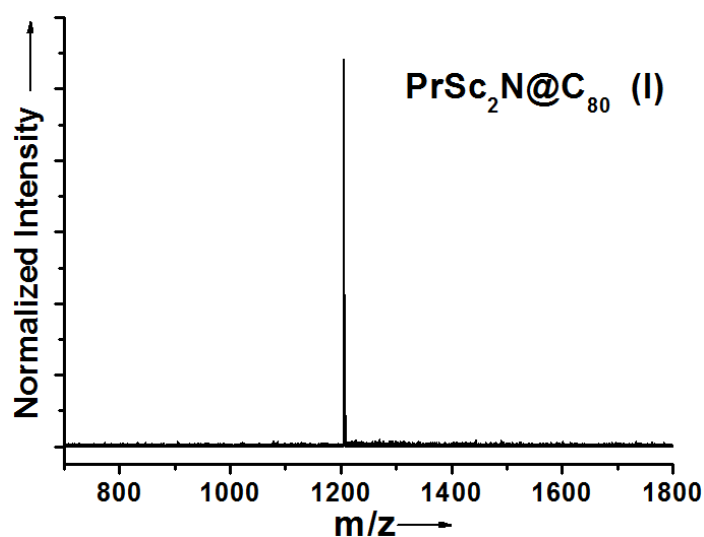


Figure 2.30 The LDI-TOF mass spectrum of purified $\text{PrSc}_2\text{N}@C_{80}$ (I).

Because the retention time of these four compounds ($\text{PrSc}_2\text{N@C}_{80}$ (I) and $\text{Pr}_2\text{ScN@C}_{80}$ (I), $\text{PrSc}_2\text{N@C}_{78}$ and $\text{Sc}_3\text{N@C}_{78}$) in Fraction 4 is rather close. The Fraction 4 was subjected to next-step isolation by recycling HPLC on a Buckyprep column (Figure 2.29). Pure $\text{PrSc}_2\text{N@C}_{80}$ (I) was obtained by recycling HPLC on the second step after 35 cycles. All of the $\text{Sc}_3\text{N@C}_{78}$ and $\text{PrSc}_2\text{N@C}_{78}$ could be removed after 9 cycles (see Figure 2.29 b) and only trace of $\text{Pr}_2\text{ScN@C}_{80}$ (I) remained in the fraction. Finally, the removal of this minor structure could be achieved on the 35th cycle (see Figure 2.29 c). $\text{PrSc}_2\text{N@C}_{80}$ (I) was characterized by LDI-TOF mass spectroscopy which confirmed its high purity (see Figure 2.30).

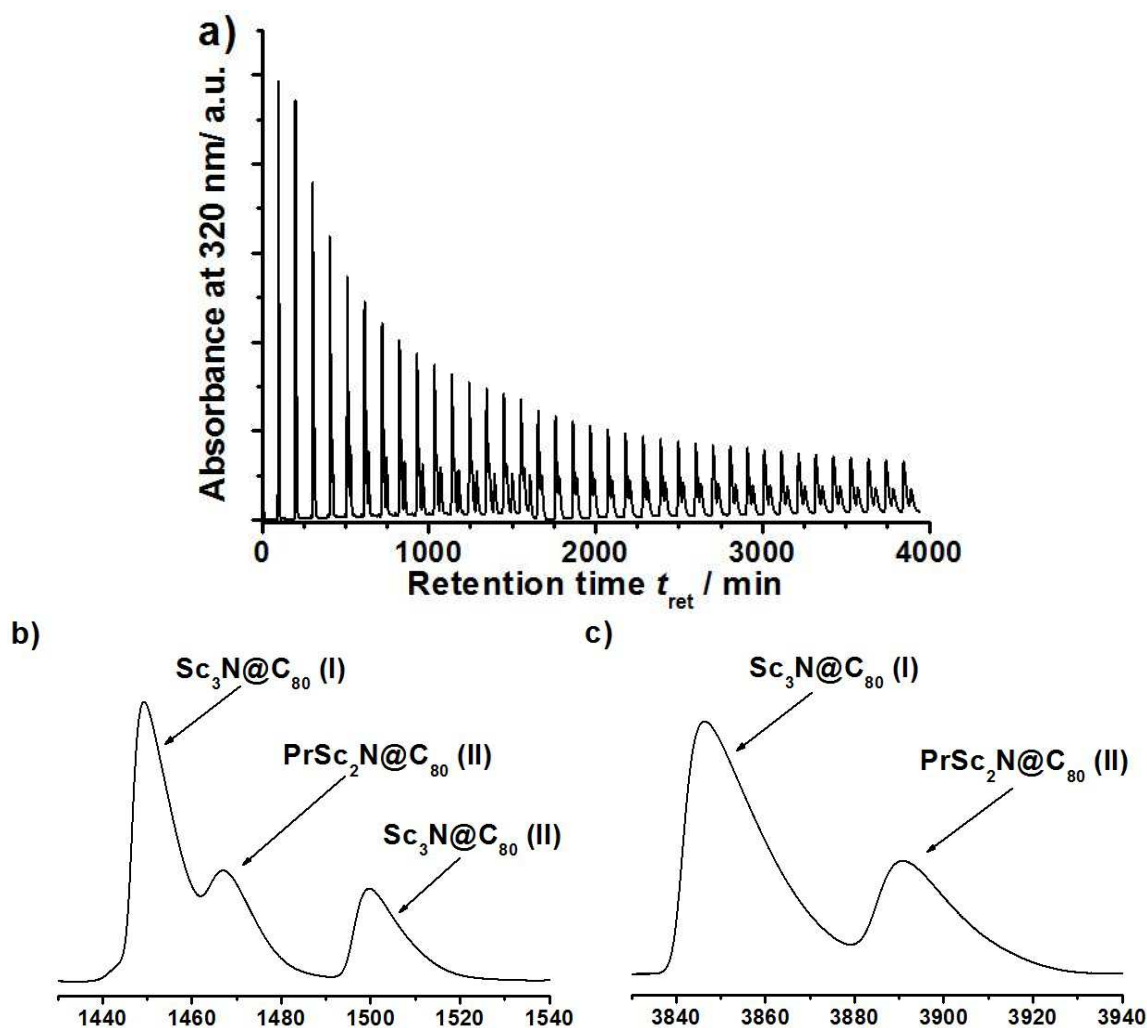


Figure 2.31 The isolation of $\text{PrSc}_2\text{N@C}_{80}$ (II). $\text{PrSc}_2\text{N@C}_{80}$ (II) was obtained by recycling HPLC after 37 cycles (10×250 mm Buckyprep column; flow rate 1.5 ml/min; injection volume is 5 ml of Fraction 5; toluene as eluent; room temperature); The enlarged views of 14th and 37th cycle from (a) are shown in (b) and (c) respectively, ($t_{ret}=1430-1540$ min and $t_{ret}=3830-3940$ min).

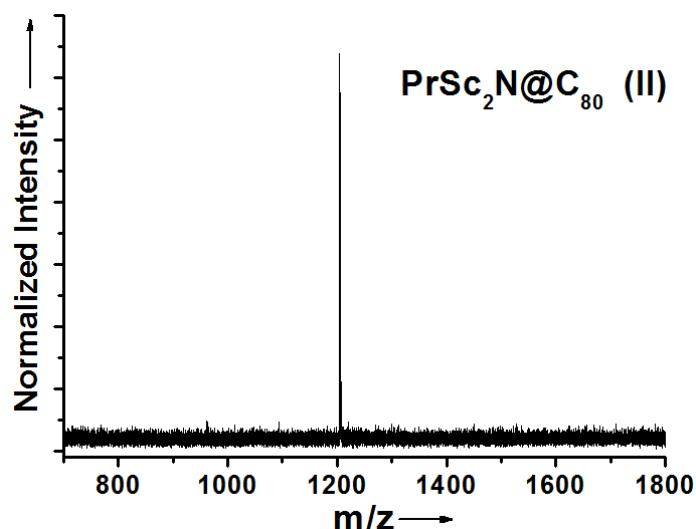


Figure 2.32 The LDI-TOF mass spectrum of purified $\text{PrSc}_2\text{N@C}_{80}$ (II).

The isolation of $\text{PrSc}_2\text{N@C}_{80}$ (II) was accomplished in two steps. Firstly, the $\text{PrSc}_2\text{N@C}_{80}$ (II) was collected with $\text{Sc}_3\text{N@C}_{80}$ (I and II) into Fraction 5 (see Figure 2.31). Secondly, similar to the case of $\text{PrSc}_2\text{N@C}_{80}$ (I), the same Buckyprep column was employed to remove two isomers of $\text{Sc}_3\text{N@C}_{80}$ and the details have been described in Figure 2.31b. The retention time of $\text{PrSc}_2\text{N@C}_{80}$ (II) is found between that of $\text{Sc}_3\text{N@C}_{80}$ (I) and $\text{Sc}_3\text{N@C}_{80}$ (II). After 37 cycles, the $\text{PrSc}_2\text{N@C}_{80}$ (II) could be obtained. The high purity of $\text{PrSc}_2\text{N@C}_{80}$ (II) was confirmed by LDI-TOF mass spectroscopy which shown in Figure 2.32.

2.5 Conclusion

The synthesis of Ho-based, Ce-based and Pr-based MMNCFs was achieved by the “reactive gas atmosphere” or “selective organic solid” route. The isolation of C₈₀-based MMNCFs which including Ho_xSc_{3-x}N@C₈₀ (I, II; x= 1, 2), Ho_xLu_{3-x}N@C₈₀ (I; x= 1, 2), Ho_xY_{3-x}N@C₈₀ (I; x= 1, 2), CeY₂N@C₈₀ (I), CeSc₂N@C₈₀ (II) and PrSc₂N@C₈₀ (I, II) was accomplished by multi-step HPLC. Additionally, Ce-based MMNCFs with carbon cage larger than C₈₀ were synthesized and isolated which include CeY₂N@C₈₄, CeY₂N@C₈₆, Ce₂YN@C₈₆, Ce₂YN@C₈₈ and CeY₂N@C₈₈. The purity of above-mentioned MMNCFs was confirmed by LDI-TOF mass spectroscopy. To understand and tune the electronic, magnetic and electrochemical properties of the MMNCFs, Ho, Ce and Pr are chosen due to their different metal ionic radii, the number of 4f-electron and magnetic moment. In the following chapter, those endohedral fullerenes will be compared according to the same carbon cage structure containing different encaged cluster or the same encapsulated cluster in different carbon cages.

It should be mentioned that Anja Grohme finished the synthesis of Ce_xSc_{3-x}N@C_{2n} compounds.

Chapter 3 Spectroscopic Characterization of Mixed Metal Nitride Clusterfullerenes

3.1 UV-Vis-NIR spectroscopy of MMNCFs

The absorptions of metal nitride clusterfullerenes (NCFs) in the visible and NIR range are predominantly due to the π - π^* excitations of the carbon cage, which are strongly dependent on the structure and the charge state of the carbon cage. A comparison of the spectra of $\text{Ho}_x\text{Sc}_{3-x}\text{N}@C_{80}$ (I, II; $x=1, 2$) in toluene solution is illustrated in Figure 3.1. The electronic absorption spectra of $\text{Ho}_x\text{Sc}_{3-x}\text{N}@C_{80}$ (I; $x=1, 2$), exhibited intermediate spectral features in comparison with $\text{Ho}_3\text{N}@C_{80}$ (I) and $\text{Sc}_3\text{N}@C_{80}$ (I). $\text{Ho}_2\text{ScN}@C_{80}$ (I) has mainly inherited the characteristic absorption feature of $\text{Ho}_3\text{N}@C_{80}$ (I) with absorption maxima at 667/696 nm, which are slightly red-shifted to 669/698 nm in $\text{Ho}_2\text{ScN}@C_{80}$ (I). Substituting the cluster Ho_2ScN for HoSc_2N led to a further red shift of this doublet to 679/713 nm. In addition, the distinct visible absorption peak observed at 399 nm of $\text{Ho}_3\text{N}@C_{80}$ (I) is shifted to 408 nm in the $\text{Ho}_2\text{ScN}@C_{80}$ (I) and disappeared in $\text{HoSc}_2\text{N}@C_{80}$ (I) and $\text{Sc}_3\text{N}@C_{80}$ (I). Similarly, the shoulder peak of $\text{Ho}_3\text{N}@C_{80}$ (I) at 557 nm and $\text{HoSc}_2\text{N}@C_{80}$ (I) at 562 nm gradually faded in $\text{HoSc}_2\text{N}@C_{80}$ (I) and $\text{Sc}_3\text{N}@C_{80}$ (I). The electronic absorption spectra of $\text{Ho}_x\text{Sc}_{3-x}\text{N}@C_{80}$ (II; $x=0-2$) are consistent with the differences in the absorption spectra of isomers II found for other MMNCFs. Correspondingly, the absorption peak at 712 nm in the spectrum of $\text{Ho}_2\text{ScN}@C_{80}$ (II) is red-shifted to 723 nm for $\text{HoSc}_2\text{N}@C_{80}$ (II), and vanished in $\text{Sc}_3\text{N}@C_{80}$ (II). The shoulder peak at 632 nm in the spectrum of $\text{Ho}_2\text{ScN}@C_{80}$ (II) retained in $\text{HoSc}_2\text{N}@C_{80}$ (II). Similarly to isomer I, the strongest absorption peak in the visible range of $\text{Ho}_2\text{ScN}@C_{80}$ (II) at 457 nm is slightly shifted to 447 nm in the spectrum of $\text{HoSc}_2\text{N}@C_{80}$ (II) and splits into a doublet peak with absorption maxima at 413/472 nm for $\text{Sc}_3\text{N}@C_{80}$ (II). The electronic absorption features of $\text{HoSc}_2\text{N}@C_{80}$ (II) exhibit an intermediate state in comparison with $\text{Ho}_2\text{ScN}@C_{80}$ (II) and $\text{Sc}_3\text{N}@C_{80}$ (II). The similarities and differences in the overall absorption spectrum of $\text{Ho}_x\text{Sc}_{3-x}\text{N}@C_{80}$ (I, II; $x=1, 2$) are comparable to those of $\text{Gd}_x\text{Sc}_{3-x}\text{N}@C_{80}$ (I, II; $x=1, 2$) reported earlier.⁶¹

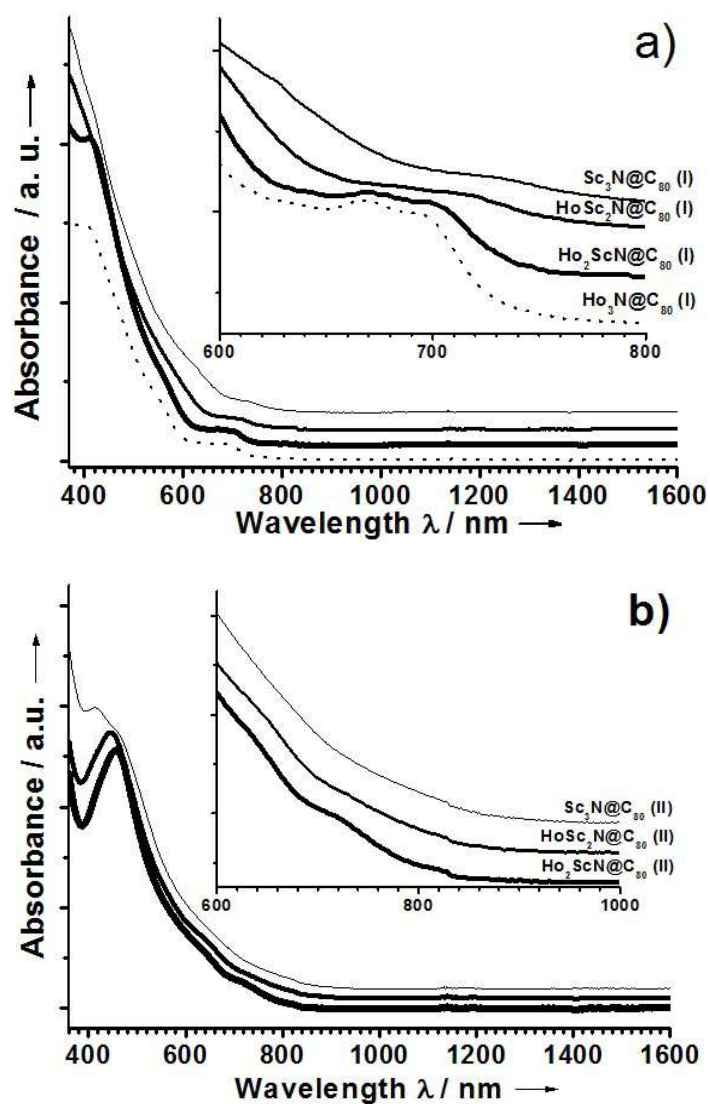


Figure 3.1 UV-vis-NIR spectra of (a) $\text{Ho}_x\text{Sc}_{3-x}\text{N}@C_{80}$ (I; $x=0-3$) and (b) $\text{Ho}_x\text{Sc}_{3-x}\text{N}@C_{80}$ (II; $x=0-2$) in toluene.

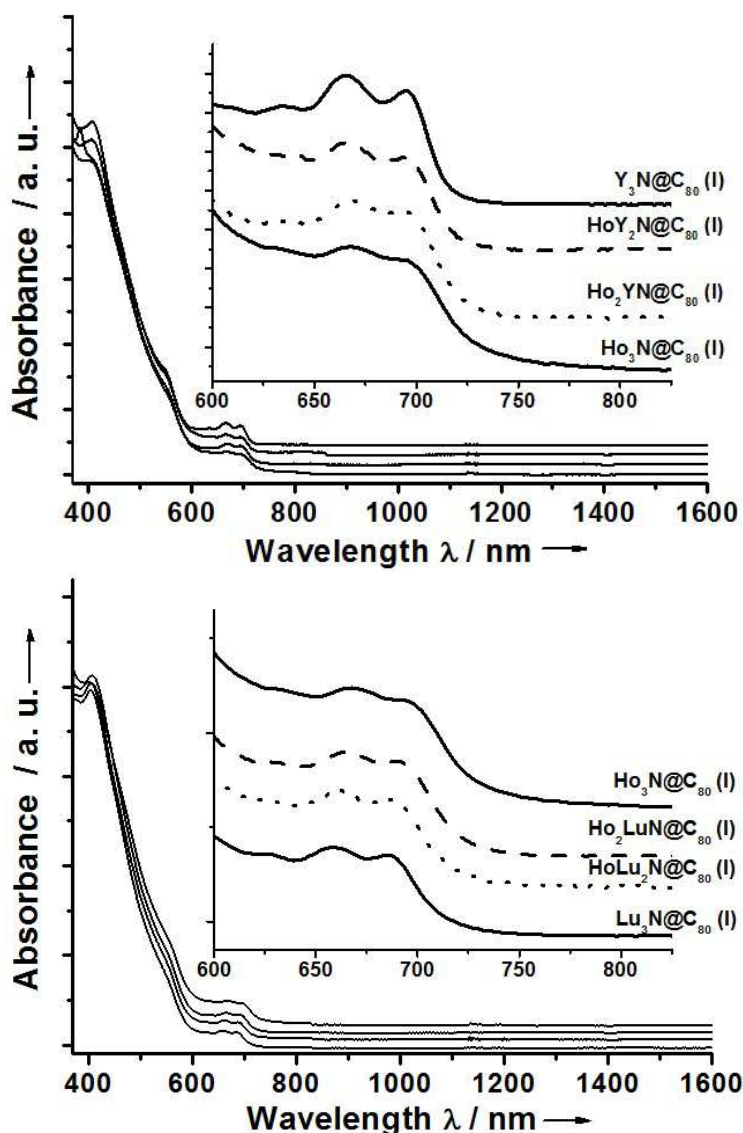


Figure 3.2 UV-vis-NIR spectra of $\text{Ho}_x\text{Y}_{3-x}\text{N}@C_{80}$ (I; $x=0-3$) and $\text{Ho}_x\text{Lu}_{3-x}\text{N}@C_{80}$ (I; $x=0-3$).

The electronic absorption spectra of $\text{Ho}_x\text{Y}_{3-x}\text{N}@C_{80}$ (I; $x=0-3$) and $\text{Ho}_x\text{Lu}_{3-x}\text{N}@C_{80}$ (I; $x=0-3$) are compared in Figure 3.2. Substituting the cluster from Ho_3N to Ho_2YN and HoY_2N do not lead to any significant shift of the doublet at 667/696 nm. However, more pronounced shifts are found in the absorption spectra of $\text{Ho}_x\text{Lu}_{3-x}\text{N}$ (I; $x=0-3$): the characteristic absorption at 659/686 nm in $\text{Lu}_3\text{N}@C_{80}$ (I) is gradually red-shifted to 661/689 nm in $\text{HoLu}_2\text{N}@C_{80}$ (I) and 667/696 nm in $\text{Ho}_2\text{LuN}@C_{80}$ (I), and further to 667/696 nm in $\text{Ho}_3\text{N}@C_{80}$ (I).

In summary, the absorption spectra of $\text{Ho}_x\text{Y}_{3-x}\text{N}@C_{80}$ (I; $x=0-3$) and $\text{Ho}_x\text{Lu}_{3-x}\text{N}@C_{80}$ (I; $x=0-3$) are quite close to each other and to those of $\text{Y}_x\text{Lu}_{3-x}\text{N}@C_{80}$ (I; $x=0-3$).⁶² The close resemblance of their electronic properties could be related to the similarity of Y^{3+} , Ho^{3+} and

Lu^{3+} in terms of their ionic radii, and the HPLC retention behavior of corresponding NCFs previous chapter.

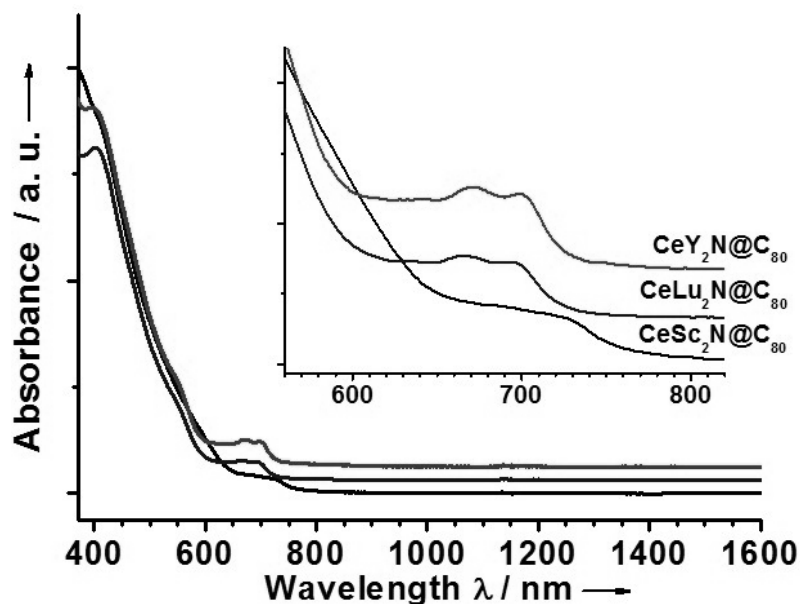


Figure 3.3 UV-Vis-NIR spectra of $\text{CeM}_2\text{N}@C_{80}$ (I; M= Y, Lu and Sc).

A comparison of the spectra of $\text{CeM}_2\text{N}@C_{80}$ (I; M=Y, Lu and Sc) in toluene solution is illustrated (see Figure 3.3). The overall absorption features of $\text{CeM}_2\text{N}@C_{80}$ (I) are quite similar, only with subtle shifts of the bands. Their absorption onset indicated that comparable optical band gaps and could be explained as the resemblance of their electronic properties when preserving Ce atom but substituting two metal atoms from Y to Lu and Sc. $\text{CeY}_2\text{N}@C_{80}$ (I) has the characteristic absorption at 671/699 nm, which are slightly blue-shifted to 666/694 nm in $\text{CeLu}_2\text{N}@C_{80}$ (I), but red-shifted to 684/726 nm in $\text{CeSc}_2\text{N}@C_{80}$ (I).

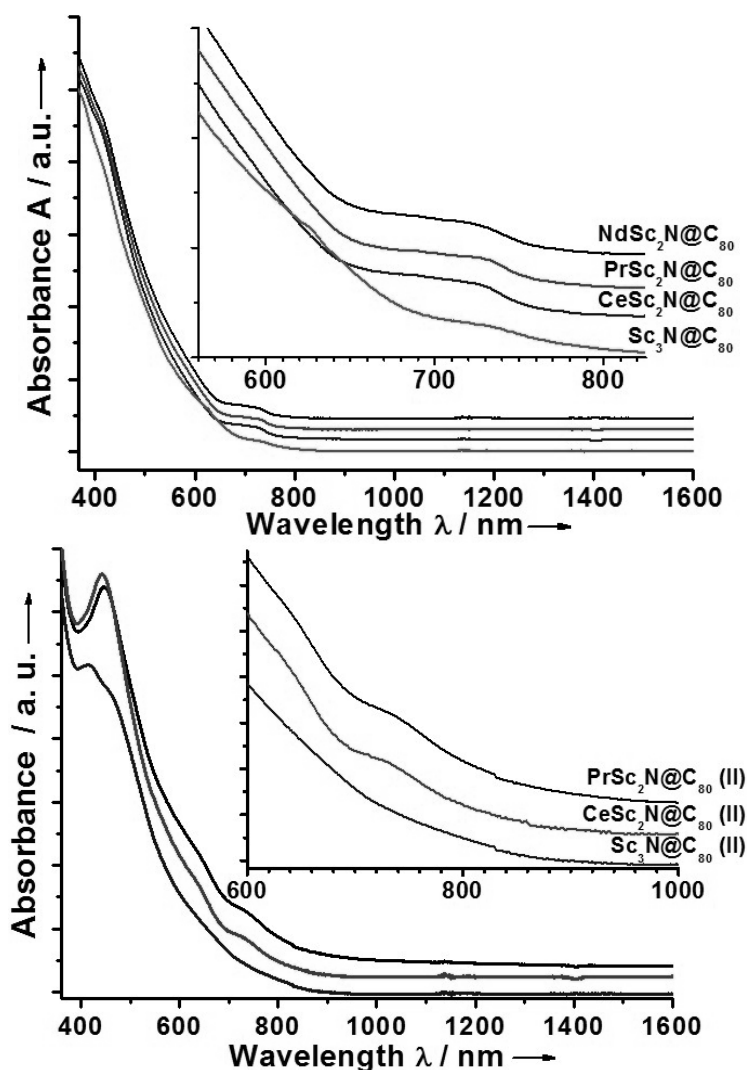


Figure 3.4 UV-Vis-NIR spectra of (up) $\text{MSc}_2\text{N@C}_{80}$ (I; M= Ce, Pr and Nd) and (bottom) $\text{MSc}_2\text{N@C}_{80}$ (I; M= Ce, Pr) which compared with $\text{Sc}_3\text{N@C}_{80}$ (I) and $\text{Sc}_3\text{N@C}_{80}$ (II) respectively.

A comparison of the spectra of $\text{MSc}_2\text{N@C}_{80}$ (I, II; M= Ce, Pr, Nd) and $\text{Sc}_3\text{N@C}_{80}$ (I, II) in toluene solution is illustrated (see Figure 3.4). The overall absorption features of $\text{MSc}_2\text{N@C}_{80}$ are quite similar, only with insignificant shifts of the bands. Their absorption onset indicated that comparable optical band gaps and could be explained as the resemblance of their electronic properties when preserving two Sc atoms but substituting Lanthanide atom from Nd to Pr and Ce. $\text{NdSc}_2\text{N@C}_{80}$ (I) has the characteristic absorption at 718 nm, which are slightly red-shifted to 724 nm in $\text{PrSc}_2\text{N@C}_{80}$ (I) and further to 728 nm in $\text{CeSc}_2\text{N@C}_{80}$ (I). According to former studies on the homogeneous metal NCFs $\text{M}_3\text{N@C}_{80}$ (I; M= Pr, Nd, Gd, Tb, Dy, Ho, Er, Tm, Lu and Y), the electronic absorption property of $\text{M}_3\text{N@C}_{80}$ fairly depends on the size of the encaged cluster. The electronic spectra of $\text{PrSc}_2\text{N@C}_{80}$, agree well with other $\text{MSc}_2\text{N@C}_{80}$ structures (I; M= Ce, Nd, Gd, Tb, Dy, Er, Lu and Y).⁶³ Because their

electronic spectra are dominated by the C₈₀ (I) cage and the insignificant shifts causing by changing the MSc₂N cluster which is dominated by the corresponding lanthanide metal ions. Figure 3.4 (bottom) shows that electronic absorption spectra of MSc₂N@C₈₀ (II) is different from its isomer (I), which agrees well with the differences in the absorption spectra of isomers I and II of M₃N@C₈₀ (M= Sc, Lu, Y). Substituting one Sc atom with Ce or Pr, the significant change of the electronic absorption could be observed. Firstly, the strongest absorption peak in the spectrum of PrSc₂N@C₈₀ (II) is found to blue-shift from 446 nm to 442 nm in CeSc₂N@C₈₀ (II). Secondly, the shoulder peak around 725 nm in the spectrum of PrSc₂N@C₈₀ (II) remains almost unchanged in CeSc₂N@C₈₀ (II), but becomes undetectable in Sc₃N@C₈₀ (II).

In Figure 3.5, a comparison of the -Vis-NIR spectra of Ce_xY_{3-x}N@C_{2n} (x= 0-2; 2n= 84, 86 and 88) in toluene solution is demonstrated. Previous studies demonstrated the reliability of UV-Vis-NIR for the characterization of endohedral fullerenes. The UV/Vis/NIR spectra of Dy₃N@C_{2n} (2n= 78-88) compounds have been reported by our group previously.⁶⁵ The optical band-gap of the Dy₃N@C_{2n} could be classified into two ranges depending on the cage size of fullerenes. As above-mentioned, no Ce-based MMNCFs has been isolated and characterized in the carbon cage from C₈₄ to C₈₈ so far.⁶⁶ In general, the spectra of Ce-based MMNCFs are comparable to the M₃N@C_{2n} (2n= 84-88) for each cage which indicates the identical cage symmetry and similar electronic structure. Substituting the encaged cluster from Y₃N to CeY₂N in the C₈₄ cage, the strongest visible absorption peak of CeY₂N@C₈₄ is 622 nm, which is exactly identical to Y₃N@C₈₄. Such an absorption feature agrees well with reported structures including Gd₃N@C₈₄, Dy₃N@C₈₄ and Tm₃N@C₈₄. CeY₂N@C₈₆ presents reasonable correspondence to the spectra of Y₃N@C₈₆. There is a marginal difference between the characteristic absorption peak at 636 nm in Y₃N@C₈₆ and at 633 nm CeY₂N@C₈₆. The absorption peaks of Y₃N@C₈₈ at 727/975/1034 nm slightly shift to 747/972/1039 nm in CeY₂N@C₈₈ and 755/975/1046 nm in Ce₂YN@C₈₈. This suggests that the resemblance of their electronic structures among Y₃N@C₈₈, CeY₂N@C₈₈ and Ce₂YN@C₈₈.

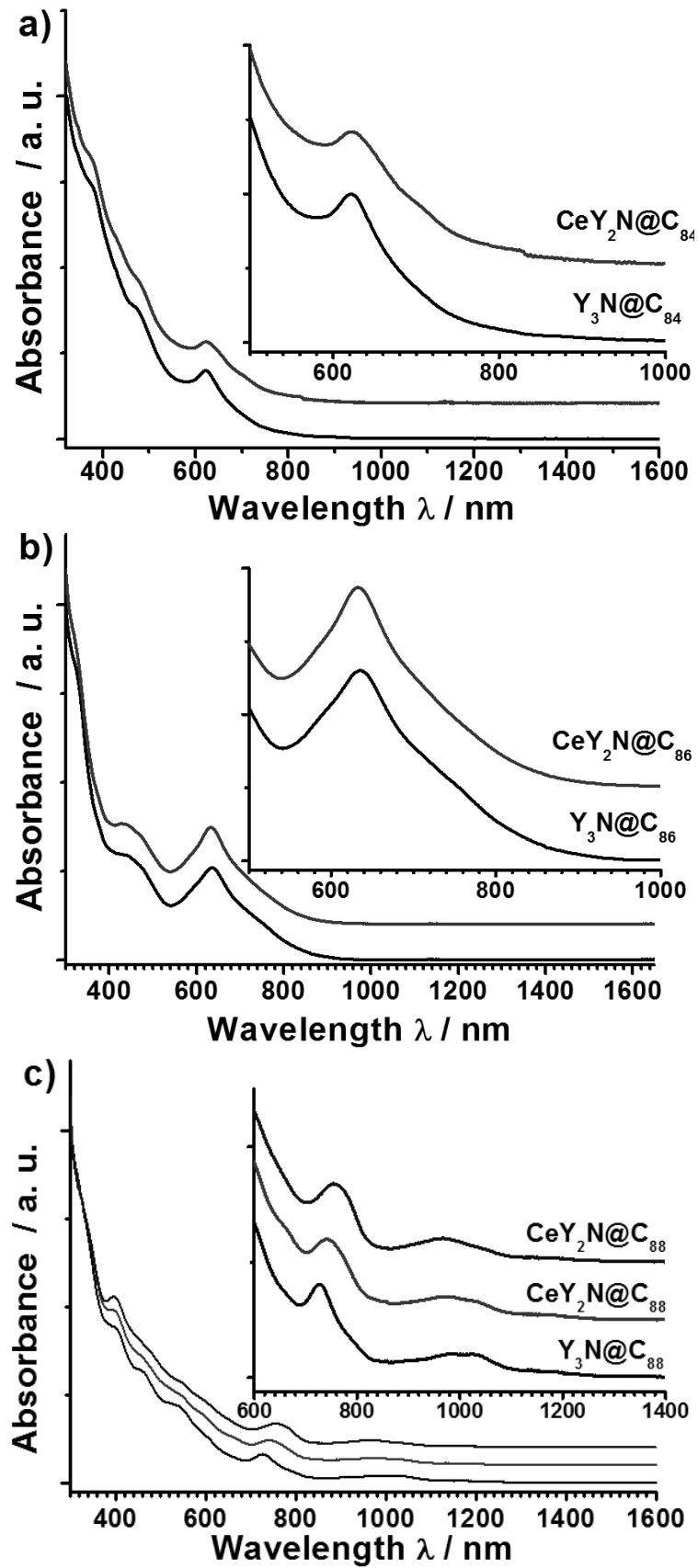


Figure 3.5 UV-Vis-NIR spectra of $\text{Ce}_x\text{Y}_{3-x}\text{N@C}_{2n}$ ($x=0-2$; $2n=84, 86$ and 88).

3.2 Vibrational spectroscopy of MMNCFs

3.2.1 FTIR Vibrational Spectroscopic study of MMNCFs

Vibrational spectroscopy is a useful tool to analyze the structure of fullerenes due to its high structural sensitivity and its higher time resolution as compared to NMR spectroscopy.^{29,35,37,67} The FTIR spectra of $\text{Ho}_x\text{Sc}_{3-x}\text{N}@C_{80}$ (I, II; $x=0-3$) compared in Figure 3.6 show a clear similarity of the tangential cage modes ($800 - 1600 \text{ cm}^{-1}$) and radial cage modes ($400 - 600 \text{ cm}^{-1}$) within each group of MMNCFs with the same cage isomer. The spectra of the MMNCFs (isomer I) are also virtually identical to those of other $\text{M}_3\text{N}@C_{80}$ structures (I; $\text{M} = \text{Sc}, \text{Y}, \text{Gd}, \text{Tb}, \text{Dy}, \text{Ho}, \text{Er}, \text{Tm}$). This result enables us to assign the cage isomer, $C_{80}\text{-}I_h(7)$ to all structures of isomer I. Likewise, cage modes in the spectra of $\text{Ho}_x\text{Sc}_{3-x}\text{N}@C_{80}$ (II; $x=1, 2$) are very similar to those of $\text{Gd}_x\text{Sc}_{3-x}\text{N}@C_{80}$ (II; $x=1, 2$) and $\text{Lu}_x\text{Sc}_{3-x}\text{N}@C_{80}$ (II; $x=1, 2$) with $D_{5h}(6)$ carbon cage.

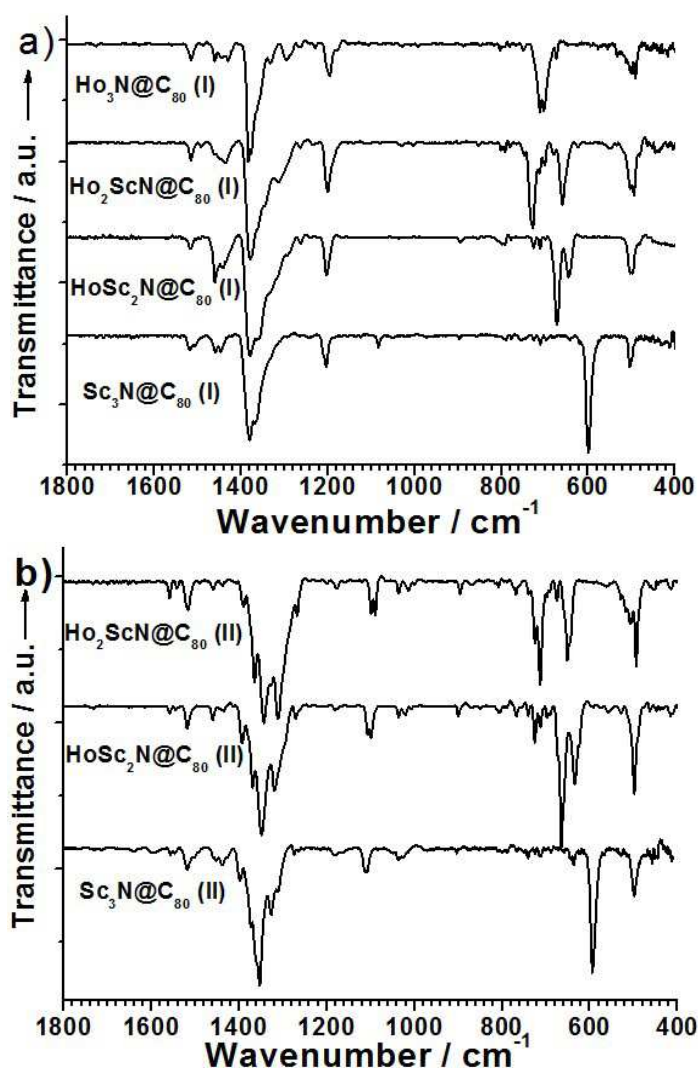


Figure 3.6 FTIR spectra of (a) $\text{Ho}_x\text{Sc}_{3-x}\text{N}@C_{80}$ (I; $x=0-3$) and (b) $\text{Ho}_x\text{Sc}_{3-x}\text{N}@C_{80}$ (II; $x=0-2$).

Figure 3.5 displays that the antisymmetric metal-nitrogen stretching vibrational modes of $\text{Ho}_x\text{Sc}_{3-x}\text{N}@C_{80}$ (I, II; $x=0-3$), which are assigned to the most intense low-energy IR lines in the $600 - 800 \text{ cm}^{-1}$ range and which are sensitively dependent on the composition of the encaged $\text{Ho}_x\text{Sc}_{3-x}\text{N}$ cluster. For $\text{Ho}_x\text{Sc}_{3-x}\text{N}@C_{80}$ (I; $x=0-3$), the anti-symmetric M–N stretching vibrational mode ($\nu_{\text{M-N}}$), which is two-fold degenerate for a homogeneous cluster (at 599 cm^{-1} in $\text{Sc}_3\text{N}@C_{80}$ (I) and around 710 cm^{-1} in $\text{Ho}_3\text{N}@C_{80}$ (I)), was found to be split for the $\text{Ho}_x\text{Sc}_{3-x}\text{N}$ clusters (645 and 673 cm^{-1} for $\text{HoSc}_2\text{N}@C_{80}$, 660 and 728 cm^{-1} for $\text{Ho}_2\text{ScN}@C_{80}$) (Figure 3.6a). Our recent reports on the analysis of vibrational spectra of the MMNCFs combined with DFT calculations have shown that the geometry parameters of the nitride cluster are strongly influenced by the ionic radii of the metal atoms. In particular, an inherent strain of all non-Sc $\text{M}_3\text{N}@C_{80}$ caused by the limited space inside the carbon cage become appreciably released when the metal atoms is replaced by one or two Sc atoms with smaller ionic radius. As a result, substitution of Ho atoms by Sc results in the synchronous elongation of the Ho-N bonds and shortening of the Sc-N bonds (in comparison to $\text{Ho}_3\text{N}@C_{80}$ and $\text{Sc}_3\text{N}@C_{80}$). With the variation of the cluster composition, the $\nu_{\text{Sc-N}}$ shifts from 599 cm^{-1} in $\text{Sc}_3\text{N}@C_{80}$ (I) to 673 cm^{-1} in $\text{HoSc}_2\text{N}@C_{80}$ (I) and to 728 cm^{-1} in $\text{Ho}_2\text{ScN}@C_{80}$ (I). When the Sc_3N cluster is replaced by the $\text{Ho}_x\text{Sc}_{3-x}\text{N}$ cluster within $C_{80}:D_{5h}$, the M-N stretching vibrational modes have a similar splitting (see Figure 3.6 b).

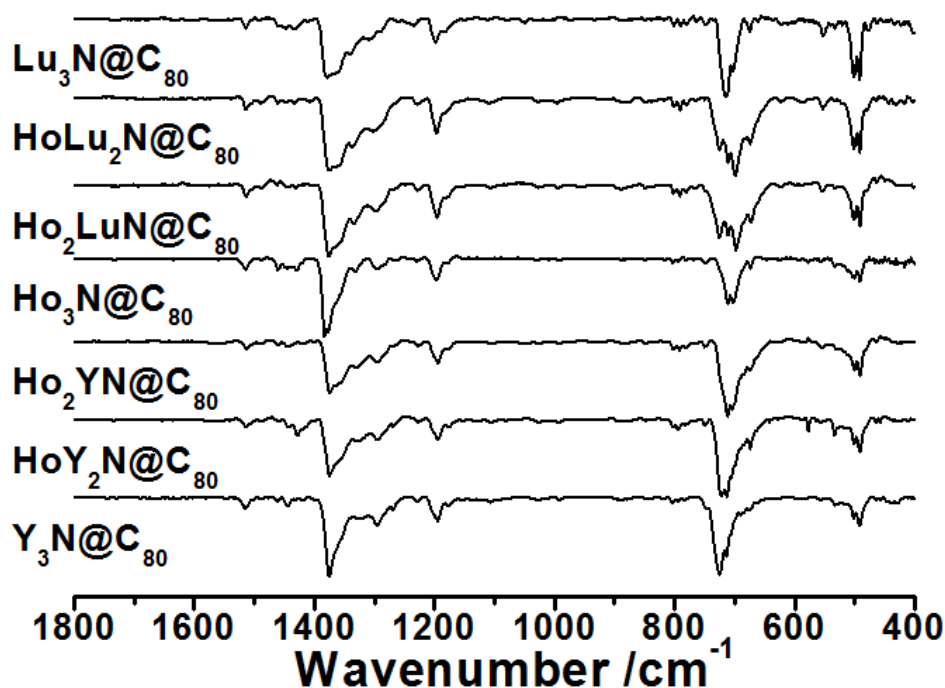


Figure 3.7 The FTIR spectra of (a) $\text{Ho}_x\text{Y}_{3-x}\text{N}@C_{80}$ and $\text{Ho}_x\text{Lu}_{3-x}\text{N}@C_{80}$ (I; $x=0-3$).

The FTIR spectra of $\text{Ho}_x\text{Y}_{3-x}\text{N}@C_{80}$ and $\text{Ho}_x\text{Lu}_{3-x}\text{N}@C_{80}$ (I; $x=1, 2$) are compared with $\text{M}_3\text{N}@C_{80}$ (I; M= Ho, Y and Lu) in Figure 3.7. Their tangential and radial cage vibrational

modes are virtually identical to those of other $M_3N@C_{80}$ structures (I; $M= Y, Lu, Ho, Dy, Gd$ and Tm) which allow us to assign the same cage isomer ($C_{80:I_h}$). But in contrast to $Ho_xSc_{3-x}N@C_{80}$ (I; $x= 1, 2$), no considerable splitting of antisymmetric M-N stretching vibrational modes has been observed in $Ho_xY_{3-x}N@C_{80}$ or $Ho_xLu_{3-x}N@C_{80}$ (I; $x= 1, 2$) due to similar ionic radii of Lu^{3+} (0.85 Å), Ho^{3+} (0.90 Å) and Y^{3+} (0.90 Å).⁶² Switching the encaged cluster from Lu_3N to Ho_3N , and further to Y_3N results in the change of ν_{M-N} from 703/715 cm^{-1} in $Lu_3N@C_{80}$ (I) to 703/712 cm^{-1} in $Ho_3N@C_{80}$ (I), and further to 714/725 cm^{-1} in $Y_3N@C_{80}$ (I). X-ray single crystal studies have shown that Lu_3N cluster is planar in $Lu_3N@C_{80}$ (I) and Y_3N cluster is slightly pyramidal in $Y_3N@C_{80}$ (I) (the N being 0.083 Å displaced out of Y_3 plane). Theoretical calculation predicted that Ho_3N is still a planar structure inside the carbon cage. The magnitude of the splitting of antisymmetric M-N stretching vibrational modes of $Ho_xLu_{3-x}N@C_{80}$ (I) is larger than in the case of $Ho_xY_{3-x}N@C_{80}$ (I) which could be understood as the ionic radii difference between $Ho^{3+}-Lu^{3+}$ and $Ho^{3+}-Y^{3+}$. FTIR analysis demonstrated marginal shifts caused by shrinking of the encaged nitride cluster, that is, in the order of $Y_3N@C_{80} \rightarrow HoY_2N@C_{80} \rightarrow Ho_2YN@C_{80} \rightarrow Ho_3N@C_{80} \rightarrow Ho_2LuN@C_{80} \rightarrow HoLu_2N@C_{80} \rightarrow Lu_3N@C_{80}$. The M-N stretching frequency is correlated with the structure of M_3N , which is dependent on the cluster size and/or the radius of metal ions as discussed above. However, it is impossible to distinguish ν_{Ho-N} , ν_{Y-N} and ν_{Lu-N} from each other according to the abovementioned data.

$M_3N@C_{80}$	ν_{M-N} / cm^{-1}
$Y_3N@C_{80}$	715, 725
$HoY_2N@C_{80}$	713, 722
$Ho_2YN@C_{80}$	704, 712
$Ho_3N@C_{80}$	703, 712
$Ho_2LuN@C_{80}$	673, 698, 715, 725
$HoLu_2N@C_{80}$	674, 699, 711, 725
$Lu_3N@C_{80}$	703, 715

Table 3.1 Characteristic antisymmetric metal-nitrogen vibrational modes of Ho-based MMNCFs.

The FTIR spectra of the isomer I of $M_2ScN@C_{80}$ ($M= Gd, Dy, Ho, Lu$ and Sc) is presented in the Figure 3.8a. As stated, ν_{M-N} is generally split in $M_xSc_{3-x}N@C_{80}$ ($x= 1, 2$), the high-frequency vibrational mode has been definitively assigned to ν_{Sc-N} . By considering the ionic

radius of the Lanthanide metal Ln^{3+} (Ce^{3+} : 1.03 Å, Pr^{3+} : 1.01 Å, Nd^{3+} : 0.995 Å, Gd^{3+} : 0.94 Å, Tb^{3+} : 0.92 Å, Dy^{3+} : 0.91 Å, Ho^{3+} : 0.90 Å, Er^{3+} : 0.88 Å, Lu^{3+} : 0.85 Å; Sc^{3+} : 0.75 Å), our results agree well with the previous studies of $\text{Gd}_2\text{ScN@C}_{80}$ (I) and $\text{Dy}_2\text{ScN@C}_{80}$ (I), and $\text{Lu}_2\text{ScN@C}_{80}$ (I). For $\text{M}_2\text{ScN@C}_{80}$ (I), $\nu_{\text{Sc-N}}$ steadily increases from 599 cm^{-1} in $\text{Sc}_3\text{N@C}_{80}$ (I) to 710 cm^{-1} (M= Lu), 725 cm^{-1} (Er), 728 cm^{-1} (Ho), 737 cm^{-1} (Dy), 749 cm^{-1} (Tb), 759 cm^{-1} (Gd) and 769 cm^{-1} (Nd). Meanwhile, $\nu_{\text{Ln-N}}$ gradually decreases from 668 cm^{-1} in $\text{Lu}_2\text{ScN@C}_{80}$ (I) to 661 cm^{-1} (M= Er and Ho), and further to 737 cm^{-1} (Dy), 659 cm^{-1} (Dy), 658 cm^{-1} (Tb), 649 cm^{-1} (Gd) and 598 cm^{-1} (Nd). The magnitude of the splitting of antisymmetric M-N stretching vibrational modes of $\text{M}_2\text{ScN@C}_{80}$ ($\Delta\nu = \nu_{\text{Sc-N}} - \nu_{\text{Ln-N}}$) became remarkable since the metal ionic radii difference between the encaged Sc and Lanthanide metal in the order of Lu, Er, Ho, Dy, Tb, Gd and Nd), see Figure 3.8b.

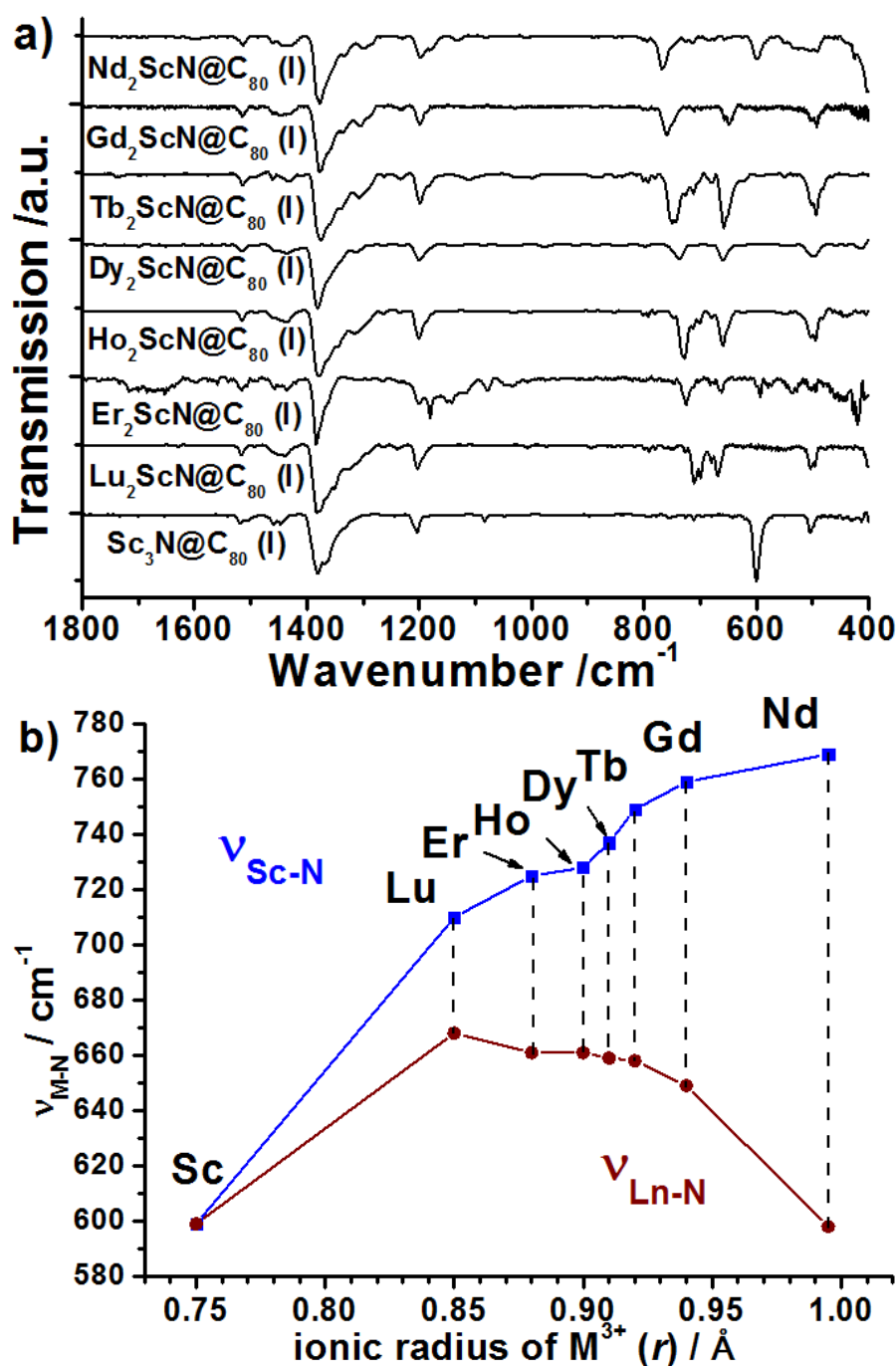


Figure 3.8 FTIR spectra of (a) Ln₂ScN@C₈₀(I; Ln = Nd, Gd, Tb, Dy, Ho, Er and Lu) and Sc₃N@C₈₀(I); (b) the dependence of ν_{Sc-N} and ν_{Ln-N} of Ln₂ScN@C₈₀ on the ionic radius (r) of the encaged Lanthanide metal.

In contrast to the Ln₂ScN@C₈₀(I), in the series of LnSc₂N@C₈₀(I) the shifts including ν_{Sc-N} and ν_{Ln-N} are less pronounced: a) ν_{Sc-N} of LuSc₂N@C₈₀(I) (652 cm⁻¹) shifts to 667 cm⁻¹ (Er), 672 cm⁻¹ (Ho), 678 cm⁻¹ (Dy), 684 cm⁻¹ (Tb), 694 cm⁻¹ (Gd), 715 cm⁻¹ (Nd) to 718 cm⁻¹ (Pr) and 728 cm⁻¹ (Ce), see Figure 3.9a. The good linear correlation between the frequency and ionic radius is observed for the data points from Lu to Ce for LnSc₂N@C₈₀(I) (Figure 3.9b); b) ν_{Ln-N} of LuSc₂N@C₈₀(I) (652 cm⁻¹) shifts to 647 cm⁻¹ (Er), 645 cm⁻¹ (Ho), 647 cm⁻¹ (Dy, Tb

and Gd), 637 cm^{-1} (Nd) to 639 cm^{-1} (Pr) and further to 644 cm^{-1} (Ce). Noticeably, the $\nu_{\text{Sc-N}}$ increases in the order of lanthanide metal ionic radius from Lu (0.85 \AA) to Ce (1.03 \AA). However, the changes of $\nu_{\text{Ln-N}}$ fluctuate in the range from 652 cm^{-1} to 637 cm^{-1} .

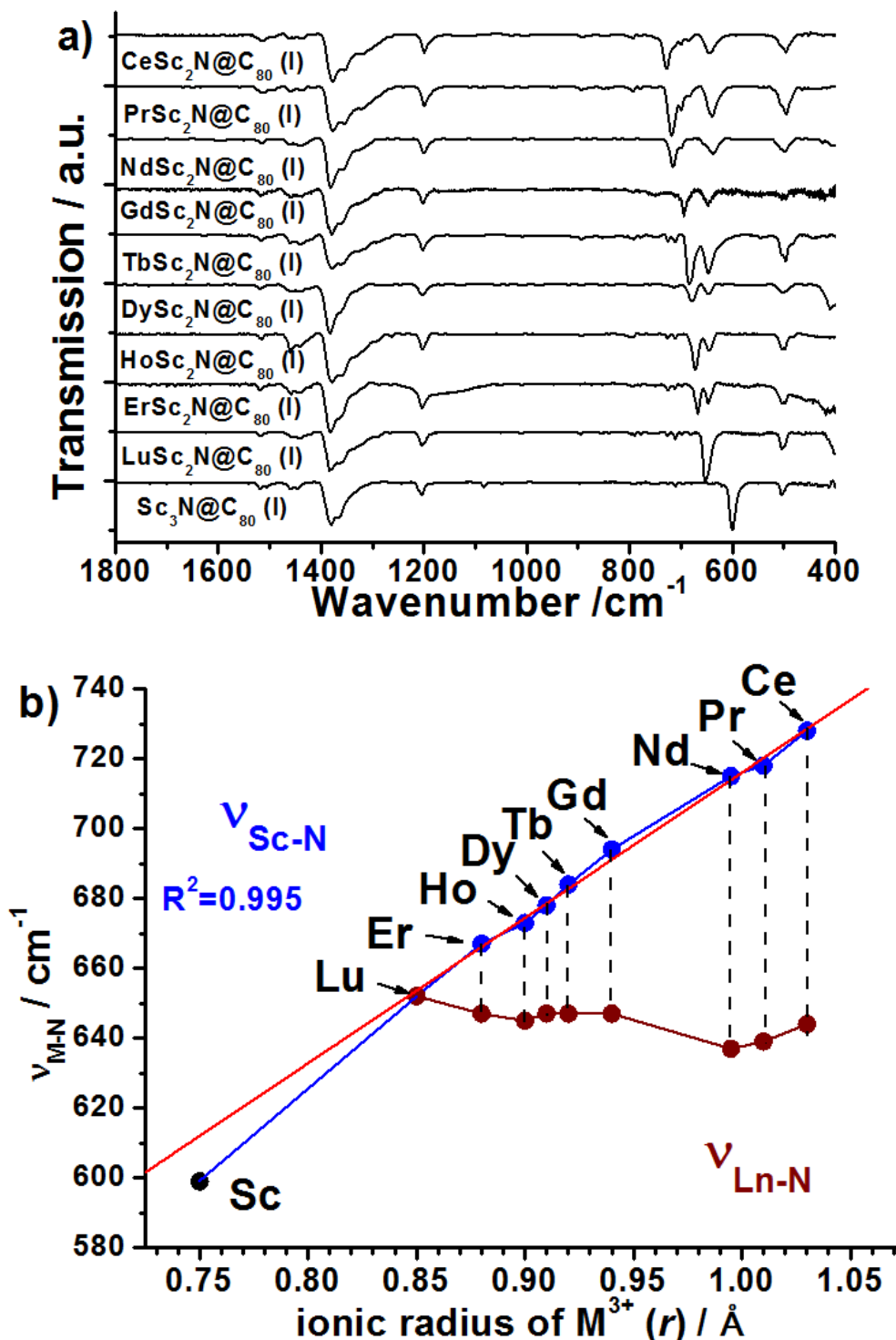


Figure 3.9 FTIR spectra of (a) $\text{LnSc}_2\text{N@C}_{80}$ (I; Ln= Ce, Pr, Nd, Gd, Tb, Dy, Ho, Er and Lu) and $\text{Sc}_3\text{N@C}_{80}$ (I); (b) the dependence of $\nu_{\text{Sc-N}}$ and $\nu_{\text{Ln-N}}$ of $\text{LnSc}_2\text{N@C}_{80}$ on the ionic radius (r) of the engaged Lanthanide metal.

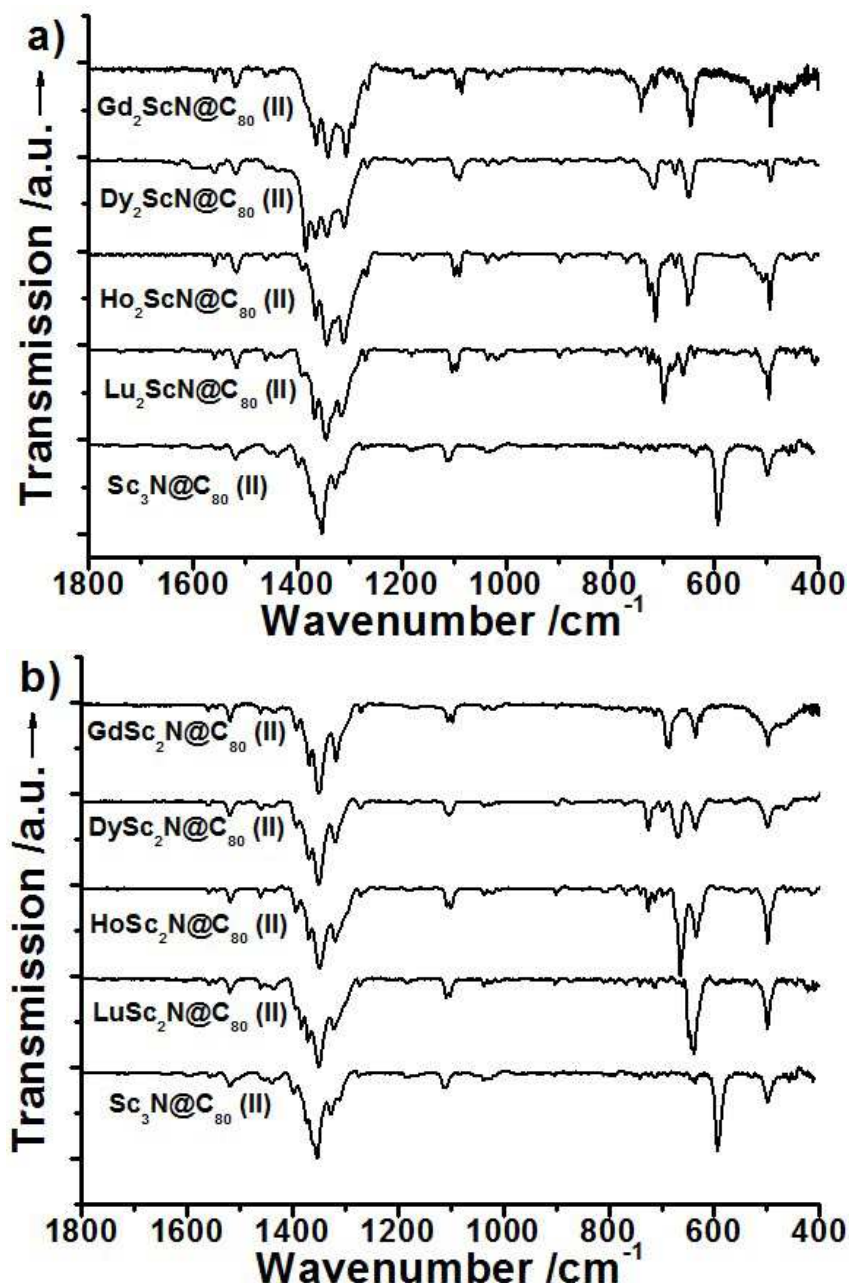


Figure 3.10 FTIR spectra of MSc₂N@C₈₀ (a) and M₂ScN@C₈₀ (b) (II; M= Gd, Dy, Ho and Lu; x= 1, 2) compared with Sc₃N@C₈₀ (II).

Due to the relatively low yield and complicated process of purification, only several structures of isomer II M_xSc_{3-x}N@C₈₀ have been obtained. Comparison of the FTIR spectra for those M₂ScN@C₈₀ and MSc₂N@C₈₀ (M= Gd, Dy, Ho and Lu; x= 1, 2) is demonstrated in Figure 3.10. For M₂ScN@C₈₀ (II), $\nu_{\text{Sc-N}}$ increases from 594 cm⁻¹ in Sc₃N@C₈₀ (II) to 697 cm⁻¹ (Lu), 714 cm⁻¹ (Ho), 716 cm⁻¹ (Dy), and 741 cm⁻¹ (Gd). Similar to the MSc₂N@C₈₀ (I), $\nu_{\text{Ln-N}}$ declines from 661 cm⁻¹ (Lu) to 651 cm⁻¹ (Ho), 650 cm⁻¹ (Dy) and 646 cm⁻¹ (Gd). Switching the cage symmetry of C₈₀ from I to II results in that FTIR spectra of MSc₂N@C₈₀ (II) demonstrates less prominent shifts, $\nu_{\text{Sc-N}}$ of Sc₃N@C₈₀ (II) (594 cm⁻¹) shifts to 649 cm⁻¹ (Lu),

665 cm^{-1} (Ho), 669 cm^{-1} (Dy) and 685 cm^{-1} (Gd). Since the radius of Ho^{3+} is somewhat smaller than that of Gd^{3+} and Dy^{3+} , the fluctuations of $\nu_{\text{Sc-N}}$ induced by encaged Ho atom(s) are less prominent than those for Gd and Dy but larger than Lu. As discussed above, the splitting of $\nu_{\text{M-N}}$ is considerably dependent on two factors: the composition of the encaged cluster (M_2ScN or MSc_2N) and the symmetry of carbon cage (I_h or D_{5h}). It could be summarized that: (a) for carbon cage with the same symmetry (I_h or D_{5h}), the splitting of $\nu_{\text{M-N}}$ in $\text{M}_2\text{ScN}@C_{80}$ is stronger than in $\text{MSc}_2\text{N}@C_{80}$; (b) for $\text{Ln}_2\text{ScN}@C_{80}$ and $\text{LnSc}_2\text{N}@C_{80}$, the splitting of $\nu_{\text{M-N}}$ in $\text{Ln}_2\text{ScN}@C_{80}$ is stronger than in $\text{LnSc}_2\text{N}@C_{80}$ due to the change of cage symmetry; (c) the good linearity based on $\nu_{\text{Sc-N}}$ from Lu to Ce for $\text{LnSc}_2\text{N}@C_{80}$ (I) could be obtained (R^2 is 0.995) and (d) for the encaged metal with similar metal ionic radii (e.g. Ho^{3+} and Y^{3+}), it is difficult to distinguish $\nu_{\text{M-N}}$ modes.

3.2.2 Raman Spectroscopic study of MMNCFs

The Raman spectra of nitride cluster fullerenes commonly consist of four regions: the tangential C_{80} modes in the range of 1000 - 1600 cm^{-1} ; a gaplike region from 815 to 1000 cm^{-1} , the radial breathing cage modes between 200 and 815 cm^{-1} , and the low-energy metal cage modes below 200 cm^{-1} .⁶⁸ A detailed analysis of low-energy metal cage modes is shown below, which give us more information on the structure of the cluster and cluster-cage interaction.

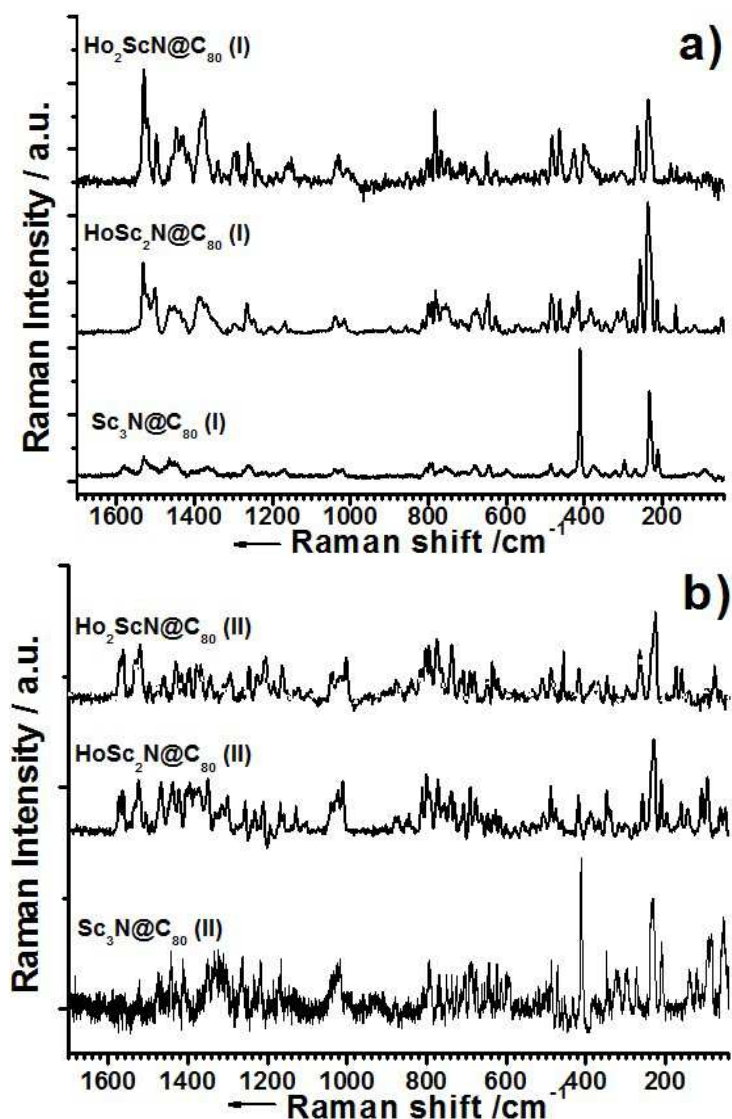


Figure 3.11 Raman spectra of (a) $\text{Ho}_x\text{Sc}_{3-x}\text{N@C}_{80}$ (I; $x=0-2$) and (b) $\text{Ho}_x\text{Sc}_{3-x}\text{N@C}_{80}$ (II; $x=0-2$) measured at 120 K and with the laser wavelength of 647 nm.

A comparison of the Raman spectra of $\text{Ho}_x\text{Sc}_{3-x}\text{N@C}_{80}$ (I, II; $x=0-2$) is presented in the Figure 3.11. Similar to the IR spectra, spectral patterns of the $\text{Ho}_x\text{Sc}_{3-x}\text{N@C}_{80}$ MMNCFs with the same carbon cage are rather similar and are considerably different when two cage isomers of the same cluster composition are compared with each other. Some differences in the relative intensity of the Raman bands could be ascribed to the different resonance effects of the specific structures. To investigate the interaction between the $\text{Ho}_x\text{Sc}_{3-x}\text{N}$ cluster and the C_{80} cage, the low-energy part of the vibrational pattern in the Raman spectrum was studied as well, due to its correlation to the bond formation between the nitride cluster and carbon cage. The low-energy part of the Raman spectra of $\text{Ho}_x\text{Sc}_{3-x}\text{N@C}_{80}$ (I, II; $x=0-2$) observed at 120 K with the laser wavelength of 647 nm consisted of the radial C_{80} cage modes and of cluster-based modes ranging from 220 to 40 cm^{-1} (Figure 3.12). The cluster-based modes included

the in-plane cluster deformation mode and the frustrated translations and rotations of the nitride cluster, which provided critical information on the interaction between the entrapped nitride cluster and the C₈₀ cage. As shown in our earlier report on the Raman/DFT study on the Gd_xSc_{3-x}N@C₈₀, the medium-intensity Raman lines of Sc₃N@C₈₀ (I) at 210 cm⁻¹ referred to the frustrated in-plane cluster translation with a partial contribution from the in-plane M₃N deformation. The two-fold degenerate mode of the homogeneous Sc₃N cluster is split into two components for the HoSc₂N and Ho₂ScN mixed cluster similar to the antisymmetric M-N modes in the IR spectra (this mode is also two-degenerate in the homogeneous nitride clusterfullerenes). In the Raman spectrum of the isomer I, two lines at 213/166 cm⁻¹ for HoSc₂N@C₈₀ and at 178/162 cm⁻¹ for Ho₂ScN@C₈₀ are assigned to this kind of vibrations. Compared to isomer I, the subtle shifts of lines for isomer II of Ho_xSc_{3-x}N@C₈₀ could be determined, 211/160 cm⁻¹ for the HoSc₂N@C₈₀ and 173/159 cm⁻¹ for Ho₂ScN@C₈₀, due to the alteration of the cage symmetry. Based on experimental and earlier theoretical studies, the difference between the Gd_xSc_{3-x}N@C₈₀ and Ho_xSc_{3-x}N@C₈₀ ($x= 1, 2$), could be explained by the increasing mass of the metal cluster and the decreasing cluster-cage force constants.

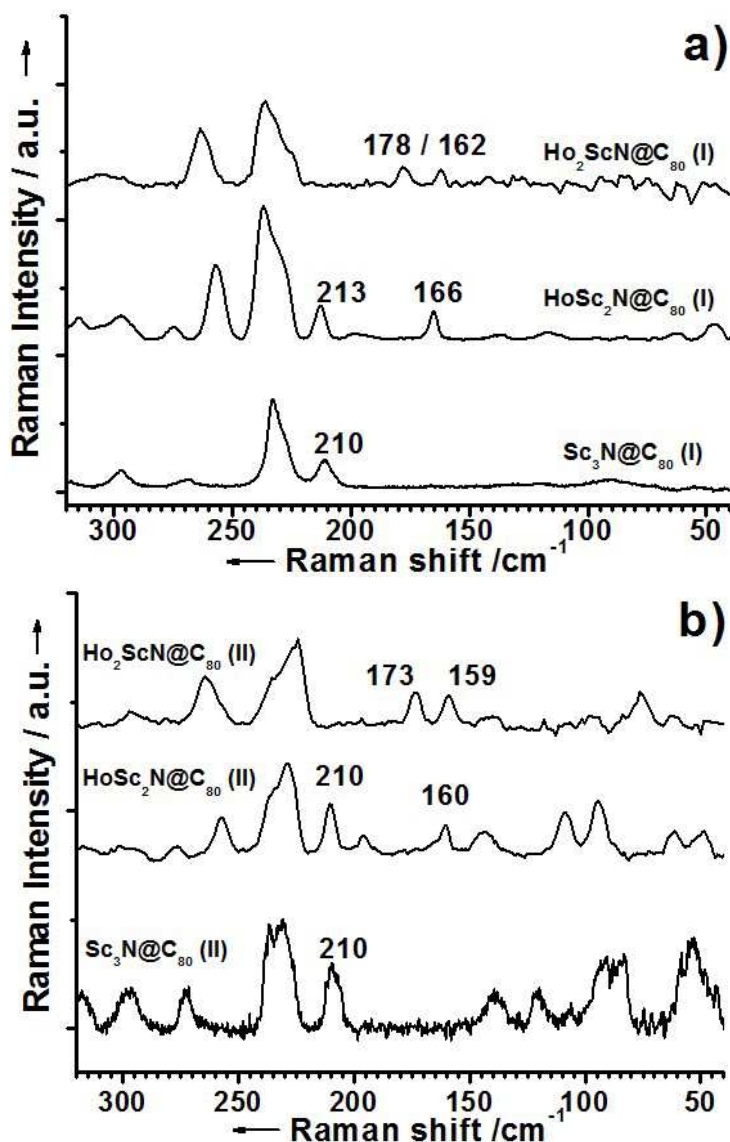


Figure 3.12 The low-energy Raman spectra of $\text{Ho}_x\text{Sc}_{3-x}\text{N}@C_{80}$ (I, II; $x=0-2$) measured at 120 K and with the laser wavelength of 647 nm.

The low-energy Raman spectrum of $\text{Ho}_x\text{Lu}_{3-x}\text{N}@C_{80}$ (I; $x=1, 2$) are compared with $\text{Ho}_3\text{N}@C_{80}$ (I), see Figure 3.13a. Comparable to their FTIR spectra, the metal-cage stretching vibrational modes of HoLu_2N and Ho_2LuN do not lead to any significant splitting and behave as the mode of homogeneous Ho_3N cluster (160 cm^{-1}). In the contrary, the metal-cage vibrational mode of $\text{Ho}_x\text{Y}_{3-x}\text{N}$ (I; $x=1, 2$) is split into two components for the HoY_2N and Ho_2YN mixed cluster, although these two clusterfullerenes are almost undistinguishable in their FTIR spectra. In Figure 3.12b, two peaks at $196/170\text{ cm}^{-1}$ for $\text{HoY}_2\text{N}@C_{80}$ and at $181/163\text{ cm}^{-1}$ for $\text{Ho}_2\text{YN}@C_{80}$ are assigned to this kind of vibrations. It is reasonable that for $\text{Ho}_x\text{Lu}_{3-x}\text{N}@C_{80}$ ($x=1, 2$) structures could not be effectively distinguished from both the FTIR and the low-energy Raman spectra due to the similarity of both the ionic radii and mass of Ho and Lu.

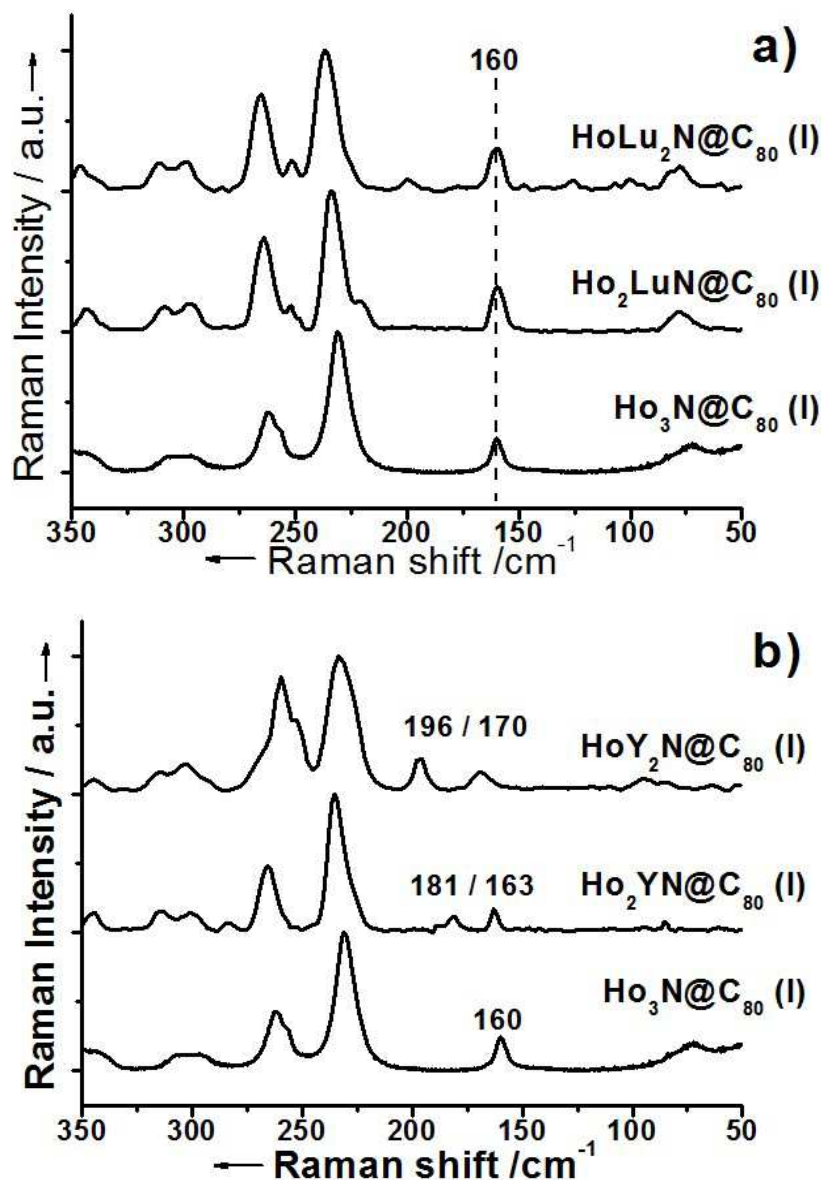


Figure 3.13 The low-energy Raman spectra of (a) $\text{Ho}_x\text{Lu}_{3-x}\text{N}@C_{80}$ (I; $x=1-3$) and (b) $\text{Ho}_x\text{Y}_{3-x}\text{N}@C_{80}$ (I; $x=1-3$) were obtained at 120 K and with the laser wavelength of 647 nm.

3.3 NMR spectroscopy of Ln-based MMNCFs

In the present state of the NCFs knowledge, ^{13}C NMR spectra could be regarded as a definitive proof for determining the symmetry of the carbon cage. The studies of Cerium-based MMNCFs ($\text{CeSc}_2\text{N@C}_{80}$ and $\text{CeLu}_2\text{N@C}_{80}$) showed that even the single 4f-electron on the Ce atom induces considerable paramagnetic chemical shift and broadening of the ^{13}C NMR lines.^{52,54} Similar effects were observed in numerous ^{13}C NMR studies of Ce-based mono-⁵⁰ and dimetallofullerenes^{50,53,69-72} and their derivatives.^{73,74} To our knowledge, the only paramagnetic ^{13}C NMR studies of non-Ce lanthanide metallofullerenes were reported for three isomers of Tm@C_{82} ⁷⁵ and for the Pr@C_{82}^- anion.^{76,77} The influence of multiple 4f-electrons on the carbon cage is still unresolved question which requires further study.

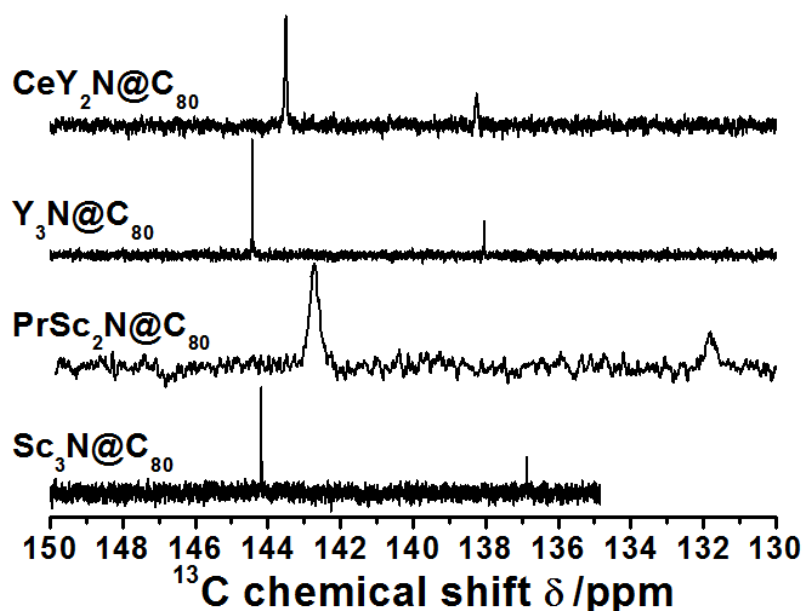


Figure 3.14 ^{13}C NMR spectra of $\text{CeY}_2\text{N@C}_{80}$ (I), $\text{PrSc}_2\text{N@C}_{80}$ (I), $\text{Y}_3\text{N@C}_{80}$ (I) and $\text{Sc}_3\text{N@C}_{80}$ (I) respectively at 298 K.

The 125 MHz ^{13}C NMR spectra of $\text{CeY}_2\text{N@C}_{80}$ (I) and $\text{PrSc}_2\text{N@C}_{80}$ (I) at 298 K presented in Figure 3.14 exhibit two peaks. Similar to $\text{Sc}_3\text{N@C}_{80}$ (I)⁸ and $\text{Y}_3\text{N@C}_{80}$ (I)⁵⁵, the intensity ratio of these two peaks is 3:1, which is characteristic for NCFs with the C_{80} (I_h) cage isomer. As introduced in the previous reports about the ^{13}C NMR study of $\text{Y}_x\text{Lu}_{3-x}\text{N@C}_{80}$ (I) and $\text{Lu}_x\text{Sc}_{3-x}\text{N@C}_{80}$ (I; $x=0-3$), the geometrical factor influences on the chemical shifts of MMNCFs without considering paramagnetic contribution. For $\text{CeY}_2\text{N@C}_{80}$ (I), two $\delta(^{13}\text{C})$ signals around 144 and 138 ppm are still close to the $\text{Y}_3\text{N@C}_{80}$ (I) which indicates these ^{13}C NMR chemical shifts are changed by 4f¹-Ce³⁺ paramagnetic contribution as well. However, it

seems that the ^{13}C chemical shifts of $\text{PrSc}_2\text{N@C}_{80}$ (I) are majorly dominated by the paramagnetic action of $4f^2\text{-Pr}^{3+}$.

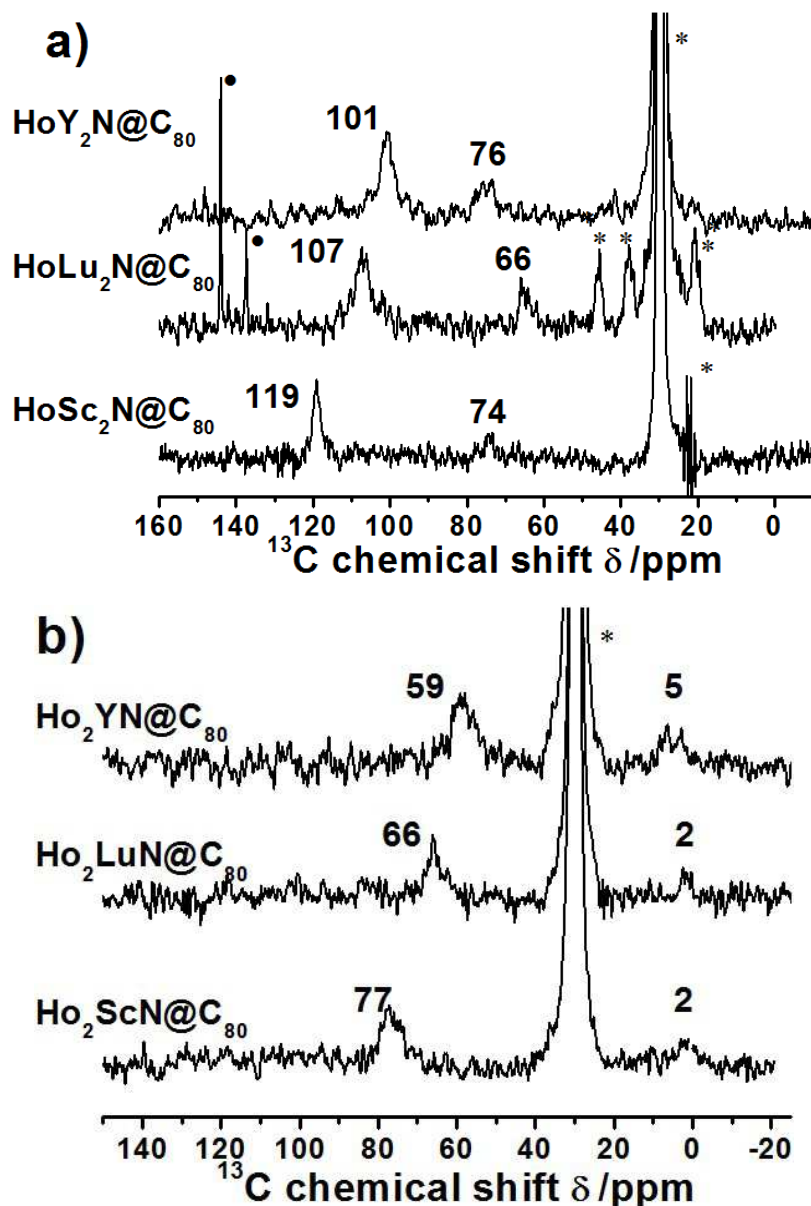


Figure 3.15 ^{13}C NMR spectra of (a) $\text{HoM}_2\text{N@C}_{80}$ and (b) $\text{Ho}_2\text{MN@C}_{80}$ (I; M= Y, Lu and Sc) $\text{CS}_2/\text{d}_6\text{-acetone}$ at the room temperature. Black dots denote $\text{Lu}_3\text{N@C}_{80}$ (I) in (a). Asterisks denote the signals of the solvent.

Herein, we report the first ^{13}C NMR spectroscopy of $\text{Ho}_x\text{M}_{3-x}\text{N@C}_{80}$ (I; M= Y, Lu and Sc; $x= 1\text{-}2$) which obtained at room temperature exhibit two broad peaks with chemical shift of 119 and 74 ppm ($\text{HoSc}_2\text{N@C}_{80}$), 107 and 66 ppm ($\text{HoLu}_2\text{N@C}_{80}$), 101 and 76 ppm ($\text{HoY}_2\text{N@C}_{80}$), 77 and 2 ppm ($\text{Ho}_2\text{ScN@C}_{80}$), 66 and 2 ppm ($\text{Ho}_2\text{LuN@C}_{80}$), 59 and 5 ppm ($\text{Ho}_2\text{YN@C}_{80}$), respectively (see Figure 3.15). The intensity ratio of those two peaks is

roughly 3:1 for each structure, which is characteristic for classical NCF with the C_{80} (I_h) cage isomer as $CeY_2N@C_{80}$ (I) and $PrSc_2N@C_{80}$ (I).

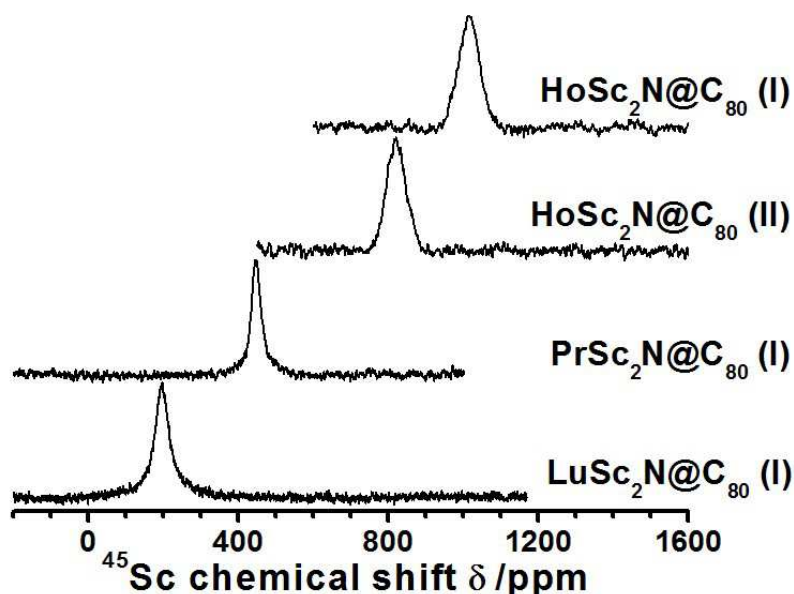


Figure 3.16 ^{45}Sc NMR spectra of $\text{HoSc}_2\text{N}@C_{80}$ (I, II), $\text{PrSc}_2\text{N}@C_{80}$ (I) measured in the solution of $\text{CS}_2/d_6\text{-acetone}$ at 298 K which compared with $\text{LuSc}_2\text{N}@C_{80}$ (I).

The ^{45}Sc NMR spectroscopy of $\text{LuSc}_2\text{N}@C_{80}$ (I), $\text{PrSc}_2\text{N}@C_{80}$ (I), $\text{HoSc}_2\text{N}@C_{80}$ (I) and $\text{HoSc}_2\text{N}@C_{80}$ (II) are compared in Figure 3.16. Each of above mentioned compounds exhibit a single and symmetric peak which indicates the dynamic behavior of the two Sc atoms encaged in the carbon cage. Substituting the involved lanthanide metal from $4f^1\text{-Ce}^{3+}$ to $4f^2\text{-Pr}^{3+}$ and $4f^{10}\text{-Ho}^{3+}$, paramagnetic chemical shifts induced by the corresponding lanthanide metal are different. Switching the symmetry of the carbon cage from I_h to D_{5h} but preserving encapsulated HoSc_2N , the significant difference between the two isomers of $\text{HoSc}_2\text{N}@C_{80}$ could be observed. More discussions about the magnetic properties of MMNCFs will be completed in the next chapter, which related to the involved lanthanide metal and the geometry of encaged cluster and/or the carbon cage.

3.4 Conclusion

In summary, $\text{Ho}_x\text{Sc}_{3-x}\text{N}@C_{80}$ (I, II; $x=1, 2$), $\text{Ho}_x\text{Lu}_{3-x}\text{N}@C_{80}$ (I; $x=1, 2$), $\text{Ho}_x\text{Y}_{3-x}\text{N}@C_{80}$ (I; $x=1, 2$), $\text{CeY}_2\text{N}@C_{80}$ (I), $\text{Ce}_x\text{Y}_{3-x}\text{N}@C_{2n}$ ($2n=84, 86$ and 88 ; $x=1-3$), $\text{CeSc}_2\text{N}@C_{80}$ (II), $\text{PrSc}_2\text{N}@C_{80}$ (I, II) were characterized. A systematic comparison of the UV-Vis-NIR, FTIR and Raman spectroscopic studies indicates that the vibrational modes of $\text{Ho}_x\text{M}_{3-x}\text{N}@C_{80}$ ($M=\text{Sc, Lu, Y}$; $x=1, 2$) resemble to $\text{Ho}_3\text{N}@C_{80}$ (I) and $\text{M}_3\text{N}@C_{80}$ (I; $M=\text{Sc, Lu, Y}$). The 4f electron(s) located on the encaged lanthanide metal (*e.g.* $4f^1\text{-Ce}^{3+}$, $4f^2\text{-Pr}^{3+}$ and $4f^{10}\text{-Ho}^{3+}$) results in remarkable ^{13}C NMR paramagnetic chemical shifts. The ^{45}Sc NMR spectroscopic study demonstrated that lanthanide-induced paramagnetic shifts are influenced by both the component of metal nitride cluster and the geometry of encapsulated cluster and carbon cage. Particularly, based on the current available data of the diamagnetic metal, such as Sc, Lu, Y, could help us tune the paramagnetic properties of MMNCFs which substantially broaden potential applications of EMFs. The state of paramagnetic lanthanide metals in MMNCFs and their electrochemical properties will be presented in the following chapters.

Chapter 4 Magnetic Properties of Mixed Metal Nitride Clusterfullerenes

4.1 ^{13}C NMR spectroscopic study of $\text{CeM}_2\text{N@C}_{80}$

As introduced in the former reports, there are two kinds of carbon atoms within the $\text{C}_{80}\text{-}I_h$, the pyrene-type carbon atoms (triple-hexagon junctions, THJs, whose NMR signals appear at chemical shifts of 137-138 ppm) and corannulene-type carbon atoms (pentagon/hexagon/hexagon junctions, PHHJs, whose NMR signals appear at a higher shift of ca 144 ppm). Without the consideration of paramagnetic contribution, the appreciable upfield-shifts are induced by shrinking the size of the encaged nitride cluster in the order of $\text{Y}_3\text{N@C}_{80} \rightarrow \text{Y}_2\text{LuN@C}_{80} \rightarrow \text{YLu}_2\text{N@C}_{80} \rightarrow \text{Lu}_3\text{N@C}_{80} \rightarrow \text{Lu}_2\text{ScN@C}_{80} \rightarrow \text{LuSc}_2\text{N@C}_{80}$ (summarized in Table 4.1).

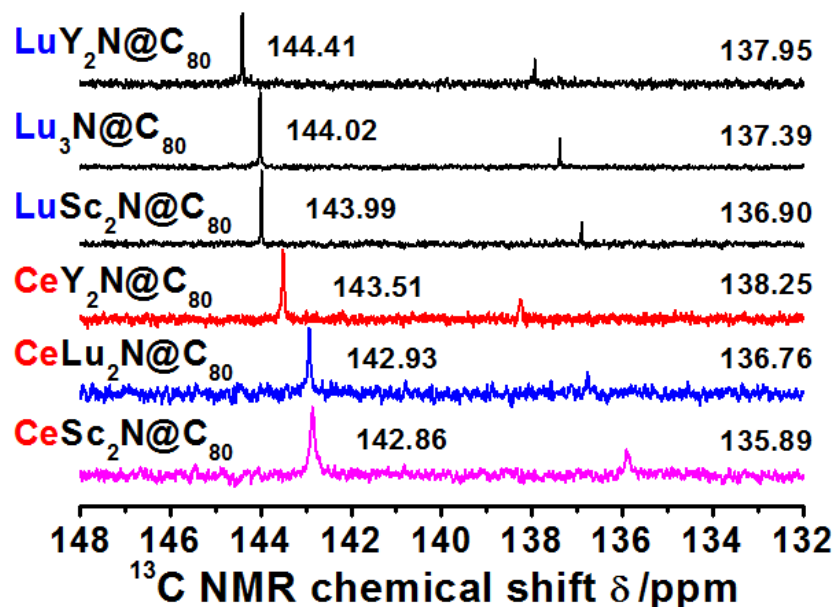


Figure 4.1 The 125 MHz ^{13}C NMR spectra of $\text{CeM}_2\text{N@C}_{80}$ and $\text{LuM}_2\text{N@C}_{80}$ (I; M= Sc, Lu and Y) in $\text{CS}_2/\text{d}_6\text{-acetone}$ at 298 K.

The 125 MHz ^{13}C NMR spectra of $\text{CeM}_2\text{N@C}_{80}$ (M= Sc, Lu, Y) obtained at 288 K exhibit two peaks with the intensity ratio of 3:1 (Figure 4.1), which unambiguously proves the $I_h(7)$ symmetry of the carbon cage and rapid rotation of the CeM_2N cluster in all these NCFs.

Established on the current knowledge, $\text{CeY}_2\text{N@C}_{80}$ has a dual advantage in ^{13}C NMR study of C_{80} -based MMNCFs as a result of the competition between geometrical factor of large cluster and weakly paramagnetic contribution, because both of these two terms inherently originate from the nature of Ce^{3+} . Firstly, because of the substantially different ionic radii of Ce^{3+} (1.03 Å) and Y^{3+} (0.90 Å), CeY_2N has a larger size than Y_3N inside the same C_{80} (I) cage. Secondly, recent studies on the $\text{CeLu}_2\text{N@C}_{80}$ and $\text{CeSc}_2\text{N@C}_{80}$ demonstrated that the single 4f-electron on Ce^{3+} ($4f^1 5d^0$) resulted in chemical upfield-shifts due to the paramagnetic contribution. Compared to the typical $\delta(^{13}\text{C})$ values in diamagnetic $\text{M}_3\text{N@C}_{80-I_h(7)}$ NCFs, the ^{13}C NMR signals in $\text{CeM}_2\text{N@C}_{80}$ experience a paramagnetic shift of 1-3 ppm due to the single 4f electron of Ce^{3+} .

	PHHJs / ppm	THJs / ppm	$\Delta \delta$ / ppm
CeY₂N@C₈₀	143.51	138.25	5.26
CeLu₂N@C₈₀	142.93	136.76	6.17
CeSc₂N@C₈₀	142.86	135.89	6.97
Y₃N@C₈₀	144.44	138.04	6.40
Y₂LuN@C₈₀	144.41	137.95	6.46
YLu₂N@C₈₀	144.22	137.66	6.56
Lu₃N@C₈₀	144.02	137.39	6.63
Lu₂ScN@C₈₀	143.99	137.12	6.87
LuSc₂N@C₈₀	143.99	136.90	7.09
Sc₃N@C₈₀	144.18	136.87	7.31

Table 4.1 125 MHz ^{13}C NMR chemical shift data (ppm) of $\text{CeM}_2\text{N@C}_{80}$ (I; M= Sc, Lu, Y), compared with $\text{Y}_x\text{Lu}_{3-x}\text{N@C}_{80}$ (I) and $\text{Lu}_x\text{Sc}_{3-x}\text{N@C}_{80}$ (I) (x= 0-3) MMNCFs in CS_2/d_6 -acetone at 298 K.

In these two respects large metal ionic radius and unpaired 4f-electron will cause competitive ^{13}C NMR chemical shifts. Under the weakly paramagnetic contribution from Ce^{3+} , the pattern of chemical downfield-shifts from $\text{CeSc}_2\text{N@C}_{80}$ (I) to $\text{CeLu}_2\text{N@C}_{80}$ (I) and further to $\text{CeY}_2\text{N@C}_{80}$ (I) agrees well with our former studies on the cage pyramidalization induced by the increasing the size of endohedral cluster as $\text{LuSc}_2\text{N} \rightarrow \text{Lu}_3\text{N} \rightarrow \text{LuY}_2\text{N}$. With small metal ion radius of Sc^{3+} (0.75 Å) and Lu^{3+} (0.85 Å), the downfield-shifts of THJs and PHHJs are largely dominated by the paramagnetic contribution which has been supported by

crystal structure data and DFT calculation respectively. But, in the case of $\text{CeY}_2\text{N@C}_{80}$ (I) the geometrical factor influences on the THJs slightly more than the paramagnetic contribution of PHHJs (for $\text{Y}_3\text{N@C}_{80}$ (I): 138.04 ppm and for $\text{CeLu}_2\text{N@C}_{80}$ (I): 138.25 ppm). Such a kind of unique chemical shifts agrees well with our former π -orbital axis vector (POAV) analysis^{78,79} that the THJs are much more sensitive than PHHJs for the pyramidalization of the carbon atoms (C_{80-I_h}) with endohedral clusters. In due turn, a perfect linear correlation between pyramidalization of the carbon atoms and a chemical shift was established. Figure 4.1 shows that the same reasoning applies also to $\text{CeM}_2\text{N@C}_{80}$.

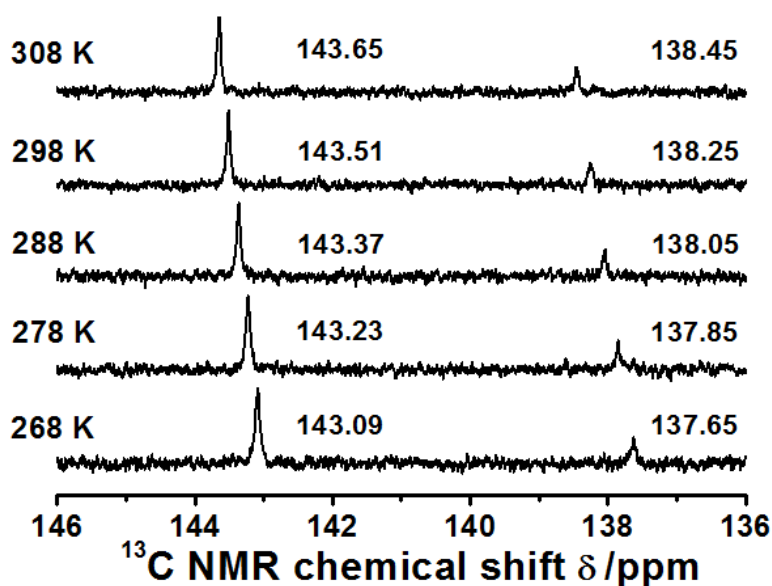


Figure 4.2 The variable-temperature ^{13}C NMR spectra of $\text{CeY}_2\text{N@C}_{80}$ (I) in the temperature range of 268-308 K.

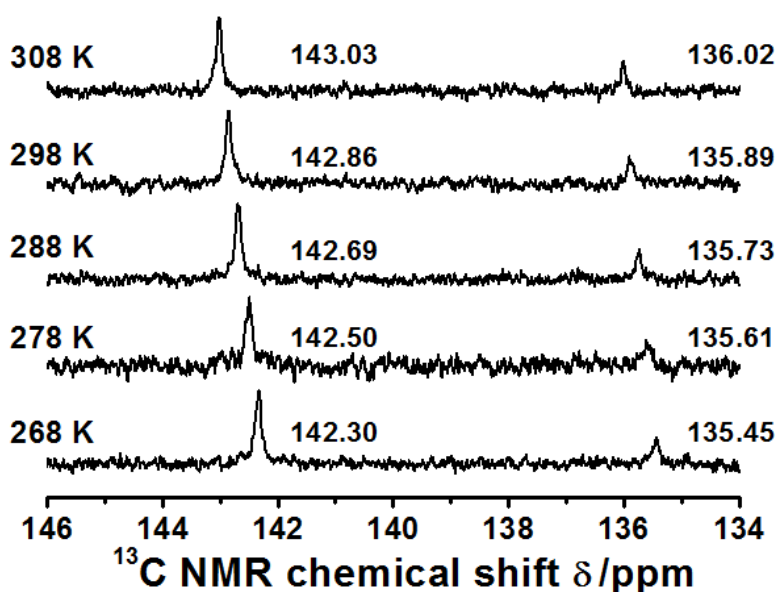


Figure 4.3 The variable-temperature ^{13}C NMR spectra of $\text{CeSc}_2\text{N@C}_{80}$ (I) in the temperature range of 268-308 K.

In the range of 268-308 K, the variable-temperature ^{13}C NMR studies of $\text{CeY}_2\text{N@C}_{80}$ (I) and $\text{CeSc}_2\text{N@C}_{80}$ (I) were for the first time performed to understand the effect of the size of different CeM_2N (see Figure 4.2 and 4.3). Similar to $\text{CeLu}_2\text{N@C}_{80}$ (I), hyperfine chemical shifts in paramagnetic molecule in solution could be expressed as Fermi contact (δ_{fc}) and pseudo-contact (δ_{pc}) shifts, which scale with temperature as T^{-1} and T^{-2} (here T is the absolute temperature), respectively. Since the contact term δ_{fc} is negligible based on the former studies of Ce-based endohedral fullerenes, the chemical shift can be expressed as $\delta = \delta_{\text{dia}} + c_{\text{pc}} \cdot T^{-2}$. The diamagnetic term (δ_{dia}) can be estimated by extrapolating the δ dependence to $T^{-2}=0$, while the c_{pc} is determined as an increment of the linear dependence δ vs T^{-2} . In Figure 4.4, extrapolation to $T^{-2}=0$ gave δ_{dia} (c_{pc}) values of 145.38/140.92 ppm (-0.17×10^6 K 2 / -0.24×10^6 K 2) for $\text{CeY}_2\text{N@C}_{80}$ (I) and 145.29/137.93 ppm (-0.22×10^6 K 2 / -0.17×10^6 K 2) for $\text{CeSc}_2\text{N@C}_{80}$ (I) respectively, and those are comparable to the $\text{CeLu}_2\text{N@C}_{80}$ (I) value (145.12/139.93 ppm, -0.19×10^6 K 2 / -0.28×10^6 K 2). The extrapolated δ_{dia} chemical shifts are in the range of the values found for diamagnetic $\text{M}_3\text{N@C}_{80}$ NCFs thus confirming the prevalence of the pseudocontact term. The c_{pc} constants are all near -0.20×10^6 K 2 which is comparable to the values in $\text{Ce}_2\text{@C}_{80}\text{-}I_h$ with freely circulating Ce atoms and are significantly smaller than c_{pc} constants in Ce-EMFs with more restricted motion ($\text{Ce}_2\text{@C}_{80}\text{-}D_{5h}$) or localized position of Ce atoms ($\text{Ce}_2\text{@C}_{72}$ or $\text{Ce}_2\text{@C}_{78}$).

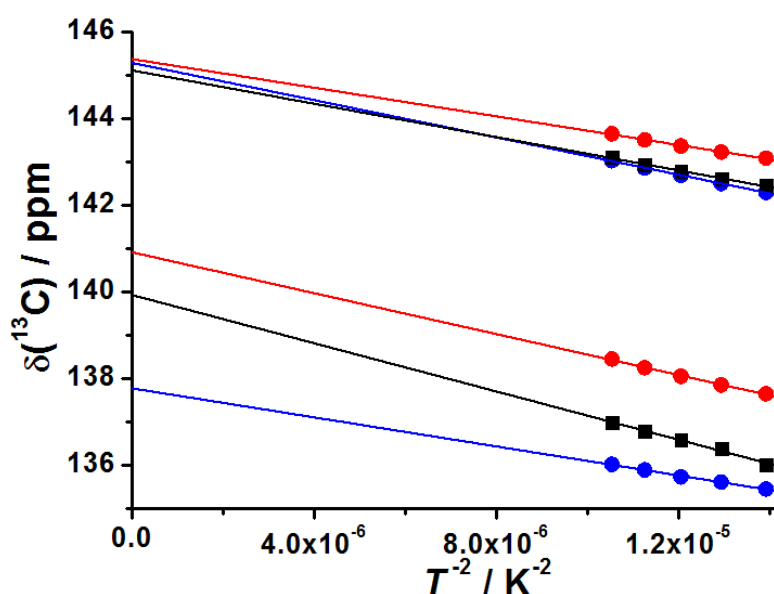


Figure 4.4 The line-fitting plots for ^{13}C NMR chemical shift δ vs. T^{-2} are shown for $\text{CeY}_2\text{N@C}_{80}$ (I) (red), $\text{CeLu}_2\text{N@C}_{80}$ (I) (black) and $\text{CeSc}_2\text{N@C}_{80}$ (I) (blue).

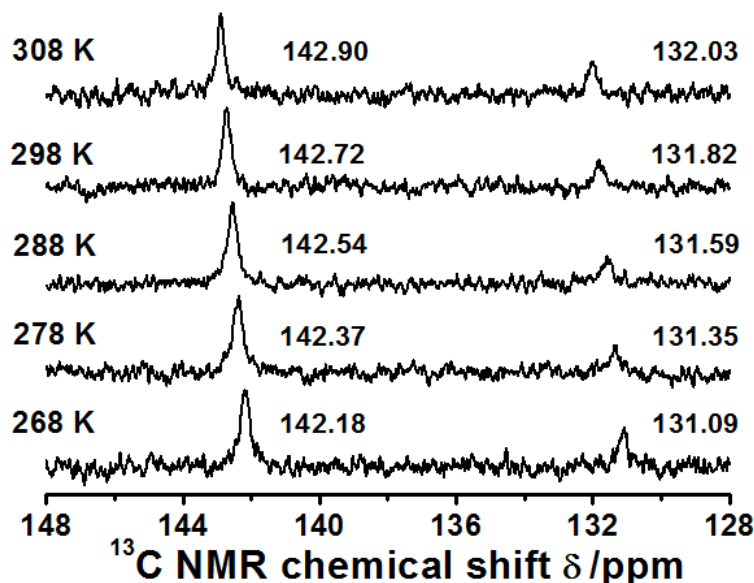


Figure 4.5 The variable-temperature ^{13}C NMR spectra of $\text{PrSc}_2\text{N@C}_{80}$ (I) in the temperature range of 268-308 K.

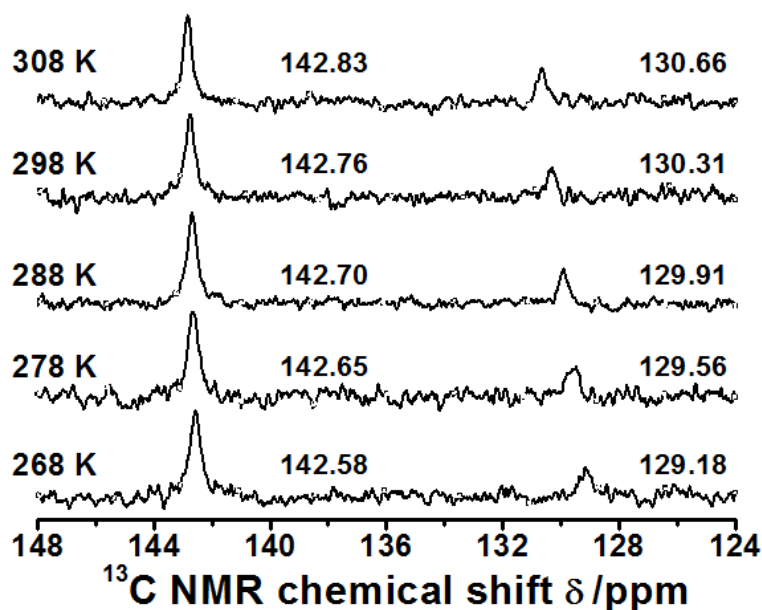


Figure 4.6 The variable-temperature ^{13}C NMR spectra of $\text{NdSc}_2\text{N@C}_{80}$ (I) in the temperature range of 268-308 K.

In Figure 4.5 and 4.6, the variable-temperature ^{13}C NMR studies of $\text{PrSc}_2\text{N@C}_{80}$ (I) and $\text{NdSc}_2\text{N@C}_{80}$ (I) were performed to measure the effect of Pr^{3+} and Nd^{3+} in ^{13}C NMR characterization. Extrapolation to $T^{-2}=0$ gave $\delta_{\text{dia}}(c_{\text{pc}})$ values of $\text{PrSc}_2\text{N@C}_{80}$ (I) are 145.14 and 134.95 ppm ($-0.21 \times 10^6 \text{ K}^2$ and $-0.27 \times 10^6 \text{ K}^2$). However, the extrapolated values of $\text{NdSc}_2\text{N@C}_{80}$ (I) are 143.58 and 135.24 ppm ($-0.07 \times 10^6 \text{ K}^2$ and $-0.44 \times 10^6 \text{ K}^2$) which behave different compare to $\text{CeSc}_2\text{N@C}_{80}$ (I) and $\text{PrSc}_2\text{N@C}_{80}$ (I).

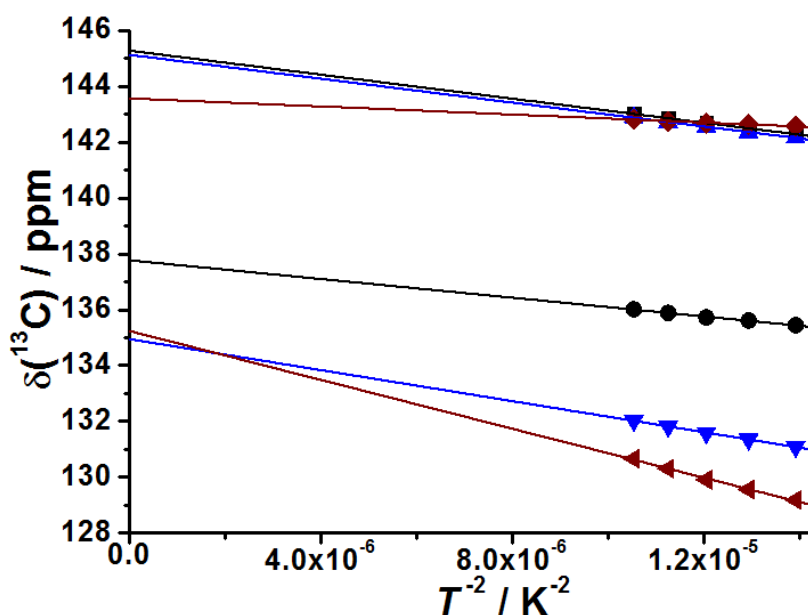


Figure 4.7 The line-fitting plots for ^{13}C chemical shift δ vs. T^{-2} are shown for $\text{CeSc}_2\text{N}@C_{80}$ (I) (black), $\text{PrSc}_2\text{N}@C_{80}$ (I) (blue) and $\text{NdSc}_2\text{N}@C_{80}$ (I) (brown).

The 125 MHz ^{13}C NMR spectra of $\text{Ho}_x\text{Sc}_{3-x}\text{N}@C_{80}$ (I; $x = 1-2$) obtained at room temperature exhibit two broad peaks with chemical shift of 119 and 74 ppm ($\text{HoSc}_2\text{N}@C_{80}$), and 77 and 2 ppm ($\text{Ho}_2\text{ScN}@C_{80}$), respectively (Figure 4.8). The paramagnetic shift of the ^{13}C NMR lines induced by each Sc-to-Ho substitution is 25 - 40 ppm for the more intense peak and 60-70 ppm for the second peak. For comparison, the shift of the ^{13}C lines in $\text{CeM}_2\text{N}@C_{80}$ ($M = \text{Sc, Lu, Y}$) in comparison to $\text{Sc}_3\text{N}@C_{80}$ they did not exceed 2 ppm. Such a large difference in the lanthanide-induced shift obviously originates from the much higher effective magnetic moment of $4f^{10}\text{-Ho}^{3+}$ ($10.6 \mu_B$)⁵¹ than $4f^1\text{-Ce}^{3+}$ ($2.54 \mu_B$)². A complete interpretation of the paramagnetic chemical shift can be achieved only by the combination of two factors, local instantaneous paramagnetic shifts of carbon atoms induced by Ho^{3+} and the internal motion of the encapsulated metal nitride cluster which averages these interactions on the NMR time scale. Replacing the $\text{Ho}_x\text{Sc}_{3-x}\text{N}$ cluster with $\text{Ho}_x\text{Lu}_{3-x}\text{N}$ and $\text{Ho}_x\text{Y}_{3-x}\text{N}$ resulted in varying the geometry of Ho-based endohedral cluster and the interaction between the encaged Ho ion and the neighboring carbon atoms.

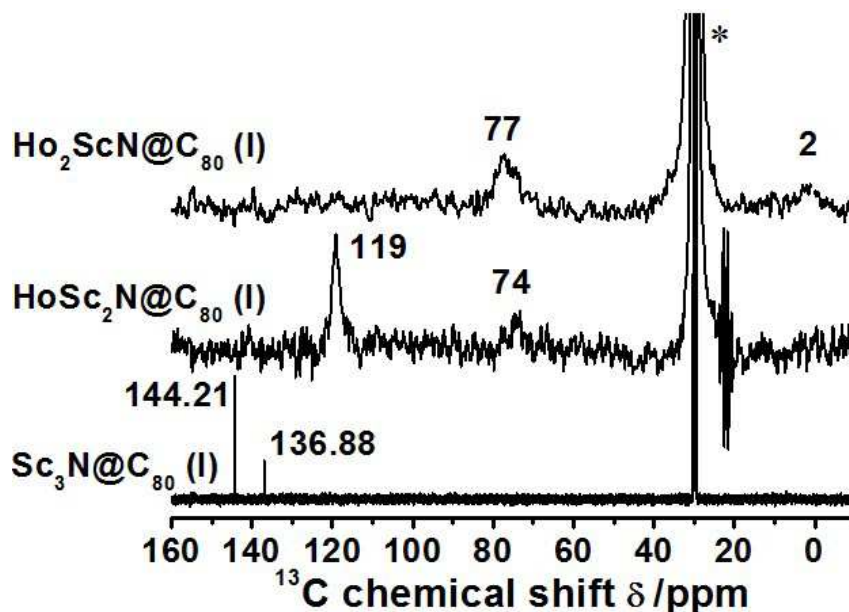


Figure 4.8 ^{13}C NMR spectra of $\text{Ho}_x\text{Sc}_{3-x}\text{N}@C_{80}$ (I; $x= 0-2$) CS_2/d_6 -acetone at the room temperature. An asterisk denotes the signal of the solvent.

The ^{13}C NMR spectra of $\text{HoM}_2\text{N}@C_{80}$ and $\text{Ho}_2\text{MN}@C_{80}$ (I; $M= \text{Sc}, \text{Lu}$ and Y) are shown in Figure 4.9. For $\text{HoM}_2\text{N}@C_{80}$ and $\text{Ho}_2\text{MN}@C_{80}$ (I; $M= \text{Sc}, \text{Lu}$ and Y), all of these Ho-containing structures exhibited roughly two peaks in the ratio of 3:1, which is characteristic for C_{80} -based NCFs with the I_h symmetry. Based on our studies on $\text{CeM}_2\text{N}@C_{80}$ (I; $M= \text{Sc}, \text{Lu}$ and Y) in section 4.1, the ^{13}C NMR chemical shifts could be induced by geometrical factor of encaged cluster and by paramagnetic contribution from encaged lanthanide metal respectively. It could be expected that substituting the metal atom(s) from Sc to Lu and Y in $\text{HoM}_2\text{N}@C_{80}$ and $\text{Ho}_2\text{MN}@C_{80}$ influence the geometry of the encaged nitride cluster which supported by vibrational spectroscopic studies as introduced in the Chapter 3. Switching Ho-based cluster from HoSc_2N to HoLu_2N and further to HoY_2N leads to two broad peaks with chemical shift of 107 and 66 ppm ($\text{HoLu}_2\text{N}@C_{80}$), and 101 and 76 ppm ($\text{HoY}_2\text{N}@C_{80}$), respectively (see Figure 4.9). Similarly, after substituting the cluster from Ho_2ScN to Ho_2LuN and Ho_2YN , two broader peaks with 66 and 2 ppm for $\text{Ho}_2\text{LuN}@C_{80}$ and 59 and 5 ppm for $\text{Ho}_2\text{YN}@C_{80}$ were obtained respectively. Different to former studies on $\text{CeM}_2\text{N}@C_{80}$ (I; $M= \text{Sc}, \text{Lu}, \text{Y}$) structures, the chemical shift of PHHJs and THJs, in $\text{Ho}_x\text{M}_{3-x}\text{N}@C_{80}$ (I; $M= \text{Sc}, \text{Lu}, \text{Y}$), is definitely dominated by the paramagnetic contribution from Ho^{3+} . However, it should be pointed out that the geometrical factors still play an important role in inducing the chemical shift. For instance, the chemical shift of THJs of $\text{HoY}_2\text{N}@C_{80}$ and $\text{Ho}_2\text{YN}@C_{80}$ are smaller than $\text{Ho}_x\text{Sc}_{3-x}\text{N}@C_{80}$ and $\text{Ho}_x\text{Lu}_{3-x}\text{N}@C_{80}$. This indicates that two factors influence the chemical shift simultaneously. Full analysis of these factors is still underway.

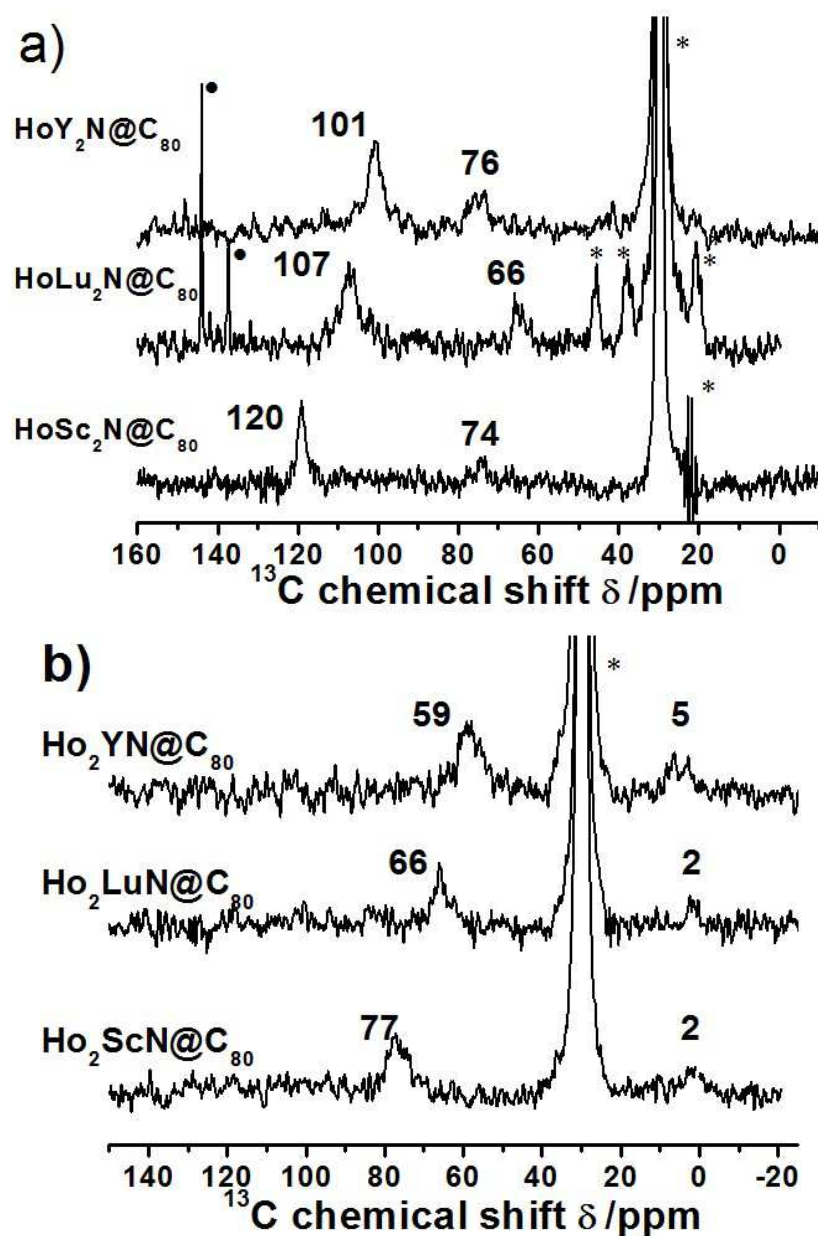


Figure 4.9 ^{13}C NMR spectra of HoM₂N@C₈₀ and Ho₂MN@C₈₀ (I; M= Sc, Lu and Y) CS₂/d₆-acetone at the room temperature. Black dots denote Lu₃N@C₈₀ (I) in a). Asterisks denote the signal of the solvent.

4.2 ^{45}Sc NMR spectroscopic study of MMNCFs

The NMR studies of magnetic properties of endohedral fullerenes are limited to the Ce-containing structures ($\text{Ce}@C_{2n}$, $\text{Ce}_2@C_{2n}$ and $\text{CeSc}_2\text{N}@C_{80}$ (I)). To explore the influence caused by other lanthanide metals, it is quiet necessary to extend this field. Compared to Ce-containing endohedral fullerenes, Pr-containing structures could be regarded as the good candidate not only due to one more 4f-electron but similar ionic radius to Ce^{3+} as well. Figures 4.10-4.13 display the 125 MHz ^{45}Sc NMR spectra of $\text{PrSc}_2\text{N}@C_{80}$ (I) obtained in the temperature range of 268-308 K. The single and symmetric peak indicates the dynamic behavior of the Sc atoms engaged in the carbon cage. For ^{45}Sc NMR, the extrapolation to $T^{-2}=0$ gave c_{pc} values of $12.05 \times 10^6 \text{ ppm} \cdot \text{K}^2$ for $\text{PrSc}_2\text{N}@C_{80}$ (I), and this is comparable to the $\text{CeSc}_2\text{N}@C_{80}$ (I) ($6.60 \times 10^6 \text{ ppm} \cdot \text{K}^2$)⁵² and $\text{NdSc}_2\text{N}@C_{80}$ (I) ($4.37 \times 10^6 \text{ ppm} \cdot \text{K}^2$). These results agree well with the theory of Lanthanide-induced pseudocontact shifts with variable crystal field parameters. In principle, the observed pseudocontact contribution to ^{13}C and ^{45}Sc NMR shifts for lanthanide-containing endohedral fullerenes in solution is originated from the anisotropy in the susceptibility. To understand the role of lanthanide metal in the studies of ^{13}C and ^{45}Sc NMR chemical shifts, we performed ^{45}Sc NMR on $\text{MSc}_2\text{N}@C_{80}$ (I) with variation of the engaged cluster composition (from Ce to Pr and Nd). From the comparison of the ^{45}Sc NMR spectra of $\text{MSc}_2\text{N}@C_{80}$, the lanthanide-induced NMR chemical shifts do not only rely on the number of 4f-electron(s) and/or the magnetic moment of Ln^{3+} but the anisotropy in the susceptibility as well. In principle, the magnetic moment of Nd^{3+} ($3.62 \mu_{\text{B}}$) is larger than Pr^{3+} ($3.58 \mu_{\text{B}}$) and Ce^{3+} ($2.54 \mu_{\text{B}}$) because Nd has one more unpaired 4f electron than Pr^{3+} , but the ^{45}Sc NMR chemical shifts of $\text{PrSc}_2\text{N}@C_{80}$ (I) (455 ppm) is much stronger than $\text{CeSc}_2\text{N}@C_{80}$ (I) (280 ppm) and $\text{NdSc}_2\text{N}@C_{80}$ (I) (361 ppm).

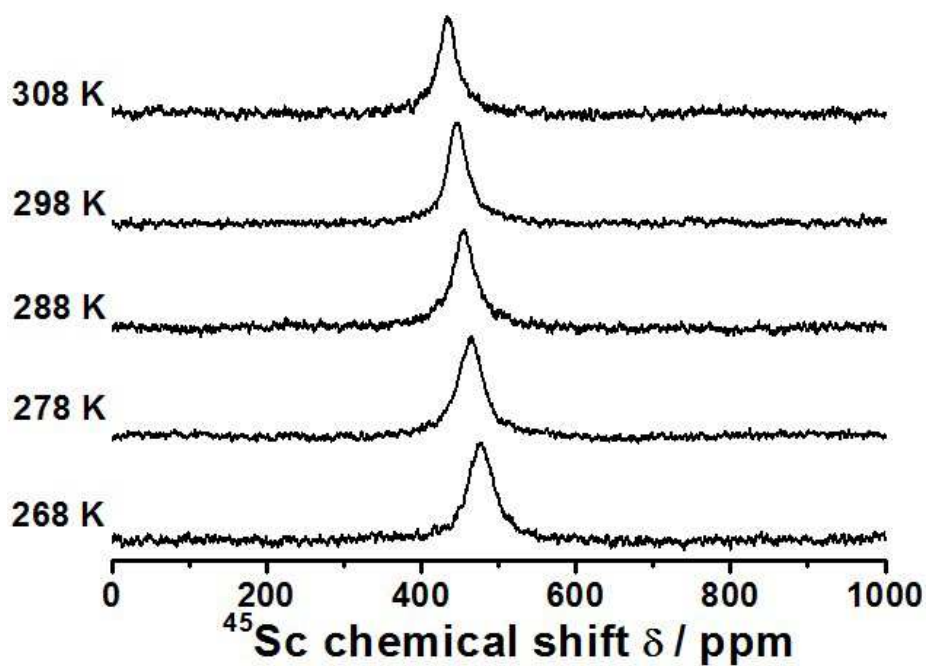


Figure 4.10 The variable-temperature ^{45}Sc NMR spectra of $\text{PrSc}_2\text{N}@C_{80}$ (I) in the temperature range of 268-308 K.

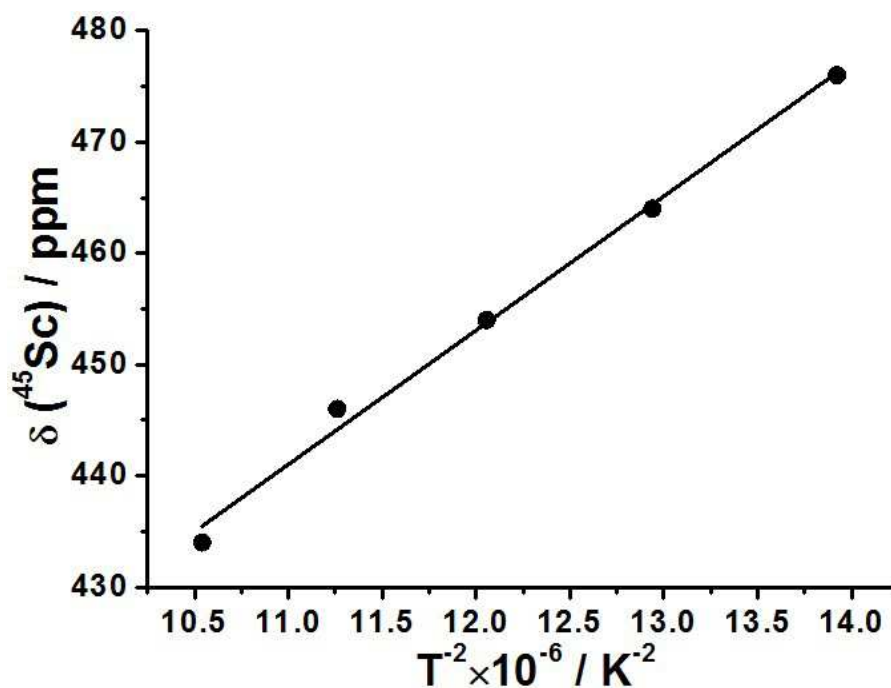


Figure 4.11 The line-fitting plots for ^{45}Sc NMR chemical shift δ vs. T^{-2} are shown for $\text{PrSc}_2\text{N}@C_{80}$ (I).

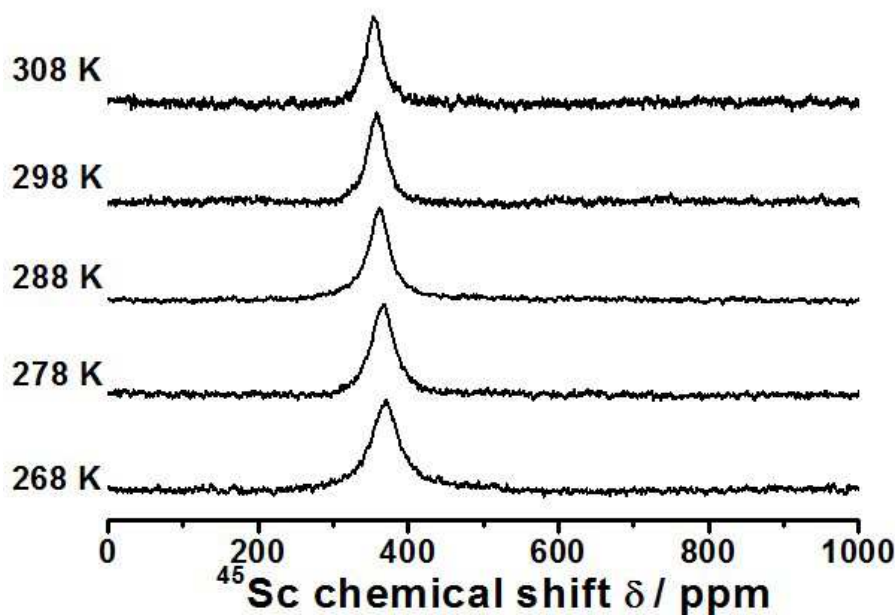


Figure 4.12 The variable-temperature ^{45}Sc NMR spectra of $\text{NdSc}_2\text{N@C}_{80}$ (I) in the temperature range of 268-308 K.

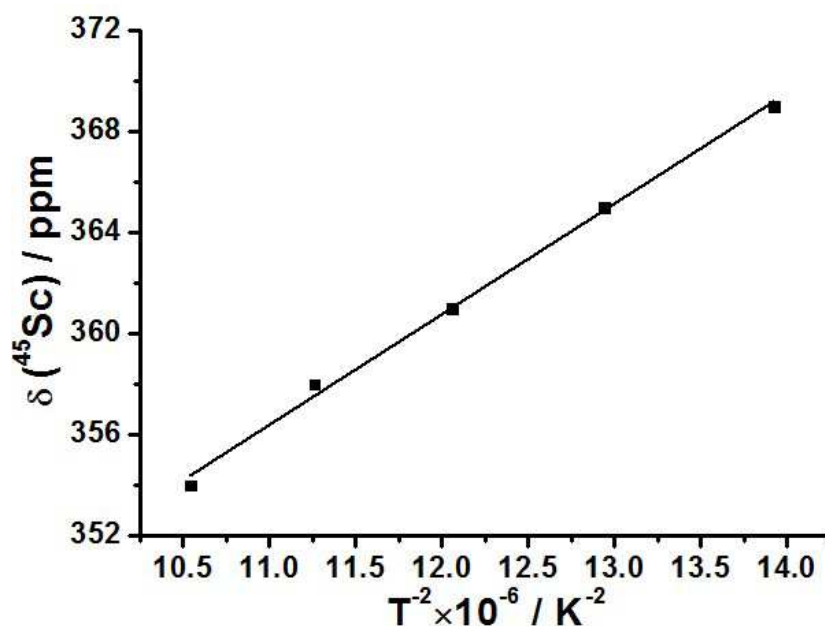


Figure 4.13 The line-fitting plots for ^{45}Sc NMR chemical shift δ vs. T^{-2} are shown for $\text{NdSc}_2\text{N@C}_{80}$ (I).

Large temperature-dependent paramagnetic shifts were also observed in the ^{45}Sc NMR spectra of $\text{HoSc}_2\text{N@C}_{80}$ (I, II) shown in Figure 4.14-4.15. In the temperature range from 268 K to 308 K in the CS_2 solution, both compounds exhibited single ^{45}Sc NMR peak, showing that two Sc atoms are averaged by the cluster dynamics. In comparison to the ^{45}Sc signals in $\text{Sc}_3\text{N@C}_{80}$ ($\delta = 199.5$ ppm for I_h and 211.7 ppm for D_{5h} isomers), ^{45}Sc chemical shifts of $\text{HoSc}_2\text{N@C}_{80}$ are shifted downfield by ca 900 ppm for the I_h -cage ($\delta = 1178$ -956 ppm) and

700 ppm for the D_{5h} -cage ($\delta = 950$ -786 ppm), while the line is ca 1.5 times broader (note that the ^{45}Sc lines are intrinsically broadened because of the quadruple moment of Sc). Importantly, for the same compound, paramagnetic shift of the ^{45}Sc signal is much higher than that in the ^{13}C NMR spectrum, which can be explained by a dynamic nature of the ^{13}C NMR. In ^{13}C NMR, the measured signal is averaged for all carbon atoms of a given type (and hence it has contribution both from the atoms which are far away from the Ho ion and have small instant paramagnetic contribution and from those which are close to Ho). On the contrary, the HoSc_2N cluster has rigid geometry with constant Sc–Ho distances. As a result, ^{45}Sc NMR is a more sensitive probe of the paramagnetic effect of Ho atom.

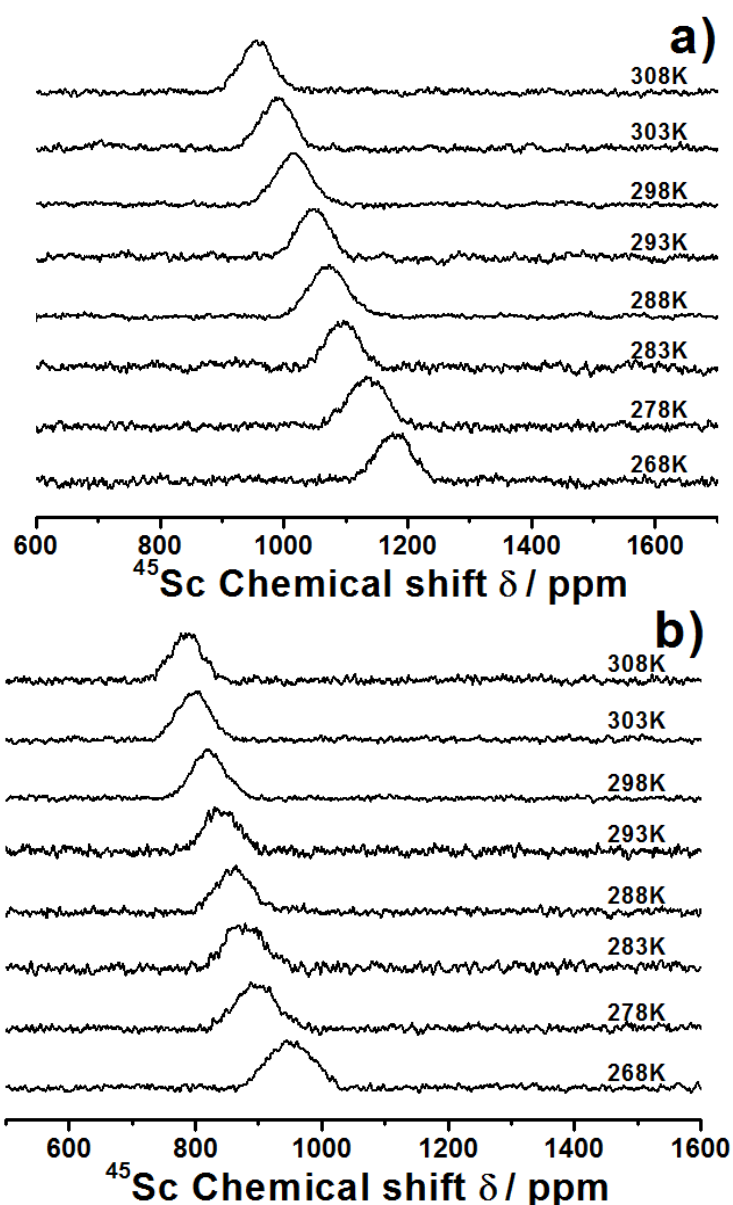


Figure 4.14 ^{45}Sc NMR spectra of (a) $\text{HoSc}_2\text{N}@C_{80}$ (I) and (b) $\text{HoSc}_2\text{N}@C_{80}$ (II) measured at the different temperature.

The main contributions to paramagnetic chemical shifts in solution are Fermi contact (δ_{fc}) and pseudo-contact (δ_{pc}) shifts, which scale with temperature as T^{-1} and T^{-2} (here T is absolute temperature), respectively. For Ce-based mono- or dimetallofullerenes and MMNCFs, the temperature-dependent NMR studies revealed that the contact term δ_{fc} is negligible, and the chemical shift can be simply expressed as $\delta = \delta_{dia} + c_{pc} \cdot T^{-2}$. For $\text{HoSc}_2\text{N@C}_{80}$, the diamagnetic term (δ_{dia}) can be estimated by extrapolating δ dependence to $T^{-2}=0$, while the c_{pc} is determined as an increment of the linear dependence δ vs T^{-2} . If the assumption that pseudocontact shift is the dominant term is correct, δ_{dia} should be close to the ^{45}Sc chemical shift of $\text{Sc}_3\text{N@C}_{80}$ isomers ($\delta = 200\text{-}212$ ppm).^{8,34} For both isomers, extrapolation to $T^{-2}=0$ yielded $\delta_{dia} = 271$ ppm. For comparison, extrapolation to $T^{-1}=0$ gave δ_{dia} values of -531 and -319 ppm for I_h and D_{5h} isomers, respectively, which is substantially further from the $\text{Sc}_3\text{N@C}_{80}$ value. Thus, the prevalence of the pseudocontact term is confirmed for $\text{HoSc}_2\text{N@C}_{80}$. At the same time, the difference between extrapolated δ_{dia} values and experimental value for $\text{Sc}_3\text{N@C}_{80}$ is rather large which indicates that the contact term is probably not negligible. Precise estimation of the contact term contribution to lanthanide paramagnetic shift is not possible at this moment and requires a study of a series of $\text{MSc}_2\text{N@C}_{80}$ MMNCFs with different lanthanides.

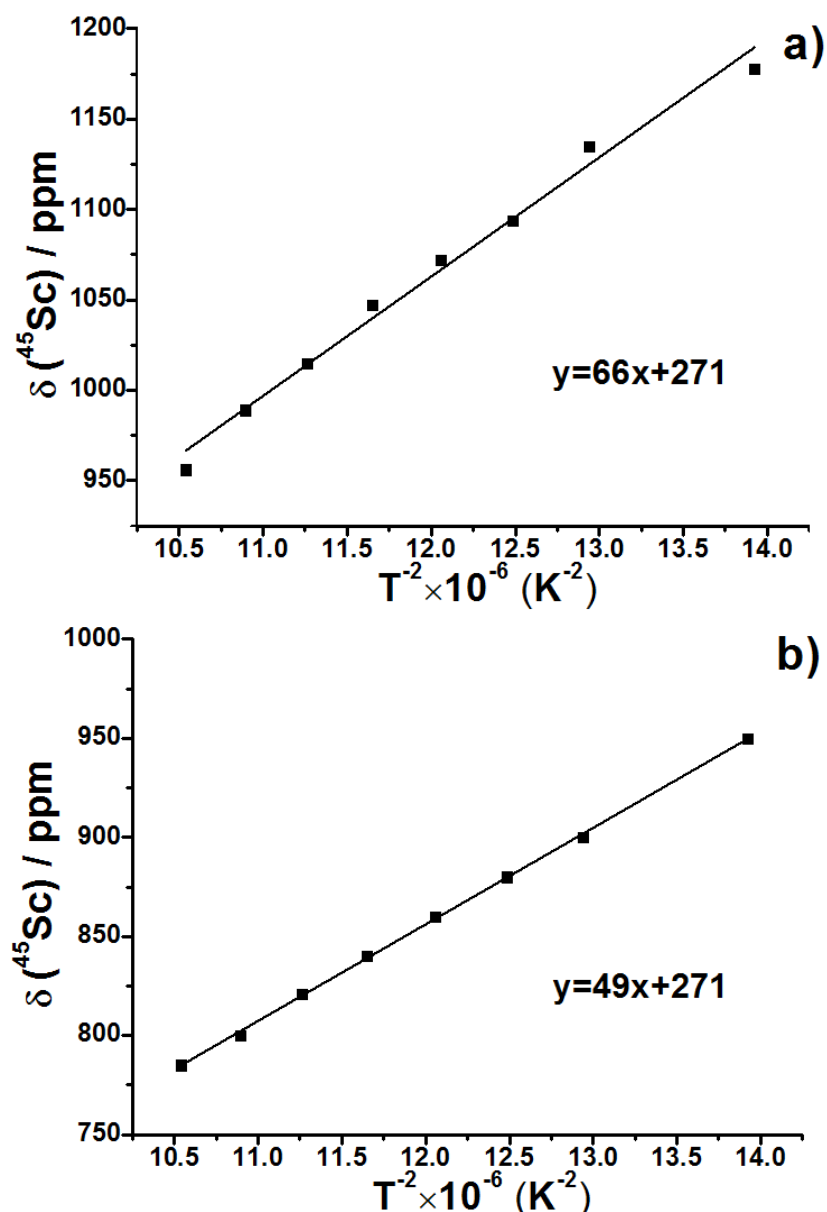


Figure 4.15 The line-fitting plots for chemical shift δ vs. T^{-2} are shown for a) $HoSc_2N@C_{80}$ (I) and $HoSc_2N@C_{80}$ (II).

Interestingly, although δ_{dia} values for the two isomers of $HoSc_2N@C_{80}$ are identical, their c_{pc} values determined from the linear fitting of experimental data by the $\delta_{dia} + c_{pc} \cdot T^{-2}$ function are substantially different: for the I_h isomer, the fitting gives $c_{pc} = 66 \pm 3 \text{ ppm} \cdot K^2$, while c_{pc} of the D_{5h} isomer is found to be $49 \pm 0.5 \text{ ppm} \cdot K^2$. The reason for such a significant variation is not clear at this moment; possibly, the difference of c_{pc} constants partially reflects the difference in the geometrical structure of the $HoSc_2N$ cluster inside different carbon cages (note that c_{pc} scales with the distance R between paramagnetic center and the atom of interest as R^{-3}).⁸⁰ FTIR spectroscopy (see above) demonstrated that the frequencies of the metal-nitrogen modes in $HoSc_2N@C_{80}$ (II) are ca. 10 cm^{-1} lower than in $HoSc_2N@C_{80}$ (I), which means that corresponding bond lengths in the D_{5h} isomer are somewhat longer. Besides,

single-crystal X-ray studies of $M_3N@C_{80}-D_{5h}$ ($M = Sc, Tb, Tm$) also show that the nitride cluster inside the $C_{80}-D_{5h}$ cage tends to be somewhat more distorted from the trigonal symmetry than in the I_h isomers. In addition to the geometrical changes, distortion of the cluster may also change the crystal-field splitting parameters and hence also affect the c_{pc} values.

It is also instructive to compare pseudocontact shifts in MMNCFs with different lanthanides. Variable-temperature ^{45}Sc chemical shifts of $MSc_2N@C_{80}-I_h$ ($M = Ce - Nd$) described above give c_{pc} values of $4.4 - 12.05 \text{ ppm}\cdot\text{K}^2$, which is an order of magnitude smaller than found in this work for $HoSc_2N@C_{80}-I_h$. A ten-fold increase of the c_{pc} value for $HoSc_2N@C_{80}$ is reasonable taking into account a higher magnetic moment of Ho^{3+} when compared to that of Ce^{3+} . In particular, in the framework of Bleaney theory, if the difference in geometrical and crystal-field parameters for $CeSc_2N@C_{80}$ and $HoSc_2N@C_{80}$ are neglected, the ratio of pseudocontact shifts induced by Ce^{3+} and Ho^{3+} at room temperature is expected to be $-6.3/-39.0$,⁸¹ which is close to the experimentally determined ratio of c_{pc} values for ^{45}Sc .

4.3 The analysis of NMR spectroscopy of $\text{LnSc}_2\text{N@C}_{80}$

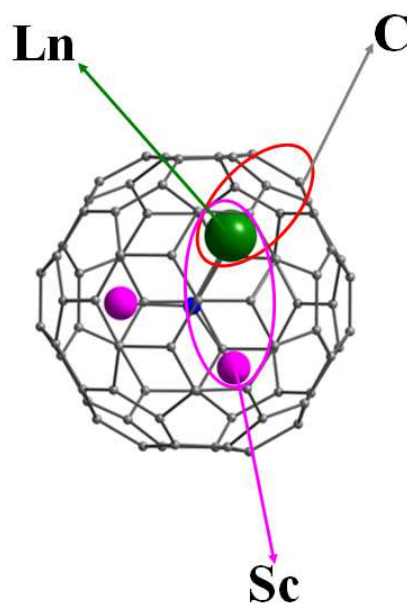


Figure 4.15 The scheme of lanthanide-induced paramagnetic shifts in $\text{LnSc}_2\text{N@C}_{80}$.

The pseudocontact contribution to the NMR shifts for lanthanide complexes in solution is derived from the anisotropy in the susceptibility. Lanthanide-induced ^{13}C and ^{45}Sc NMR shifts in MMNCFs are illustrated in Figure 4.15. The paramagnetic chemical shifts originate from the contribution of Pseudocontact (δ^{PC}) and Fermi contact (δ^{con}) terms which provide valuable information. For C_{80} -based metal nitride clusterfullerenes, it could be considered as a good chance to compare their paramagnetic NMR chemical shifts of $\text{LnSc}_2\text{N@C}_{80}$ (I) due to their relatively high yield, similar metal ionic radius and identical electronic properties of the carbon cage but encaging switchable lanthanide metals with different magnetic properties. However, MMNCFs are strikingly different to the organic metallic complex. Moreover, the lanthanide metal-containing encaged cluster substantially complicates the analysis of the paramagnetic chemical shifts due to the free rotating cluster inside carbon cage, which different from organic metallic complexes with rigid structures.

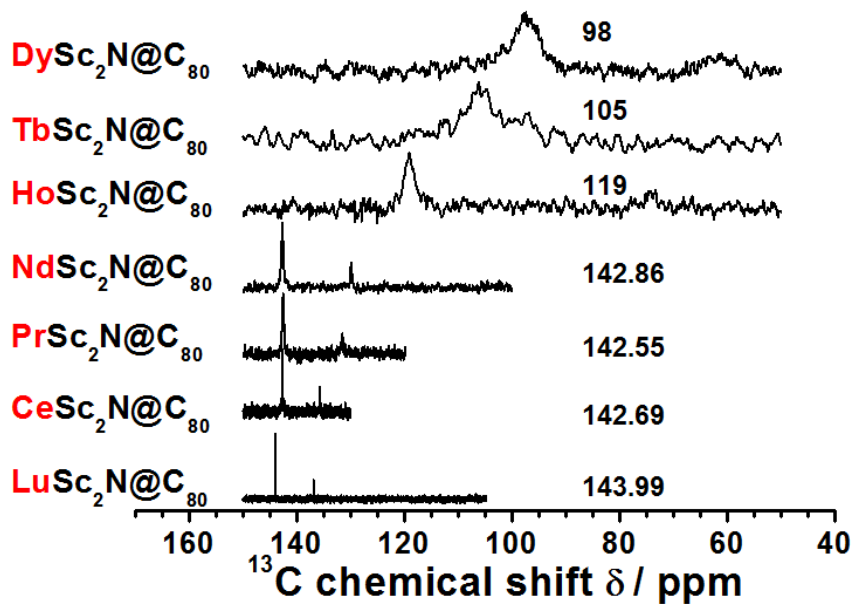


Figure 4.16 ^{13}C NMR spectra of $\text{LnSc}_2\text{N@C}_{80}$ (I; Ln= Ce, Pr, Nd, Tb, Dy, Ho and Lu) $\text{CS}_2/\text{d}_6\text{-acetone}$ at 288 K.

$$\delta_{\text{Ln}}^{\text{para}}(i) = \delta_{\text{Ln}}^{\text{con}}(i) + \delta_{\text{Ln}}^{\text{PC}}(i) = \langle S_z \rangle_{\text{Ln}} \cdot F(i) + C_{\text{Ln}} \cdot B \cdot G(i) \quad -- \quad (4.1)$$

$$\frac{\delta_{\text{Ln}}^{\text{para}}(i)}{\langle S_z \rangle_{\text{Ln}}} = F(i) + \frac{C_{\text{Ln}}}{\langle S_z \rangle_{\text{Ln}}} B \cdot G(i) \quad -- \quad (4.2)$$

$$\delta_{\text{Ln}}^{\text{PC}}(i) = B \cdot G(i) \cdot C_{\text{Ln}} \quad -- \quad (4.3)$$

$$\delta_{\text{Ln}}^{\text{con}}(i) = F(i) \cdot \langle S_z \rangle_{\text{Ln}} \quad -- \quad (4.4)$$

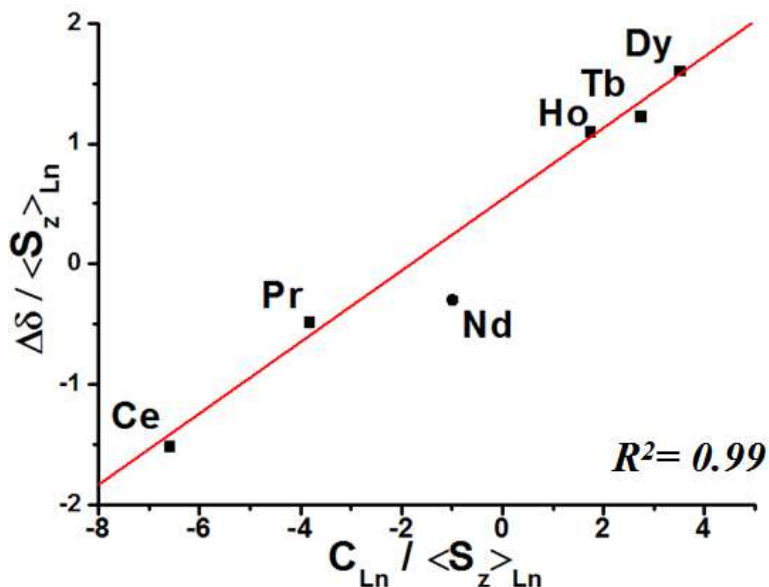


Figure 4.17 Plots of $\Delta\delta / \langle S_z \rangle_{\text{Ln}}$ vs. $C_{\text{Ln}} / \langle S_z \rangle_{\text{Ln}}$ for ^{13}C NMR chemical shifts of $\text{LnSc}_2\text{N@C}_{80}$ (I; Ln= Ce, Pr, Nd, Tb, Dy, Ho and Lu).

	Ce	Pr	Nd	Ho	Tb	Dy
$C_{Ln}^{[a]}$	-6.48	-11.41	-4.46	-39.25	-96.84	-100.00
$\langle S_z \rangle$	0.98	2.97	4.49	-22.63	-31.82	-28.54
δ^{PC}	-1.92	-3.38	-1.32	-11.64	-25.75	-29.65
δ^{con}	0.53	1.60	2.41	-12.17	-17.11	-15.34

Table 4.2 The list of C_{Ln} , $\langle S_z \rangle$, δ^{PC} and δ^{con} . ^[a]The values of C_{Ln} and $\langle S_z \rangle$ are fundamental parameters of given lanthanide ions.

The paramagnetic chemical shift δ^{para} can be defined as the difference between δ^{obs} observed shift from paramagnetic compound and δ^{dia} obtained from diamagnetic reference compound. For of $LnSc_2N@C_{80}$ (I), La^{3+} , Y^{3+} or Lu^{3+} is regarded as suitable standards. In our system, $LuSc_2N@C_{80}$ (I) is chosen and compared with Ce-, Pr-, Nd-, Ho-, Tb- and Dy-involved structures. The ^{13}C NMR spectra of $LnSc_2N@C_{80}$ (I; Ln= Ce, Pr, Nd, Tb, Dy, Ho and Lu) are obtained at 288K and presented in Figure 4.16. As introduced by Reilley and co-workers,⁸² the separation of δ^{PC} and δ^{con} from δ^{para} can be achieved via Equations 4.1 - 4.4. δ^{con} can be attributed to the unpaired electron delocalization from the Ln^{3+} onto the nucleus i and influence neighboring atom(s) through chemical bonds. But, as increasing number of bonds between Ln and i , its influences become marginally small. δ^{con} is proportional to the expectation values of S_z for that Ln^{3+} . In Equation 4.1, $F(i)$ is a proportionality constant which specially depends on the specific nucleus i . However, δ^{PC} includes geometric information of the target compound. Based on Bleaney's theory and further developed by Mironov et al, the δ^{PC} could be simply described as the contribution of the sum of C_{Ln} and $B \cdot G(i)$. Particularly, $B \cdot G(i)$ cover the parameters comprising of the magnetic anisotropy and the corresponding crystal field. Since C_{Ln} and $\langle S_z \rangle_{Ln}$ are known, the plotting of $\delta_{Ln}^{para}(i) / \langle S_z \rangle_{Ln}$ vs. $C_{Ln} / \langle S_z \rangle_{Ln}$ covering Ce, Pr, Ho, Tb and Dy yields intercept ($F(i)$) and slope ($B \cdot G(i)$) value simultaneously. After those mathematical treatments, δ^{para} and δ^{con} could be written in the form of Equation 4.3 and 4.4. The values of δ^{con} and δ^{PC} computed this way are listed in the Table 4.2. By comparing δ^{con} and δ^{PC} , it should be noted that the good linear fitting ($R^2 = 0.99$) can be obtained without considering Nd which suggested that for $NdSc_2N@C_{80}$ requires further studies. Moreover, the ^{45}Sc NMR characterization of $LnSc_2N@C_{80}$ pointed out that the unique behavior of $NdSc_2N@C_{80}$ as well, see Figure 4.18.

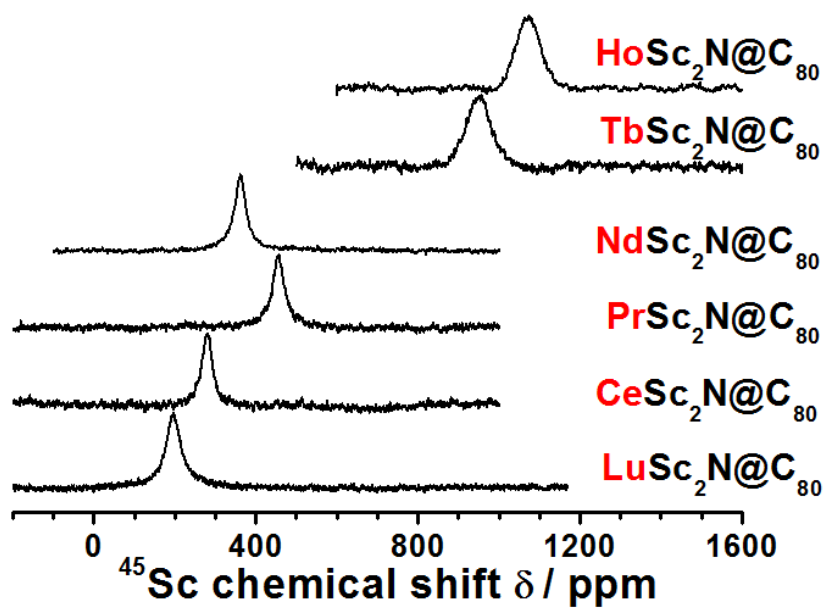


Figure 4.18 ^{45}Sc NMR spectra of $\text{LnSc}_2\text{N@C}_{80}$ (I; M= Ce, Pr, Nd, Tb, Ho and Lu) $\text{CS}_2/\text{d}_6\text{-acetone}$ at 288 K.

4.4 Conclusion

In summary, we performed ^{13}C and ^{45}Sc NMR study of a series of lanthanide-involved MMNCFs. Variable temperature ^{13}C NMR study of $\text{CeM}_2\text{N}@C_{80}$ ($M = \text{Sc}, \text{Lu}, \text{Y}$) reveals that paramagnetic ^{13}C NMR chemical shifts originate from the unpaired 4f-electron on Ce^{3+} in CeM_2N cluster. The single 4f electron located on the engaged Ce^{3+} induces the weakly paramagnetic up-field chemical shifts which combined with the down-field chemical shifts induce the pyramidal CeY_2N . Strikingly different to $\text{CeSc}_2\text{N}@C_{80}$, $\text{PrSc}_2\text{N}@C_{80}$ and $\text{NdSc}_2\text{N}@C_{80}$, $4f^{10}\text{-Ho}^{3+}$ results in a remarkable broadness of the NMR peaks and extraordinary paramagnetic chemical shifts in the ^{13}C and ^{45}Sc NMR spectra. The variable-temperature ^{45}Sc NMR spectroscopic study demonstrated that the Ho-induced paramagnetic shift is dominated by the pseudocontact term. As the first successful and comprehensive report on the ^{13}C and ^{45}Sc NMR with more than the unpaired 4f-electron on the engaged nitride cluster with different cage symmetry, the study of $\text{HoSc}_2\text{N}@C_{80}$ (I and II) shows the possibilities for further detailed studies of the state of paramagnetic metal atoms in MMNCFs. Due to the well-known fact that lanthanide contraction, the primary ^{13}C and ^{45}Sc NMR analysis of $\text{LnSc}_2\text{N}@C_{80}$ (I) was achieved which could be improved in with considering the slight changes in the crystal field parameters based on the combination of theoretical calculations and the confirmation of their single crystal structures in the future. The good linear fitting ($R^2 = 0.99$) could be obtained by considering the encapsulating LnSc_2N cluster ($\text{Ln} = \text{Ce}, \text{Pr}, \text{Nd}, \text{Tb}, \text{Dy}, \text{Ho}, \text{Lu}$) inside $C_{80}:I_h$ cage which indicated the fantastic nature of magnetic anisotropy of lanthanide metals. The potential application of single molecular magnet could be expected.

Chapter 5 Electrochemical Study of Ce-based Mixed Metal Nitride Clusterfullerenes

The electrochemical properties of MMNCFs are naturally dependent on the carbon cage and encaged species.^{45,83} The extensive experimental and theoretical studies demonstrated that all of the lanthanide involved C₈₀-based (*I_h*) homogeneous metal NCFs had similar redox behaviors and the M₃N cluster plays a marginal part in the contribution to the LUMO of the endohedral fullerenes, except for Sc₃N. The knowledge about the electrochemical properties is that the oxidation or reduction of metal NCFs occurs by changing the charge state of the carbon cage.^{84,85} For M₃N@C₈₀ (except for M= Sc), the spin state of the cation and anion can be described as mostly locating on the carbon cage, whereas the inner cluster remains redox-inert. Although the great progress in synthesis of new class of endohedral fullerenes has been already achieved, seeking new strategies to activate the metal nitride cluster inside the carbon cage and further tune the electronic properties of metal NCFs becomes a big challenge. Our group recently reported the electrochemical study of MMNCFs which enlightened us how to influence and manipulate the electronic state of NCFs. As revealed from previous studies, it is well known that MMNCFs inherit the electronic properties of metal NCFs and take the advantage of their relatively higher yield. To tune the electronic properties of NCFs, mixed metal nitride cluster template provides a convenient platform to achieve this goal. By selectively encapsulating the redox-active metal, the oxidation behaviors of NCFs could be tuned by endohedral species rather than be dominated by the charge transfer on the carbon cage. For instance, both of TiM₂N@C₈₀ (M = Sc, Y)^{45,56,86} proceed through a change of the valence state of the Ti atom. Redox behaviour of endohedral Ce is another exquisite example of the special role of the mixed-metal nitride cluster. Whereas the valence state of Ce^{III} in Ce₂@C_{2n} (2n= 72, 78, 80), Ce@C₈₂, or Ce₃N@C_{2n} (2n= 88, 92, 96) remains unaffected by the electrochemical oxidation of the EMF molecules, an unprecedented negative shift of the oxidation potential of CeLu₂N@C₈₀ in comparison to the standard values of M₃N@C₈₀ NCFs was discovered and tentatively assigned to the endohedral oxidation of Ce^{III} to Ce^{IV}. Remarkably, examples of the Ce^{IV}/Ce^{III} redox couple in organolanthanide chemistry are rather scarce (e.g., Ce(C₈H₈)₂,⁸⁷ Ce(Cp)₃(O-*i*-Pr),⁸⁸ Ce(octaethylporphyrin)₂,⁸⁹ a recent work on the

Ce complexes in the Shibasaki's heterobimetallic framework),⁹⁰ and finding of such couple in EMF opens a new dimension in organocerium chemistry.⁹¹⁻⁹⁸ In this chapter, we exhibit that the redox potential of the Ce^{IV}/Ce^{III} couple in the CeM₂N and Ce₂MN cluster systematically varies with the radius of the second metal and the size of the carbon cage (from C₈₀ to C₈₈).

5.1 Electrochemical study of CeY₂N@C₈₀

The electrochemical studies of CeM₂N@C₈₀ (I; M= Sc, Lu and Y) and PrSc₂N@C₈₀ were performed in *o*-DCB solution with TBAPF₄ as supporting electrolyte at room temperature which are shown in Figure 5.1 and summarized in Table 5.1. In the cathodic range, CeY₂N@C₈₀ exhibits two electrochemically irreversible reduction steps with half-wave potentials (E_p) at -1.36 V and -1.88 V (all potentials hereafter are vs. Fc(Cp)₂⁺⁰). Variation of the E_p values with different cluster composition of CeM₂N did not exceed 0.10 V. This behavior is typical for M₃N@C₈₀ NCFs and is consistent with the carbon cage-based reductions. In the anodic range, CeY₂N@C₈₀ exhibits one electrochemically reversible reduction step with half-wave potential at -0.07 V. It should be noted that the electrochemical oxidation behavior of PrSc₂N@C₈₀ is similar to those of M₃N@C₈₀ (M= Sc, Y or lanthanide metal). However, the oxidation behavior of the CeM₂N@C₈₀ is significantly different from that of PrSc₂N@C₈₀ or other M₃N@C₈₀. Significantly, the $E_{1/2}$ difference between CeSc₂N@C₈₀ and PrSc₂N@C₈₀ is 0.31 V. Furthermore, the substantial negative shifts could be induced by enlarging the size of the encaged cluster in the order of CeSc₂N@C₈₀ (0.33 V) → CeLu₂N@C₈₀ (0.01 V) → CeY₂N@C₈₀ (-0.07 V). Thus, enlarging the size of the encaged CeM₂N cluster induces substantial negative shift (up to 0.40 V) of the oxidation potential. It could be found that the electrochemical energy gaps of Ce-based MMNCFs are mainly dependent on the oxidation potential rather than reduction potential.

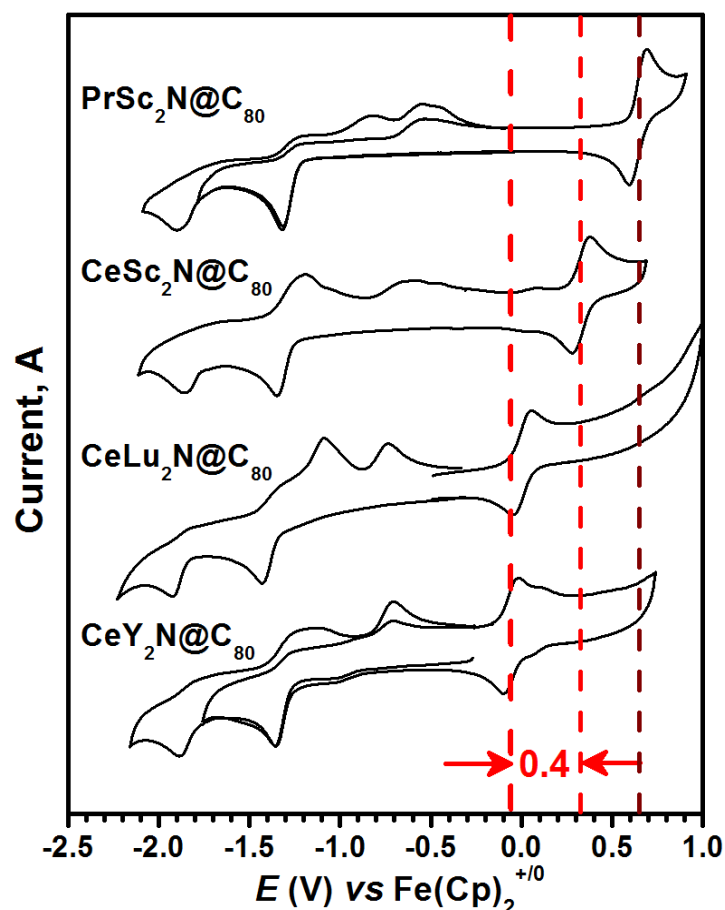


Figure 5.1 Cyclic voltammograms of $\text{CeM}_2\text{N@C}_{80}$ ($M = \text{Sc, Lu and Y}$) and $\text{PrSc}_2\text{N@C}_{80}$ measured at room temperature in *o*-DCB solution with TBABF_4 as supporting electrolyte, scan rate 100 mV/s.

Compound	method	$E_{1/2}(\text{ox})$	$E_p(\text{red-I})$	$E_p(\text{red-II})$	gap_{EC}
$\text{CeY}_2\text{N@C}_{80}$	CV	-0.07	-1.36	-1.88	1.30
	SWV	-0.06	-1.32	-1.83	1.25
$\text{CeLu}_2\text{N@C}_{80}$	CV	0.01	-1.43	-1.92	1.44
	SWV	0.01	-1.39	-1.88	1.40
$\text{CeSc}_2\text{N@C}_{80}$	CV	0.33	-1.34	-1.87	1.67
	SWV	0.33	-1.31	-1.83	1.64
$\text{PrSc}_2\text{N@C}_{80}$	CV	0.64	-1.32	-1.91	1.96
	SWV	0.64	-1.26	-1.83	1.91

Table 5.1 Redox potentials of $\text{CeM}_2\text{N@C}_{80-I_h(7)}$ and $\text{PrSc}_2\text{N@C}_{80-I_h(7)}$. (a) All values in V versus $\text{Fe}(\text{Cp})_2^{+/0}$ couple; (b) CV denotes cyclic voltammetry, SWV denotes square-wave voltammetry, $E_{1/2}$ is half-wave potential (for CV), and E_p is a peak potential.

The large difference between the oxidation potentials of $\text{CeLu}_2\text{N@C}_{80}$ and other $\text{M}_3\text{N@C}_{80}$ NCFs ($E_{1/2} \sim 0.6\text{--}0.7$ V) served as a first indication of the Ce-based redox process in $\text{CeLu}_2\text{N@C}_{80}$. Likewise, the endohedral oxidation of Ce can be postulated for $\text{CeY}_2\text{N@C}_{80}$ studied in this work. Significantly more positive oxidation potential of $\text{CeSc}_2\text{N@C}_{80}$ raises the question whether it can be assigned to the endohedral $\text{Ce}^{\text{IV}}/\text{Ce}^{\text{III}}$ couple as well, or whether

an oxidation of the carbon cage takes place. For comparison, we have studied redox properties of $\text{PrSc}_2\text{N@C}_{80}$ as the closest analogue of $\text{CeSc}_2\text{N@C}_{80}$ with a similar size of the nitride cluster. Reversible oxidation of $\text{PrSc}_2\text{N@C}_{80}$ is found at +0.64 V, in close similarity to many other $\text{M}_3\text{N@C}_{80}$ molecules. The $E_{1/2(\text{ox})}$ difference of 0.31 V between $\text{CeSc}_2\text{N@C}_{80}$ and $\text{PrSc}_2\text{N@C}_{80}$ indicates that oxidation of $\text{CeSc}_2\text{N@C}_{80}$ is a Ce-based process.

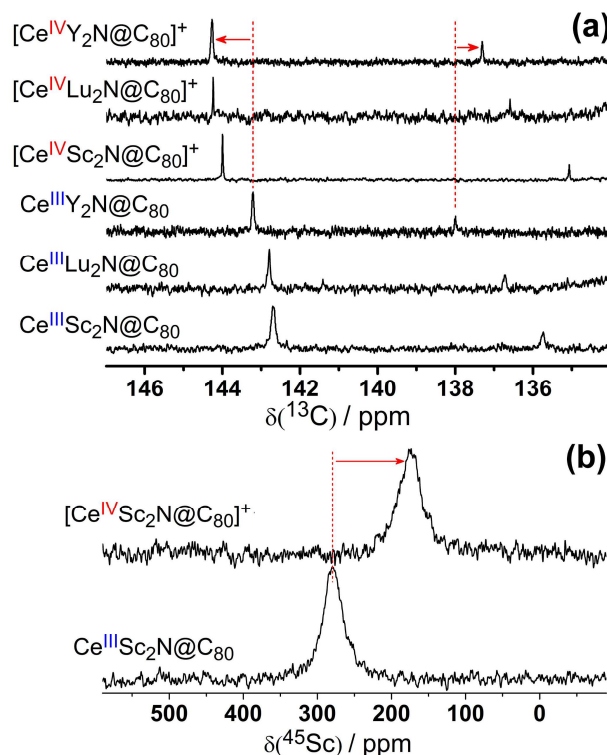


Figure 5.2 (a) ^{13}C NMR spectra of paramagnetic $\text{Ce}^{\text{III}}\text{M}_2\text{N@C}_{80}$ ($\text{M} = \text{Sc}, \text{Lu}, \text{Y}$) and their oxidized diamagnetic counterparts $[\text{Ce}^{\text{IV}}\text{Y}_2\text{N@C}_{80}]^+$ measured in *o*- d_4 -DCB at 288 K; (b) ^{45}Sc NMR spectra of $\text{CeSc}_2\text{N@C}_{80}$ and $[\text{CeSc}_2\text{N@C}_{80}]^+$.

A compelling evidence of the endohedral oxidation of Ce^{III} in all studied $\text{CeM}_2\text{N@C}_{80}$ NCFs is obtained by ^{13}C NMR spectroscopy. If the oxidation of $\text{CeM}_2\text{N@C}_{80}$ is a fullerene-based process, their radical cations are expected to give no measurable NMR spectra, whereas an endohedral $\text{Ce}^{\text{III}} \rightarrow \text{Ce}^{\text{IV}}$ oxidation should produce diamagnetic cations accessible by ^{13}C NMR spectroscopy without a paramagnetic shift. $[\text{CeM}_2\text{N@C}_{80}]^+$ cations were obtained in *o*-DCB solution by reacting NCFs with $[\text{Fe}(\text{Cp})_2]^+[\text{BF}_4]^-$ ($\text{M} = \text{Y}$) or $\text{Ag}^+[\text{PF}_6]^-$ ($\text{M} = \text{Sc}, \text{Lu}$). The spectra measured after addition of the oxidation agent (Figure 5.2a) show a two-line pattern similar to $\text{CeM}_2\text{N@C}_{80}$, but the peaks are shifted to the lower field, close to the chemical shifts of diamagnetic $\text{M}_3\text{N@C}_{80}$ NCFs and δ_{dia} values determined for $\text{CeM}_2\text{N@C}_{80}$ in the VT-NMR studies (Table 5.2). Furthermore, the peak at $\delta = 280$ ppm in the ^{45}Sc NMR spectrum of $\text{CeSc}_2\text{N@C}_{80}$ is shifted to 175 ppm in $[\text{CeSc}_2\text{N@C}_{80}]^+[\text{PF}_6]^-$,

which is close to the value of $\delta(^{45}\text{Sc}) = 190$ ppm measured for $\text{Sc}_3\text{N@C}_{80}$ in *o*-DCB (Figure 5.2b). Thus, NMR spectroscopy unambiguously proves that diamagnetic $[\text{Ce}^{\text{IV}}\text{M}_2\text{N@C}_{80}]^+$ cations are produced.

$\text{CeM}_2\text{N@C}_{80}$	$q = 0$ ^[a]			$q = +1$
	δ	$c_{\text{pc}}^{[b]} \times 10^6 \text{ K}^2$	δ_{dia}	δ
$\text{CeSc}_2\text{N@C}_{80}$	142.69	-0.22	145.29	144.02
	135.74	-0.17	137.93	135.08
$\text{CeLu}_2\text{N@C}_{80}$	142.79	-0.20	144.85	144.24
	136.72	-0.23	139.06	136.59
$\text{CeY}_2\text{N@C}_{80}$	143.22	-0.17	145.38	144.27
	138.00	-0.24	140.92	137.31

Table 5.2 ^{13}C NMR chemical shifts (δ , ppm) in $\text{CeM}_2\text{N@C}_{80}\text{-}I_h(7)$; [a] The data are given for a neutral state ($q=0$) and the cationic state ($q=+1$); [b] c_{pc} and δ_{dia} are obtained in CS_2 solution in the 268-208 K range.

As far as the endohedral oxidation of Ce^{III} is confirmed, the question to be considered is why the oxidation potential of the Ce^{III} in the CeM_2N cluster depends so strongly on the second cluster metal, M, which is not involved in the redox process? To address this problem we have performed DFT calculations of the $\text{CeM}_2\text{N@C}_{80}$ and $\text{M}_3\text{N@C}_{80}$ molecules in the neutral and charged states. Table 5.3 lists the ionization potentials (IP) of the molecules under study. Two ionization pathways, $\text{Ce}^{\text{III}} \rightarrow \text{Ce}^{\text{IV}}$ (IP_{Ce}) and oxidation of the fullerene cage (IP_{cage}), were analyzed. The former was modeled by the singlet state of the $[\text{CeM}_2\text{N@C}_{80}]^+$ cation, whereas the latter was addressed by studying the triplet state of $[\text{CeM}_2\text{N@C}_{80}]^+$.

molecule ^[a]	IP_{Ce}	IP_{cage}	$d_{\text{M-N}}(0 \rightarrow +1)^{[b]}$	$d_{\text{Ce-N}}(0 \rightarrow +1)$
$\text{CeY}_2\text{N@C}_{80}$	6.34	6.96	2.052→2.117	2.100→1.956
$\text{Y}_3\text{N@C}_{80}$		6.95	2.048	
$\text{CeLu}_2\text{N@C}_{80}$	6.50	6.95	2.012→2.090	2.108→1.994
$\text{Lu}_3\text{N@C}_{80}$		6.93	2.043	
$\text{CeSc}_2\text{N@C}_{80}$	6.85	6.96	1.946→2.047	2.192→2.051
$\text{Sc}_3\text{N@C}_{80}$		6.90	2.025	

Table 5.3 DFT-computed IP and bond lengths in $\text{CeM}_2\text{N@C}_{80}$ and $\text{M}_3\text{N@C}_{80}$ (M = Sc, Lu, Y). [a] IP values in eV, bond length in Å; [b] M–N bonds are slightly different in CeM_2N clusters (within 0.01 Å), the mean values are listed.

Computed IPs of $M_3N@C_{80}$ NCFs and IP_{cage} values of $CeM_2N@C_{80}$ are all within the range of 6.90–6.96 eV (Table 5.3). Hence, if oxidation of $CeM_2N@C_{80}$ molecules were a cage-based process, similar oxidation potentials could be expected. However, in perfect agreement with electrochemical data, computation shows that removal of the $4f^1$ electron from Ce^{III} is more energetically favourable, i.e. IP_{Ce} is lower than IP_{cage} for all $CeM_2N@C_{80}$. Furthermore, IP_{Ce} values show noticeable variation with the second metal (from 6.34 eV in $CeY_2N@C_{80}$ to 6.85 eV in $CeSc_2N@C_{80}$) and follow the same trend as found in oxidation potentials. Thus, there is a qualitative agreement with experimental electrochemical data and hence the results of calculations can be used for a more detailed analysis of the role of the second cluster metal.

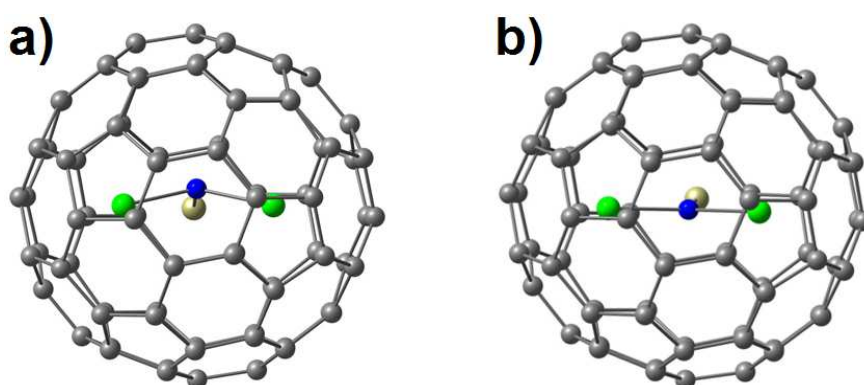


Figure 5.3 DFT-optimized structures of (a) $Ce^{III}Y_2N@C_{80}$ and (b) $[Ce^{IV}Y_2N@C_{80}]^+$.

For $CeSc_2N@C_{80}$, DFT predicts a planar $CeSc_2N$ cluster with the Ce–N bond length of 2.192 Å (experimental value is 2.184 Å) in Figure 5.3 and 5.4. The Sc–N bond length is only 1.946 Å (exp. 1.933/1.944 Å), considerably shorter than 2.025 Å in $Sc_3N@C_{80}$. When two Sc atoms in $CeSc_2N$ are replaced by Lu with the larger ionic radius, the Ce–N bond becomes shorter (2.108 Å), and the length of Lu–N bonds (2.012 Å) is decreased compared to $Lu_3N@C_{80}$ (2.043 Å). In $CeY_2N@C_{80}$ the Ce–N bond length is shortened to 2.100 Å, whereas the averaged Y–N bond length, 2.052 Å, is virtually identical to that in $Y_3N@C_{80}$, 2.048 Å. This analysis shows that the C_{80} cage provides a limited interior space, and encapsulation of the large Ce^{3+} ion within the CeM_2N cluster results in a significant strain leading to the shortening of the M–N bonds as compared to their lengths in $M_3N@C_{80}$. Obviously, this strain is increasing with the ionic radius of M^{3+} . Furthermore, as the Y_3N cluster in $Y_3N@C_{80}$ is already strongly strained the Y–N bonds cannot become shorter in $CeY_2N@C_{80}$. Instead, to increase the length of the Ce–N bond, the nitrogen atom is displaced above the CeY_2 plane by 0.408 Å and the CeY_2N cluster becomes pyramidal ($CeSc_2N$ and $CeLu_2N$ clusters are planar). This situation is similar to that in $Gd_3N@C_{80}$ with pyramidal Gd_3N cluster.

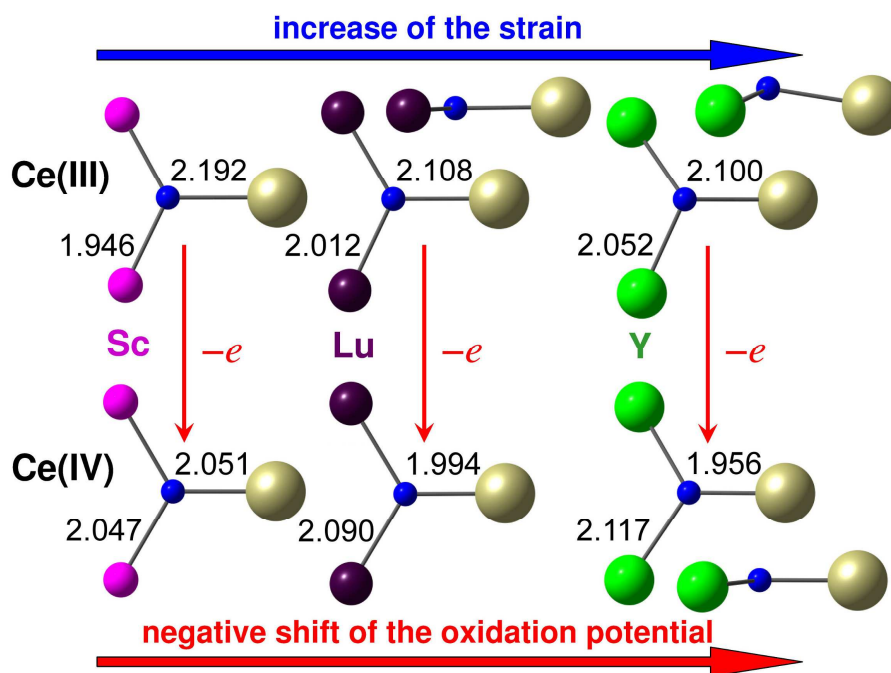


Figure 5.4 DFT-optimized bond lengths (Å) of the $\text{Ce}^{\text{III}}\text{M}_2\text{N}$ and $\text{Ce}^{\text{IV}}\text{M}_2\text{N}$ clusters ($\text{M} = \text{Y}, \text{Lu}$ and Sc) in $\text{CeM}_2\text{N}@C_{80}$ and $[\text{CeM}_2\text{N}@C_{80}]^+$, respectively.

When Ce-based oxidation of $\text{CeM}_2\text{N}@C_{80}$ takes place, the inner strain is reduced because ionic radius of Ce^{4+} (0.85 Å) is dramatically smaller than that of Ce^{3+} (1.03 Å). Hence, Ce–N bonds in $[\text{Ce}^{\text{IV}}\text{M}_2\text{N}@C_{80}]^+$ cations are much shorter than in corresponding neutral molecules, whereas M–N bonds are longer (in fact, even longer than in $\text{M}_3\text{N}@C_{80}$). The effect is most apparent for yttrium: the Y–N bonds in $[\text{CeY}_2\text{N}@C_{80}]^+$, 2.117 Å, are longer than in $\text{Y}_3\text{N}@C_{80}$, 2.048 Å, whereas the Ce–N bond is as short as 1.956 Å and the $\text{Ce}^{\text{IV}}\text{Y}_2\text{N}$ cluster is planar. Based on the optimized bond lengths, we can conclude that the effective radius of Ce^{IV} in NCFs is comparable to that of Sc. Thus, the Ce-induced strain in the CeM_2N cluster is released when Ce is oxidized and a substitution of one M atom in the M_3N cluster by the "small" Ce^{4+} allows the release of the inner strain of the engaged clusters.

We can thus conclude that the driving force of the Ce^{III} oxidation in $\text{CeM}_2\text{N}@C_{80}$ molecules is the release of the inherent strain caused by the large size of the cluster and the limited inner space of the carbon cage. The larger the cluster, the stronger the strain and hence the molecule is more eager to be oxidized. An increase of the ionic radius of the second cluster metal in $\text{CeM}_2\text{N}@C_{80}$ (Sc, Lu, Y) increases the size of the cluster and hence shifts the oxidation potential to more negative values. In other words, the difference in the oxidation potentials of endohedral Ce^{III} ions allows the electrochemical determination of the strain energy in NCFs. As far as we know, this is the first discovery of a relationship between the redox potential of an endohedral fullerenes and the geometry of endohedral species.

5.2 Electrochemical study of $\text{Ce}_x\text{Y}_{3-x}\text{N}@C_{2n}$ ($2n= 84, 86, 88$)

Due to the inherent strain between the metal nitride cluster and carbon cage, the general and relative yield of NCFs is quite sensitive to the kind of entrapped metal.⁹⁹ The NCFs experienced rapid development in recent years, most of metal nitride clusters could be preferably stabilized by the C_{80-I_h} cage.¹⁰⁰ The unique strategy of mixed metal nitride cluster template enhances the general yield of MMNCFs. So far, the Sc-based MMNCFs have been widely studied in the form of $\text{LnSc}_2\text{N}@C_{80}$ (Ln= La, Ce, Nd, Gd, Tb, Dy, Ho, Er, Lu, Y and Ti) and in the form of $\text{M}_2\text{ScN}@C_{80}$ (M= Nd, Gd, Dy, Ho, Er, Lu and Y). Nevertheless, for the cage size larger than C_{80} the yield of Sc-based MMNCFs strikingly declined which becomes the bottleneck for the extensive studies. Interestingly, Gd-based NCFs firstly exhibited that the most abundant product toward $\text{Gd}_3\text{N}@C_{84-88}$.⁴³ As explained by Echegoyen *et al.*, the increase of the cluster size results in the shift of the major product toward $\text{Ln}_3\text{N}@C_{88-96}$ (Ln= La, Ce Pr and Nd). Therefore, the series of lanthanide-based NCFs could be divided into two groups by taking into account of the difference of their ionic radii regarding Gd^{3+} as the threshold: a) Group I: La, Ce, Pr and Nd; b) Group II: Gd, Tb, Dy, Ho, Er, Tm and Lu. The electrochemical studies of $\text{Gd}_3\text{N}@C_{2n}$ ($2n= 80-88$) were performed by Echegoyen *et al.* which indicated that increasing the cage size does not significantly affect their reduction potentials, but considerably influences their oxidation potentials. Their further studies demonstrated $\text{Ln}_3\text{N}@C_{88}$ (Ln= Ce, Pr and Nd) behave similar to $\text{Gd}_3\text{N}@C_{88}$ with the first oxidation at low potentials (c.a. 0.06-0.08 V). As the natural obstacle of homogenous metal NCFs with extremely small or large metal ionic radius, in the case of Sc, no $\text{Sc}_3\text{N}@C_{2n}$ structure with cage larger than C_{80} was confirmed; in the case of La and Ce, no $\text{Ce}_3\text{N}@C_{2n}$ or $\text{La}_3\text{N}@C_{2n}$ with cage size smaller than C_{88} was isolated and characterized. After the first successful attempt of $\text{CeM}_2\text{N}@C_{80}$ (M= Sc, Lu, Y), it would be a fantastic chance to wander in the garden of Ce-based MMNCFs with cage between C_{80} and C_{88} with the supporting of second metal as ‘*scaffold metal*’. For lanthanide metal with the ionic radius smaller than Gd^{3+} , the distribution of the product is similar to that of $\text{Y}_3\text{N}@C_{2n}$ (Ln= Tb-Lu) with the preferred formation of $\text{Ln}_3\text{N}@C_{80}$. With the radius of 0.90 Å, the geometry of the Y_3N inside the C_{80} cage is slightly pyramidal which could be considered as the advantage to sustain the suitable cluster-cage strain as in the case of $\text{Ce}_x\text{Y}_{3-x}\text{N}@C_{2n}$ ($2n= 84$ and 86). We hypothesize that once combining Y with the lanthanide metal (Ln= La, Ce, Pr and Nd): a) the mixed metal nitride cluster $\text{Ln}_x\text{Y}_{3-x}\text{N}$ could be feasibly entrapped to the cage as small as C_{80} due to the effective tailoring of the cluster size; b) the product distribution could be induced to a novel pattern which enhances the relative yield of the $\text{Ce}_x\text{Y}_{3-x}\text{N}@C_{84-88}$ ($x= 1, 2$); c) the electrochemical,

paramagnetic and spectroscopic properties of Ce/Y MMNCFs with cage size smaller than C_{88} could be realized.

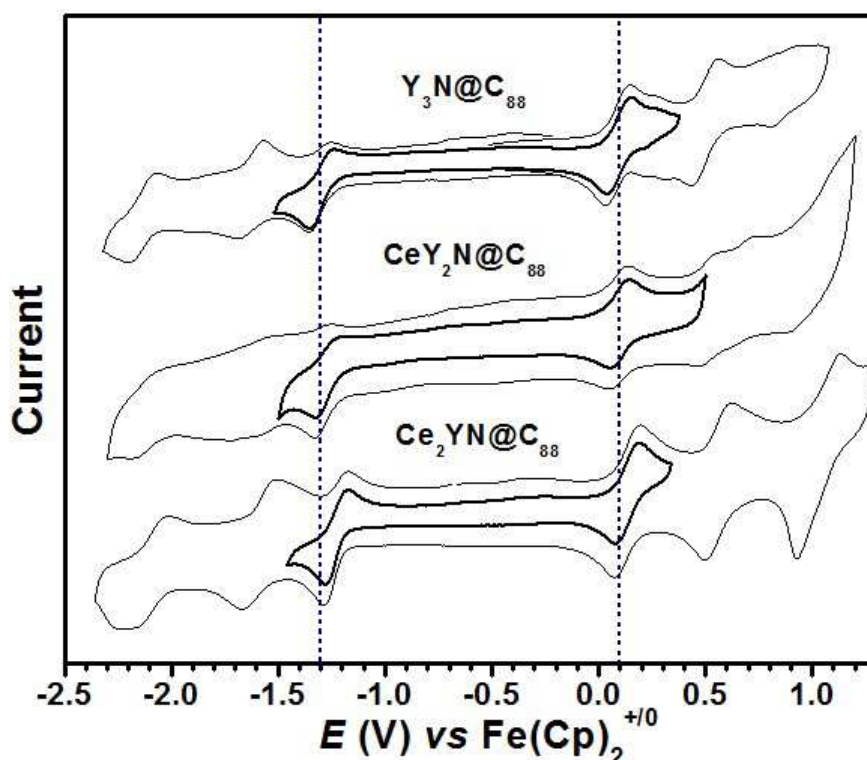


Figure 5.5 Cyclic voltammogram of $Y_3N@C_{88}$, $CeY_2N@C_{88}$ and $Ce_2YN@C_{88}$ (vs. $Fc(Cp)_2^{+/0}$) measured in *o*-DCB solution with 0.1 M TBABF₄ as supporting electrolyte, scan rate is 100 mV /s.

The electrochemical measurements of Ce-based MMNCFs were performed (vs. $Fc(Cp)_2^{+/0}$) in *o*-dichlorobenzene (*o*-DCB) solution with 0.1 M TBABF₄ as supporting electrolyte. The cyclic voltammetry (CV) and square-wave voltammetry (SWV) of $Y_3N@C_{88}$, $CeY_2N@C_{88}$ and $Ce_2YN@C_{88}$ are compared in Figure 5.5 and summarized in Table 5.4. In the cathodic range, $Y_3N@C_{88}$ exhibits two electrochemically reversible reduction steps with $E_{1/2}$ at -1.30 and -1.62 V and one irreversible step with E_p near at -2.13 V. In the anodic range, two electrochemically reversible oxidation steps ($E_{1/2}$) at 0.10 and 0.50 V are observed which agree well with known structures $M_3N@C_{88}$ (M= Ce, Pr, Nd, Gd and Y).^{43,101,102} Substituting the encaged cluster from Y_3N to CeY_2N or Ce_2YN does not considerably influence the reduction behaviors of the $Ce_xY_{3-x}N@C_{88}$ ($x= 1, 2$). However, the oxidation behaviors of $CeY_2N@C_{88}$ exhibited four electrochemical steps which are different to $Y_3N@C_{88}$ and $Ce_2YN@C_{88}$. Although the redox potentials of $Ce_xY_{3-x}N@C_{88}$ measured in our system are slightly higher than previous results, their electrochemical gap (EC_{gap}) of are almost the same (~1.40 V; calculated as the difference of peak potential measured by SWV). No considerable

contribution was observed from the presence of endohedral Ce atom(s) in $Ce_xY_{3-x}N@C_{88}$ ($x=1, 2$).

Compounds	method	ox-II	ox-I	red-I	red-II	EC_{gap}
$Y_3N@C_{88}$	CV	0.50	0.10	-1.30	[-1.62]	1.40
	SW	0.51	0.10	-1.29	-1.62/-1.83	1.39
$CeY_2N@C_{88}$	CV	0.53	0.10	-1.29	[-1.62/-1.70]	1.39
	SW	0.53	0.10	-1.28	-1.60	1.38
$Ce_2YN@C_{88}$	CV	0.55	0.13	-1.25	[-1.56/-1.69]	1.38
	SW	0.55	0.13	-1.25	-1.62	1.37
$Y_3N@C_{88}$	CV	0.43	0.03	[-1.43]	[-1.70]	1.46
$Gd_3N@C_{88}$	CV	0.45	0.05	[-1.39]	[-1.71]	1.44
$Gd_3N@C_{88}$	CV	0.49	0.06	[-1.43]	[-1.74]	1.49
$Nd_3N@C_{88}$	CV	0.53	0.07	[-1.36]	[-1.75]	1.43
$Pr_3N@C_{88}$	CV	0.54	0.09	[-1.34]	[-1.72]	1.43
$Ce_3N@C_{88}$	CV	0.63	0.08	[-1.30]	[-1.57]	1.38
$Y_3N@C_{86}$	CV	[0.87]	0.36	[-1.33]	[-1.73]	1.69
	SW	0.78	0.36	-1.28	-1.68	1.65
$CeY_2N@C_{86}$	CV	0.82	0.27	[-1.38]	[-1.76]	1.65
	SW	0.83	0.27	-1.34	-1.73	1.61
$Ce_2YN@C_{86}$	CV		0.17	[-1.35]	[-1.75]	1.52
	SW		0.16	-1.32	-1.71	1.48
$Gd_3N@C_{86}$	CV		0.33	[-1.39]	[-1.72]	1.72
$Nd_3N@C_{86}$	CV		0.36	[-1.46]	[-1.79]	1.82
$Pr_3N@C_{86}$	CV		0.31	[-1.48]	[-1.80]	1.79
$Y_3N@C_{84}$	CV	0.75	0.34	[-1.35]	[-1.78]	1.69
	SW	0.75	0.34	-1.30	-1.73	1.64
$CeY_2N@C_{84}$	CV	0.81	0.22	[-1.36]	[-1.81]	1.58
	SW	0.82	0.23	-1.29	-1.75	1.52
$Nd_3N@C_{84}$	CV		0.31	[-1.44]		1.75
$Gd_3N@C_{84}$	CV		0.32	[-1.37]	[-1.76]	1.69

Table 5.4 Redox potential of $Ce_xM_{3-x}N@C_{2n}$ ($2n= 84, 86, 88$) compared with $M_3N@C_{2n}$, (a) All values in V versus $Fe(Cp)_2^{+/0}$ couple; (b) CV denotes cyclic voltammetry, SWV denotes square-wave voltammetry, $E_{1/2}$ is half-wave potential (for CV), and E_p is a peak potential; [] - peak potentials for irreversible steps.

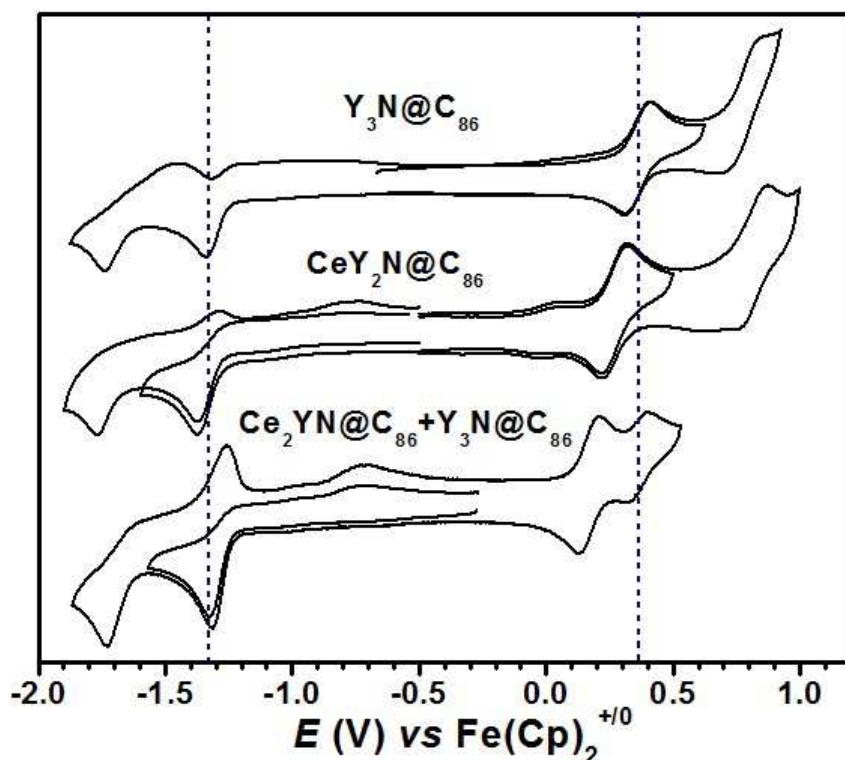


Figure 5.6 Cyclic voltammogram of $Y_3N@C_{86}$, $CeY_2N@C_{86}$ and the mixture of $Ce_2YN@C_{86}$ and $Y_3N@C_{86}$ measured in *o*-DCB solution with 0.1 M TBABF₄ as supporting electrolyte, scan rate is 100 mV /s.

As aforementioned, with slight shrinking of cage size from C₈₈ to C₈₆, Ce₃N@C₈₆ could be determined from mass spectrum but no pure structure has been isolated. Therefore, typical metal NCFs including Gd₃N@C₈₆, Nd₃N@C₈₆ and Pr₃N@C₈₆ were employed as references for the electrochemical study of Ce_xY_{3-x}N@C₈₆ (x = 0-2), see Table 5.4. Due to the retention time of Ce₂YN@C₈₆ and Y₃N@C₈₆ is very close, these two compounds were collected in the same fraction but no other structure is detected from mass spectrum characterization. The reduction potentials for Ce_xY_{3-x}N@C₈₆ are in good agreement with reported results, see Figure 5.6. It should be noted that replacing one Y with Ce, the oxidation potentials of CeY₂N@C₈₆ ($E_{1/2}$ = 0.27 V) is slightly lower than Y₃N@C₈₆ ($E_{1/2}$ = 0.36 V) and other M₃N@C₈₆ systems (Gd: 0.33 V, Nd: 0.36 V and Pr: 0.31 V).⁴³ It became more convincing that Ce₂YN cluster encaged into C₈₆ cage results in its first oxidation potential lower to 0.17 V. The second reversible oxidation behavior could be unambiguously assigned to the minor structure Y₃N@C₈₆ in this fraction due to its $E_{1/2}$ (~0.36 V). Hence, the electrochemical gaps of Ce_xY_{3-x}N@C₈₆ are dependent on the endohedral Ce atom(s) and distinguished with previous known MMNCFs with C₈₆ cage.

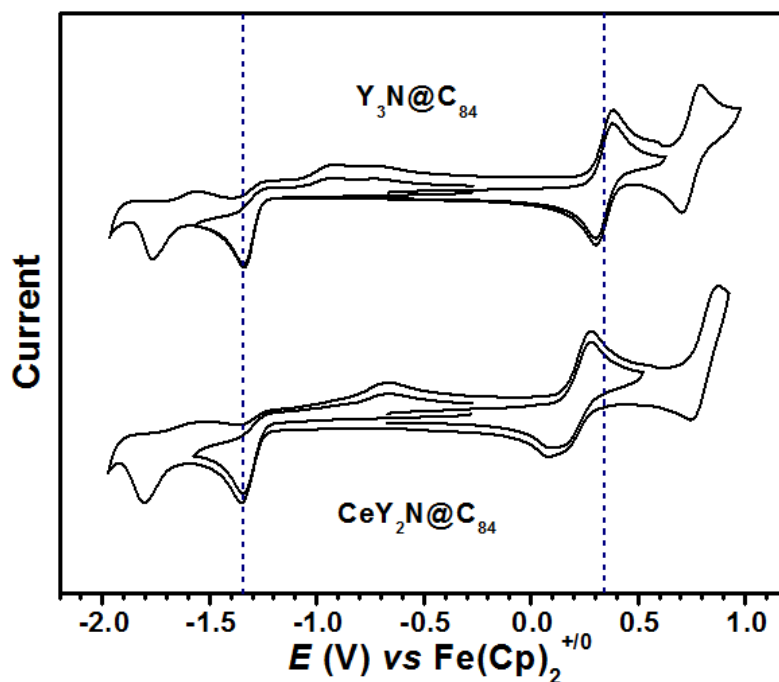


Figure 5.7 Cyclic voltammogram of $Y_3N@C_{84}$ and $CeY_2N@C_{84}$ measured in o-DCB solution with 0.1 M TBABF₄ as supporting electrolyte, scan rate is 100 mV /s.

To further investigate Ce-induced the electrochemical oxidation potential shifts, $Y_3N@C_{84}$ and $CeY_2N@C_{84}$ were studied in the same process, see Figure 5.7. For $Y_3N@C_{84}$, it is the first time to observe the two reversible electrochemical oxidation steps among the presence of metal NCFs with $C_{84}-C_s$ cage. The first oxidation step of $Y_3N@C_{84}-C_s$ at $E_{1/2} = 0.34$ V agrees well with $Gd_3N@C_{84}-C_s$ and $Nd_3N@C_{84}-C_s$ reported by Echegoyen *et al.*⁴³ Switching the cluster from Y_3N to CeY_2N conducts unanticipated fact that the first electrochemical oxidation step of $CeY_2N@C_{84}$ becomes irreversible but the second step remains reversible. Once increasing the scan rate from 0.1 to 1.0 V s⁻¹, the reversibility of the oxidation step could be gradually improved, see Figure 5.8. The reduction behaviors of $CeY_2N@C_{84}$ and $Y_3N@C_{84}$ are almost identical, the electrochemical gap of $CeY_2N@C_{84}$ strongly correlated to the size of the encaged cluster which is consistent with our recent report on $CeM_2N@C_{80}$.

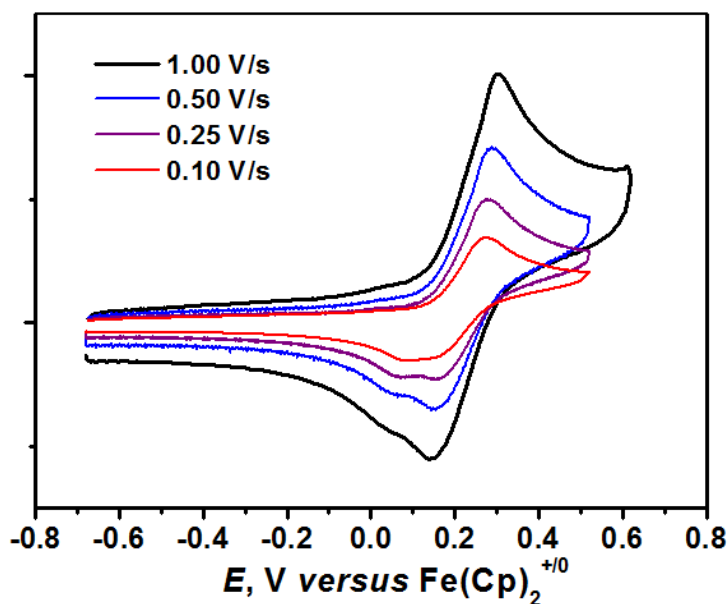


Figure 5.8 CV scan rate study of the first reduction wave of $\text{CeY}_2\text{N@C}_{84}$. Scan rates of 0.10, 0.25, 0.50, 1.00 V/s.

compound ^[a]	IP_{Ce}	IP_{cage}	$\Delta\text{IP}^{[b]}$	$E_{1/2}(\text{ox})$	$d_{\text{Ce-N}}^{[c]}$	$d_{\text{Y-N}}$
$\text{Y}_3\text{N@C}_{88}$		6.22		0.10		2.185
$\text{CeY}_2\text{N@C}_{88}\text{-a}$	6.80	6.23	-0.57	0.10	2.231	2.161
$\text{CeY}_2\text{N@C}_{88}\text{-b}$	6.49	6.22	-0.27	0.10	2.230	2.164
$\text{Ce}_2\text{YN@C}_{88}\text{-a}$	6.57	6.22	-0.35	0.13	2.220	2.130
$\text{Ce}_2\text{YN@C}_{88}\text{-b}$	6.60	6.22	-0.38	0.13	2.218	2.122
$\text{Ce}_2\text{YN@C}_{88}\text{-c}$	6.62	6.22	-0.40	0.13	2.219	2.122
$\text{Ce}_3\text{N@C}_{88}$	6.41	6.26	-0.15			
$\text{Y}_3\text{N@C}_{86}$		6.56		0.36		2.161
$\text{CeY}_2\text{N@C}_{86}$	6.78	6.55	-0.23	0.27	2.200	2.137
$\text{Ce}_2\text{YN@C}_{86}$	6.50	6.54	0.04	0.17	2.192	2.099
$\text{Ce}_3\text{N@C}_{86}$	6.32	6.58	0.26			
$\text{Y}_3\text{N@C}_{84}$		6.51		0.34		2.145
$\text{CeY}_2\text{N@C}_{84}\text{-a}$	6.46	6.53	0.07	0.22	2.211	2.109
$\text{CeY}_2\text{N@C}_{84}\text{-b}$	6.59	6.54	-0.05	0.22	2.166	2.127

Table 5.5 DFT-computed IP and bond lengths in $\text{Ce}_x\text{M}_{3-x}\text{N@C}_{2n}$ and $\text{Y}_3\text{N@C}_{2n}$ ($x=1, 2$; $2n=84-88$). [a] IP values in eV; [b] $\Delta\text{IP} = \text{IP}_{\text{cage}} - \text{IP}_{\text{Ce}}$. [c] The mean values of M–N bonds are listed.

Table 5.5 shows that computed IP_{Ce} values of $Ce_xY_{3-x}N@C_{88}$ ($x=0-3$) is higher than IP_{cage} . Consequently, the oxidation of $Ce_2YN@C_{88}$ and $CeY_2N@C_{88}$ molecules is a cage-based process due to their first reduction and oxidation potentials are similar to $Gd_3N@C_{88}$ and $Y_3N@C_{88}$. Our calculations point out that even Ce_3N inside the C_{88} cage, the IP_{cage} is still lower than the IP_{Ce} which is consistent with the electrochemical studies that all of $Ce_xY_{3-x}N@C_{88}$ ($x=0-3$) which behave similar to $Gd_3N@C_{88}$, $Nd_3N@C_{88}$ and $Pr_3N@C_{88}$. Computed ΔIP (the difference between IP_{cage} and IP_{Ce}) of $Ce_xY_{3-x}N@C_{2n}$ ($x=1, 2; 2n=84, 86$) MMNCFs are smaller than the case of $CeM_2N@C_{80}$ ($M=Sc, Lu, Y$). The DFT-optimized structure of $Ce_xY_{3-x}N@C_{2n}$ ($2n=84-88$) are presented in Figure 5.9 - 5.12. Based on our current results, it could be presumed that the different position of CeY_2N and Ce_2YN cluster inside the carbon cage (from C_{84} to C_{88}) play an essential role in the ionization potentials of C_{84-} and C_{86-} compounds. For $CeY_2N@C_{88}$ -(a, b) and $Ce_2YN@C_{88}$ -(a, b, c), each of $Ce_xY_{3-x}N$ unit is planar in the flattened carbon cage. The positions of the Ce atom(s) do not influence their electrochemical behaviors. Shrinking the cage size from C_{88} to C_{86} and further to C_{84} results in the increasing of the inner strain between the encaged cluster and carbon cage which decreasing the Ce-N bond length and driving the Ce-induced oxidation potential negatively shift. Secondly, the primary calculations suggest that the IP_{Ce} could be lower than the IP_{cage} by comparing the conformer $CeY_2N@C_{84}$ -a and $CeY_2N@C_{84}$ -b. In the C_{84} - C_y cage, the single Ce atom locating at the pentagon/pentagon pair is more energy favorable than the case of Y atom which is good agreement with the negative shifts of oxidation potential. However, the theoretical calculations underestimate the energy level of ionized Ce in $Ce_2YN@C_{86}$ and $CeY_2N@C_{86}$.

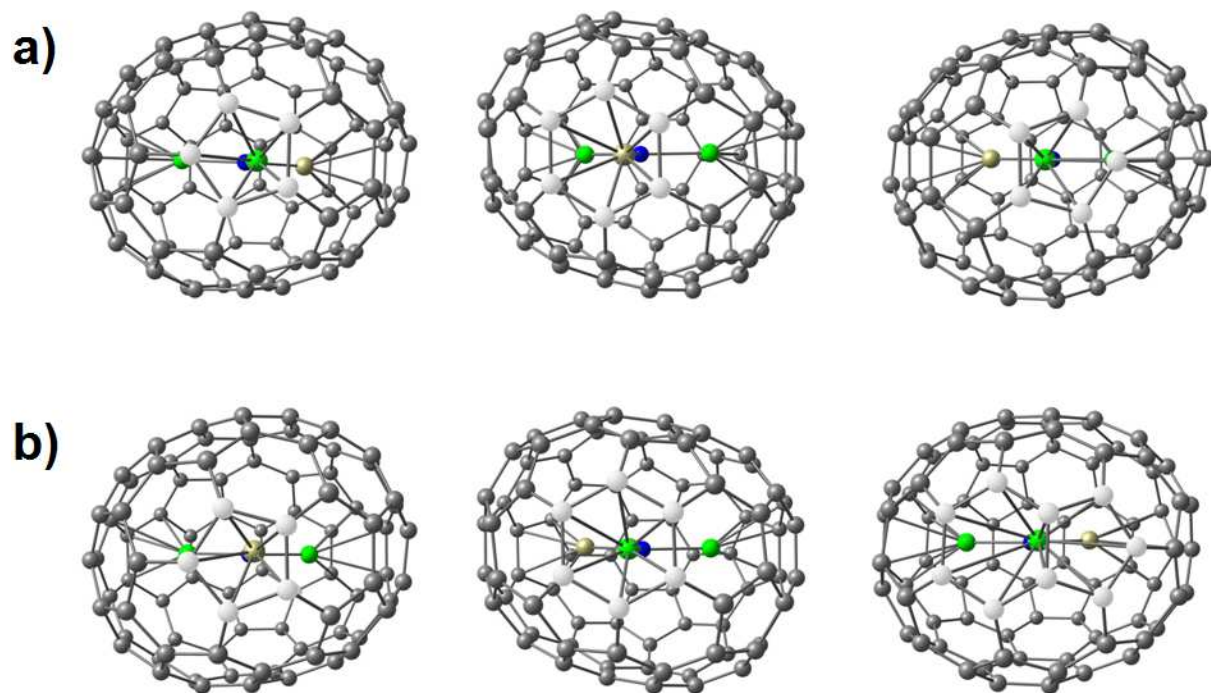


Figure 5.9 DFT-optimized structures of (a) $\text{CeY}_2\text{N}@C_{88}\text{-a}$ and (b) $\text{CeY}_2\text{N}@C_{88}\text{-b}$.

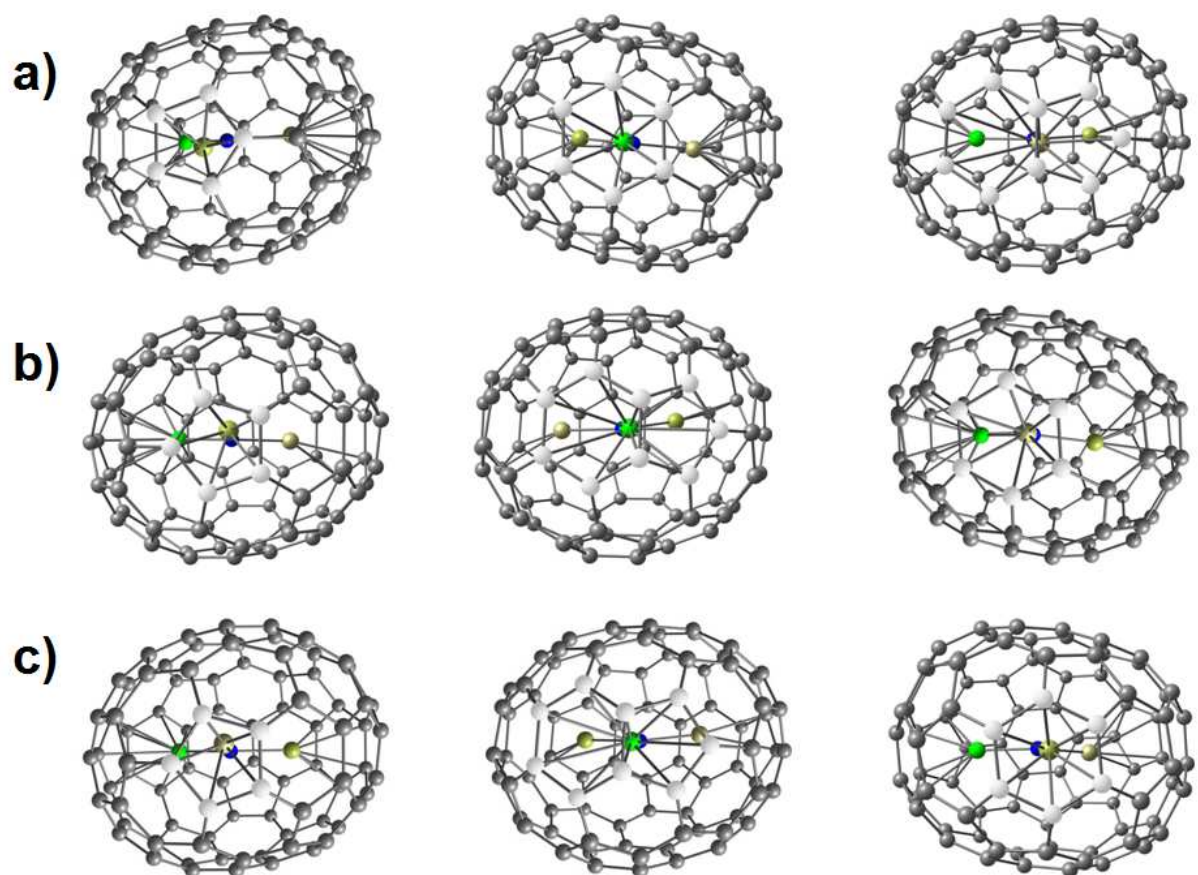


Figure 5.10 DFT-optimized structures of (a) $\text{Ce}_2\text{YN}@C_{88}\text{-a}$, (b) $\text{Ce}_2\text{YN}@C_{88}\text{-b}$ and (c) $\text{Ce}_2\text{YN}@C_{88}\text{-c}$.

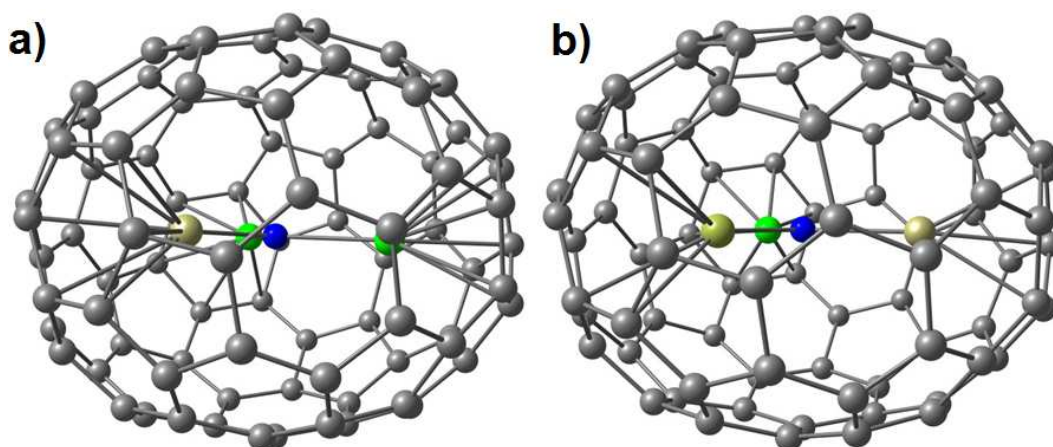


Figure 5.11 DFT-optimized structures of (a) $\text{CeY}_2\text{N}@C_{86}$ and (b) $\text{Ce}_2\text{YN}@C_{86}$.

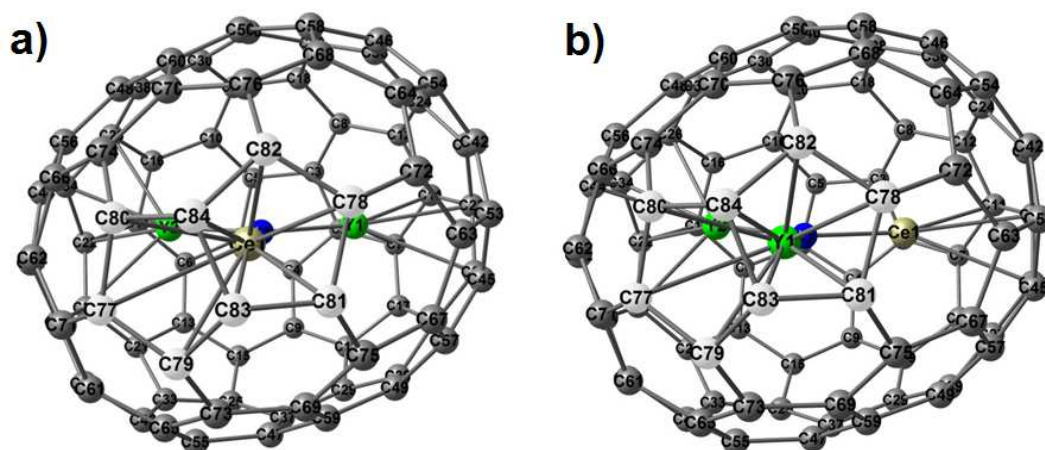


Figure 5.12 DFT-optimized structures of (a) $\text{CeY}_2\text{N}@C_{84}\text{-a}$ and (b) $\text{CeY}_2\text{N}@C_{84}\text{-b}$.

5.3 Conclusion

In summary, we performed electrochemical study of a series of Ce-based compounds, $Ce_xY_{3-x}N@C_{2n}$ ($x=1, 2$; $2n=84, 86, 88$). We have found that electrochemical oxidation of $CeY_2N@C_{80}$ is an endohedral redox process with the oxidation of Ce^{III} to Ce^{IV} state in CeY_2N . The unambiguous proof is provided by ^{13}C NMR spectroscopy of the $[CeM_2N@C_{80}]^+$ cations. Although the second cluster metal M (M= Sc, Lu and Y) is not involved in the redox process, the oxidation potential of $CeM_2N@C_{80}$ was found to be a function of the ionic radius of this metal covering the range of 0.4 V; more negative values were found for larger metal ions (Y^{3+}). This phenomenon is explained by the inherent strain in the $Ce^{III}M_2N@C_{80}$ fullerenes caused by the large size of the $Ce^{III}M_2N$ cluster and the release of this strain when Ce^{IV} with small ionic radius is formed. In the case of yttrium, this causes a change of the cluster geometry from pyramidal in the neutral $CeY_2N@C_{80}$ to planar in the cation. Expanding from carbon cage from C_{80} to C_{86} , the decrease of the strain between encage

CeY_2N cluster and C_{2n} cage was revealed by the electrochemical studies of their redox potentials. Based on the systematical electrochemical studies of $Ce_xY_{3-x}N@C_{2n}$ ($2n= 84-88$; $x= 0-2$), it could be concluded that the oxidation potential of Ce-based MMNCFs: a) for the C_{88} cage, there is no significant contribution coming from the encaged Ce atom(s) which is considered as the cage-dominated process; b) for $Ce_xY_{3-x}N@C_{86}$, changing the number of entrapped Ce atom significantly induced the negative shift of the oxidation potential which was regarded as the Ce-based process; c) for $Ce_xY_{3-x}N@C_{2n}$ ($x=1, 2$; $2n=80-88$), preserving the endohedral cluster but increasing the size of carbon cage from C_{80} to C_{88} results in the releasing the inherent strain between the entrapped cluster and carbon cage.

Conclusion of Thesis

In this thesis, Ce-, Pr-, Ho-based and Sc-, Lu- and Y-involved mixed metal nitride clusterfullerenes (MMNCFs) were synthesized by “reactive gas atmosphere” or “selective organic solid” route. Metal nitride cluster template (M_3N) provides a convenient platform for the construction of rare-earth containing endohedral fullerenes in the form of mixed metal nitride cluster fullerenes ($Ln_xM_{3-x}N@C_{2n}$; Ln=lanthanide metal). Different metals and carbon cages can be regarded as the infinite building blocks for the endohedral fullerenes family. Sc, Lu and Y are employed as the second metal (M) to tune: (a) the size and the geometry of entrapped mixed metal nitride cluster; (b) the inherent strain between encaged species and carbon cage; (c) the paramagnetic contribution from Ln^{3+} ($Ln_xM_{3-x}N@C_{80}$) to ^{13}C and ^{45}Sc NMR chemical shifts; (d) the electrochemical oxidation potential of $Ce_xY_{3-x}N@C_{2n}$. The isolation of (a) C_{80} -based MMNCFs which including $Ho_xSc_{3-x}N@C_{80}$ (I, II; $x=1, 2$), $Ho_xLu_{3-x}N@C_{80}$ (I; $x=1, 2$), $Ho_xY_{3-x}N@C_{80}$ (I; $x=1, 2$), $CeY_2N@C_{80}$ (I), $CeSc_2N@C_{80}$ (II) and $PrSc_2N@C_{80}$ (I, II) was accomplished by multi-step HPLC. Moreover, Ce-based MMNCFs with cage size larger than C_{80} were isolated which include $CeY_2N@C_{84}$, $CeY_2N@C_{86}$, $Ce_2YN@C_{86}$, $Ce_2YN@C_{88}$ and $CeY_2N@C_{88}$. The purity of above-mentioned MMNCFs was confirmed by LDI-TOF mass spectroscopy.

The UV-vis-NIR absorption spectra of above-mentioned $Ln_xM_{3-x}N@C_{2n}$ (I, II; $x=1, 2$; Ln= Ce, Pr, Ho; M= Sc, Lu, Y; $2n=80-88$) measured in toluene are similar and exhibit only subtle shifts of the bands' wavelengths. These spectra are also comparable to those of many other $M_3N@C_{80}$ NCFs with the $I_h(7)$ carbon cage and show that (a) electronic properties of $CeM_2N@C_{80}$ (I; M= Sc, Lu, Y), $Ho_xM_{3-x}N@C_{80}$ (I; M= Sc, Lu, Y), $LnSc_2N@C_{80}$ (I, II; Ln= Ce and Pr) are not significantly altered by switching the second metal; (b) the characteristic absorption feature of $Ce_xY_{3-x}N@C_{2n}$ ($x=0-2$; $2n=84, 86, 88$) is essentially dependent on the carbon cage and (c) Ce has seemingly no contribution to the frontier orbital compared to other lanthanide metals.

The vibrational spectroscopy is employed to reveal the structure information on endohedral fullerenes due to its high structural sensitivity. On the one hand, FTIR spectra own its advantages for the analyzing the antisymmetric metal-nitrogen stretching vibrational modes (ν_{M-N}) of $Ln_xM_{3-x}N@C_{80}$ (I, II; $x=0-3$), which are assigned to the most intense low-energy IR lines in the $600-800\text{ cm}^{-1}$ range and which are sensitively dependent on the composition of the

encaged $\text{Ln}_x\text{M}_{3-x}\text{N}$ cluster. It could be concluded that (a) for carbon cage with the same symmetry (I_h or D_{5h}), the splitting of $\nu_{\text{M-N}}$ in $\text{M}_2\text{ScN@C}_{80}$ is stronger than in $\text{MSc}_2\text{N@C}_{80}$; (b) for $\text{Ln}_2\text{ScN@C}_{80}$ and $\text{LnSc}_2\text{N@C}_{80}$, the splitting of $\nu_{\text{M-N}}$ in $\text{Ln}_2\text{ScN@C}_{80}$ is stronger than in $\text{LnSc}_2\text{N@C}_{80}$ due to the inherent strain between the encapsulated cluster and carbon cage; (c) the good linearity based on $\nu_{\text{Sc-N}}$ from Lu to Ce for $\text{LnSc}_2\text{N@C}_{80}$ (I) could be obtained and (d) for the encaged metal with similar metal ionic radii (e.g. Ho^{3+} and Y^{3+}), it is different to distinguish $\nu_{\text{M-N}}$ modes. On the other hand, Raman spectra could provide critical information on the interaction between the entrapped metal nitride cluster and the C_{80} cage. The low-energy Raman spectra of Ho-based MMNCFs ($\text{Ho}_x\text{M}_{3-x}\text{N@C}_{80}$, $\text{M} = \text{Sc, Lu and Y}$) are interpreted as the big difference in the term of their mass makes noteworthy distinction.

To understand and tune magnetic properties of the MMNCFs, Ce, Pr and Ho are chosen due to their strikingly different metal ionic radii, the different number of 4f-electron and magnetic moment. Meanwhile, Sc, Lu and Y are selected as second metal (M) to change the size of $\text{Ln}_x\text{M}_{3-x}\text{N}$ and inner strain between encaged cluster and carbon cage. In this thesis, those endohedral fullerenes are compared in the form of $\text{CeM}_2\text{N@C}_{80}$ (I; $\text{M} = \text{Sc, Lu, Y}$), $\text{Ho}_x\text{M}_{3-x}\text{N@C}_{80}$ (I; $\text{M} = \text{Sc, Lu, Y}$) and $\text{LnSc}_2\text{N@C}_{80}$ (I; $\text{Ln} = \text{Ce, Pr, Nd, Tb, Dy, Ho and Lu}$) based on the same carbon cage symmetry which containing different encaged cluster or the same encapsulated cluster in different carbon cage. The 4f electron(s) located on the encaged lanthanide metals (e.g. $4f^1\text{-Ce}^{3+}$, $4f^2\text{-Pr}^{3+}$ and $4f^{10}\text{-Ho}^{3+}$) results in remarkable ^{13}C NMR paramagnetic chemical shifts. Considering two Sc atoms have no significant influence to the ^{13}C NMR spectra, those paramagnetic chemical shifts could be clearly assigned as contribution from the corresponding Lanthanide metals in the LnSc_2N cluster. Reviewing the MMNCFs in the form of $\text{LnSc}_2\text{N@C}_{80}$ (I; $\text{Ln} = \text{Ce, Pr, Nd, Tb, Dy, Ho and Lu}$), the encaged metal with different magnetic moment could result in the two broad peaks in the ^{13}C NMR spectra. Particularly, the THJs carbon atoms of the $\text{C}_{80}:I_h$ demonstrated lanthanide metal dependent paramagnetic chemical shifts. According to the Bleaney's theory and Reilley method, the paramagnetic chemical shift could be deducted which provide valuable parameters comprising of the magnetic anisotropy and the corresponding crystal field. By selectively choosing the same scaffold metals M ($\text{M} = \text{Sc, Lu, Y}$), the ^{13}C NMR chemical shifts of PHHJs and THJs in $\text{CeM}_{3-x}\text{N@C}_{80}$ and $\text{Ho}_x\text{M}_{3-x}\text{N@C}_{80}$ (I; $\text{M} = \text{Sc, Lu, Y}$) are remarkably different. For Ho-based MMNCFs, it could be expected that chemical shifts definitely were dominated by the paramagnetic contribution from encaged $4f^{10}\text{-Ho}^{3+}$. However, it should be pointed out that the geometrical factors still play an important role in inducing the chemical shifts.

The temperature-dependent ^{45}Sc NMR spectroscopic study demonstrated that lanthanide metal-induced paramagnetic chemical shifts are co-influenced by the component of nitride cluster and the geometry of mixed metal nitride cluster and carbon cage. The free rotation of encapsulated cluster inside carbon cage complicated the interpretation of the ^{45}Sc NMR behaviors and the isolation separation of the contribution of Pseudocontact (δ^{PC}) and Fermi contact (δ^{con}) terms.

The convincing proofs of the strain-driven endohedral redox couple $\text{Ce}^{\text{IV}}/\text{Ce}^{\text{III}}$ in mixed metal nitride clusterfullerenes $\text{CeM}_2\text{N@C}_{80}$ (M= Sc, Lu, Y) were presented by the characterization of cyclic voltammtry and ^{13}C NMR spectroscopy. The neutral state ^{13}C NMR spectra of $\text{Ce}^{\text{III}}\text{M}_2\text{N@C}_{80}$ and their cationic form ($[\text{Ce}^{\text{IV}}\text{M}_2\text{N@C}_{80}]^+$) which produced by the addition of the oxidation agent were compared and interpreted. The two-line pattern of ^{13}C NMR spectrum and weakly paramagnetic shifts agreed well with previous reports on the $\text{M}_3\text{N@C}_{80}$ (M= Sc, Lu, Y). It should be highlighted that the ^{45}Sc NMR spectrum of $\text{CeSc}_2\text{N@C}_{80}$ with $\delta(^{45}\text{Sc})= 280$ ppm in neutral state is found to shift to 175 ppm in $[\text{CeSc}_2\text{N@C}_{80}]^+[\text{PF}_6]^-$, which is close to the value of $\delta(^{45}\text{Sc})= 190$ ppm measured for $\text{Sc}_3\text{N@C}_{80}$ in *o*-DCB. Therefore, the ^{13}C and ^{45}Sc NMR spectroscopy definitely confirmed that diamagnetic $[\text{Ce}^{\text{IV}}\text{M}_2\text{N@C}_{80}]^+$ cations are produced.

Based on the systematic studies of their electrochemical behaviors, it could be concluded that the oxidation potentials of Ce/Y-involved MMNCFs: (a) the substantial shifts of the oxidation potential of $\text{CeM}_2\text{N@C}_{80}$ (M= Sc, Lu, Y) which induced by enlarging the size of the CeM_2N cluster could be up to 0.40 V in the order of $\text{CeSc}_2\text{N@C}_{80}$ (0.33 V) \rightarrow $\text{CeLu}_2\text{N@C}_{80}$ (0.01 V) \rightarrow $\text{CeY}_2\text{N@C}_{80}$ (-0.07 V). The electrochemical energy gaps of Ce-based MMNCFs are mainly dependent on the oxidation potential rather than reduction potential; (b) for the $\text{Ce}_x\text{Y}_{3-x}\text{N@C}_{88}$ cage, it could be confirmed as cage dominated process due to switching the encaged cluster from Y_3N to CeY_2N or Ce_2YN does not induce the oxidation potential shifts; (c) for C_{86} -concerned Ce-containing compounds, the oxidation potential negatively shifted which was regarded as the Ce-based process changing the number of entrapped Ce in the case of CeY_2N and Ce_2YN cluster inside of C_{86} cage; (d) the comparison of the electrochemical oxidation behaviors of $\text{CeY}_2\text{N@C}_{84}$ and $\text{Y}_3\text{N@C}_{84}$ revealed that the negative oxidation potential shift actually is a Ce-based process which influenced by the inherent strain between the CeY_2N cluster and C_{84} cage.

Reference

- (1) Heath, J. R.; O'Brien, S. C.; Zhang, Q.; Liu, Y.; Curl, R. F.; Tittel, F. K.; Smalley, R. E.: Lanthanum complexes of spheroidal carbon shells. *J Am Chem Soc* **1985**, *107*, 7779-7780.
- (2) Kratschmer, W.; Lamb, L. D.; Fostiropoulos, K.; Huffman, D. R.: Solid C₆₀: a new form of carbon. *Nature* **1990**, *347*, 354-358.
- (3) Klingeler, R.; Kann, G.; Wirth, I.; Eisebitt, S.; Bechthold, P. S.; Neeb, M.; Eberhardt, W.: La@C₆₀: A metallic endohedral fullerene. *The Journal of Chemical Physics* **2001**, *115*, 7215.
- (4) Chai, Y.; Guo, T.; Jin, C.; Haufler, R. E.; Chibante, L. P. F.; Fure, J.; Wang, L.; Alford, J. M.; Smalley, R. E.: Fullerenes with metals inside. *The Journal of Physical Chemistry* **1991**, *95*, 7564-7568.
- (5) Akasaka, T.; Nagase, S.; Kobayashi, K.; Wälchli, M.; Yamamoto, K.; Funasaka, H.; Kako, M.; Hoshino, T.; Erata, T.: ¹³C and ¹³⁹La NMR Studies of La₂@C₈₀: First Evidence for Circular Motion of Metal Atoms in Endohedral Dimetallofullerenes. *Angewandte Chemie International Edition in English* **1997**, *36*, 1643-1645.
- (6) Popov, A. A.; Zhang, L.; Dunsch, L.: A Pseudoatom in a Cage: Trimetallofullerene Y₃@C₈₀ Mimics Y₃N@C₈₀ with Nitrogen Substituted by a Pseudoatom. *Acs Nano* **2010**, *4*, 795-802.
- (7) Iiduka, Y.; Wakahara, T.; Nakajima, K.; Tsuchiya, T.; Nakahodo, T.; Maeda, Y.; Akasaka, T.; Mizorogi, N.; Nagase, S.: ¹³C NMR spectroscopic study of scandium dimetallofullerene, Sc₂@C₈₄ vs. Sc₂C₂@C₈₂. *Chem Commun* **2006**, *0*, 2057-2059.

- (8) Stevenson, S.; Rice, G.; Glass, T.; Harich, K.; Cromer, F.; Jordan, M. R.; Craft, J.; Hadju, E.; Bible, R.; Olmstead, M. M.; Maitra, K.; Fisher, A. J.; Balch, A. L.; Dorn, H. C.: Small-bandgap endohedral metallofullerenes in high yield and purity. *Nature* **1999**, *401*, 55-57.
- (9) Stevenson, S.; Mackey, M. A.; Stuart, M. A.; Phillips, J. P.; Easterling, M. L.; Chancellor, C. J.; Olmstead, M. M.; Balch, A. L.: A Distorted Tetrahedral Metal Oxide Cluster inside an Icosahedral Carbon Cage. Synthesis, Isolation, and Structural Characterization of $\text{Sc}_4(\mu_3\text{-O})_2@I_h\text{-C}_{80}$. *J Am Chem Soc* **2008**, *130*, 11844-11845.
- (10) Dunsch, L.; Yang, S.; Zhang, L.; Svitova, A.; Oswald, S.; Popov, A. A.: Metal Sulfide in a C_{82} Fullerene Cage: A New Form of Endohedral Clusterfullerenes. *J Am Chem Soc* **2010**, *132*, 5413-5421.
- (11) Dunsch, L.; Krause, M.; Noack, J.; Georgi, P.: Endohedral nitride cluster fullerenes: Formation and spectroscopic analysis of $\text{L}_{3-x}\text{M}_x\text{N}@C_{2n}$ ($0 \leq x \leq 3$; $\text{N}=39,40$). *Journal of Physics and Chemistry of Solids* **2004**, *65*, 309-315.
- (12) Shinohara, H.; Yamaguchi, H.; Hayashi, N.; Sato, H.; Ohkohchi, M.; Ando, Y.; Saito, Y.: Isolation and spectroscopic properties of scandium fullerenes ($\text{Sc}_2@C_{74}$, $\text{Sc}_2@C_{82}$, and $\text{Sc}_2@C_{84}$). *The Journal of Physical Chemistry* **1993**, *97*, 4259-4261.
- (13) Kikuchi, K.; Nakahara, N.; Wakabayashi, T.; Honda, M.; Matsumiya, H.; Moriwaki, T.; Suzuki, S.; Shiromaru, H.; Saito, K.; Yamauchi, K.; Ikemoto, I.; Achiba, Y.: Isolation and identification of fullerene family: C_{76} , C_{78} , C_{82} , C_{84} , C_{90} and C_{96} . *Chem Phys Lett* **1992**, *188*, 177-180.
- (14) Meier, M. S.; Selegue, J. P.: Efficient preparative separation of C_{60} and C_{70} . Gel permeation chromatography of fullerenes using 100% toluene as mobile phase. *The Journal of Organic Chemistry* **1992**, *57*, 1924-1926.

- (15) Tagmatarchis, N.; Aslanis, E.; Shinohara, H.; Prassides, K.: Isolation and Spectroscopic Study of a Series of Mono- and Dierbium Endohedral C₈₂ and C₈₄ Metallofullerenes. *The Journal of Physical Chemistry B* **2000**, *104*, 11010-11012.
- (16) Wang, C.-R.; Inakuma, M.; Shinohara, H.: Metallofullerenes Sc₂@C₈₂ (I, II) and Sc₂@C₈₆ (I, II): isolation and spectroscopic studies. *Chem Phys Lett* **1999**, *300*, 379-384.
- (17) Okazaki, T.; Lian, Y.; Gu, Z.; Suenaga, K.; Hisanori, S.: Isolation and spectroscopic characterization of Sm-containing metallofullerenes. *Chem Phys Lett* **2000**, *320*, 435-440.
- (18) Xu, Z.; Nakane, T.; Shinohara, H.: Production and Isolation of Ca@C₈₂ (I-IV) and Ca@C₈₄ (I, II) Metallofullerenes. *J Am Chem Soc* **1996**, *118*, 11309-11310.
- (19) Okimoto, H.; Kitaura, R.; Nakamura, T.; Ito, Y.; Kitamura, Y.; Akachi, T.; Ogawa, D.; Imazu, N.; Kato, Y.; Asada, Y.; Sugai, T.; Osawa, H.; Matsushita, T.; Muro, T.; Shinohara, H.: Element-Specific Magnetic Properties of Di-Erbium Er₂@C₈₂ and Er₂C₂@C₈₂ Metallofullerenes: A Synchrotron Soft X-ray Magnetic Circular Dichroism Study. *The Journal of Physical Chemistry C* **2008**, *112*, 6103-6109.
- (20) Inoue, T.; Tomiyama, T.; Sugai, T.; Okazaki, T.; Suematsu, T.; Fujii, N.; Utsumi, H.; Nojima, K.; Shinohara, H.: Trapping a C₂ Radical in Endohedral Metallofullerenes: Synthesis and Structures of (Y₂C₂)@C₈₂ (Isomers I, II, and III). *The Journal of Physical Chemistry B* **2004**, *108*, 7573-7579.
- (21) Chen, N.; Beavers, C. M.; Mulet-Gas, M.; Rodríguez-Fortea, A.; Munoz, E. J.; Li, Y.-Y.; Olmstead, M. M.; Balch, A. L.; Poblet, J. M.; Echegoyen, L.: Sc₂S@C_s(10528)-C₇₂: A Dimetallic Sulfide Endohedral Fullerene with a Non Isolated Pentagon Rule Cage. *J Am Chem Soc* **2012**, *134*, 7851-7860.
- (22) Tsuchiya, T.; Wakahara, T.; Shirakura, S.; Maeda, Y.; Akasaka, T.; Kobayashi, K.; Nagase, S.; Kato, T.; Kadish, K. M.: Reduction of Endohedral Metallofullerenes: A Convenient Method for Isolation. *Chem Mater* **2004**, *16*, 4343-4346.

- (23) Yang, Y.; Arias, F.; Echegoyen, L.; Chibante, L. P. F.; Flanagan, S.; Robertson, A.; Wilson, L. J.: Reversible Fullerene Electrochemistry: Correlation with the HOMO-LUMO Energy Difference for C₆₀, C₇₀, C₇₆, C₇₈, and C₈₄. *J Am Chem Soc* **1995**, *117*, 7801-7804.
- (24) Xu, J.; Li, M.; Shi, Z.; Gu, Z.: Electrochemical Survey: The Effect of the Cage Size and Structure on the Electronic Structures of a Series of Ytterbium Metallofullerenes. *Chemistry – A European Journal* **2006**, *12*, 562-567.
- (25) Elliott, B.; Yu, L.; Echegoyen, L.: A Simple Isomeric Separation of D_{5h} and I_h Sc₃N@C₈₀ by Selective Chemical Oxidation. *J Am Chem Soc* **2005**, *127*, 10885-10888.
- (26) Angeli, C. D.; Cai, T.; Duchamp, J. C.; Reid, J. E.; Singer, E. S.; Gibson, H. W.; Dorn, H. C.: Purification of Trimetallic Nitride Templated Endohedral Metallofullerenes by a Chemical Reaction of Congeners with Eutectic 9-Methylanthracene. *Chem Mater* **2008**, *20*, 4993-4997.
- (27) Akiyama, K.; Hamano, T.; Nakanishi, Y.; Takeuchi, E.; Noda, S.; Wang, Z.; Kubuki, S.; Shinohara, H.: Non-HPLC Rapid Separation of Metallofullerenes and Empty Cages with TiCl₄ Lewis Acid. *J Am Chem Soc* **2012**, *134*, 9762-9767.
- (28) Olmstead, M. M.; de Bettencourt-Dias, A.; Duchamp, J. C.; Stevenson, S.; Marciu, D.; Dorn, H. C.; Balch, A. L.: Isolation and Structural Characterization of the Endohedral Fullerene Sc₃N@C₇₈. *Angewandte Chemie International Edition* **2001**, *40*, 1223-1225.
- (29) Dunsch, L.; Yang, S.: Metal Nitride Cluster Fullerenes: Their Current State and Future Prospects. *Small* **2007**, *3*, 1298-1320.
- (30) Yang, S.; Popov, A. A.; Dunsch, L.: Violating the isolated pentagon rule (IPR): the endohedral non-IPR C₇₀ cage of Sc₃N@C₇₀. *Angew Chem Int Ed Engl* **2007**, *46*, 1256-9.
- (31) Iezzi, E. B.; Duchamp, J. C.; Fletcher, K. R.; Glass, T. E.; Dorn, H. C.: Lutetium-based Trimetallic Nitride Endohedral Metallofullerenes: New Contrast Agents. *Nano Lett* **2002**, *2*, 1187-1190.

- (32) Krause, M.; Dunsch, L.: Isolation and Characterisation of Two $\text{Sc}_3\text{N}@C_{80}$ Isomers. *Chemphyschem* **2004**, *5*, 1445-1449.
- (33) Cai, T.; Xu, L.; Anderson, M. R.; Ge, Z.; Zuo, T.; Wang, X.; Olmstead, M. M.; Balch, A. L.; Gibson, H. W.; Dorn, H. C.: Structure and Enhanced Reactivity Rates of the D_{5h} $\text{Sc}_3\text{N}@C_{80}$ and $\text{Lu}_3\text{N}@C_{80}$ Metallofullerene Isomers: The Importance of the Pyracylene Motif. *J Am Chem Soc* **2006**, *128*, 8581-8589.
- (34) Yang, S.; Popov, A. A.; Chen, C.; Dunsch, L.: Mixed Metal Nitride Clusterfullerenes in Cage Isomers: $\text{Lu}_x\text{Sc}_{3-x}\text{N}@C_{80}$ ($x = 1, 2$) As Compared with $\text{M}_x\text{Sc}_{3-x}\text{N}@C_{80}$ ($M = \text{Er, Dy, Gd, Nd}$). *The Journal of Physical Chemistry C* **2009**, *113*, 7616-7623.
- (35) Dunsch, L.; Yang, S.: Endohedral clusterfullerenes-playing with cluster and cage sizes. *Phys Chem Chem Phys* **2007**, *9*, 3067-3081.
- (36) Yang, S.; Kalbac, M.; Popov, A.; Dunsch, L.: A Facile Route to the Non-IPR Fullerene $\text{Sc}_3\text{N}@C_{68}$: Synthesis, Spectroscopic Characterization, and Density Functional Theory Computations (IPR=Isolated Pentagon Rule). *Chemistry – A European Journal* **2006**, *12*, 7856-7863.
- (37) Popov, A. A.: Metal-Cage Bonding, Molecular Structures and Vibrational Spectra of Endohedral Fullerenes: Bridging Experiment and Theory. *Journal of Computational and Theoretical Nanoscience* **2009**, *6*, 292-317.
- (38) Popov, A. A.; Dunsch, L.: Structure, Stability, and Cluster-Cage Interactions in Nitride Clusterfullerenes $\text{M}_3\text{N}@C_{2n}$ ($M = \text{Sc, Y}$; $2n = 68-98$): a Density Functional Theory Study. *J Am Chem Soc* **2007**, *129*, 11835-11849.
- (39) Popov, A. A.; Avdoshenko, S. M.; Pendas, A. M.; Dunsch, L.: Bonding between strongly repulsive metal atoms: an oxymoron made real in a confined space of endohedral metallofullerenes. *Chem Commun* **2012**, *48*, 8031-8050.

- (40) Valencia, R.; Rodríguez-Forteza, A.; Clotet, A.; de Graaf, C.; Chaur, M. N.; Echegoyen, L.; Poblet, J. M.: Electronic Structure and Redox Properties of Metal Nitride Endohedral Fullerenes $M_3N@C_{2n}$ ($M=Sc, Y, La, \text{ and } Gd; 2n=80, 84, 88, 92, 96$). *Chemistry – A European Journal* **2009**, *15*, 10997-11009.
- (41) Chaur, M. N.; Melin, F.; Ashby, J.; Elliott, B.; Kumbhar, A.; Rao, A. M.; Echegoyen, L.: Lanthanum Nitride Endohedral Fullerenes $La_3N@C_{2n}$ ($43 \leq n \leq 55$): Preferential Formation of $La_3N@C_{96}$. *Chemistry – A European Journal* **2008**, *14*, 8213-8219.
- (42) Yang, S.; Zalibera, M.; Rapta, P.; Dunsch, L.: Charge-Induced Reversible Rearrangement of Endohedral Fullerenes: Electrochemistry of Tridysprosium Nitride Clusterfullerenes $Dy_3N@C_{2n}$ ($2n=78, 80$). *Chemistry – A European Journal* **2006**, *12*, 7848-7855.
- (43) Chaur, M. N.; Melin, F.; Elliott, B.; Athans, A. J.; Walker, K.; Holloway, B. C.; Echegoyen, L.: $Gd_3N@C_{2n}$ ($n = 40, 42, \text{ and } 44$): Remarkably Low HOMO–LUMO Gap and Unusual Electrochemical Reversibility of $Gd_3N@C_{88}$. *J Am Chem Soc* **2007**, *129*, 14826-14829.
- (44) Melin, F.; Chaur, M. N.; Engmann, S.; Elliott, B.; Kumbhar, A.; Athans, A. J.; Echegoyen, L.: The Large $Nd_3N@C_{2n}$ ($40 \leq n \leq 49$) Cluster Fullerene Family: Preferential Templating of a C_{88} Cage by a Trimetallic Nitride Cluster. *Angewandte Chemie* **2007**, *119*, 9190-9193.
- (45) Popov, A. A.; Chen, C.; Yang, S.; Lipps, F.; Dunsch, L.: Spin-Flow Vibrational Spectroscopy of Molecules with Flexible Spin Density: Electrochemistry, ESR, Cluster and Spin Dynamics, and Bonding in $TiSc_2N@C_{80}$. *ACS Nano* **2010**, *4*, 4857-4871.
- (46) Sakaguchi, K.; Fujii, R.; Kodama, T.; Nishikawa, H.; Ikemoto, I.; Achiba, Y.; Kikuchi, K.: Production and Characterization of Heteroatom-encapsulated Metallofullerene, $CaHo@C_{82}$. *Chemistry Letters* **2007**, *36*, 832-833.

- (47) Kikuchi, K.; Akiyama, K.; Sakaguchi, K.; Kodama, T.; Nishikawa, H.; Ikemoto, I.; Ishigaki, T.; Achiba, Y.; Sueki, K.; Nakahara, H.: Production and isolation of the isomers of dimetallofullerenes, HoTm@C_{82} and $\text{Tm}_2\text{@C}_{82}$. *Chem Phys Lett* **2000**, *319*, 472-476.
- (48) Cagle, D. W.; Thrash, T. P.; Alford, M.; Chibante, L. P. F.; Ehrhardt, G. J.; Wilson, L. J.: Synthesis, Characterization, and Neutron Activation of Holmium Metallofullerenes. *J Am Chem Soc* **1996**, *118*, 8043-8047.
- (49) Akasaka, T.; Wakahara, T.; Nagase, S.; Kobayashi, K.; Waelchli, M.; Yamamoto, K.; Kondo, M.; Shirakura, S.; Okubo, S.; Maeda, Y.; Kato, T.; Kako, M.; Nakadaira, Y.; Nagahata, R.; Gao, X.; Van Caemelbecke, E.; Kadish, K. M.: La@C_{82} Anion. An Unusually Stable Metallofullerene. *J Am Chem Soc* **2000**, *122*, 9316-9317.
- (50) Yamada, M.; Wakahara, T.; Lian, Y.; Tsuchiya, T.; Akasaka, T.; Waelchli, M.; Mizorogi, N.; Nagase, S.; Kadish, K. M.: Analysis of Lanthanide-Induced NMR Shifts of the Ce@C_{82} Anion. *J Am Chem Soc* **2006**, *128*, 1400-1401.
- (51) Wolf, M.; Müller, K.-H.; Skourski, Y.; Eckert, D.; Georgi, P.; Krause, M.; Dunsch, L.: Magnetic Moments of the Endohedral Cluster Fullerenes $\text{Ho}_3\text{N@C}_{80}$ and $\text{Tb}_3\text{N@C}_{80}$: The Role of Ligand Fields. *Angewandte Chemie International Edition* **2005**, *44*, 3306-3309.
- (52) Wang, X.; Zuo, T.; Olmstead, M. M.; Duchamp, J. C.; Glass, T. E.; Cromer, F.; Balch, A. L.; Dorn, H. C.: Preparation and Structure of $\text{CeSc}_2\text{N@C}_{80}$: An Icosahedral Carbon Cage Enclosing an Acentric CeSc_2N Unit with Buried f Electron Spin. *J Am Chem Soc* **2006**, *128*, 8884-8889.
- (53) Yamada, M.; Nakahodo, T.; Wakahara, T.; Tsuchiya, T.; Maeda, Y.; Akasaka, T.; Kako, M.; Yoza, K.; Horn, E.; Mizorogi, N.; Kobayashi, K.; Nagase, S.: Positional Control of Encapsulated Atoms Inside a Fullerene Cage by Exohedral Addition. *J Am Chem Soc* **2005**, *127*, 14570-14571.

- (54) Zhang, L.; Popov, A. A.; Yang, S.; Klod, S.; Rapta, P.; Dunsch, L.: An endohedral redox system in a fullerene cage: the Ce based mixed-metal cluster fullerene $\text{Lu}_2\text{CeN@C}_{80}$. *Phys Chem Chem Phys* **2010**, *12*, 7840-7847.
- (55) Fu, W.; Xu, L.; Azurmendi, H.; Ge, J.; Fuhrer, T.; Zuo, T.; Reid, J.; Shu, C.; Harich, K.; Dorn, H. C.: ^{89}Y and ^{13}C NMR Cluster and Carbon Cage Studies of an Yttrium Metallofullerene Family, $\text{Y}_3\text{N@C}_{2n}$ ($n = 40-43$). *J Am Chem Soc* **2009**, *131*, 11762-11769.
- (56) Yang, S.; Chen, C.; Popov, A. A.; Zhang, W.; Liu, F.; Dunsch, L.: An endohedral titanium(III) in a clusterfullerene: putting a non-group-III metal nitride into the $\text{C}_{80}\text{-Ih}$ fullerene cage. *Chem Commun* **2009**, *0*, 6391-6393.
- (57) Chen, N.; Fan, L.-Z.; Tan, K.; Wu, Y.-Q.; Shu, C.-Y.; Lu, X.; Wang, C.-R.: Comparative Spectroscopic and Reactivity Studies of $\text{Sc}_{3-x}\text{Y}_x\text{N@C}_{80}$ ($x = 0-3$). *The Journal of Physical Chemistry C* **2007**, *111*, 11823-11828.
- (58) Stevenson, S.; Chancellor, C. J.; Lee, H. M.; Olmstead, M. M.; Balch, A. L.: Internal and External Factors in the Structural Organization in Cocrystals of the Mixed-Metal Endohedrals ($\text{GdSc}_2\text{N@I}_h\text{-C}_{80}$, $\text{Gd}_2\text{ScN@I}_h\text{-C}_{80}$, and $\text{TbSc}_2\text{N@I}_h\text{-C}_{80}$) and Nickel(II) Octaethylporphyrin. *Inorg Chem* **2008**, *47*, 1420-1427.
- (59) Olmstead, M. M.; de Bettencourt-Dias, A.; Duchamp, J. C.; Stevenson, S.; Dorn, H. C.; Balch, A. L.: Isolation and Crystallographic Characterization of $\text{ErSc}_2\text{N@C}_{80}$: an Endohedral Fullerene Which Crystallizes with Remarkable Internal Order. *J Am Chem Soc* **2000**, *122*, 12220-12226.
- (60) Chen, N.; Zhang, E.-Y.; Wang, C.-R.: C_{80} Encaging Four Different Atoms: The Synthesis, Isolation, and Characterizations of ScYErN@C_{80} . *The Journal of Physical Chemistry B* **2006**, *110*, 13322-13325.
- (61) Yang, S.; Popov, A.; Kalbac, M.; Dunsch, L.: The Isomers of Gadolinium Scandium Nitride Clusterfullerenes $\text{Gd}_x\text{Sc}_{3-x}\text{N@C}_{80}$ ($x=1, 2$) and Their Influence on Cluster Structure. *Chemistry – A European Journal* **2008**, *14*, 2084-2092.

- (62) Yang, S.; Popov, A. A.; Dunsch, L.: Carbon Pyramidalization in Fullerene Cages Induced by the Endohedral Cluster: Non-Scandium Mixed Metal Nitride Clusterfullerenes. *Angewandte Chemie International Edition* **2008**, *47*, 8196-8200.
- (63) Yang, S.; Popov, A. A.; Dunsch, L.: Large mixed metal nitride clusters encapsulated in a small cage: the confinement of the C₆₈-based clusterfullerenes. *Chem Commun* **2008**, *0*, 2885-2887.
- (64) Yang, S.; Popov, A. A.; Dunsch, L.: The Role of an Asymmetric Nitride Cluster on a Fullerene Cage: The Non-IPR Endohedral DySc₂N@C₇₆. *The Journal of Physical Chemistry B* **2007**, *111*, 13659-13663.
- (65) Yang, S.; Dunsch, L.: A Large Family of Dysprosium-based Trimetallic Nitride Endohedral Fullerenes: Dy₃N@C_{2n} (39 ≤ n ≤ 44). *The Journal of Physical Chemistry B* **2005**, *109*, 12320-12328.
- (66) Chaur, M. N.; Valencia, R.; Rodríguez-Forteza, A.; Poblet, J. M.; Echegoyen, L.: Trimetallic Nitride Endohedral Fullerenes: Experimental and Theoretical Evidence for the M₃N⁶⁺@C_{2n}⁶⁻ model. *Angewandte Chemie International Edition* **2009**, *48*, 1425-1428.
- (67) Popov, A. A.; Yang, S.; Dunsch, L.: Endohedral Fullerenes. *Chemical Reviews* **2013**.
- (68) Krause, M.; Kuzmany, H.; Georgi, P.; Dunsch, L.; Vietze, K.; Seifert, G.: Structure and stability of endohedral fullerene Sc₃N@C₈₀: A Raman, infrared, and theoretical analysis. *The Journal of Chemical Physics* **2001**, *115*, 6596.
- (69) Yamada, M.; Wakahara, T.; Tsuchiya, T.; Maeda, Y.; Kako, M.; Akasaka, T.; Yoza, K.; Horn, E.; Mizorogi, N.; Nagase, S.: Location of the metal atoms in Ce₂@C₇₈ and its bis-silylated derivative. *Chem Commun* **2008**, *0*, 558-560.
- (70) Feng, L.; Suzuki, M.; Mizorogi, N.; Lu, X.; Yamada, M.; Akasaka, T.; Nagase, S.: Mapping the Metal Positions inside Spherical C₈₀ Cages: Crystallographic and Theoretical Studies of Ce₂@D_{5h}-C₈₀ and Ce₂@I_h-C₈₀. *Chemistry – A European Journal* **2013**, *19*, 988-993.

- (71) Yamada, M.; Wakahara, T.; Tsuchiya, T.; Maeda, Y.; Akasaka, T.; Mizorogi, N.; Nagase, S.: Spectroscopic and Theoretical Study of Endohedral Dimetallofullerene Having a Non-IPR Fullerene Cage: Ce₂@C₇₂. *The Journal of Physical Chemistry A* **2008**, *112*, 7627-7631.
- (72) Yamada, M.; Mizorogi, N.; Tsuchiya, T.; Akasaka, T.; Nagase, S.: Synthesis and Characterization of the D5h Isomer of the Endohedral Dimetallofullerene Ce₂@C₈₀: Two-Dimensional Circulation of Encapsulated Metal Atoms Inside a Fullerene Cage. *Chemistry – A European Journal* **2009**, *15*, 9486-9493.
- (73) Takano, Y.; Aoyagi, M.; Yamada, M.; Nikawa, H.; Slanina, Z.; Mizorogi, N.; Ishitsuka, M. O.; Tsuchiya, T.; Maeda, Y.; Akasaka, T.; Kato, T.; Nagase, S.: Anisotropic Magnetic Behavior of Anionic Ce@C₈₂ Carbene Adducts. *J Am Chem Soc* **2009**, *131*, 9340-9346.
- (74) Maeda, Y.; Miyashita, J.; Hasegawa, T.; Wakahara, T.; Tsuchiya, T.; Feng, L.; Lian, Y.; Akasaka, T.; Kobayashi, K.; Nagase, S.; Kako, M.; Yamamoto, K.; Kadish, K. M.: Chemical Reactivities of the Cation and Anion of M@C₈₂ (M = Y, La, and Ce). *J Am Chem Soc* **2005**, *127*, 2143-2146.
- (75) Kodama, T.; Ozawa, N.; Miyake, Y.; Sakaguchi, K.; Nishikawa, H.; Ikemoto, I.; Kikuchi, K.; Achiba, Y.: Structural Study of Three Isomers of Tm@C₈₂ by ¹³C NMR Spectroscopy. *J Am Chem Soc* **2002**, *124*, 1452-1455.
- (76) Ding, J.; Yang, S.: Isolation and Characterization of Pr@C₈₂ and Pr₂@C₈₀. *J Am Chem Soc* **1996**, *118*, 11254-11257.
- (77) Akasaka, T.; Okubo, S.; Kondo, M.; Maeda, Y.; Wakahara, T.; Kato, T.; Suzuki, T.; Yamamoto, K.; Kobayashi, K.; Nagase, S.: Isolation and characterization of two Pr@C₈₂ isomers. *Chem Phys Lett* **2000**, *319*, 153-156.
- (78) Heine, T.; Bühl, M.; Fowler, P. W.; Seifert, G.: Modelling the ¹³C NMR chemical shifts of C₈₄ fullerenes. *Chem Phys Lett* **2000**, *316*, 373-380.

- (79) Sun, G.; Kertesz, M.: Isomer Identification for Fullerene C₈₄ by ¹³C NMR Spectrum: A Density-Functional Theory Study. *The Journal of Physical Chemistry A* **2001**, *105*, 5212-5220.
- (80) Bleaney, B.: Nuclear magnetic resonance shifts in solution due to lanthanide ions. *Journal of Magnetic Resonance (1969)* **1972**, *8*, 91-100.
- (81) Reilley, C. N.; Good, B. W.; Desreux, J. F.: Structure-independent method for dissecting contact and dipolar NMR shifts in lanthanide complexes and its use in structure determination. *Analytical Chemistry* **1975**, *47*, 2110-2116.
- (82) Di Pietro, S.; Piano, S. L.; Di Bari, L.: Pseudocontact shifts in lanthanide complexes with variable crystal field parameters. *Coordination Chemistry Reviews* **2011**, *255*, 2810-2820.
- (83) Chaur, M. N.; Aparicio-Anglès, X.; Mercado, B. Q.; Elliott, B.; Rodríguez-Fortea, A.; Clotet, A.; Olmstead, M. M.; Balch, A. L.; Poblet, J. M.; Echegoyen, L.: Structural and Electrochemical Property Correlations of Metallic Nitride Endohedral Metallofullerenes. *The Journal of Physical Chemistry C* **2010**, *114*, 13003-13009.
- (84) Rapta, P.; Popov, A. A.; Yang, S.; Dunsch, L.: Charged states of Sc₃N@C₆₈: an in situ spectroelectrochemical study of the radical cation and radical anion of a non-IPR fullerene. *J Phys Chem A* **2008**, *112*, 5858-65.
- (85) Zhang, L.; Chen, N.; Fan, L.; Wang, C.; Yang, S.: Electrochemistry of Sc₃N@C₇₈ and Sc₃N@C₈₀ (Ih): On achieving reversible redox waves of the trimetal nitride endohedral fullerenes. *Journal of Electroanalytical Chemistry* **2007**, *608*, 15-21.
- (86) Chen, C.; Liu, F.; Li, S.; Wang, N.; Popov, A. A.; Jiao, M.; Wei, T.; Li, Q.; Dunsch, L.; Yang, S.: Titanium/Yttrium Mixed Metal Nitride Clusterfullerene TiY₂N@C₈₀: Synthesis, Isolation, and Effect of the Group-III Metal. *Inorg Chem* **2012**, *51*, 3039-3045.

- (87) Streitwieser, A.; Kinsley, S. A.; Rigsbee, J. T.; Fragala, I. L.; Ciliberto, E.: Photoelectron spectra and bonding in cerocene, bis(π -[8]annulene)cerium(IV). *J Am Chem Soc* **1985**, *107*, 7786-7788.
- (88) Gulino, A.; Casarin, M.; Conticello, V. P.; Gaudiello, J. G.; Mauermann, H.; Fragala, I.; Marks, T. J.: Efficient synthesis, redox characteristics, and electronic structure of a tetravalent tris(cyclopentadienyl)cerium alkoxide complex. *Organometallics* **1988**, *7*, 2360-2364.
- (89) Buchler, J. W.; Scharbert, B.: Metal complexes with tetrapyrrole ligands. 50. Redox potentials of sandwichlike metal bis(octaethylporphyrinates) and their correlation with ring-ring distances. *J Am Chem Soc* **1988**, *110*, 4272-4276.
- (90) Robinson, J. R.; Carroll, P. J.; Walsh, P. J.; Schelter, E. J.: The Impact of Ligand Reorganization on Cerium(III) Oxidation Chemistry. *Angewandte Chemie International Edition* **2012**, *51*, 10159-10163.
- (91) Donohoe, R. J.; Duchowski, J. K.; Bocian, D. F.: Hole delocalization in oxidized cerium(IV) porphyrin sandwich complexes. *J Am Chem Soc* **1988**, *110*, 6119-6124.
- (92) R. Antonio, M.; Soderholm, L.; W. Williams, C.; Ullah, N.; C. Francesconi, L.: Redox behavior of cerium in heteropolyoxotungstate complexes. *Journal of the Chemical Society, Dalton Transactions* **1999**, *0*, 3825-3830.
- (93) Cui, Y.; Chen, G.; Ren, J.; Qian, Y.; Huang, J.: Syntheses, Structures and Magnetic Behaviors of Di- and Trinuclear Pivalate Complexes Containing Both Cobalt(II) and Lanthanide(III) Ions. *Inorg Chem* **2000**, *39*, 4165-4168.
- (94) Behrsing, T.; Bond, A. M.; Deacon, G. B.; Forsyth, C. M.; Forsyth, M.; Kamble, K. J.; Skelton, B. W.; White, A. H.: Cerium acetylacetonates—new aspects, including the lamellar clathrate $[\text{Ce}(\text{acac})_4] \cdot 10\text{H}_2\text{O}$. *Inorganica Chimica Acta* **2003**, *352*, 229-237.

- (95) Ashley, A.; Balazs, G.; Cowley, A.; Green, J.; Booth, C. H.; O'Hare, D.: Bis(permethylpentalene)cerium - another ambiguity in lanthanide oxidation state. *Chem Commun* **2007**, 0, 1515-1517.
- (96) Arif, A. M.; Gray, C. J.; Alan Hart, F.; Hursthouse, M. B.: Synthesis and structure of lanthanide complexes of a mixed donor macrocyclic ligand. *Inorganica Chimica Acta* **1985**, 109, 179-183.
- (97) Xu, J.; Radkov, E.; Ziegler, M.; Raymond, K. N.: Plutonium(IV) Sequestration: Structural and Thermodynamic Evaluation of the Extraordinarily Stable Cerium(IV) Hydroxypyridinonate Complexes I. *Inorg Chem* **2000**, 39, 4156-4164.
- (98) Buchler, J. W.; Dippell, T.: Oxidation and Reduction of Cerium(IV) Sandwich Complexes with Porphyrin Ligands Linked by Aliphatic Diether Bridges of Variable Chain Length. *European Journal of Inorganic Chemistry* **1998**, 1998, 445-449.
- (99) Chaur, M. N.; Melin, F.; Ortiz, A. L.; Echegoyen, L.: Chemical, Electrochemical, and Structural Properties of Endohedral Metallofullerenes. *Angewandte Chemie International Edition* **2009**, 48, 7514-7538.
- (100) Tarábek, J.; Yang, S.; Dunsch, L.: Redox Properties of Mixed Lutetium/Yttrium Nitride Clusterfullerenes: Endohedral $\text{Lu}_x\text{Y}_{3-x}\text{N}@C_{80}$ (I) ($x=0-3$) Compounds. *Chemphyschem* **2009**, 10, 1037-1043.
- (101) Fu, W.; Zhang, J.; Champion, H.; Fuhrer, T.; Azuremendi, H.; Zuo, T.; Zhang, J.; Harich, K.; Dorn, H. C.: Electronic Properties and ^{13}C NMR Structural Study of $\text{Y}_3\text{N}@C_{88}$. *Inorg Chem* **2011**, 50, 4256-4259.
- (102) Chaur, M. N.; Melin, F.; Elliott, B.; Kumbhar, A.; Athans, A. J.; Echegoyen, L.: New $\text{M}_3\text{N}@C_{2n}$ Endohedral Metallofullerene Families (M=Nd, Pr, Ce; $n=40-53$): Expanding the Preferential Templating of the C_{88} Cage and Approaching the C_{96} Cage. *Chemistry – A European Journal* **2008**, 14, 4594-4599.

Acknowledgement

Foremost, I would like to thank my supervisor, Prof. Dr. Lothar Dunsch, for his supervision and encouragement during my Ph.D. study at IFW. I respect to his tremendous enthusiasm and extensive knowledge that dedicated to fullerenes science. Besides my supervisor in Leibniz Institute for Solid State and Materials Research Dresden (IFW Dresden), I would like to express my sincere gratitude to Prof. Dr. Rainer Beckert in Friedrich-Schiller-Universität for solid support all the time. Meanwhile, I would like to thank the rest of my dissertation committee.

In particular, I thank Dr. Alexey A Popov in IFW Dresden for theoretical work during my study. I appreciate his guidance and contribution to my work. There are several colleagues in our department that I would like to acknowledge which includes Frank Ziegs, Sandra Schiemenz, Marco Rosenkranz, Birgit Urban, Alexander Berger, Christine Malbrich, Anja Grohme, David Kunhardt, Runshuang Lu, Qingming Deng, Dr. Sabrina Klod, Dr. Evgenia Dmitrieva, Dr. Kinga Haubner, Dr. Lin Zhang, Dr. Chuanbao Chen, Dr. Anna Svitova and Dr. Shangfeng Yang. This dissertation contains their supportive advice as well. I will benefit from the scientific and technical knowledge I learnt from them in the rest of my scientific career. It has been a great pleasure for me to work in our department.

Additionally, I would like to thank Prof. Lou-Zhen Fan in Beijing Normal University and Prof. Chun-Ru Wang in Institute of Chemistry Chinese Academy of Sciences for introducing me to the field of fullerene researches many years ago.

Finally, I would like to thank my parents for their encouraging during I study in Dresden.

Appendix: Experimental details

1. Synthesis and Extraction

As mentioned in Figure 1.1, the sketch of the apparatus for synthesizing endohedral metallofullerenes (EMFs) is demonstrated. Before DC-arc discharging, two core-drilled graphite rods were filled with the mixture of metal/graphite or metal oxide/graphite. In general, for the productions of NCFs or MMNCFs, two kinds of nitrogen source were commonly used in our group including ammonia (NH_3) as reactive gas and guanidine thiocyanate as the solid state source as described previously. Pumping the generator is a quite necessary step for enhancing the yield of metal NCFs and depressing the yield of empty fullerenes by removing the air in the generator. In the presence of 50 mbar He atmosphere, 15 A current is applied for the preheating of the graphite rods around 20 minutes. For the “reactive gas atmosphere” method, the 20 mbar NH_3 and 200 mbar He are filled into the generator after the preheating process which described in the section of the synthesis of $\text{Ho}_x\text{Sc}_{3-x}\text{N}@C_{80}$ (I, II; $x=1, 2$). For “selective organic solid” (SOS) route, guanidine thiocyanate (GT) which mixed with metal oxide (CeO_2 , Pr_6O_{11} , Ho_2O_3 , Lu_2O_3 , Sc_2O_3 , Y_2O_3) and graphite powder is filled into the core-drilled rods as well. The molar ratio of Ln/M/GT/C is 1:1:2.5:15 (Ln= lanthanide metal; M= Sc, Y). By applying 100 A current, two metal oxide containing graphite rods are fixed as anode and cathode. Switching connection with the DC apparatus, the rods on both sides could be regarded as anode alternatively during the evaporation. The distance between anode and cathode is about 1 cm by moving the two rods forward as the conduction of the evaporation. After DC-arc discharging, the soot was collected and pre-extracted by acetone for 1 hour and further Soxhlet-extracted by CS_2 for 20 hours. The extraction solution was dried with the protection of N_2 flow and the crude fullerenes containing mixture is dissolved in toluene solution for the isolation in the next step.

2. HPLC isolation

In general, the isolation of metal NCFs and MMNCFs is performed by multi-step HPLC with toluene as the eluent. The first step running in a Hewlett-Packard instrument (series 1100), a combination of two analytical 4.6×250 mm Buckyprep columns (Nacalai Tesque,

Japan) was applied. The second- and third-step isolation were performed by a recycling HPLC (Sunchrom, Germany) using a Buckyprep column or a Buckyclutcher column (Nacalai Tesque, Japan) and toluene as the eluent. The UV detector set to 320 nm was employed for fullerenes detection for all steps.

3. Spectroscopic and electrochemical characterizations

The purity of the isolated MMNCFs compounds was checked by laser desorption/ionization time-of-flight (LDI-TOF) MS analysis running in both and positive and negative ion modes (Biflex III, Bruker, Germany). UV-Vis-NIR spectra of isolated MMNCFs structures dissolved in toluene were recorded by using a UV-Vis-NIR MPC-3100 spectrometer (Shimadzu, Japan) at 1 nm resolution, and a quartz cell of 1 mm path length. For FTIR and Raman characterization of MMNCFs, the drops of solution state sample was dried on the surface of KBr single crystal disk which recorded by using an IFS 66v spectrometer (Bruker, Germany) at room temperature. The 125 MHz ^{13}C NMR and 121.5 MHz ^{45}Sc NMR spectroscopic measurements were performed at in a multiprobe head PH 1152Z on an Avance 500 spectrometer (Bruker, Germany) at room temperature in carbon disulfide solution with d_6 -acetone as a lock or o - d_4 -DCB solution. Cyclic voltammetric experiments were conducted with a PAR 273 potentiostat at room temperature in the glove box. A standard three-electrode system contains a Platinum wires and a silver wire served as the working, counter, and pseudoreference electrodes, respectively. The distilled o -DCB solvent is used. The supporting electrolyte is TBABF₄ (0.1 M). The potentials were measured against the Fe(Cp)₂⁺⁰ couple which regarded as the internal standard.

Curriculum Vitae

Personal Information

First Name	Yang	Family Name	Zhang
Date of Birth	1983.03.07	Place of Birth	Beijing
Nationality	China	Sex	Male
Marital Status	Single	Subject	Chemistry
Institute	Leibniz Institute for Solid State and Materials Research Dresden		
Office Number	+493514659713	Email	y.zhang@ifw-dresden.de
Address	Helmholtzstr. 20, 01069, Dresden, Germany		

Academic Background

2009.09 – Present	Leibniz Institute for Solid State and Materials Research Dresden PhD student supervised by Prof. Dr. Lothar Dunsch Major in synthesis and characterization of mixed metal nitride clusterfullerenes.
2006.09 – 2009.09	Beijing Normal University, Department of Chemistry Master Degree of Science, supervised by Prof. Dr. Louzhen Fan Major in synthesis and characterization of fullerene nanomaterials and Semiconductor Nanomaterials
2006.09 – 2009.09	Beijing Forest University, Department of Material Science and Technology Bachelor Degree of Chemical Engineering Major study in Chemical Engineering of Wood Products

List of Publication

1. **Yang Zhang**, Wei Liu, Lang Jiang, Louzhen Fan*, Chunru Wang, Wenping Hu, Haizheng Zhong, Yongfang Li and Shihe Yang*
Template-free solution growth of highly regular, crystal orientation-ordered C₆₀ nanorod bundles, *Journal of Materials Chemistry*, **2010**, 20, 953 - 956.
2. **Yang Zhang**, Lang Jiang, Hui Li, Louzhen Fan*, Wenping Hu, Chunru Wang, Yongfang Li, Shihe Yang*
Single-Crystalline C₆₀ Nanostructures by Sonophysical Preparation: Tuning Hollow Nanobowls as Catalyst Supports for Methanol Oxidation, *Chemistry-A European Journal*, **2011**, 17, 4921 - 4926.
3. **Yang Zhang**, Alexey A Popov, Sandra Schiemenz, and Lothar Dunsch*
Synthesis, Isolation and Spectroscopic Characterization of Holmium-Based Mixed Metal Nitride Clusterfullerenes: Ho_xSc_{3-x}N@C₈₀ (x= 1, 2), *Chemistry-A European Journal*, **2011**, 31, 9691 - 9698.
4. **Yang Zhang**, Sandra Schiemenz, Alexey A Popov* and Lothar Dunsch*
The Strain-Driven Endohedral Redox Couple Ce^{IV}/Ce^{III} in Nitride Clusterfullerenes CeM₂N@C₈₀ (M = Sc, Y, Lu), *submitted*.
5. **Yang Zhang**, Sandra Schiemenz, Alexey A Popov* and Lothar Dunsch*, The Scaffold Metals Dominate the Electrochemical Behaviors of Ce^{III/IV} Redox Couple in the Mixed Metal Nitride Clusterfullerenes: Ce_xM_{3-x}N@C₈₄₋₈₈ (x= 1, 2; M= Sc, Y), *to be submitted*.
6. **Yang Zhang**, Sandra Schiemenz, Alexey A Popov* and Lothar Dunsch*, Paramagnetic NMR study and Electrochemical Behaviours of Lanthanide-Involved Mixed Metal Nitride LnSc₂N (Ln= La, Ce and Pr) in C₈₀:D_{5h} Carbon Cage, *to be submitted*.
7. **Yang Zhang**, Sandra Schiemenz, Alexey A Popov* and Lothar Dunsch*, Paramagnetic Properties of Ho-based Mixed Metal Nitride Clusterfullerenes: Ho_xM_{3-x}N@C₈₀ (M= Sc, Y, Lu; x= 1, 2), *to be submitted*.
8. **Yang Zhang**, Sandra Schiemenz, Alexey A Popov* and Lothar Dunsch*, Paramagnetic Chemical Shifts of Mixed Metal Nitride Clusterfullerenes LnSc₂N@C₈₀ (Ln= La, Ce, Pr, Nd, Tb, Dy, Ho, Er, Tm, Lu) in Solution NMR Depending on Lanthanide Ions, *under preparation*.

Jena, 01.05.2013

Yang Zhang

Ich erkläre, dass ich die vorliegende Arbeit selbstständig und nur unter Verwendung der angegebenen Hilfsmittel, persönlichen Mitteilungen und Quellen angefertigt habe.

Jena, 16.10.2013

Yang Zhang